

NASA Technical Memorandum 86016

Flow-Separation Patterns
on Symmetric Forebodies

(NASA-TM-86016) FLOW-SEPARATION PATTERNS ON
SYMMETRIC FOREBODIES (NASA) 142 p Avail:
NTIS EC A07/MF A01 CSCL 01A

N87-24397

Unclass

G3/02 0022088

Earl R. Keener

JANUARY 1986

NASA

NASA Technical Memorandum 86016

Flow-Separation Patterns on Symmetric Forebodies

Earl R. Keener

Ames Research Center

Moffett Field, California



National Aeronautics
and Space Administration

Scientific and Technical
Information Branch

1986

TABLE OF CONTENTS

	Page
NOMENCLATURE	v
SUMMARY	1
1. INTRODUCTION	1
2. EXPERIMENT	2
Test Facilities	2
Models	2
Test Conditions and Procedures	3
3. FLOW-VISUALIZATION METHODS	3
Schlieren Method	3
Vapor-Screen Method	3
Vapor-Trail Method	3
Oil-Flow (Streak) Method	3
Sublimation Method	4
4. SCHLIEREN, VAPOR-SCREEN, AND VAPOR-TRAIL FLOW VISUALIZATION STUDIES	4
Effect of Angle of Attack	5
Effects of Mach Number	5
Effects of Reynolds Number	6
Vortex Bursting	6
Effect of Blunt Nose	6
Position of Vortex Shedding	6
5. OIL-FLOW AND SUBLIMATION VISUALIZATION STUDIES	7
Effect of Oil on Force Measurements	7
Previous Oil-Flow Results	7
Pointed Tangent Ogive: Fineness Ratio = 3.5	7
Effect of Angle of Attack at $R_d = 0.3 \times 10^6$	7
Effect of Angle of Attack at $R_d = 0.5 \times 10^6$	8
Effect of Angle of Attack at $R_d = 0.8 \times 10^6$	8
Effects of Angle of Attack at $R_d = 2.0 \times 10^6$	15
Effects of Reynolds Number	15
Effects of Mach Number	15
Effect of Angle of Attack on Blunt-Nose 3.5-Ogive	16
Pointed Tangent Ogive: Fineness Ratio = 2.5	17
6. FLOW ANGLES AND SEPARATION BOUNDARIES	17
Measured Surface Flow Angles	17
Location of Separation	18
Flow-Separation Boundaries	18
Effects of Transition	18
7. CONCLUSION	18
Angle-of-Attack Effects	19
Reynolds Number and Mach Number Effects	19
Fineness-Ratio Effects	20
Bluntness Effects	20
REFERENCES	21

NOMENCLATURE

C_N	normal-force coefficient: (normal force)/ qS
C_Y	side-force coefficient: (side force)/ qS ; right side force is positive
d	reference base diameter
ℓ	reference length
M	free-stream Mach number
q	free-stream dynamic pressure
R_d	Reynolds number based on model base diameter, d
r_N	nose radius
S	reference base area
x	axial distance behind forebody tip
y	lateral distance above body axis in plane of symmetry
α	angle of attack
δ_e	potential-flow angle of edge of boundary layer
δ_N	semivortex angle of pointed nose
δ_s	surface-flow (skin-friction-line) angle from oil-flow tests
θ	meridian angle measured from bottom centerline; left side is positive looking upstream

Abbreviations used in oil-flow patterns:

B	swept, three-dimensional laminar separation bubble, which must be an open-vortex-type flow (because of axial flow in the bubble core) rather than a closed vortex, as in two-dimensional flow
BL	boundary layer
CI	crossflow-induced instability in the boundary layer causing near-streamwise vortices that are immersed in the laminar boundary layer; this is a three-dimensional transitional phenomenon of swept wings and inclined bodies
LS	primary laminar separation
L,T	laminar and turbulent boundary layer
SS	secondary separation (on lee side)
TR	boundary-layer transition from sublimation tests

PRECEDING PAGE BLANK NOT FILMED

TRS primary transitional boundary-layer separation; a type of primary separation pattern that consists of a combination of a swept laminar-separation “bubble” followed by (1) transition to turbulence, (2) reattachment of the turbulent boundary layer, and (3) primary separation of the turbulent boundary layer

TS primary turbulent boundary-layer separation

SUMMARY

Flow-visualization studies of ogival, parabolic, and conical forebodies were made in a comprehensive investigation of the various types of flow patterns. Schlieren, vapor-screen, oil-flow, and sublimation flow-visualization tests were conducted over an angle-of-attack range from 0° to 88° , over a Reynolds-number range from 0.3×10^6 to 2.0×10^6 (based on base diameter), and over a Mach number range from 0.1 to 2. Several forebody models were tested; however, most of the tests were made with a tangent ogive forebody having a fineness ratio of 3.5, chosen because this forebody experiences large asymmetric forces at high angles of attack at low speed. The principal effects of angle of attack, Reynolds number, and Mach number on the occurrence of vortices, the position of vortex shedding, the principal surface-flow-separation patterns, the magnitude of surface-flow angles, and the extent of laminar and turbulent flow for symmetric, asymmetric, and wake-like flow-separation regimes are presented.

It was found that the two-dimensional cylinder analogy was helpful in a qualitative sense in analyzing both the surface-flow patterns and the external flow field. The oil-flow studies showed three types of primary separation patterns at the higher Reynolds numbers owing to the influence of boundary-layer transition: primary-laminar, primary-transitional, and primary-turbulent separation. The effect of angle of attack and Reynolds number is to change the axial location of the onset and extent of the primary transitional and turbulent separation regions. Crossflow inflectional-instability vortices were observed on the windward surface at angles of attack from 5° to 55° . Their effect is to promote early transition. At low angles of attack, near 10° , an unexpected laminar-separation bubble occurs over the forward half of the forebody. At high angles of attack, at which vortex asymmetry occurs, the results support the proposition that the principal cause of vortex asymmetry is the hydrodynamic instability of the inviscid flow field. On the other hand, boundary-layer asymmetries also occur, especially at transitional Reynolds numbers; they contribute significantly to the flow asymmetry. The position of asymmetric vortex shedding moves forward with increasing angle of attack and with increasing Reynolds number, and moves rearward with increasing Mach number.

1. INTRODUCTION

The flight envelopes of modern aircraft and missiles have been extended to include very high angles of attack. The incidence range of interest for aircraft extends to about 60° during some maneuvers and to 90° for inadvertent excursions, including stall and spin. For some missile applications the angle of incidence can range to 180° . Hence, an extensive knowledge of the aerodynamics of wing and body combinations over this large incidence range is required.

The aerodynamics of bodies at high angles of attack is especially interesting because of the wide variety of flow phenomena that are dependent on Mach number and Reynolds number. Several excellent reviews of the development of the current knowledge of body aerodynamics were presented by Chapman et al. (ref. 1), Nielsen (ref. 2), Spearman (ref. 3), and Ericsson and Reding (ref. 4). Some of the principal body flow patterns were reviewed and their topology analyzed by Hunt (ref. 5) and by Tobak and Peake (refs. 6 and 7). Papers presenting flow-visualization results for long bodies that are pertinent to this paper are given in

references 8-23. They include flow-field studies using schlieren and vapor-screen flow-visualization techniques.

Four principal flow regimes have been found to occur on bodies as the angle of attack is increased: (1) unseparated, potential, vortex-free flow, (2) symmetric vortex flow, (3) steady, asymmetric vortex flow, and (4) unsteady wake-like vortex flow. The most spectacular flow phenomenon is the occurrence of a large asymmetric flow separation, with a large accompanying side force when a symmetric body with a pointed nose is pitched to high angles of attack. Force measurements and vapor-screen flow visualization have shown that the asymmetric flow is often relatively steady at first, and repeatable, rather than oscillating (switching) like a Karman vortex street. Research in 1950 by Allen and Perkins (ref. 10) led them to suggest the so-called impulsive flow analogy. They pointed out that there exists an analogy between the crossflow at various stations along the body and the development with time of the flow about a cylinder starting from rest. Thus, the flow in the cross-plane for the more forward sections contains a symmetric pair of vortices on the lee side. These vortices increase in strength with axial distance and eventually, if the body is long enough, are

asymmetrically shed to form a vortex street as viewed in the moving cross plane. Viewed with respect to the stationary body, the shed vortices appear to be fixed. As the angle of attack is increased, the asymmetric flow can occur first on the aft section of the body and move forward with increasing incidence. If the pointed forebody of a long body is slender, with a fineness ratio (ratio of length to base diameter) of 3 or more, the largest asymmetric flow and side force occurs when the flow asymmetry reaches the forebody (ref. 19). If the pointed forebody of a long body is not slender, with a fineness ratio of less than 3, or if the forebody is blunted, the side force is greatly reduced and is more sensitive to body imperfections, so that the side forces are less repeatable.

Vortex flow asymmetry has been suggested by Keener and Chapman (ref. 24) to be principally the effect of a hydrodynamic (inviscid) instability in the initially symmetric vortex formation and the interaction of the vortices (which increase in strength with incidence) with the surrounding potential flow field. In addition to the hydrodynamic instability, the vortex asymmetry is also strongly affected by boundary-layer (viscous) asymmetries resulting from transition and separation differences on each side of the body. Ericsson and Reding (ref. 4) have emphasized the importance of these boundary-layer asymmetries and have shown that the ratio of side force to normal force appears to peak in the critical Reynolds-number range. Asymmetry in either the vortex flow field or the boundary layer on the windward will cause symmetry in the other. It follows that it is important to understand the influence of each of these hydrodynamically and boundary-layer-induced asymmetries.

In addition to the foregoing studies of the long-body models, Keener and Chapman conducted a comprehensive investigation of several forebody models to determine the contribution of the forebody alone to body aerodynamics. The models represent the forebodies of aircraft or missiles. Results of force tests on the forebody models have been previously reported (refs. 24 to 30). Side forces were measured that were as large as 1.5 times the maximum normal force. These side forces varied considerably with Reynolds number and decreased, with increasing Mach number, to nearly zero at supersonic speeds. It was found that the angle of attack at onset of side force can be correlated with the nose semiapex angle δ_N by the simple formula, onset $\alpha = 2\delta_N$. Further, it was found that these side forces can be reduced or eliminated by nose bluntness, nose strakes, nose booms, boundary-layer trips, or by using forebodies with fineness ratio of 2.5, or less.

The flow field that occurs on bodies is still not well understood, and experiments are presently being conducted with flow-visualization methods. This paper presents photographs of the flow-field and surface-flow patterns that were observed when several flow-visualization methods were used. Schlieren and vapor-screen photographs show the occurrence, steadiness, and position of vortices and vortex shedding. Oil-flow and sublimation photographs give an indication of

typical surface-flow-separation patterns, the magnitude of surface-flow angles, and the extent of laminar and turbulent flow for symmetric, asymmetric, and wake-like flow-separation regimes. A wide range of test conditions are presented: angles of attack from 0° to 88° , Reynolds numbers from 0.3×10^6 to 2×10^6 (based on base diameter), and Mach numbers from 0.25 to 2. Most of the studies were made using a tangent-ogive forebody having a fineness ratio of 3.5.

The author wishes to extend his thanks to Gary Chapman and Murray Tobak, Ames Research Center, and to Dr. Mark Morkovin, Professor (retired), Illinois Institute of Technology, for their contributions to the analysis of the flow-visualization results.

2. EXPERIMENT

Test Facilities

Force, oil-flow, and sublimation tests were conducted at low speeds in the 12-Foot Pressure Wind Tunnel at Ames Research Center to determine the effect of Reynolds number. This is a variable-pressure, low-turbulence, continuous-flow facility with a Mach number range from 0.1 to 0.7 (with a model installed at high incidence) and a unit Reynolds number capability up to $2 \times 10^6/\text{m}$ at $M = 0.25$. The turbulence level was measured to be less than 0.3% of the free-stream velocity. Force, oil-flow, schlieren, and vapor-screen tests were conducted in the 6- by 6-Foot Transonic/Supersonic Wind Tunnel to determine the effect of transonic and supersonic Mach numbers from 0.25 to 2.0. This is a variable pressure, continuous-flow facility that provides continuous Mach number variations from 0.25 to 2.3. The test section has a slotted floor and ceiling with provisions for boundary-layer removal. The turbulence level is within 1.5% of the free-stream velocity.

Models

Flow-visualization tests were performed on all six of the forebody models (table 1) used in the force-test program (ref. 25). Five of the forebodies were bodies of revolution: three tangent ogives having fineness ratios (ratio of length to base diameter) of 2.5, 3.5, and 5.0; a paraboloid; and a 10° semiapex angle cone. All the forebodies, except the ogive with a 2.5 fineness ratio, had removable nose-tip sections of various nose radii up to 16.7% of the base radius. One ogive ($l/d = 3.5$) was provided with short strakes (7.9 cm long) at the nose starting at $x = 1.9$ cm. A cylindrical afterbody ($l/d = 3.5$) was available that could be clamped to the sting but remain free of the forebody. A sixth body was designed with an elliptic cross section and tangent-ogive planform that could be tested with either the major axis

(ℓ /(base width) = 3.5) or the minor axis (ℓ /(base width) = 5) perpendicular to the crossflow velocity, to match the respective planforms of the circular ogives with fineness ratios of 3.5 and 5, respectively. Throughout the paper, these ogive forebodies are referred to simply as the 2.5-, 3.5-, and 5.0-ogives.

Test Conditions and Procedures

The investigation was conducted over a Reynolds number range of 0.3×10^6 to 2×10^6 (based on the base diameter) at $M = 0.25$. This Reynolds number range includes most of the critical range of about 0.2×10^6 to 0.5×10^6 , for which boundary-layer transition for a circular cylinder occurs at $\theta = 90^\circ$, and extends into the supercritical range. Experiments were also conducted at Mach numbers from 0.1 to 2.0 at $R_d = 0.8 \times 10^6$. The angle of sideslip was zero. In each tunnel, two model-support setups were used to cover the angle-of-attack ranges. Figures 1 and 2 show the test installations. In the 12-ft tunnel the angle of attack ranges were from 0° to 45° and from 36° to 88° on the floor-mounted support system; and in the 6-ft tunnel the ranges were from 0° to 28° and from 28° to 58° on a centerbody, offset support system having 15° and 45° offset supports. Most of the flow-visualization tests were done with the 3.5-ogive forebody, using a pointed nose or blunt nose with either 8.3% or 16.7% bluntness (percent of nose to base radius) and a nose strake configuration. Selective tests were made with the remaining forebodies. Aerodynamic forces and moments were measured during each flow-visualization test, using an internal six-component, strain-gage balance.

3. FLOW-VISUALIZATION METHODS

Schlieren Method

The schlieren optical-flow-visualization method for observing density variations is described in references 31 and 32. Allen and Perkins (ref. 9) found that the schlieren image revealed the traces of the cores of the body vortices. The centers of the vortex cores are often clearly seen as abrupt changes in light intensity from dark to light. In the present test, the schlieren system in the 6-ft tunnel was used to observe the vortex traces at Mach numbers as low as 0.25.

Vapor-Screen Method

The vapor-screen method (refs. 10 and 31) is used to visualize a cross-sectional view of the vortices in a flow field and, hence, to determine the degree of asymmetry and unsteadiness. Allen and Perkins (ref. 10) found that the fog

that occurs in supersonic wind tunnels when the air is not dry can be used to make the vortices visible. Water is added to the tunnel until a moderately dense fog occurs. A thin sheet (screen) of bright light, produced by high-intensity mercury-vapor lamps or by a laser, is projected through the tunnel window. The light is scattered by the water particles, and the screen of light becomes highly visible. It was found that when the screen of light (vapor-screen) was viewed from behind, whether directly behind or at an angle, the traces of the vortices were visible as dark spots in a light background and that these dark spots could be photographed. It is thought that at supersonic speeds the water vapor forms ice crystals that are centrifuged out of the vortex centers; wakes from wings are also visible as dark areas in the light background.

Subsequently, it was found that the vortices could be observed and photographed at Mach numbers as low as 0.6; however, the vortices appear as white spots. When water is added to the tunnel at subsonic Mach numbers, the vapor condenses first in the vortex cores, similar to the vortices that appear over the wings of aircraft in highly humid weather. At Mach numbers near 1, combinations of both white and black areas can exist in the same photograph, formed by condensation or evaporation resulting from changes in local pressure and temperature, depending on the test conditions.

Figure 3 shows the vapor-screen apparatus in the 6-ft tunnel. This system used two light boxes, one on each side of the tunnel test section, each having six 1,000-W mercury-vapor lamps. A 70-mm still camera and a 16-mm variable-speed movie camera were mounted on the sting support to photograph the vortices.

Vapor-Trail Method

At subsonic speeds, the vortex trails can be illuminated and photographed by floodlights located 90° to the cameras (like ceiling floodlights) because the water-vapor condenses first in the vortex. The procedure consists of increasing the water-vapor content in the airstream until the vortices can be visualized as condensation trails. This method can provide a quick view of the vortex field at subsonic speeds as low as $M = 0.6$.

Oil-Flow (Streak) Method

A thorough description of the oil-flow-visualization method is given by Maltby (ref. 33). Basically, a mixture of oil and a pigment, such as titanium dioxide, is spread over the model, which is painted a contrasting background color (e.g., white on black). It has been found that if an oil of proper viscosity with respect to the surface shear stress is used, the oil will not always flow as a sheet but will often flow in

streaks in the direction of the surface skin-friction lines. Thus, skin-friction lines can be observed by the oil-flow method. Separation lines that are formed by the oil streaks (because oil accumulates at these lines) can also be seen by this method. Less frequently, the oil can be used to indicate transition location. However, this is more often done by the sublimation method (see Sublimation Method below). For the test herein, the pointed models were not painted black (which is normally done for use with white paint pigment for contrast), because the presence of rough flat black paint was found to drastically change the magnitude of the side forces (ref. 28). Instead, for most of the tests the bare models were coated uniformly with a mixture of lampblack in motor oils of various viscosities (depending on the velocity and incidence), together with a few drops of oleic acid for better dispersion of the lampblack in the oil. The blunt-nose model was painted black, and oil-flow photographs were obtained using white titanium dioxide.

When oil accumulates at a separation line, the oil forms a puddle that can obscure the local flow lines. It was found that the separation lines were formed more clearly if before the test the oil on the windward was wiped with a soft paper towel. The thin coat of oil that remained formed oil streaks that were adequate for visualization, and the separation lines were clear.

The most difficult part of the analysis of the oil-flow patterns is the interpretation of the external flow field from the surface patterns. Occasionally, there are two or more possible ways to connect the external flow field to the surface-oil-flow patterns (skin-friction lines). In recent years, several experimenters have been working on developing basic rules for interpreting the topology of oil-flow patterns, with the objective of simplifying the correct interpretation (e.g., Tobak and Peake, refs. 6 and 7). These guidelines are still incomplete, however, and there are strong differences of opinion about them, especially when they are applied to complex flow patterns. It should be acknowledged that photographs of complex flow patterns can be easily misinterpreted. Consequently, it is the author's opinion that sketches should not be presented unless accompanied by clear photographs.

Sublimation Method

The sublimation technique (described in ref. 33) was used for determining the position of boundary-layer transition. The models were sprayed with a saturated solution of biphenyl dissolved in trichloroethane 1,1,1. This solution dries on contact with the model surface and presents a white appearance. As the wind tunnel is operated, the process of sublimation takes place, with the turbulent boundary-layer regions subliming first and, therefore, showing up as clean areas on the model surface; the laminar regions remain white. Solutions other than biphenyl can be used to produce

different rates of sublimation for various tunnel operating conditions. Trichloroethane 1,1,1 solvent has recently been substituted for petroleum ether because it is considerably less flammable. Also, it was recently found that nonflammable Freon can often be used.

4. SCHLIEREN, VAPOR-SCREEN, AND VAPOR-TRAIL FLOW VISUALIZATION STUDIES

When the forebodies are pitched to high angles of attack, the flow separates on the sides and the separation sheets roll up into vortices in the leeward flow field. It is known from previous studies (refs. 1-7) that the vortices are usually first symmetrically oriented; then, as angle of attack is increased, one vortex is shed (discharged, detached). This means that the separation sheet ceases to feed vorticity into the vortex and the vortex is no longer "attached" to the surface by the separation sheet. The fluid-mechanical process at the vortex shedding is not clearly understood; however, recent descriptions by Peake and Tobak (ref. 6) suggest that separation sheets should not tear, but that the shedding topology should be continuous. The shedding position might be related to the accumulative strength of the vortices and to the resulting "crowding" of the vortices as the vortex strength builds. The theory demands, and experiment has shown, that a new vortex must form, so that the separation line should continue. Next, the vortex on the opposite side is shed, asymmetric to the first, and a new vortex starts on that side. The vortex characteristics for the present models were investigated using the schlieren and vapor-screen visualization methods.

Figures 4 and 5 are schlieren photographs of vortex traces for the 3.5- and 5-ogive forebodies, taken at $M = 0.25, 0.6$, and 2.0 at $R_d = 0.8 \times 10^6$ and 1.8×10^6 . Figure 6 shows the effect of Reynolds number on the vortex traces for the 3.5-ogive at $M = 0.6$ and $\alpha = 40^\circ$. Angles of attack and side-force coefficients are listed for each photograph. The dark rings in the photographs are caused by variations in density in the 12-cm-thick, 115-cm-diam tunnel windows. Figures 7 and 8 are photographs of vapor-screen cross sections of the vortex traces for $M = 0.6, 0.8$, and 2.0 . Sketches from movies are also included when the photographs were not clear. The movies are especially helpful because the vapor-screen position was moved over the length of the forebody while the camera was running. Side-force coefficients are listed on each figure, both with water vapor and without it. (The side-force coefficients without water vapor are not necessarily identical to those listed for the schlieren photographs, or to those reported in references 26 and 27, because they were determined from different parts of the test program.) Figure 9 shows a vapor-trail photograph for the 3.5-ogive for $M = 0.6$, $\alpha = 45^\circ$, and $R_d = 0.8 \times 10^6$. Figures 10 and 11 are plots of

the position of vortex shedding, determined from the schlieren photographs (figs. 4-6).

Effect of Angle of Attack

It was found that traces of the vortices could be observed in the schlieren system at Mach numbers as low as 0.25. The first schlieren photographs for which vortex traces are visible for the 3.5- and 5-ogives are for $\alpha = 40^\circ$ and 30° , respectively (figs. 4(a) and 5(a)). At these angles, vortex asymmetry must occur because large side-force coefficients occur (maximum $|C_Y| = 1.9$ and 2.6 , respectively). In most of the photographs, only one trace is seen. Therefore, this is interpreted to mean that this vortex trace represents the vortex that is farthest from the surface and that sheds first. Note that in each photograph for each ogive that the vortex is close to the surface over the forward half of the forebody and is shed near the midsection. As the angle of attack increases, the position of shedding moves forward to near the nose tip at $\alpha = 55^\circ$ and 40° , respectively, for the 3.5- and 5-ogives, and the first-shed vortex streams back almost parallel with the free stream. The angle ranges from 2° to 6° and is related to vortex strength, according to Thomson and Morrison (ref. 15). The first-shed vortex is strikingly visible for a long distance beyond the forebody base so that the vortex must be tightly wound (concentrated). In figure 5(a), a second vortex is faintly visible as a light streak close to the surface of the 5-ogive at $\alpha = 55^\circ$. Unlike the first vortex trace, the second vortex trace disappears at $x/\ell \approx 0.5$, which is believed to indicate vortex shedding. It is also probable that the disappearance of the vortex trace indicates the occurrence of vortex bursting. More will be said later about vortex shedding and bursting.

It is interesting that the asymmetric vortex pattern in the schlieren photograph of either the 3.5- or 5-ogive forebody at $\alpha = 55^\circ$ is in general agreement with the asymmetric smoke-flow pattern for the slender, pointed nose of an aircraft model presented by Chambers et al. (ref. 18), where a smoke-flow photograph shows the first vortex streaming almost streamwise off the nose tip and the second vortex is close to the surface.

Effects of Mach Number

$M = 0.6$ — The most noticeable effect of Mach number at $M = 0.6$ is observed in the schlieren photographs for the 3.5-ogive at $\alpha = 55^\circ$ (fig. 4(b), $R_d = 0.8 \times 10^6$). The trace of the first-shed vortex is much closer to the surface than it was at $M = 0.25$, and it disappears at $x/\ell \approx 0.2$. The side-force coefficient is much reduced from 1.9 at $M = 0.25$ for the 3.5-ogive to 0.8 at $M = 0.6$. Vapor-screen photographs (fig. 7(b)) at $\alpha = 55^\circ$, show a moderate asymmetry over the rear half. The vortex is not concentrated, but is quite

diffused, which explains why the vortex trace in the schlieren photograph disappears. It is interesting to consider the disappearance of the trace at $x/\ell \approx 0.2$. First of all, vortex shedding must occur where the trace disappears. Secondly, there is evidence that vortex bursting also occurs where the trace disappears. This vortex diffusion and the probability of vortex bursting is discussed in greater detail later in this section (Vortex Bursting).

For the 5-ogive (fig. 5(b)) at $R_d = 0.8 \times 10^6$, there is very little effect of Mach number in either the position of the schlieren vortex traces or in the side-force coefficients, which are large. In the vapor-screen photographs at $\alpha = 35^\circ$ to 58° (fig. 8(b)) the first-shed vortex is very prominent and tightly wound (concentrated) for the full length of the forebody. This is the same vortex that is prominently seen in the schlieren photographs. The second vortex is faintly visible near the surface, but is clearer than it was for the 3.5-ogive (fig. 4(b)).

With regard to the steadiness of the vortices, the vapor-screen movies show that the vortices are steady at $\alpha = 30^\circ$, 40° , and 45° for both the 3.5- and 5-ogive forebodies. At $\alpha = 50^\circ$ to 58° , the movies show that the vortices are unsteady, but not switching, at the rearward stations.

$M = 0.8$ — At $M = 0.8$ (fig. 5(c)), the schlieren vortex traces for the 5-ogive are closer to the surface than at $M = 0.6$, and the side force is slightly reduced from that at $M = 0.6$. The vapor-screen vortex pattern (fig. 8(b)) is still quite asymmetric at $M = 0.8$. At $\alpha = 40^\circ$ and 45° , a third vortex can be seen on the right side under the first vortex that has lifted off the surface. At $\alpha = 50^\circ$ to 58° , the vortex pattern is more diffused and unsteady; however, in the movies the sense of vortex pattern did not "switch" back and forth repeatedly. On the other hand, the sense did change between angles of attack of 50° and 55° and the side-force coefficient changed sign as well as magnitude from -2.0 to 1.2 .

$M = 2.0$ — As the Mach number increases to supersonic, the side force decreases to zero for even the slender forebody. Nevertheless, vortex traces can still be seen in the schlieren photographs at $\alpha = 30^\circ$ (figs. 4(d) and 5(e)) and 40° (fig. 4(d)). (Photographs at higher angles of attack were not clear.) For both forebodies, one vortex trace and one shock-wave trace can be seen so that the vortex trace must be from a symmetric pair of vortices. The vapor-screen photographs (fig. 8(c)) and movies show that vortex asymmetry did occur at $\alpha = 40^\circ$ for the 5-ogive forebody, even though the side forces were zero. These vortices appear to shed off the nose tip and to cluster high above the body. Shock waves were visible on each side of the vortices at $\alpha = 45^\circ$, as shown in the vapor-screen sketches (fig. 8(c)).

The black line close to the body and nearly parallel to the body in the schlieren photographs is the trace of a shock wave located between the vortices. Similar shock lines that are nearly parallel to the body have appeared in previous tests, for

example, in those of Thomson and Morrison (ref. 15) and Jones and O'Hare (ref. 16).

At $\alpha = 55^\circ$ for the 5-ogive, the flow pattern changed to a hazy, elongated wake. Within this wake, the flow is probably not steady, and there probably are vortices that are shed rapidly in the alternating manner of the wake of a swept cylinder. This shedding could be regular or irregular, according to the Reynolds number.

The vortex asymmetry at $M = 2$ is not surprising, of course, since the first vortex asymmetry that was photographed and reported occurred at $M = 2$ on bodies tested in the Ames 1-by 3-Foot Supersonic Wind Tunnel by Allen and Perkins (ref. 10) and others (e.g., refs. 11-13). As a result of their studies, Allen and Perkins proposed the impulsive flow analogy (ref. 10), which is described in the Introduction.

It has been suggested (ref. 1) that the absence of a side force is the result of the reduction of the contribution of the leeside pressures to the total force. In addition, the local shock waves isolate the vortex flow-field pressures from the body. This means that whatever asymmetric pressures might exist in the vortex flow field are not propagated to the surface to affect the pressures and the boundary-layer separation position on each side.

The foregoing schlieren and vapor-screen results do not give any additional evidence to explain why the side force for the 3.5-ogive decreases at a lower Mach number than for the 5-ogive. One conjecture is that the local Mach number on each side near the nose is higher for the forebody with the lower fineness ratio.

Effects of Reynolds Number

The most noticeable effect of Reynolds number in the available photographs for the 3.5-ogive can be seen in the results for $M = 0.6$ at $\alpha = 40^\circ$ (fig. 6). At $R_d = 0.8 \times 10^6$, a vortex trace is visible for the full length of the forebody. Vortex asymmetry must occur, because there is an appreciable side force ($C_Y = 1.0$). Vortex shedding probably starts at $x/\ell \approx 0.5$, where a small break in the vortex trace occurs. In contrast, at $R_d = 1.8 \times 10^6$ and $\alpha = 40^\circ$, the first asymmetric vortex is shed at $x/\ell \approx 0.3$. Therefore, the position of vortex shedding (plotted in fig. 10) moves forward with increasing Reynolds number.

For the 5-ogive the most obvious effect of Reynolds number at $M = 0.6$ and $\alpha = 30^\circ, 40^\circ$, and 55° (figs. 5(b) and (c)) is the much lower side-force coefficient at $R_d = 1.8 \times 10^6$ ($C_Y = 0.6$) than at $R_d = 0.8 \times 10^6$ ($C_Y = 2.5$). (Reference 27 shows that the side-force coefficient reached a maximum of 1.4 at $\alpha = 48^\circ$). These low values of side force indicate that there is very little flow asymmetry at $\alpha = 30^\circ, 40^\circ$, and 55° . The approximate positions of vortex shedding (plotted in fig. 11) for the first and second vortices are almost symmetric at $R_d = 1.8 \times 10^6$ and $\alpha = 40^\circ$ and 55° . No vapor-screen photographs were taken at $R_d = 1.8 \times 10^6$.

Vortex Bursting

It is interesting to consider the cause of the occurrence of the wave in the vortex trace in the schlieren photographs in figure 4(c). The wave must be caused by some kind of instability in the vortex. The wave is followed by the disappearance of the trace at $x/\ell \approx 0.2$, immediately downstream of the wave.

The wave and diffusion were investigated further, using the vapor-trail method. Figure 9 shows that the wave in the vortex trace appears in the vapor-trail photographs at $M = 0.6, R_d = 1.8 \times 10^6$, and $\alpha = 45^\circ$ (5° greater than that for the schlieren photograph). When these vortex trails were observed from the side windows, the vortices were very distinct and tightly wound near the nose as long as they were attached. Note that a distinct wave (instability) occurs where the first vortex is shed, which must be similar to the wave in the schlieren photographs at $\alpha = 40^\circ$ and $R_d = 1.8 \times 10^6$ (fig. 4(c)). Also, the wave appears, in some respects, to be similar to the so-called Crow instability that occurs in the vortex trails off wing tips. Immediately downstream of the wave, it can clearly be seen in the vapor floodlight that the vortex is diffused over an expanding cross-sectional area, which explains why the vortex disappears in the schlieren photographs (fig. 4(c)). It is speculated that the vortex burst phenomenon occurs in this case when the vortex detaches. In water-tunnel flow-visualization tests (ref. 28), vortex bursting has been clearly observed off the forebody of aircraft models in the vicinity of the canopy.

Effects of Blunt Nose

Vapor screen tests were made at $M = 0.6$ for the 3.5-ogive with the 8.3% bluntness-ratio nose. At $\alpha = 55^\circ$ an interesting effect of bluntness occurred, which is shown in figure 7(a). A vortex pair is seen above the main vortex in the first photograph at $x/\ell = 0.48$. In the movies, this vortex pair is clearly seen to rise off the body above the primary vortex pair and to rotate in a direction counter to that of the main vortex pair (in the same direction as secondary vortices). Although the source of the shedding of this vortex pair is not known, even from the oil-flow studies, it is assumed that the vortices originate at the blunt nose.

Position of Vortex Shedding

The longitudinal location at which the first and second vortices were shed from the 3.5- and 5-ogives was determined from the schlieren photographs for Mach numbers of 0.25 and 0.6. The results are presented in figures 10 and 11.

Method of measuring— Figures 10 and 11 include sketches that show the method that was used to determine the positions of vortex shedding.

At angles of attack at which the vortex traces become visible, the vortex pattern is often asymmetric. The longitudinal and vertical positions (x/d and y/d) for *shedding of the first vortex* was taken to be the point at which the vortex first starts to curve away from the body (the break in curvature indicated by a circle in the sketch).

The *second-shed vortex* can be seen at the higher angles of attack close to the body. It often disappears before it can be seen to curve away from the body. Consequently, the location of shedding of the second vortex is taken to be the point in the schlieren photograph where the vortex disappears, as discussed previously. Where discernible in the original photographs, the position of shedding of the second vortex is plotted in figures 10 and 11.

The *third-shed vortex* is discernible for the 5-ogive (fig. 8), and, like the second vortex, it disappears where it is shed. This estimated position of shedding is plotted in figure 11.

Measurements of the position of vortex shedding— Although there is considerable scatter in the measured positions for vortex shedding in figures 9 and 10 for $M = 0.6$, several trends are apparent. As expected, the positions where shedding of the vortices occurs move forward with increasing angle of attack. Secondly, these positions also move forward with increasing Reynolds number, which can be seen in figure 10 for the 3.5-ogive at $\alpha = 40^\circ$ and $R_d = 0.8 \times 10^6$ and 1.8×10^6 . This is also seen in figure 11 for the 5-ogive at $\alpha = 30^\circ$ and 40° , by comparing the positions of the first-shed vortex at $R_d = 0.8 \times 10^6$ and 1.8×10^6 . Note that the first and second vortices are almost symmetric and that the side-force coefficients are much lower at $R_d = 1.8 \times 10^6$. It is also observed from the available data for the second and third vortices for the 5-ogive at $R_d = 1.8 \times 10^6$ (fig. 11) that the positions for vortex shedding are spaced widely apart at the lower angles of attack when the flow asymmetry is large and that they move closer together as the angle of attack increases.

5. OIL-FLOW AND SUBLIMATION VISUALIZATION STUDIES

Surface-flow patterns over a wide range of angles of attack and at several Reynolds numbers are illustrated with both oil-flow and sublimation results in figures 12 to 25. Most of the oil-flow tests were conducted in the 12-ft wind tunnel. Force measurements with and without oil on the model are presented in figure 12. Preliminary oil-flow results are shown in figure 13, followed by new oil-flow and sublimation results in figures 14 to 25. The presentation begins with the lowest Reynolds number tested, $R_d = 0.3 \times 10^6$

(figs. 14 and 15), and progresses through increasing Reynolds numbers, $R_d = 0.5 \times 10^6$, 0.8×10^6 , and 2×10^6 (figs. 16–21). This presentation includes sketches of the oil-flow pattern for $R_d = 0.8 \times 10^6$ (fig. 19) and a proposed flow-field model for $\alpha = 40^\circ$ and $R_d = 0.8 \times 10^6$ (fig. 20). Figures 22–24 summarize the effects of Reynolds number, Mach number, and bluntness, respectively, on the oil-flow patterns. Figure 25 presents oil-flow patterns for the 2.5-ogive forebody.

Effect of Oil on Force Measurements

Force measurements with and without the presence of lampblack/oil mixture for the pointed 3.5-ogive forebody, measured during the present test at $M = 0.25$ and $R_d = 0.8 \times 10^6$ and 2×10^6 , are compared in figure 12. The presence of the oil did not change the side force for most of the tests, except at $\alpha = 60^\circ$, where the side force was almost doubled by the presence of the oil. The oil probably increases the asymmetry of the boundary layer. Note that in these oil-flow tests it was less important that the magnitude of the side forces be essentially the same when measured with and without oil, than it was that the results be representative of strong asymmetric flow. However, one should always measure the side force during all high-angle-of-attack tests with oil, because of the possible effects of the oil on the forces.

Previous Oil-Flow Results

The oil-flow photographs in figure 13 were presented previously in reference 25. The figure shows the strong flow asymmetry on the lee for the pointed 3.5-ogive forebody at $\alpha = 55^\circ$, $M = 0.25$, and $R_d = 0.8 \times 10^6$. These photographs also show the dramatic effect of bluntness (8% of base radius) and short (0.15-ℓ), narrow (0.006-ℓ) strakes, both of which induce symmetric flow patterns and reduce or eliminate measured side forces.

Pointed Tangent Ogive: Fineness Ratio = 3.5

Effects of angle of attack at $R_d = 0.3 \times 10^6$

It is interesting to compare the Reynolds number effects for the 3.5-ogive forebody with those in the critical Reynolds number range of 0.1×10^6 to 0.5×10^6 , based on the base diameter (ref. 20), for a two-dimensional circular cylinder placed with its axis transverse to the flow. In this critical Reynolds number range, the primary flow-separation for the cylinder changes from a subcritical, laminar-type of separation, located at $\theta \approx 80^\circ$, through a transitional-type of separation, located at $\theta \approx 135^\circ$, to a supercritical, turbulent-type of separation, located at $\theta \approx 110^\circ$. According to

reference 4, the effective local Reynolds number on a body at angle of attack should be approximately $R_d/\sin 2\alpha$. At a Reynolds number of 0.3×10^6 for these oil-flow photographs, the effective local Reynolds numbers for $20^\circ < \alpha < 90^\circ$ are in the transitional region for the rearward half of the forebody, but are subcritical for the forward 25% of the forebody, where vortex formation originates at high incidence. This Reynolds number of $R_d = 0.3 \times 10^6$ was the lowest that seemed feasible for testing this model because of the low dynamic pressure of only 1436 N/m^2 , or 30 lb/ft^2 .

$\alpha = 0^\circ$ — At $\alpha = 0^\circ$ (fig. 14(a)) the oil flow was very sluggish; consequently, there were no flow streaks, even though No. 5 weight SAE oil was used. Attempts with lighter weight oil were unsuccessful because the oil did not dry during the run and flowed from the force of gravity after the air flow was stopped. The boundary-layer flow must be laminar. If the transition Reynolds number (based on length of laminar flow) is at least 3×10^6 , as suggested in reference 22, then boundary-layer transition on the 3.5-ogive should occur at about $x/\ell \approx 2.86$, which is more than the length of that forebody ($\ell = 53.3 \text{ cm}$).

$\alpha = 20^\circ$ — At $\alpha = 20^\circ$ (fig. 14(b)) there are no flow streaks in the region around the bottom centerline. However, in the vicinity of $\theta = 45^\circ$ there are weak flow streaks that disappear into a sheet of accumulated oil between $\theta = 90^\circ$ and 135° . This is followed by light scrubbing (thinning) of the oil in the vicinity of $\theta = 135^\circ$ to 225° , which indicates either transition to turbulent flow or separation. There are no distinct flow streaks, nor clear evidence of vortex flow; however, separation and vortex flow should occur at this angle of attack since the angle of attack is greater than the nose half-angle of 16.2° . (This is a common rule of thumb for vortex separation to occur on cones (ref. 8).) The flow does appear to be streamwise and slightly spreading away from $\theta = 135^\circ$. A sublimation test was made at this test condition; the resulting photographs (fig. 15(a)) indicate that the boundary layer is laminar up to $\theta \approx 135^\circ$, where transition to turbulence occurs.

$\alpha = 30^\circ$ — At $\alpha = 30^\circ$ (fig. 14(c)), there is considerably more scrubbing in the oil flow and the flow streaks are clearer. It is seen that the boundary layer separates along the full length of the forebody at $\theta \approx \pm 100^\circ$. This location indicates that a subcritical, laminar-type of separation is occurring, since laminar separation of a circular cylinder occurs at $\theta = 80^\circ$ to 100° . Note the second pair of separation lines on the lee of the first pair. The oil-flow streaks on both sides of each separation line are directed toward the second pair of separation lines, indicating that these are secondary flow-separation lines. They result from the separation of the reversed flow from the principal vortices that originally reattached at $\theta = 180^\circ$.

$\alpha = 40^\circ$ — At $\alpha = 40^\circ$ (fig. 14(d)), a small side force ($C_Y = 0.6$) occurs. It is clearly evident that subcritical, laminar-type separation lines occur at $\theta \approx \pm 90^\circ$ and that secondary separation lines occur at $\theta \approx \pm 160^\circ$, both over the full length of the forebody. There is no obvious asymmetry in the oil-flow streaks. The sublimation photographs in figure 15(b) show that transition occurs at $\theta > 90^\circ$, verifying that the primary separation at $\theta = \pm 90^\circ$ is laminar.

$\alpha = 45^\circ$ — At $\alpha = 45^\circ$ (fig. 14(e)), the side force is large ($C_Y = 1.8$). Full-length, subcritical, laminar-type separation lines occur at $\theta \approx \pm 90^\circ$, but they are not obviously asymmetric. Secondary flow-separation lines occur that are approximately symmetric over the forward two thirds of the forebody length. Over the rearward third of the forebody, the flow is obviously asymmetric on the lee. It would appear that the vortex on the left side lifts off the surface, since the secondary separation line disappears. This would rotate the resultant force to the right, giving a right side force, as measured.

$\alpha = 55^\circ$ — At $\alpha = 55^\circ$ (fig. 14(f)), the side force is maximum ($C_Y = 3.4$), and full-length, subcritical laminar-type separation lines occur that appear to be asymmetrically located at $\theta \approx 80^\circ$ to 90° on the left side and at $\theta \approx -90^\circ$ to -100° on the right side. Secondary separation lines begin at the nose tip but extend to only $x/\ell \approx 0.25$. Over the rest of the length the flow is obviously asymmetric on the lee.

Effect of Angle of Attack at $R_d = 0.5 \times 10^6$

One oil-flow test was made at $R_d = 0.5 \times 10^6$ at $\alpha = 40^\circ$. The oil-flow lines are clearer at this Reynolds number than at $R_d = 0.3 \times 10^6$. Both laminar and secondary separation lines extend over the full length of the forebody, similar to those at $R_d = 0.3 \times 10^6$. The flow lines between the secondary separation lines are not symmetrical over the rear third of the forebody, and there is a small side force ($C_Y = 0.6$).

One obvious difference from the lower Reynolds number of 0.3×10^6 is the appearance of an additional heavy oil line between the laminar and secondary separation lines on each side, extending forward from the base to $x/\ell = 0.4$. Based on the oil-flow results at $R_d = 0.8 \times 10^6$ and $\alpha = 40^\circ$ (discussed in the next section), the boundary layer is experiencing primary transitional separation (laminar separation, turbulent reattachment, then turbulent separation).

Effects of Angle of Attack at $R_d = 0.8 \times 10^6$

This section presents a comprehensive documentation of the flow patterns for the pointed 3.5-ogive at $R_d = 0.8 \times 10^6$ from oil-flow and sublimation methods (figs. 17 and 18), along with detailed interpretive sketches. Sketches of the

oil-flow and sublimation patterns on the body surface are presented in figure 19 as they would appear if the body surface were "unwrapped," showing the principal features of the surface-flow patterns (skin-friction, separation, and transition lines). This Reynolds number is slightly above the critical Reynolds number range of 0.1×10^6 to 0.5×10^6 for a circular cylinder (ref. 20), and, therefore, the effects of boundary-layer transition are included. The oil-flow results were taken at 5° increments in angle of attack to ensure that flow patterns would be obtained in each of the four flow regimes: free-vortex flow; symmetric-vortex flow; steady, asymmetric vortex flow; and unsteady, wake-like vortex flow.

In the following detailed discussion the reader will be presented with a surprising variety of complex flow patterns. However, it was found that these complex looking patterns are often a combination of several simple flow patterns that are very similar to the two-dimensional flow patterns that are known to occur on a circular cylinder with increasing Reynolds number (e.g., see Morkovin, ref. 34). This similarity is called the two-dimensional cylinder analogy and these flow patterns will be described as the discussion progresses. It is also helpful to think in terms of local (localized, embedded) and global (holographic) flow features. With these comments in mind, it is recommended that the reader first read the discussion of the results for $\alpha = 40^\circ$ (below) in which four of the basic flow patterns are discussed.

$\alpha = 0^\circ$ — At $\alpha = 0$ (fig. 17(a)), the lampblack oil-flow streaks are much clearer than they are at the lower Reynolds numbers. Regularly spaced, prominent oil streaks are formed. At $\alpha > 0$, similar streaks result from local vortices induced by local instability caused by the crossflow over the body. However, at $\alpha = 0$ the heavy streaks must not be an indication of a vortex array but must result from the local interaction of the flow of air over the combination of oil and pigment. Also, the possible occurrence of local vortices in the boundary-layer flow was not verified by the sublimation tests at $\alpha = 0$ (fig. 18(a)). Note the many fine, U-shaped oil streaks in the close-up view (fig. 17(a)). The spaces between the more prominent oil streaks are covered with these small, fine, U-shaped streaks, and the trailing lines appear to merge, forming the heavier streaks. The occurrence of the U-shaped streaks is induced locally by the collection of many small deposits of the fine-grain lampblack pigment, so that filaments of lampblack are silted downstream from both edges of the deposit, forming the U-shaped streaks.

The location of boundary-layer transition at this Reynolds number should be rearward of any substantial and favorable pressure gradient, which excludes most of the forebody from turbulent flow. Transition Reynolds numbers of 3×10^6 or higher are common for cones (ref. 22). The Reynolds number at the base, based on the length of 53.55 cm, is 2.8×10^6 . The sublimation photograph at $\alpha = 0$ (fig. 18(a)) indicates that the boundary layer was laminar over the length of the forebody.

$\alpha = 5^\circ$ — At $\alpha = 5^\circ$ (figs. 17(b) and 19(a)), there is a noticeable crossflow owing to incidence. The magnitude of the local oil-streak angle is astounding because the surface oil-flow angle δ_s on the sides at $\theta = \pm 90^\circ$ is as high as 24° at $x/l = 0.2$, which is about 4.8α , or 2.4 times the potential external flow angle¹ δ_e of 2α . Rearward of $x/l = 0.2$, δ_s decreases with length to about 10° at $x/l = 0.5$ to 1.0 for a cylinder at $\alpha = 5^\circ$ and $\theta = 90^\circ$. It is interesting that the local oil-streak angle of 10° over the rear half of the forebody is equal to the potential-flow angle at the edge of the boundary layer. The significantly higher oil-streak angles ahead of $x/l = 0.5$ must be induced by a pressure gradient normal to the potential-flow streamlines at the edge of the boundary layer that is larger than that for a circular cylinder. The result is that the local velocity distribution in the boundary layer between the edge and the surface is highly skewed in the direction ahead of the inviscid streamline. This is one of several flow features that are not predicted by the two-dimensional cylinder crossflow patterns.

In the forward half of the forebody the oil thickens for a short distance on the lee, forming a patch of oil. This is probably the accumulation of oil for a thickening laminar boundary layer (fig. 17(b)). However, note that within the patch of oil there are heavy oil streaks that are at an angle to the local skin-friction lines and that are regularly spaced. It was thought that these heavy oil streaks were related to inflectional instability; however, no such streaks or striations appeared in this region in the sublimation test (fig. 18(b)). On the other hand, if boundary-layer transition is occurring, the transition process can be highly intermittent, causing the multiple oil streaks. These heavy oil streaks appear to converge downstream, as if in the process of forming a turbulent line of separation (in which skin-friction lines coalesce from both the windward and the lee). On the lee of the thickened patch of oil, the oil is scrubbed (thinned) and the sublimation material is sublimed, indicating that transition occurred and that the flow is turbulent to the base. This local transitional disturbance is one of the local features of forebody flows at low incidences and transitional Reynolds numbers.

As soon as a body departs from zero angle of attack, the crossflow, in general, and the large skewness, in particular, increase the possibility of local boundary-layer inflectional instability. This is similar to the instability that occurs on swept wings and that results in nearly streamwise arrays of vortices in the laminar boundary layer and induces early transition (e.g., refs. 35 to 38). The appearance of striations

¹The external flow angle δ_e is determined by calculating, using potential theory, the crossflow component of velocity V_N (normal to the axis and parallel to the surface) at $\theta = 90^\circ$ for a two-dimensional cylinder. Crossflow velocity V_N is twice the crossflow component of the free-stream velocity $V_{N,\infty}$. This velocity of $2V_{N,\infty}$ is then combined with the axial component of the free-stream velocity, $V_{\infty} \cos \alpha$. The resulting flow angle is $\delta_e = 2 \tan \alpha$, or 2α for small angles of attack.

in the biphenyl material in the sublimation test (fig. 18(b)) indicates the presence of a streamwise array of vortices and confirms the occurrence of crossflow inflectional instability in the boundary layer. These striations can be clearly seen and are shown in the close-up photograph; they appear on the windward surface of the model from the midsection forward to the nose tip. Inflectional instability tends to promote local transition to turbulence over the forward half of the forebody where the flow is expected to be laminar. This is one mechanism by which the shape of the forebody can affect the local flow conditions through the distribution of crossflow angle along the length. The inflectional instability is another feature not predicted by the two-dimensional cylinder crossflow patterns.

Transition occurs along an oblique irregular line that starts at $x/l \approx 0.5$ and $\theta \approx 90^\circ$, which is approximately the location of the leeward edge of the patch of oil. With increasing length, the transition line moves rapidly to the windward to $\theta \approx 45^\circ$ near the base. On the top surface ($\theta > 90^\circ$) transition "wraps" around the location of the patch of oil. (For some unknown reason the sublimation material on the right side, top view, was completely sublimed.) The location of transition was added to the sketch in figure 19(a). It is surprising that transition moves forward so quickly at the small incidence of $\alpha = 5^\circ$. One effect that induces early transition is the formation of the minimum pressure line and the adverse pressure gradient due to the crossflow. The other effect shown here is the boundary-layer crossflow inflectional instability that occurs at low angles of attack; it must cause transition earlier than if the boundary layer was completely laminar with no crossflow instability vortices. This influence of crossflow instability on early transition is an important effect not occurring in the crossflow patterns for a two-dimensional cylinder.

$\alpha = 10^\circ$ — At $\alpha = 10^\circ$ (figs. 17(c) and 19(b)), the oil-streak angles on the sides at $\theta = \pm 90^\circ$ are about 41° near the nose. This is about twice the potential angle of 20° , so that once again the boundary-layer flow is highly skewed over the forward part of the forebody. Sublimation photographs (fig. 18(c)) show that an array of regularly spaced striations occurred on the windward surface from near the base forward to the nose tip, indicating the existence of an array of vortices from crossflow inflectional instability.

At $\alpha = 10^\circ$, the oil-flow pattern is considerably different from that at $\alpha = 5^\circ$. The patch of thickened oil that occurred at $\alpha = 5^\circ$ develops into a band of oil on each side at $\alpha = 10^\circ$, located at $\theta \approx \pm 135^\circ$ and extending from the nose tip to $x/l = 0.45$, where the ends of the oil bands on each side appear to be swept away by the crossflow behind them. It is believed that primary laminar separation (LS in the sketch in fig. 19(b)) occurs at the band of oil. The term "primary" refers to the separation of the windward flow in contrast to "secondary" separation of the leeward flow at higher angles of attack. The symmetric separation lines on each side exist

to the nose tip. However, according to conical-flow concepts, local separation at the nose tip was not expected until $\alpha \approx \delta_N = 16.5^\circ$, the nose semiapex angle for the 3.5-ogive.

In the region away from the nose at $0.2 < x/l < 0.45$ on the lee of the band of oil, the oil streaks continue toward the leeward, instead of reversing direction, as expected, behind a separation line. This flow pattern indicates that the boundary layer reattaches. One way that this can happen is if transition occurs in the separated shear layer, similar to the flow in a two-dimensional bubble or in the swept bubble on the leading edge of a swept wing. In these cases, the separated streamlines spread or bend because of the turbulence, and the flow reattaches to the surface. (There is still no accurate description of this attaching mechanism.) In this regard, one can examine the sublimation photos (fig. 18(c)) to determine if reattachment occurs by looking for a sublimed area on the lee surface. The biphenyl remained on the surface completely around the nose on the forward third of the forebody, except for two narrow sublimed streaks at $\theta \approx \pm 160^\circ$. When the sublimation photograph is superimposed over the oil-flow photograph, each sublimed streak falls on the leeward of the separation oil lines, as expected for reattached flow. The remaining sublimation material between the two sublimed streaks at $\theta \approx 170^\circ$ to 110° is not as heavy as the sublimation material on the windward, but its existence makes the interpretation more difficult. The effective Reynolds number is low in this region close to the nose, so that the flow should usually be completely separated into a pair of separation vortices with reattachment at $\theta = 180^\circ$. However, consider also that there is a strong axial flow on the lee of the nose, because the local surface angle is positive ($\delta_N = 6.5^\circ$). This strong axial flow might be capable of forcing the separated windward flow to reattach on the leeward surface at $\theta < 180^\circ$. As stated before, reattachment can be seen farther rearward at $0.2 < x/l < 0.45$. The original photographs indicate that the leeward flow is axially directed all the way to the nose, so that the strong axial flow reattaches the laminar separated flow all the way forward to the nose. Such reattached flow is often called a laminar separation bubble.

The complete flow pattern follows in general the impulsive-flow analogy of Allen and Perkins (ref. 10), which is frequently used as a guide to the development of cross-sectional flow fields with body length at high angles of attack. It is interesting at this point to look at the flow-visualization results obtained by Bouard and Coutanceau (fig. 6(a) in ref. 39) for an impulsively started circular cylinder. Their first photograph for $R_d = 9500$ shows a pair of small vortices with their centers at $\theta \approx \pm 140^\circ$. This separated flow does not reattach until $\theta = 180^\circ$. From these photographs it can be conjectured that a strong axial flow, as in the case of the pointed nose of the 3.5-ogive could reattach the flow. It is even possible that the separated laminar boundary layer reattaches without transition as a result of the axial flow. Note that this axial flow and the effects of crossflow inflectional instability are not part of the two-dimensional

cylinder flow analogy; however, inflectional instability vortices are not expected to affect the separation line.

An interesting detail occurs on the left side where the laminar separation is interrupted by a disturbance at the junction of the nose tip. This illustrates that one can expect the frequent occurrence of highly intermittent flow, locally wiping out the separation line.

Rearward of $x/\ell = 0.45$, the band of oil does not exist, and the oil is scrubbed, indicating that boundary-layer transition (TR) occurs on the sides and terminates the laminar separation. The weak laminar-separation vortex must be swept away in the crossflow. The sublimation photographs (fig. 18(c)) show that transition did occur, similar to that which occurred at $\alpha = 5^\circ$, along an irregular oblique line starting from the rearward end of the laminar separation line. This transition line has been added to the sketch in figure 19(b).

Near the base, the oil streaks on the lee (fig. 17(c)) converge slightly, indicating that turbulent separation is imminent in this region.

$\alpha = 15^\circ$ — At $\alpha = 15^\circ$ (fig. 17(d)), a narrow line of oil occurs at $\theta = \pm 130^\circ$, indicating that primary laminar separation occurs from the nose tip back to $x/\ell \approx 0.4$. The features of the laminar separation pattern are similar to those just described for $\alpha = 10^\circ$. Note that the leeward flow deflection angle at the nose tip is only 1.5° ($\delta_N = 16.5^\circ$) so that the influence of axial flow on the lee of the nose tip is diminished whereas the crossflow is increased.

Rearward of the laminar separation line ($x/\ell > 0.4$), the oil streaks from the flow of the turbulent boundary layer curve and merge into a common oil line at $\theta \approx \pm 150^\circ$. This oil line marks the first occurrence of primary turbulent separation, which appeared to be incipient at $\alpha = 10^\circ$. On the lee of the turbulent-separation line, crossflow reversal can clearly be seen in the oil streaks.

The sublimation photographs (fig. 18(d)) verify that the boundary layer is turbulent in the rearward region. Starting at $x/\ell \approx 0.4$, where the laminar separation line ends, the transition line clearly moves to the windward of the separation line, ending almost parallel to $\theta \approx \pm 45^\circ$ at the base. Also, striations are plainly seen on the sides from $x/\ell \approx 0.80$ to the nose. The vortices from the crossflow inflectional instability must contribute to early boundary-layer transition.

Another feature of the flow at $\alpha = 15^\circ$ is that the turbulent-separation oil line on the rearward half extends forward to $x/\ell = 0.15$, which is far ahead of the rearward end of the laminar-separation line. The oil streaks flow toward this oil line from both sides, as they should for a separation line. This overlapping region of both laminar and turbulent separation is the first appearance of primary transitional separation, which is more complex than earlier simple-vortex concepts and becomes more prominent as angle of attack increases.

$\alpha = 20^\circ$ — At $\alpha = 20^\circ$ (figs. 17(e) and 19(c)), the principal features in the oil-flow patterns are the three types of primary separation: laminar, transitional, and turbulent. First, there is primary laminar separation in the forward region at a meridional angle of $\theta \approx \pm 135^\circ$. Several additional close-up photographs are presented that show details of the flow. On the windward surface, the flow pattern of the oil-streaks is especially clear as they turn downstream into the band of oil on the sides. This is a good example of the topology of skin-friction lines approaching a separation line. It is of particular interest to note how clearly the narrow band of oil can be seen (in the close-up photographs) to exist to the tip and to cross the nose tip on the leeward side, immediately behind the sharp point. This indicates that the primary laminar-separation line makes a loop around the lee surface of the tip. The minute flow pattern close to the nose tip is still not as clear as desired. Doubling or tripling the size of the model would probably not produce clearer results; nor is it possible to make meaningful flow-field measurements using probes or laser velocimetry close to the nose tip. Yet, it is close to the nose tip that the principal flow pattern is determined for the rest of the body.

The second primary separation pattern is primary transitional separation, which extends from $x/\ell = 0.35$ as far forward as $x/\ell = 0.15$, similar to these patterns for $\alpha = 15^\circ$.

The third primary separation pattern is primary turbulent separation, which occurs at $\theta \approx \pm 140^\circ$, rearward of $x/\ell \approx 0.35$, the end of the primary laminar separation line. In this region, the boundary layer is turbulent before it reaches the sides, which is verified in the sublimation photographs (fig. 18(e)). Note that the white sublimation material ends at the oil line at $x/\ell \approx 0.35$, indicating transition at this line. Rearward of $x/\ell \approx 0.35$, where the oil line disappears, the sublimation material ends along a ragged path of decreasing meridional angle to the windward.

Comparisons of the sublimation photographs from the 6-ft and the 12-ft tunnels are shown in figure 18(e). The location of boundary-layer transition is similar in both tunnels, except that the location is slightly farther forward in the 6-ft tunnel and slightly closer to the windward attachment meridian. This was expected because of the higher turbulence level in the 6-ft tunnel (about 1.5% of the free-stream velocity) than in the 12-ft tunnel (about 0.5%).

Similar to $\alpha = 5^\circ$, 10° , and 15° , the sublimation photographs in figure 18(e) for $\alpha = 20^\circ$ show striations in the sublimation material that can be seen as far forward as the nose. The striations, which are oriented roughly in the same direction as the oil streaks, indicate the presence of vortices that are produced in the boundary layer by crossflow inflectional instability.

Finally, at $\theta \approx \pm 160^\circ$, there is the first appearance of a secondary separation line; the line can be traced forward ahead of the nose-piece junction just leeward of the line. Secondary separation is a result of the separation of the reversed lee crossflow streaming from the line of

reattachment of the primary vortex flow at $\theta \approx 180^\circ$. The resulting secondary vortex rotates in a direction opposite to that of the primary vortex. The secondary separation is augmented by the suction of the primary separation vortex located in the flow above the surface tending to lift the boundary layer off the surface.

$\alpha = 25^\circ$ – At $\alpha = 25^\circ$ (fig. 17(f)), the secondary separation lines and vortex-flow patterns are fully developed and clearly exist to the nose tip, together with strong vortex-flow lines. Consequently, the separated flow from the laminar separation lines that occur on each side is for the first time clearly identified as being completely separated vortex flow, in which reattachment occurs at $\theta = 180^\circ$. The separation lines extend in length to $x/\ell = 0.47$ and the meridional location moves slightly to the windward at $\theta = \pm 110^\circ$. Primary turbulent separation exists over the rearward 40% length at $\theta \approx \pm 125^\circ$. The transitional region, which was first noticeable at $\alpha = 15^\circ$, has moved rearward to $0.30 < x/\ell < 0.47$.

$\alpha = 30^\circ, 35^\circ$ – At $\alpha = 30^\circ$ and 35° (figs. 17(g), 17(h), and 19(d)), the laminar-separation lines lengthen to $x/\ell = 0.60$ and 0.65 , respectively, and are located at $\theta \approx \pm 110^\circ$. The transitional region appears to move slightly rearward to $0.40 < x/\ell < 0.60$ at $\alpha = 30^\circ$ and to $0.40 < x/\ell < 0.65$ at $\alpha = 35^\circ$. Primary turbulent separation occurs over the rearward 40% length at $\theta \approx \pm 125^\circ$.

$\alpha = 40^\circ$ – At $\alpha = 40^\circ$ (figs. 17(i) and 19(e)), four of the five principal types of flow separation that were found in the study are very prominent; they are labeled in the sketches (fig. 19(e)). The three types of primary separation patterns occur together: (1) laminar, (2) transitional, and (3) turbulent. Note that this order of flow patterns, which occurs with increasing forebody diameter, is similar to the hierarchy of flow patterns that occurs on a circular cylinder with increasing Reynolds number, following the two-dimensional cylinder analogy. The fourth principal feature is secondary separation.

Primary laminar separation is indicated by the oil-separation lines that occur on each side at $\theta \approx 100^\circ$, starting from the nose tip and extending back to $x/\ell = 0.3$.

Primary transitional separation occurs in the region of $0.3 < x/\ell < 0.8$ where two primary separation lines occur. This same flow pattern was noted at $\alpha = 20^\circ$ and 30° for small regions. However, at $\alpha = 40^\circ$ this flow pattern is prominent and extensive. This type of separation pattern is herein termed “primary transitional separation.” The first separation line consists of primary laminar separation, followed by boundary-layer transition and reattachment. The reattachment line is not clear. The second separation line is primary turbulent separation. This line has no clear origin and so it has the appearance of an “open-like” separation (ref. 40). The aesthetic beauty of this fluid-mechanical flow pattern is one of nature’s “works of art.” “Transitional” is intended to

mean that this pattern is transitional between the primary laminar and primary turbulent-separation patterns. This pattern is not so well known in two-dimensional cylinder flows, but is included in the description by Morkovin (ref. 34). Also, Jones et al. (ref. 41) showed an oil-flow pattern at $R_d = 1.6 \times 10^6$ having two primary separations – laminar and turbulent. The laminar separation reattaches as a turbulent boundary layer, enclosing a two-dimensional bubble of flow with closed circulation. James, Paris, and Malcolm (ref. 42) found the presence of the bubble pattern in circular-cylinder pressure distributions in the Reynolds number range of $R_d = 0.9 \times 10^6$ to 1.3×10^6 . This separation pattern is the next natural hierarchy of flow separation with increasing Reynolds number following laminar separation. It occurs when the local Reynolds number is high enough that transition occurs in the separated laminar shear layer along a line that is located a short distance from the laminar separation line. When the pattern was first observed, it was thought that transitional separation might be the principal cause of flow asymmetry. However, later oil-flow tests at a low Reynolds number ($R_d = 0.3 \times 10^6$) did not show transitional separation, but nevertheless had a large side force (fig. 14).

A special comment about the “swept laminar separation bubble” is in order. The term bubble has been used informally in the description of two-dimensional laminar separation that is followed by reattachment. Similar oil-separation lines have also been observed on the leading edges of swept wings, however, and they too have been informally called laminar-separation bubbles, which refers to their characteristic flow reattachment in a short distance, forming a short “bubble-like” separation region. There is a fundamental difference in the flow within the bubble between two- and three-dimensional flows. In two-dimensional separation, the classic flow model is a closed circulation, in which the streamlines within the bubble form closed paths. In the center of the three-dimensional separated flow, there must be lateral flow, parallel to the separation line, along the axis of the bubble. As a result of this flow, viewed in a crossflow plane (cf. sketch in fig. 19(e)), the circulation zone is not closed, and the projections of streamlines in this plane do not form closed paths. Actually, this flow is technically not a bubble but rather a growing vortex. On the other hand, this type of flow is “bubble-like” because the flow pattern is almost two-dimensional in the strong crossflow over bodies or the leading edges of wings at angle of attack. In this paper the term “swept bubble” (denoted by the letter “B”) is used to refer to this type of laminar flow separation. Note that all bubbles, swept or unswept, are initiated by primary laminar separation (LS), with the term “primary” referring to the fact that in the crossflow plane, the separation is being fed from boundary-layer fluid originating at the windward meridian (in contrast to secondary separation).

At the aft end of the swept bubble one would expect to see the swept-bubble vortex leave the surface as a focus of separation (a flow pattern in which the oil streaks circulate

into a whirlpool-like center). However, a focus has never been seen in the oil flow; instead, the oil line dissipates into the boundary layer. The bubble must be very weak because the oil line is often interrupted by a turbulent wedge caused by some disturbance to the windward of the oil line. This is also true of two-dimensional laminar-separation bubbles (ref. 41). Also, the flow into the oil line is almost perpendicular on the surface, so that, in effect, the "swept bubble" appears to behave more like a two-dimensional bubble.

With regard to bubble-like flows, it may be noted that the flow-separation pattern near the nose at angles of incidence of 10° and 15° also has the characteristics of a swept bubble, since the flow reattaches in a short distance.

Primary turbulent separation occurs when transition moves upstream because of the higher local Reynolds number at the larger diameters of the rear sections, eliminating the primary laminar separation and swept bubble. Consequently, the turbulent flow remains attached until $\theta \approx 140^\circ$, where primary turbulent separation occurs. The sublimation photographs (fig. 18(f)) verify that transition occurs along the lee of the swept bubble and eliminates it by moving upstream at the rear of the forebody. The small swept bubble appears to be swept away into the boundary-layer crossflow at the end of the oil-separation line. Note that primary turbulent separation is prominent for $\alpha = 30^\circ$ but is greatly reduced at $\alpha = 40^\circ$ by the decreasing wetted length and the resulting increasing length of transitional separation. This verifies that the effective Reynolds number is lower for $\alpha = 40^\circ$ than for $\alpha = 30^\circ$, which agrees with the trend of effective Reynolds number discussed by Ericsson and Reding (ref. 4).

Similar to the flow at lower angles of attack, transition is enhanced by crossflow inflectional instability in the boundary layer. This instability causes an array of streamwise vortices that can be seen in the sublimation photographs as striations from the base forward to at least the nose-tip junction (fig. 18(f)).

Secondary separation occurs on the lee of the primary separation line at $\theta \approx \pm 160^\circ$ and extends to the nose tip. Finally, the first small flow asymmetry appears in the lee oil-flow pattern, and there is a small measured side force ($C_Y = 0.5$).

Flow model, $\alpha = 40^\circ$ — Figures 20(a) and (b) present a model of the flow field at $\alpha = 40^\circ$. Using the surface oil-flow patterns, the model describes the author's view of the development of the separated vortex flow in the three regions of primary separation at this Reynolds number: (1) laminar, (2) transitional, and (3) turbulent separation. The principal features of the flow are described for eight locations (A-G) along the forebody (fig. 20(b)). Sketches of four cross-sectional flow patterns are also shown.

The following development of the flow model follows the previous descriptions of the surface oil-flow pattern and the schlieren photographs for $\alpha = 40^\circ$. It also follows the

sequence of flow that occurs on a circular cylinder as the Reynolds number is increased. Region (1) encompasses primary laminar separation. The separated laminar flow (A) forms a symmetric pair of primary vortices that are sketched in the flow model. The vortices are tightly wound and located close to the body surface at $\alpha = 40^\circ$, according to the schlieren photographs (fig. 4(a)). A symmetric pair of secondary vortices is also formed, starting at the nose tip.

Region (2) encompasses primary transitional separation, as it has just been described. In this region, the laminar boundary layer on the windward surface continues to separate on the sides. However, it quickly reattaches owing to boundary-layer transition in the separation sheet. The reattached turbulent boundary layer separates again as primary turbulent separation. The flow model (fig. 20(b)) shows that this turbulent separation sheet must feed into the same pair of primary separation vortices that are initiated by the primary laminar separation in region (1). Therefore, the principal separation line for the primary vortex (on each side) must originate as the primary laminar separation line (A) at the nose in region (1) and must shift to the primary turbulent separation line (F) in region (2). This principal separation sheet must be continuous, since vortex sheets do not "tear" (following the topological arguments of Tobak and Peake in ref. 6). Hence, the primary vortex sheet must be "warped" as it traverses from region (1) into region (2) which is shown in the flow-model sketch (fig. 20(b)). Note that the oil streaks clearly show that the turbulent-separation line originates as an open-like separation that seems to appear "out of nowhere." The following explanation covers the origin of this turbulent separation line.

The flow model (fig. 20(b)) shows how the transitional region (2) must develop. The swept bubble originates at $x/\ell \approx 0.3$ (D) where the turbulent separation line appears to originate to the lee of the swept bubble as an open-like separation line (fig. 19(e)). The topological consideration of the origin of a swept bubble demands something like a starting focus. However, the oil streaks do not show a starting focus for the swept bubble; therefore, the surface topology at the origin of the swept bubble is not clear at (D). It is clear, however, that the primary separation sheet is completely separated forward of (D) but reattaches to the surface at (D) as a result of the effects of transition in the separation sheet that occurs almost immediately after separation (see the dashed line). It is proposed that the reattachment of the flow is similar to the reattachment of the separated shear layer in the formation of a bubble in a two-dimensional flow over an airfoil or cylinder. It is, therefore, proposed in the flow model that near the nose at (B), transition occurs off the surface in the shear layer, far from the laminar separation line (A). This transition in the shear layer (separation sheet or separation surface) is washed into the vortex core where it could affect the fluid dynamics of the core flow. As the diameter of the forebody increases, the effective local Reynolds number increases and the onset of transition in the

separation sheet moves upstream toward the laminar separation line. When the onset of transition approaches close to the laminar separation line, the spreading turbulence in the separation sheet results in the reattachment of the sheet to the surface. Thus, the separation sheet warps and "lays down" on the surface, then separates again as primary turbulent separation. The latter separation originates the turbulent separation line and the beginning appears to be open-like, with no definite origin. This transition process is accelerated by the crossflow boundary-layer instability.

At (G) (fig. 20(b)) the location of transition moves windward of the bubble, which sheds and dissipates into the turbulent boundary-layer, leaving only primary turbulent separation (H).

Finally, it is interesting to consider the nature of the boundary-layer flow into the secondary vortex and the possible influence on transition in the primary vortex. First, the secondary vortex looks like a swept laminar separation bubble in the cross-sectional view. However, the sublimation photographs (fig. 18(f)) indicate that the leeward boundary-layer flow into the secondary vortex is turbulent because the biphenyl is sublimed. In this case the turbulent boundary layer must be forced to separate from the surface by the strong suction of the primary vortex in the flow above the surface. The turbulent reattached flow from the secondary vortex might then influence transition in the primary laminar-separation vortex. Further study is required of the transition process in the lee flow in order to understand its origin and its effect.

$\alpha = 45^\circ$ — At $\alpha = 45^\circ$ (fig. 17(j)), the flow asymmetry increases and the measured side-force coefficient is 1.1. The secondary separation line on the right side extends the full length of the forebody. However, the line on the left extends to $x/\ell \approx 0.8$ and then crosses over the lee meridian. It is thought that the left vortex becomes detached from the forebody so that the flow behind the detachment point flows under the vortex. Schlieren photographs (fig. 4(h)) show a vortex being shed at angles of attack as low as 40° . One would wish to be more certain in the interpretation. This demonstrates the importance of the combination of oil-flow and schlieren flow visualization, as well as force measurements.

The secondary separation lines are symmetric over the first third of the length. However, over the rear two thirds of length, the right separation line is closer to the top centerline. (Note the locations of the secondary separation lines at the balance-pin hole.) Thus, it appears that the flow asymmetry occurs first over the rear of the forebody. The laminar separation lines on each side are located slightly asymmetrically: $\theta = 90^\circ$ on the left side and -100° on the right. The turbulent separation lines are also located asymmetrically: $\theta = 115^\circ$ on the left side and -140° on the right. On the windward, the boundary layer is mostly laminar, since the laminar separation lines extend almost the full length of the

forebody. This is the result of a shorter effective length of boundary-layer flow to the sides at high angles of attack.

$\alpha = 55^\circ, 60^\circ$ — At $\alpha = 55^\circ$ and 60° (figs. 17(k), 17(l), and 19(f)) all of the features of the oil-flow pattern are asymmetric. Maximum, relatively steady, asymmetric forces were measured ($C_Y = 2.6$ and 2.9 , respectively, and $C_Y/C_N = 1.24$ and 1.40 , respectively). Note that vortex traces are shown, as sketched from schlieren photographs. Vapor-screen movies showed that these vortices were highly asymmetric, but only slightly unsteady, and that they did not switch position. The first vortex is shed near the nose tip and passes high above the forebody, almost straight back from the nose tip. The second vortex is located close to the surface and disappears at mid-length.

The primary laminar-separation lines extend the full length on both sides, but are asymmetrically located at $\theta \approx -100^\circ$ on the right and $\theta \approx 80^\circ$ on the left, which is correct for a right side force. Primary transitional separation is clearly indicated on the right side, starting at $x/\ell \approx 0.2$, by the overlapping primary laminar and turbulent separation lines. On the left side the turbulent separation line extends ahead to $x/\ell \approx 0.4$, whereas on the right it extends to about 0.2 , so that the transitional separation is asymmetrically disposed longitudinally as well as circumferentially. In addition, the secondary separation lines on the lee are very asymmetric. The right-hand secondary separation line extends at least to the mid-length, where it is close to the top centerline. Consequently, the right-hand vortex lines cross over the lee centerline to the left side and disappear at $\theta \approx 140^\circ$. This oil-line seems to branch into several lines at $x/\ell \approx 0.3$ near the location where the first vortex is shed, according to the schlieren photograph in figure 4(a). Sometimes it is stated that a vortex "tears" when it is shed. However, from topological considerations (ref. 5) vortices do not "tear," and separation lines do not end abruptly (i.e., without a focus, for example). There must be a continuity to the vortex structure and the accompanying separation lines. In addition, a new vortex must form on the left side where the first vortex is shed. The effect of the new vortex is weak, at first; however, its effect can be seen on the lee near the base, where the vortex lines flowing toward the right side start to curve back toward the left side, as they should for a left-side vortex. Note that the steady asymmetric surface pattern roughly follows the two-dimensional cylinder-flow analogy, since circular-cylinder, mean-flow patterns have recently been shown to be asymmetric in the transitional Reynolds number regime (ref. 43).

Sublimation photographs (fig. 18(g)) show that striations occur on the windward surface from the base forward to at least $x/\ell \approx 0.2$.

$\alpha = 70^\circ$ — At $\alpha = 70^\circ$ (figs. 17(m) and 19(g)), the oil-flow pattern exhibits a small asymmetry on the lee, which is considerably reduced from that at $\alpha = 55^\circ$. However, the laminar

separation on each side is symmetric. A prominent difference from the pattern at $\alpha = 55^\circ$ occurs on the lee over the rear half, where the oil accumulates into a large, dark patch with no flow lines. From this flow pattern and those for $\alpha = 80^\circ$ and 88° , it is certain that in the region of the rear half the flow separates into an unsteady, wake-like flow, similar to that behind a swept circular cylinder. In such a flow, the vortices leave the surface on each side in an alternating pattern that could be periodic, like a vortex street, or random, depending on the Reynolds number. Ahead of $x/\ell \approx 0.5$ well-defined flow lines occur on the lee, indicating that the flow field is organized by the pointed nose over the forward half, even at this high incidence.

$\alpha = 80^\circ$ — At $\alpha = 80^\circ$ (fig. 17(n)), the large dark patch of oil with no flow lines that existed at $\alpha = 70^\circ$ has extended forward to $x/\ell \approx 0.3$. Organized flow still exists near the tip, according to the prominent flow lines on the leeward surface.

$\alpha = 88^\circ$ — At $\alpha = 88^\circ$ (figs. 17(o) and 19(h)), the accumulated patch of oil on the lee indicates wake-like separation extending forward to the nose tip. The mean side force is zero for this angle of attack. Note that the flow separation on the sides is transitional forward to $x/\ell \approx 0.2$. At $R_d = 0.8 \times 10^6$, the boundary-layer flow should be supercritical, and, hence, a length of turbulent separation was expected near the base.

Effects of Angle of Attack at $R_d = 2.0 \times 10^6$

A Reynolds number of 2.0×10^6 was chosen to make one oil-flow test, because the side force in previous tests was greatly reduced; an angle of attack of 55° was chosen for comparison with the asymmetric oil-flow patterns at lower Reynolds numbers (fig. 21). Laminar separation lines start on the sides at the nose tip, are symmetrically located at $\theta \approx \pm 100^\circ$, and extend to $x/\ell \approx \pm 0.5$ on the left side and 0.45 on the right; contrary to the pattern at $R_d = 0.8 \times 10^6$, this is only slightly asymmetric. The oil pattern is an excellent example of transitional separation, starting as $x/\ell \approx 0.2$ on each side. The oil-flow streaks on the lee of the laminar-separation lines clearly continue in the same crossflow direction toward the lee, approaching turbulent separation lines, which are slightly asymmetric about the top centerline. On the sides, some local turbulent wedges (short lengths of turbulent flow) are seen to wipe out the laminar separation lines in several spots. This is an interesting phenomenon, one in which the laminar line can be broken up into sections. The topology of the ends of the separation lines is not clear. However, it is clear that separation lines cannot end without a focus and a shed filament. These must occur on a very small scale and must be shed into the boundary layer. On the leeward surface, the vortex flow lines are asymmetric about

the top centerline. Secondary separation lines are not clear but are faintly visible in the nose region.

Effects of Reynolds Number

Figure 22 presents three oil-flow photographs for three Reynolds numbers, $R_d = 0.3 \times 10^6$, 0.8×10^6 , and 2.0×10^6 , each at $\alpha = 55^\circ$ and $\theta = 135^\circ$ for the pointed 3.5-ogive. The principal effects of Reynolds number can be seen in these photographs. Note that the location of the onset of transitional boundary-layer separation moves forward significantly with increasing Reynolds number. Thus, the region of laminar separation on the sides, which starts at the nose tip, decreases in length from full length at low Reynolds numbers to 1/5-length at $R_d = 2.0 \times 10^6$. This finding is not unexpected since this is the natural trend of the state of the boundary layer with increasing Reynolds number. However, the importance of this forward movement of the transitional separation pattern lies in the possibility that it influences the position of vortex shedding, which, according to the previous discussion, also moves forward with increasing Reynolds number.

Evidence of the forward movement of the position of vortex shedding was shown in figure 10 ($M = 0.6$) in the plot of the position of vortex shedding measured from the schlieren photographs. The measured position at the higher Reynolds number is farther forward than that at the lowest Reynolds number. In addition, the transition to turbulent separation must result in a decrease in vorticity flux from the laminar to the turbulent separation line since the velocities at separation are lower for the turbulent separation at $\theta \approx 90^\circ$. This reduces the strength of the vortex and might suppress vortex asymmetry. Note that the oil-flow pattern is more symmetrical at the highest Reynolds number of $R_d = 2.0 \times 10^6$ (see also fig. 10). This would also explain the effect of boundary-layer trips (ref. 25) which can reduce the side force considerably, an effect that is similar to increasing the Reynolds number by causing transition (and, hence, transitional separation) farther forward.

At higher Reynolds numbers in the transcritical cross-sectional Reynolds-number range, the side force increases again, but in the opposite direction (ref. 24). In the two-dimensional cylinder analogy, the mean primary separation moves from $\theta \approx \pm 135^\circ$ to $\theta \approx \pm 110^\circ$, so that the vortex strengths are larger. If these vortices are asymmetric on the forebody, the steady side force would also be larger if the mean separation moved to $\theta \approx \pm 110^\circ$.

Effects of Mach Number

Figure 23 presents oil-flow photographs that were obtained in the 6-ft tunnel at $M = 0.25$, 0.60, and 2.0 at $R_d = 0.8 \times 10^6$ and at $\alpha = 20^\circ$, 40° , and 55° for the pointed

3.5-ogive. Photographs were taken after tunnel shutdown for $M = 0.25$ and 0.6 following a suitable running time to dry the oil pattern. However, it was found that the flow pattern at $M = 2$ did not hold during shutdown and photographs were taken during the run.

$M = 0.25$ — The oil-flow patterns at $M = 0.25$ (figs. 23(a) to 23(c)) are similar to those from the 12-ft tunnel runs at $M = 0.25$; the latter were discussed previously and shown in figure 17.

$M = 0.60$ — At $M = 0.6$, an increase in length of the primary laminar-separation line can be seen in the first photographs for $\alpha = 20^\circ$ (fig. 23(a)). For example, at $M = 0.6$, the laminar-separation lines on each side extend to $x/\ell \approx 0.50$, where primary turbulent separation begins; whereas, at $M = 0.25$ the laminar separation lines extend only to $x/\ell \approx 0.30$, where primary turbulent separation begins. At $M = 0.6$, secondary separation starts at the nose tip, whereas at $M = 0.25$ it starts farther back (at $x/\ell \approx 0.20$). At $\alpha = 40^\circ$ (fig. 23(b)), the patterns are similar at both Mach numbers. The primary laminar separation lines extend to $x/\ell \approx 0.8$ at both Mach numbers, and transitional separation appears to exist at approximately $0.3 < x/\ell < 0.8$ at both Mach numbers. At $\alpha = 55^\circ$ (fig. 23(c)), the region of transitional separation is not reduced significantly from that at $M = 0.25$. However, the extensive asymmetric flow that exists at $M = 0.25$ is greatly reduced at $M = 0.6$. Consequently, the measured side force is greatly reduced (from 1.8 at $M = 0.25$ to 0.9 at $M = 0.6$ for these tests). In reference 26 it was shown that the side forces on the various forebodies are reduced as Mach number increases and are zero at $M = 1.2$ for all of the forebodies tested.

$M = 2.0$ — At $M = 2$ (figs. 23(a)–23(c)), the length of primary laminar separation extends to the base at all three angles of attack (20° , 40° , and 55°). Thus, the location of boundary-layer transition moves rearward with increasing Mach number. This trend is an agreement with the experience from wind-tunnel testing in which most models require larger boundary-layer trips to trip the boundary layer at higher Mach numbers.

Effect of Angle of Attack on Blunt-Nose 3.5-Ogive

Oil-flow tests were made with a blunt nose tip attached to the 3.5-ogive forebody at $M = 0.25$ and $R_d = 0.8 \times 10^6$. The nose tip radius was 16.7% of the base radius, the largest size of the three blunt tips available. In previous force tests, this bluntness ratio reduced the maximum side force to less than half. Photographs for $\alpha = 10^\circ$, 15° , 20° , 40° , and 55° are shown in figure 24.

For these tests, the model was painted black and polished smooth. White titanium dioxide pigment was used. Then the

model was tested upside down so that the setscrew holes were on the bottom, and so that the lee surface flow would not be obscured at the setscrew holes.

$\alpha = 10^\circ$ — In figure 24(a), the windward oil-streak angles on the sides at $\theta \approx \pm 90^\circ$ are noticeably larger near the nose than near the base; these patterns are similar to those for the pointed forebody. The angle increases from about 18° (1.8α) near the base to about 36° (3.6α) at $x/\ell \approx 0.2$. In the close-up photograph of the side view it is clear that a strong crossflow (perpendicular to the body axis) exists at the shoulder of the hemispherical nose and the ogive. An interesting flow pattern can be seen on the lee of the nose when the oil at the nose is wiped to remove excess oil. A separation line exists on the leeward edge of the hemispherical nose. The separation line is short, and each end terminates in a tiny focus. Reattachment occurs in a short distance, and a pair of tiny foci (small vortices) exists behind the separation line as a part of the reattachment mechanism. The oil-streaks rearward of the nose tend to coalesce, as if a separation line is forming.

$\alpha = 15^\circ$ — The flow pattern shown in figure 24(b) for $\alpha = 15^\circ$ is similar to that for $\alpha = 10^\circ$, except that the primary separation line on the side is more prominent. It is clear that this separation line is not connected to the separation at the nose so that the beginning of this separation is open-like, having the appearance of the separation pattern on a hemisphere cylinder (refs. 44 and 45). It appears that the primary separation is laminar back to $x/\ell \approx 0.20$ and turbulent rearward of that location, where boundary-layer transition must move to the windward of the laminar separation line.

$\alpha = 20^\circ$ — In figure 24(c) for $\alpha = 20^\circ$, the flow pattern is similar to that for $\alpha = 15^\circ$, but more clearly developed. The localized separation at the nose is similar to that seen for $\alpha = 15^\circ$, except that more than one pair of foci can be seen in the reattachment process. These must form a tiny series of foci with saddle points in between to accommodate the three-dimensional reattachment process. The local primary separation on the sides is clearly laminar ahead of $x/\ell \approx 0.20$ and turbulent behind. A secondary separation line is evident leeward of the primary turbulent separation line. The beginning of the secondary separation is open-like in the close-up photograph of figure 24(c). It is interesting to note that the general surface-flow pattern behind the blunt nose at $x/\ell > 0.1$ is similar to that for the pointed nose at $\alpha = 20^\circ$ (fig. 17(e)).

$\alpha = 40^\circ$ — In figure 24(d) for $\alpha = 40^\circ$, the oil-flow pattern at the blunt-nose tip changes from the pattern seen for $\alpha = 20^\circ$, in which the separation bubble at the nose tip is not connected to the separation lines on the sides, to a pattern at $\alpha = 40^\circ$ in which the primary laminar-separation lines on each side wrap around the blunt nose in a continuous line.

Secondary separation lines extend from the base forward to the lee of the laminar separation line at the blunt nose, and their starting point is not clear. Perhaps they are also open-like separation lines. Transitional separation occurs at $0.4 < x/\ell < 0.8$. Over the length of the forebody, the flow-separation pattern is symmetrical. This flow pattern is similar to the flow pattern of the forebody with the pointed nose at $\alpha = 40^\circ$ (fig. 17(i)).

$\alpha = 55^\circ$ — Figure 24(e) for $\alpha = 55^\circ$ shows that the primary laminar separation lines on each side wrap around the blunt nose in a continuous line and extend along the sides to the base. Secondary separation lines are apparent from the nose to the base. Unlike the pattern for the pointed nose, which is highly asymmetric, the flow-separation pattern is symmetric over the length of the forebody. The effect of bluntness in changing the flow pattern from asymmetrical to symmetrical appears to result from more space between the vortices than for the pointed nose, which could allow the flow symmetry to exist for the blunt nose, whereas, crowding of the vortices on the pointed nose results in a hydrodynamic instability between the vortex pair and, hence, in vortex asymmetry.

Pointed Tangent Ogive: Fineness Ratio = 2.5

Oil-flow tests were made with the 2.5-ogive at $M = 0.25$, $R_d = 0.8 \times 10^6$, and $\alpha = 30^\circ$, 40° , and 55° (fig. 25). The measured side force was zero in accordance with previous force results (ref. 30). No flow asymmetry was seen in the oil-flow patterns. Otherwise, the patterns look similar to those for the 3.5-ogive (fig. 17), in the sense that primary laminar, transitional and turbulent separation patterns occur along the length of the forebody. Their variation with increasing angle is also similar in that the transitional separation region increases in length.

Two differences in the flow patterns of the 2.5- and 3.5-ogive are noticed. First, at $\alpha = 30^\circ$, the secondary vortices do not start at the nose tip of the 2.5-ogive as they did for the 3.5-ogive. However, this is probably explained by the larger nose angle for the 2.5-ogive ($\delta_N = 22.5^\circ$) than for the 3.5-ogive ($\delta_N = 16.2^\circ$), so that the flow-deflection angles for the top ($\theta = 180^\circ$) of each forebody is less (-7.5°) for the 2.5-ogive than for the 3.5-ogive (-13.8°). However, at $\alpha = 40^\circ$ and 55° the secondary vortices extend forward to the nose tip.

The second noticeable difference occurs in the patterns for $\alpha = 30^\circ$ and 40° on the lee near $\theta = 180^\circ$. On the forward half of the vortex, lines give the appearance that the vortices are not as close together as they are for the 3.5-ogive (figs. 17(g) and (i)). Note that near $\theta = 180^\circ$ the oil streaks flow in a direction that is almost axial. They gradually drift away from $\theta = 180^\circ$ and then are suddenly caught in the vortex flow. The "space" between the vortices is especially noticeable at $\alpha = 40^\circ$, where an oil line occurs near the nose

at $\theta = 180^\circ$, indicating crossflow and axial stagnation of the airflow. This flow pattern shows that the vortices are not so crowded together for the larger nose angle of the 2.5-ogive, which allows flow symmetry to exist to higher angles of attack according to the previously mentioned formula (onset $\alpha = 2 \delta_N$). In this case no asymmetry occurs, even at $\alpha = 55^\circ$, but previous force measurements (ref. 12) showed the existence of a side force at $\alpha > 45^\circ$ at $R_d = 2 \times 10^6$. These oil-flow patterns further support the contention that a hydrodynamic instability occurs because of the crowding together of the vortices on the more slender noses.

6. FLOW ANGLES AND SEPARATION BOUNDARIES

Measured Surface Flow Angles

Figure 26 presents the measured surface oil-streak angles (skin-friction-line angles) at $\theta = \pm 45^\circ$ and $\pm 90^\circ$ on the sides of the 3.5-ogive and at $\theta = \pm 90^\circ$ on the sides of the 2.5-ogive, the 5.0-ogive, and the 20° cone for $M = 0.25$ and $R_d = 8 \times 10^6$. The angles near the nose of the 3.5-ogive at $\theta = \pm 90^\circ$ and at $\alpha = 5^\circ$ and 10° are about 5α , which is more than twice the potential-flow angle of 2α at low angles of attack. This indicates that the boundary-layer velocity profiles are highly skewed near the nose. With increasing angle of attack, the flow angle δ_s follows close to the curve for $\tan^{-1}(5 \tan \alpha)$. Note that in curved flow the boundary layer will skew in the direction of the center of the radius of curvature. Therefore, the curvature of the flow on the surface is greater near the nose than it is farther rearward, a result of the smaller body radius and the transverse pressure gradient. Note also that the flow angle decreases with increasing distance from the nose; the flow curvature also decreases with increasing distance, since the body diameter increases. Over the rear half, the oil-flow angles are close to the potential-flow angle of $\tan^{-1}(2 \tan \alpha)$.

Between $\alpha = 40^\circ$ and 70° , the flow angles on each side are asymmetric as a result of the asymmetry in the vortex flow field (see cross-hatched region). Note that most of the curves have inflections near the angles of $\alpha = 20^\circ$ and 40° . These angles are close to the onset of symmetric and asymmetric vortex flow, respectively, and these inflections represent a retardation in rate of change in surface flow angle with incidence. Evidently, a strong, favorable, crossflow pressure gradient is responsible for the increase in flow angle with increasing incidence and the resulting skewing of the boundary-layer velocity profiles. Therefore, the inflections in the δ_s versus α curves must result from changes in the variation of the crossflow pressure gradient with incidence, caused by the onset of the formation of the symmetric vortex flow field and, at higher incidence, by the onset of vortex asymmetry.

Similar results were obtained for the 3.5-ogive at $\theta = \pm 45^\circ$ and also for the 2.5- and 5-ogive at $\theta = \pm 90^\circ$.

The data for the 20° cone at $\alpha = 36^\circ$ (fig. 26(d)) show a much smaller variation with cone length than for the ogive forebody. Hence, the flow is more conical than for the ogive with respect to the surface-flow angles. These measured angles for the cone are approximately 70° , which lies between the potential flow angle of about 56° and the skewed-flow angle of about 73° that occurs on the nose of the ogive. Therefore, the cone-surface flow angles are greatly skewed from the potential flow angle over most of the cone length.

Location of Separation

Figure 27 shows the locations of the primary and secondary separation lines for $M = 0.25$ and $R_d = 0.8 \times 10^6$. The most interesting curve is that for laminar separation. This starts at $\theta = \pm 140^\circ$ at $\alpha = 10^\circ$ as a swept laminar separation bubble and develops into the primary laminar separation line at $\theta = \pm 115^\circ$ and $\alpha = 20^\circ$.

Flow-Separation Boundaries

Figure 28 shows a plot of the angle of attack for the onset of various types of flow separation at $M = 0.25$ and $R_d = 0.8 \times 10^6$. The data are similar to those presented in reference 25 for long bodies, whereas figure 28 was determined from the oil-flow patterns for the 3.5-ogive. Three separation boundaries are shown that separate the angle of attack range of 0° to 90° into four flow regimes. The vortex-free regime at small incidence represents the region of unseparated, vortex-free, potential flow. However, the sublimation studies have shown that the boundary-layer flow is not entirely vortex free at $R_d = 0.8 \times 10^6$, but inflectional instability vortices do occur. The second region is that for symmetric boundary-layer separation with symmetric vortex flows. The small region near the nose labeled "bubble" was unexpected and was described in the discussion of the oil-flow pattern for $\alpha = 5^\circ$ and 10° . It is one form of symmetric primary laminar separation. The swept-bubble region appears to be enveloped by the symmetrically separated vortex flows by $\alpha \approx 20^\circ$. The third region is that for "steady asymmetric vortices." Asymmetric flow is first noticeable in the oil-flow patterns at $\alpha \approx 40^\circ$, but appears in the side-force measurements at $\alpha \approx 32^\circ$. The fourth region of "unsteady wake-like separation" is observed in the oil-flow patterns at $\alpha \approx 60^\circ$, starting at the base and progressing forward to the nose at $\alpha \approx 90^\circ$.

Effects of Transition

Figure 29 presents a second plot of α versus x/ℓ , showing the effects of boundary-layer transition on the different types of flow patterns for the 3.5-ogive for $M = 0.25$ and $R_d = 0.8 \times 10^6$. Two boundaries are shown for the longitudinal extent of the three types of primary separation: laminar, transitional, and turbulent. The length of laminar separation and, hence, the beginning of transitional separation does not vary much over the incidence range. The effective Reynolds number for the beginning of transition separation must not vary much with incidence. The most significant change is the decreased length of turbulent separation and increasing length of transitional separation. This indicates that the effective Reynolds number for the windward flow must be higher at $\alpha = 20^\circ$, where turbulent separation starts at $x/\ell = 3.5$, than at $\alpha = 55^\circ$, where turbulent separation disappears. Ericsson and Reding (ref. 4) give a value of about 1.3 for the ratio of (effective R_d)/ R_d at $\alpha = 20^\circ$ owing to increasing effective length of laminar run. However, the results herein indicate that this forward movement of primary turbulent separation with decreasing angle of attack is strongly influenced (perhaps, most influenced) by the effects of the crossflow instability in the boundary layer at angles of attack of 55° and below. This conclusion is verified by the abrupt, large rearward movement of the location of transition as the angle is reduced to $\alpha = 0$. At $\alpha = 0$ there are no crossflow effects and transition occurs only as a result of wetted length of run of the laminar boundary layer. If crossflow instability were not a factor, the location of transition would not change much between 0 and 5° , unless transition was induced by the minimum pressure and adverse, transverse pressure gradient in the crossflow.

7. CONCLUSION

Schlieren, vapor-screen, oil-flow, and sublimation flow-visualization methods were used in a comprehensive attempt to understand the various types of flow fields occurring on ogival and conical forebodies over a wide range of angles of attack, Reynolds numbers, and Mach numbers. Most of the tests were conducted with a tangent ogive having a fineness ratio of 3.5. The following remarks summarize the conclusions regarding the effects of angle of attack, Reynolds number, bluntness, and fineness ratio on the principal flow-field and surface-flow patterns.

This study resolved the surface-flow patterns existing in the four principal flow regimes that occur with increasing angles of attack: (1) unseparated, potential, vortex-free flow; (2) symmetric vortex flow; (3) asymmetric vortex flow; and (4) wake-like, unsteady vortex flow. The principal effects of Reynolds number, Mach number, bluntness, and fineness ratio on both the surface-flow patterns and the external

vortex-flow patterns were investigated. It was found that the known flow patterns of a two-dimensional circular cylinder were helpful in analyzing both the surface-flow separation patterns and the external flow field. Using this two-dimensional cylinder analogy in a qualitative sense, the complex experimental results could often be reduced to a combination of several simple flow patterns that were similar to two-dimensional flow in the local crossflow plane.

Angle-of-Attack Effects

Angle-of-attack effects on the flow pattern were determined first at a transitional Reynolds number of 0.8×10^6 , using the 3.5-ogive forebody. At low angles of attack, several interesting phenomena occurred. At an angle of attack of 5° , at which potential vortex-free flow should exist, small vortices appeared in the boundary layer, evidenced by striations in the sublimation visualization tests, that were nearly parallel to the oil streaks. These vortices are caused by three-dimensional boundary-layer inflectional instability and induce early boundary-layer transition. The striations persist to angles of attack up to 55° . It is known that these vortices do not occur at low Reynolds numbers when the boundary-layer crossflow (normal to the inviscid streamline) Reynolds number is less than about 125. It was also shown that at low angles there is a surprisingly large surface-flow angle on each side near the nose, more than twice the potential flow angle at the edge of the boundary layer. This large change in flow angle through the boundary layer must result in a large skewing of the boundary-layer flow, which would enhance the inflectional instability.

The flow was expected to be unseparated at angles of attack up to about 15° . However, on the forward half of the forebody, a swept laminar-separation bubble occurred, with reattached flow on the lee. At an angle of attack of 15° to 20° the swept-bubble flow changed to the normally expected primary laminar separation vortex. Thus, this low-angle-of-attack, transitional flow is not entirely unseparated and vortex free.

At angles of attack of 20° and higher, angles at which flow separation occurs at this transitional Reynolds number of 0.8×10^6 , the two-dimensional cylinder analogy was helpful in identifying three types of primary separation patterns that occur simultaneously along the length of the forebody: (1) primary laminar separation, which occurs near the nose; (2) primary transitional separation, which occurs near the midsection (this type of separation pattern consists of a combination of laminar separation, turbulent reattachment, and turbulent separation); and (3) primary turbulent separation, which occurs over the remainder of the forebody. These flow patterns occur because of the influence on boundary-layer transition of the increasing local Reynolds number as the local diameter increases. The locations and extent of these three types of primary separation change with angle of attack

and Reynolds number. With increasing angle of attack, the transitional separation region increases in extent, and the turbulent separation region decreases in extent. With increasing Reynolds number, the longitudinal locations of the onset of transitional and turbulent separation move forward, decreasing the extent of laminar separation. On the other hand, at a low Reynolds number (0.3×10^6) only primary laminar separation occurs over the length of the forebodies.

At angles of attack of 45° to 70° , the effect of vortex asymmetry is evident in the oil-flow patterns. At an incidence of 55° , the asymmetry in the surface-flow pattern becomes so large that the primary vortex closest to the surface actually crosses over the top centerline. It was initially thought that the occurrence of vortex asymmetry might depend principally on the occurrence of asymmetry in the transitional region of the boundary layer at transitional Reynolds numbers. However, it was found that large asymmetries in the surface-flow patterns also occur with the laminar type of separation at low Reynolds numbers. On the other hand, the contribution of boundary-layer asymmetries is also known to be significant, especially at transitional Reynolds numbers. Short lengths of the forebody can have laminar separation on one side and transitional separation on the other, followed by transitional separation on both sides, followed by a short length of transitional separation on one side and turbulent separation on the other.

Schlieren and vapor-screen photographs were taken in order to study this steady vortex asymmetry. At $\alpha = 40^\circ$ the first-shed vortex is tightly coiled near the nose, but it becomes highly diffused when it detaches from the forebody, which gives the impression of vortex breakdown (bursting). The positions of vortex shedding move forward with increasing angle of attack until at 55° the first-shed vortex detaches near the nose. Also, the spacing between the positions of shedding decreases. The vapor-screen movies show that the asymmetric vortices are relatively steady at angles of attack approaching those for maximum side force; however, at maximum side force some unsteadiness is apparent.

At very high angles of attack (70° to 88°) the surface oil-flow tests show that a stall-like separation appears over the rearward half of the forebody and moves forward. The vortices become increasingly unsteady, starting at the base, where they oscillate around a mean asymmetric position. The flow remains organized over the pointed nose until at an incidence of about 88° the stall-like flow extends to the nose tip. The vortex pattern becomes hazy, indicating that the vortex shedding is alternating, as expected for these high angles of attack.

Reynolds Number and Mach Number Effects

Although Reynolds number and Mach number do not have much effect on the onset-angle for the different vortex flow regimes, Reynolds number and Mach number greatly

affect the extent of primary laminar, transitional, and turbulent boundary-layer separations. The locations of the regions of primary transitional and turbulent separation, as well as vortex shedding, move forward with increasing Reynolds number and rearward with increasing Mach number. This suggests that the movement of the longitudinal position of boundary-layer transition affects the longitudinal position of vortex shedding.

Fineness-Ratio Effects

Vortex-flow lines are not as crowded together over the forward half of the 2.5-ogive as they are for the 3.5-ogive. This allows flow asymmetry to exist to higher angles of attack. These oil patterns further support the proposition that a hydrodynamic instability occurs on the more slender noses because of the crowding together of the vortices.

Bluntness Effects

The oil-flow patterns for the rearward two thirds of the blunt 3.5-ogive are similar to those for the pointed ogive.

However, the flow over the forward third is influenced by the bluntness. At an angle of attack of 20° , an isolated separation bubble occurs at the blunt nose tip. Primary laminar separation on the sides starts as an open-like separation line. At angles of attack of 40° and 55° , the lines of separation on the sides extend around the blunt nose. At 55° , the vortex flow lines on the lee side indicate that the vortices are more separated from each other on the blunt nose than on the pointed nose. Thus, the blunt nose appears to relieve the hydrodynamic instability caused by the crowding of the vortices, thus resulting in the asymmetric vortex formation for the pointed nose.

The foregoing results support the proposition that the principal cause of vortex asymmetry is the hydrodynamic instability of the inviscid flow field that occurs when the vortices grow to sufficient strength to interfere with each other. Asymmetries also occur in the boundary layer, especially at transitional Reynolds numbers, significantly augmenting the hydrodynamic vortex asymmetries.

Ames Research Center

National Aeronautics and Space Administration
Moffett Field, California, May 1985

REFERENCES

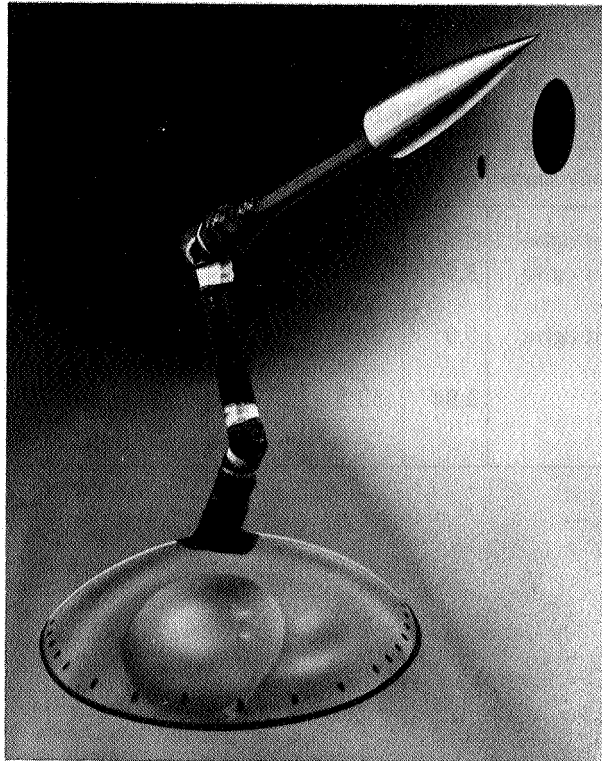
1. Chapman, Gary T.; Keener, Earl R.; and Malcolm, Gerald N.: Asymmetric Aerodynamic Forces on Aircraft at High Angles of Attack — Some Design Guides. AGARD CP-199: Stall-Spin Problems of Military Aircraft, Nov. 1975.
2. Nielsen, Jack N.: Nonlinearities in Missile Aerodynamics. AIAA Paper 78-20, January 1978.
3. Spearman, M. L.: Historical Development of World Wide Guided Missiles. AIAA Paper 78-210, January 1978.
4. Ericsson, Lars E.; and Reding, J. Peter: Vortex-Induced Asymmetric Loads in 2-D and 3-D Flows. AIAA Paper 80-0181, January 1980.
5. Hunt, B. L.: Asymmetric Vortex Forces and Wakes on Slender Bodies. AIAA Paper 82-1336, August 1982.
6. Tobak, M.; and Peake, D. J.: Topological Structures of Three-Dimensional Separated Flows. AIAA Paper 81-1260, 1981.
7. Tobak, M.; and Peake, D. J.: Topology of Three-Dimensional Separated Flows. Ann. Rev. Fluid Mech., vol. 14, 1982, pp. 61-85.
8. Moore, Franklin K.: Laminar Boundary Layer on Cone in Supersonic Flow at Large Angle of Attack. NACA-TN-2844, Nov. 1952.
9. Allen, H. Julian; and Perkins, Edward W.: A Study of Effects of Viscosity on Flow over Slender Inclined Bodies of Revolution. NACA Rep. 1048, 1951.
10. Allen, H. Julian; and Perkins, Edward W.: Characteristics of Flow over Inclined Bodies of Revolution. NACA RM-A50L07, 1951.
11. Gowen, Forrest E.; and Perkins, Edward W.: A Study of the Effects of Body Shape on the Vortex Wakes of Inclined Bodies at a Mach Number of 2. NACA RM-A53I17, 1953.
12. Perkins, Edward W.; and Kuehn, Donald M.: Comparison of the Experimental and Theoretical Distributions of Lift on a Slender Inclined Body of Revolution at $M = 2$. NACA RM-A53E01, 1953.
13. Jorgensen, Leland H.; and Perkins, Edward W.: Investigation of Some Wake Vortex Characteristics of an Inclined Ogive-Cylinder Body at Mach Number 1.98. NACA RM-A55E31, 1955.
14. Gapcynski, John P.: An Experimental Investigation of the Flow Phenomena over Bodies at High Angles of Attack at a Mach Number of 2.01. NACA RM-L55H29, 1955.
15. Thomson, K. D.; and Morrison, D. F.: The Spacing, Position, and Strength of Vortices in the Wake of Slender Cylindrical Bodies at Large Incidence. J. Fluid Mech., vol. 50, pt. 4, 1971, pp. 751-783.
16. Jones, J. H.; and Ohare, J. E.: Flow Visualization Photographs of a Yawed Tangent Ogive Cylinder at Mach Number 2. AEDC-TR-73-45, 1973.
17. Wardlaw, Andrew B., Jr.: Prediction of Yawing Force at High Angle of Attack. AIAA J., vol. 12, no. 8, Aug. 1974, pp. 1142-1144.
18. Anglin, Ernie L.; and Bowman, James S., Jr.; and Chambers, Joseph R.: Effects of a Pointed Nose on Spin Characteristics of a Fighter Airplane Model Including Correlation with Theoretical Calculations. NASA TN D-5921, 1970.
19. Kruse, Robert L.; Keener, Earl R.; Chapman, Gary T.; and Claser, Gary: Investigation of the Asymmetric Aerodynamic Characteristics of Cylindrical Bodies of Revolution with Variations in Nose Geometry and Rotational Orientation at Angles of Attack to 58° and Mach Numbers to 2. NASA TM-78533, 1979.
20. Jorgensen, Leland Howard: Prediction of Static Aerodynamic Characteristics for Slender Bodies Alone and with Lifting Surfaces to Very High Angles of Attack. NASA TR R-474, 1977.
21. Owen, F. K.; and Johnson, D. A.: Wake Vortex Measurements of Bodies at High Angle of Attack. AIAA J., vol. 18, no. 9, Oct. 1980, pp. 1173-1179.
22. Peake, David J.; Owen, F. Kevin; and Higuchi, Hiroshi: Symmetrical and Asymmetrical Separations about a Yawed Cone. AGARD CP-247, Oct. 1978.
23. Erickson, Gary E.: Water Tunnel Flow Visualization: Insight into Complex Three-Dimensional Flowfields. J. Aircraft, vol. 17, no. 9, Sept. 1980, pp. 656-662.

24. Keener, Earl R.; and Chapman, Gary T.: Similarity in Vortex Asymmetries over Slender Bodies and Wings. AIAA J., vol. 15, no. 9, Sept. 1977, pp. 1370-1372.
25. Keener, Earl R.; and Chapman, Gary T.: Onset of Aerodynamic Side Forces at Zero Sideslip on Symmetric Forebodies at High Angles of Attack. AIAA Paper 74-770, August 1974.
26. Keener, Earl R.; Chapman, Gary T.; and Kruse, Robert L.: Effects of Mach Number and Afterbody Length on Aerodynamic Side Forces at Zero Sideslip on Symmetric Bodies at High Angles of Attack. AIAA Paper 76-66, January 1976.
27. Keener, Earl R.; and Taleghani, Jamshid: Wind Tunnel Investigation of the Aerodynamic Characteristics of Five Forebody Models at High Angles of Attack at Mach Numbers from 0.25 to 2. NASA TM X-73076, 1975.
28. Keener, Earl R.; Chapman, Gary T.; Cohen, Lee; and Taleghani, Jamshid: Side Forces on a Tangent Ogive Forebody with a Fineness Ratio of 3.5 at High Angles of Attack and Mach Numbers from 0.1 to 0.7. NASA-TM X-3437, 1977.
29. Keener, Earl R.; Chapman, Gary T.; Taleghani, Jamshid; and Cohen, Lee: Side Forces on Forebodies at High Angles of Attack and Mach Numbers from 0.1 to 0.7: Two Tangent Ogives, Paraboloid and Cone. NASA TM-X-3438, 1977.
30. Keener, Earl R.; and Valdez, Jose: Side Forces on a Tangent Ogive Forebody with a Fineness Ratio of 2.5 at High Angles of Attack and Low Speed. NASA TM-X-73176, 1976.
31. Holder, D. W.; North, R. J.; and Wood, G. P.: Optical Methods for Examining the Flow in High-Speed Wind Tunnels. Part I, Schlieren Methods. Part II, Interferometer Methods. AGARDograph 23, Nov. 1956.
32. Vasil'ev, Lev. Aleksandrovich: Schlieren Methods. Translated by A. Baruch from Tenevye Metody, Israel Program for Scientific Translations, New York, 1971.
33. Maltby, R. L.: Flow Visualization in Wind Tunnels Using Indicators. AGARDograph 70, Apr. 1962.
34. Morkovin, M. V.: Flow Around a Circular Cylinder — A Kaleidoscope of Challenging Fluid Phenomena. Symposium on Fully Separated Flows, edited by A. G. Hansen, ASME, May 1964, pp. 102-118.
35. Owen, P. R.; and Randall, D. G.: Boundary Layer Transition on a Swept Back Wing. Royal Aircraft Establishment. TM Aero 277, May 1952.
36. Chapman, Gary T.: Some Effects of Leading-Edge Sweep on Boundary-Layer Transition at Supersonic Speeds. NASA TN D-1075, 1961.
37. Jillie, Don W.; and Hopkins, Edward J.: Effects of Mach Number, Leading-Edge Bluntness, and Sweep on Boundary-Layer Transition on a Flat Plate. NASA TN D-1071, 1961.
38. Tobak, M.: On Local Inflexional Instability in Boundary-Layer Flows. Zeitschrift fuer Angewandte Mathematik und Physik, vol. 24, 1973, pp. 330-354.
39. Bouard, Roger; and Coutanceau, Madeleine: The Early Stage of Development of the Wake behind an Impulsively Started Cylinder for $40 < Re < 10^4$. J. Fluid Mech., vol. 101, pt. 3, 1980, pp. 583-607.
40. Wang, K. C.: Separation Patterns of Boundary Layer over an Inclined Body of Revolution. AIAA J., vol. 10, no. 8, Aug. 1972, pp. 1044-1050.
41. Cincotta, Joseph J.; Jones, George W., Jr.; and Walker, Robert W.: Aerodynamic Forces on a Stationary and Oscillating Circular Cylinder at High Reynolds Numbers. NASA TR R-300, 1969.
42. James, W. D.; Paris, S. W.; and Malcolm, G. N.: Study of Viscous Crossflow Effects on Circular Cylinders at High Reynolds Numbers. AIAA J., vol. 18, no. 9, Sept. 1980, pp. 1066-1072.
43. Kamiya, N.; Suzuki, S.; and Nishi, T.: On the Aerodynamic Force Acting on a Circular Cylinder in the Critical Range of the Reynolds Number. AIAA Paper 79-1475, 1979.
44. Hsieh T.; and Wang K. C.: Concentrated Vortex on the Nose of an Inclined Body of Revolution. AIAA J., vol. 14, no. 5, May 1976, pp. 698-700.
45. Peake, David J.; and Tobak, Murray: Three-Dimensional Flows about Simple Components at Angle of Attack. NASA TM-84226, 1982.

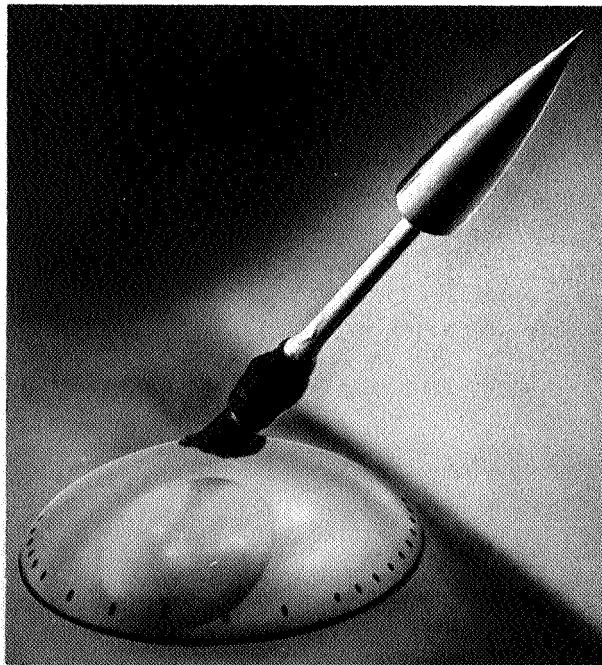
TABLE 1.— MODEL CHARACTERISTICS AND
REFERENCE DIMENSIONS

Forebody shape	ℓ/d	ℓ , cm	s , cm ²	δ_N , deg	r_N , cm
Tangent ogive	2.5	15.0	182.4	22.6	0
Tangent ogive	3.5	53.3	182.4	16.3	0, 0.317 0.635, 1.27
Tangent ogive	5.0	76.2	182.4	11.4	0, 0.635, 1.27
Cone	2.84	53.3	278.2	5.0	0, 0.635, 1.27

ORIGINAL PAGE IS
OF POOR QUALITY



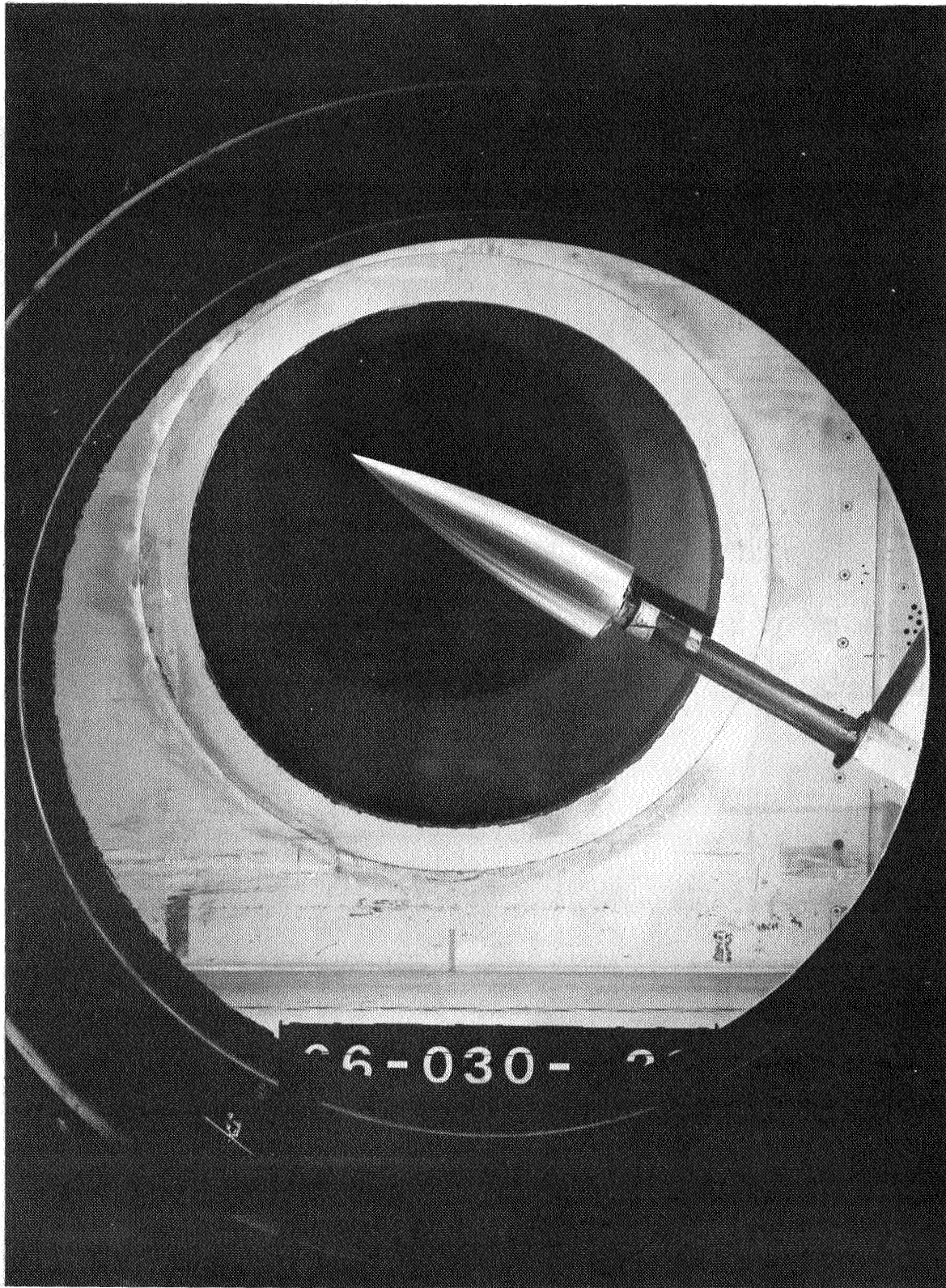
(a) STING SUPPORT FOR $\alpha = 0^\circ$ TO 45°



(b) STING SUPPORT FOR $\alpha = 36^\circ$ TO 88°

Figure 1.— Photographs of model installation on floor support system in Ames 12-Foot Pressure Wind Tunnel.

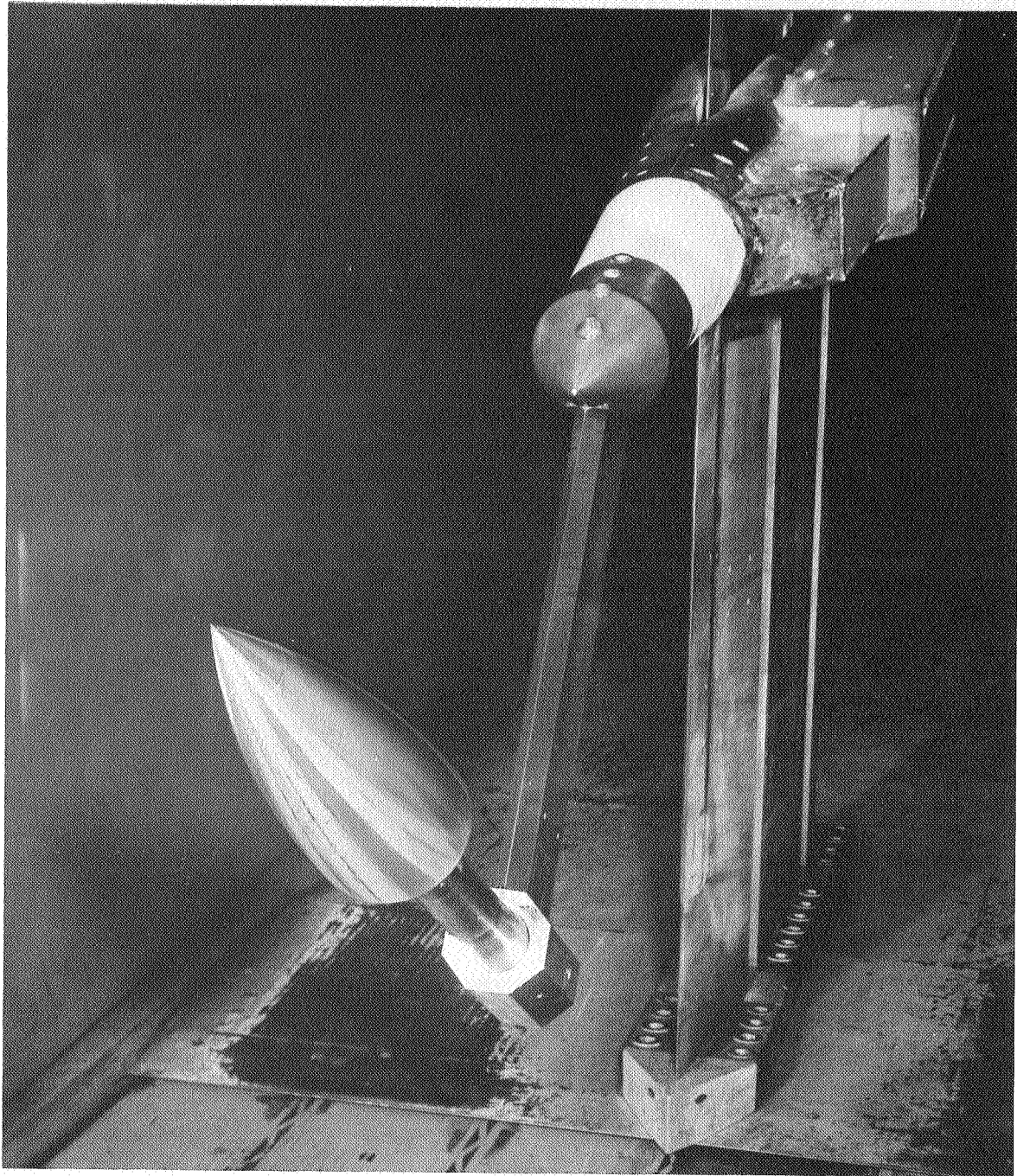
ORIGINAL PAGE IS
OF POOR QUALITY



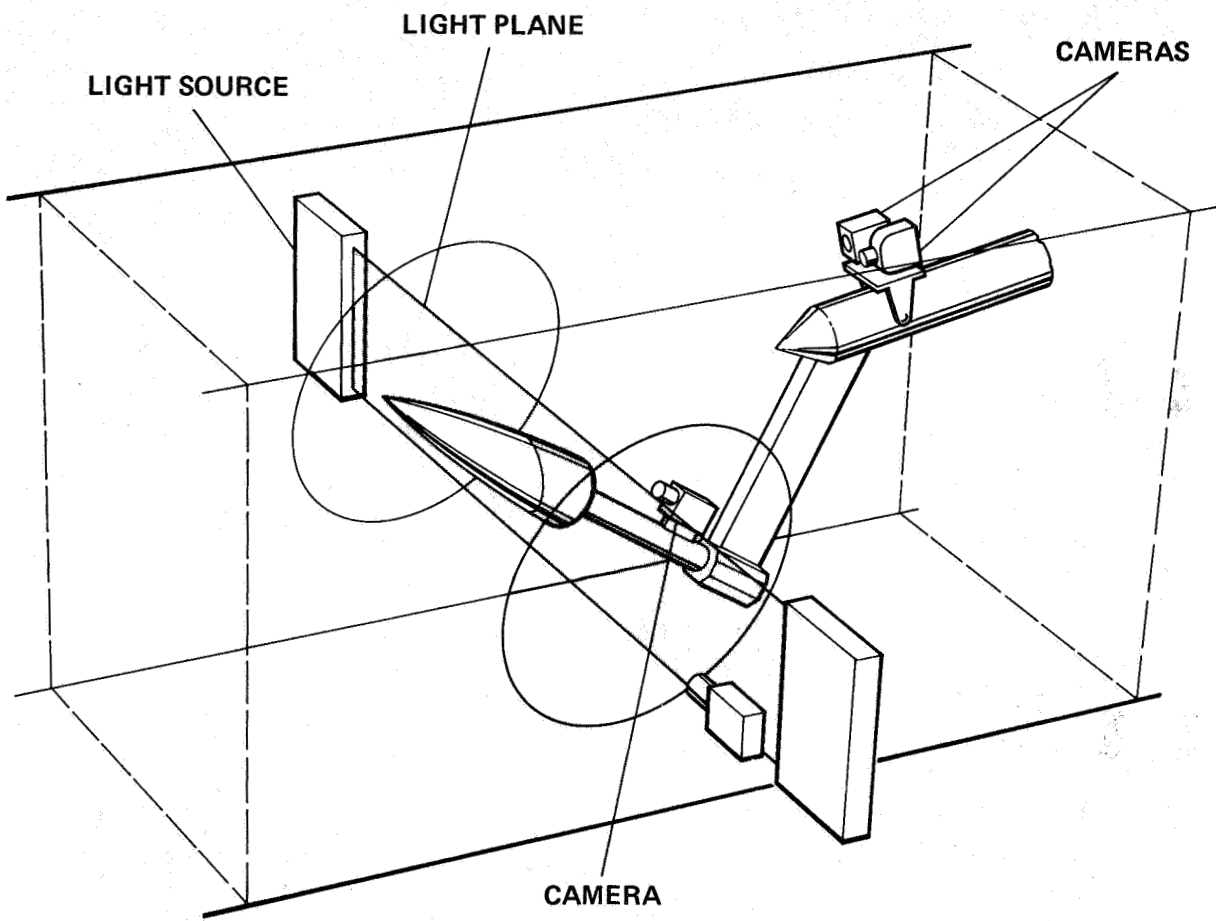
(a) Side View of straight sting support setup for $\alpha = 28^\circ$ to 58°

Figure 2.— Photographs of model installation on sting support system in Ames 6- by 6-Foot Transonic/Supersonic Wind Tunnel.

ORIGINAL PAGE IS
OF POOR QUALITY



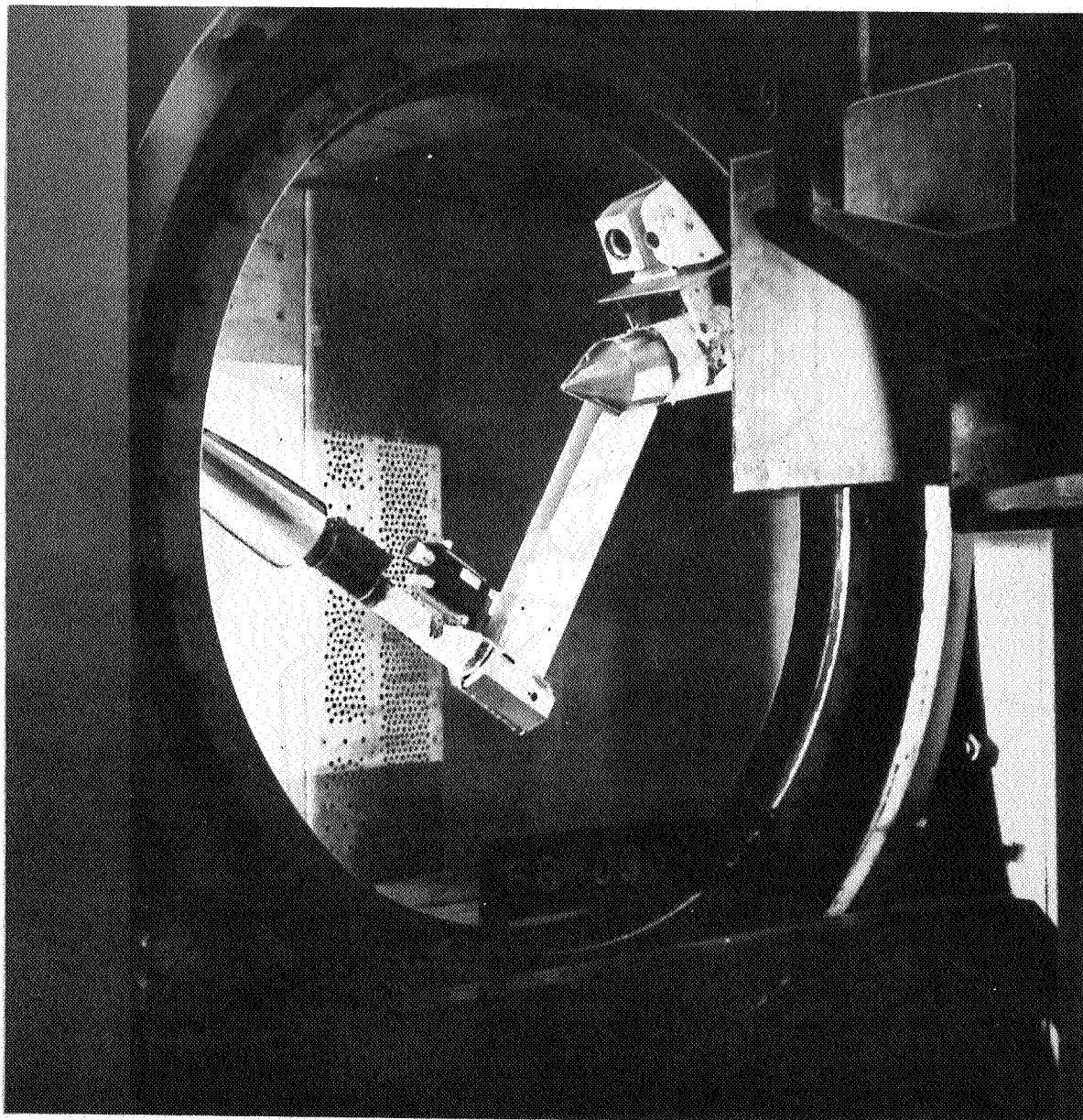
(b) THREE-QUARTER FRONT VIEW OF STING SUPPORT SETUP
FOR $\alpha = 28^\circ$ TO 58°



(a) SKETCH

Figure 3.— Vapor-screen apparatus in 6-ft wind tunnel.

ORIGINAL PAGE IS
OF POOR QUALITY



(b) PHOTOGRAPH

ORIGINAL PAGE IS
OF POOR QUALITY

C_Y α , deg

0.9 40



α , deg C_Y

45 1.6



1.9 50



55 1.0



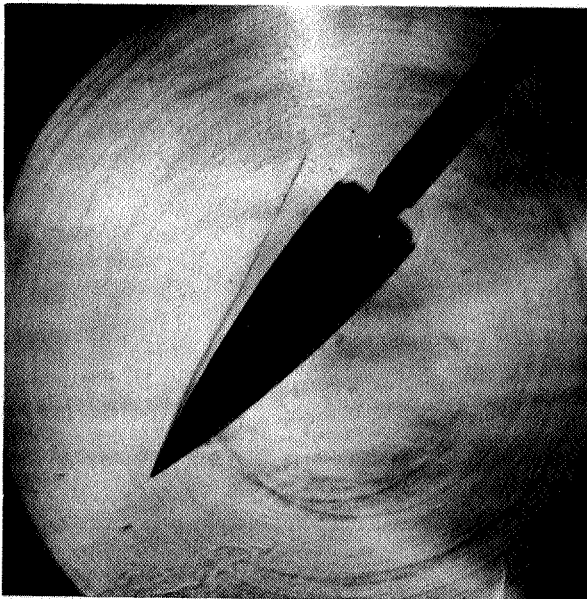
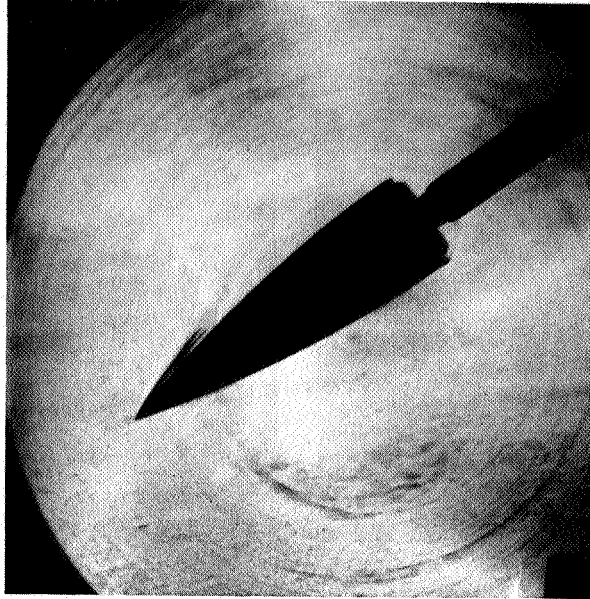
(a) $M = 0.25$, $R_d = 0.8 \times 10^6$

Figure 4.— Schlieren photographs of 3.5-ogive.

ORIGINAL PAGE IS
OF POOR QUALITY

α , deg Cy

55 0.8



α , deg Cy

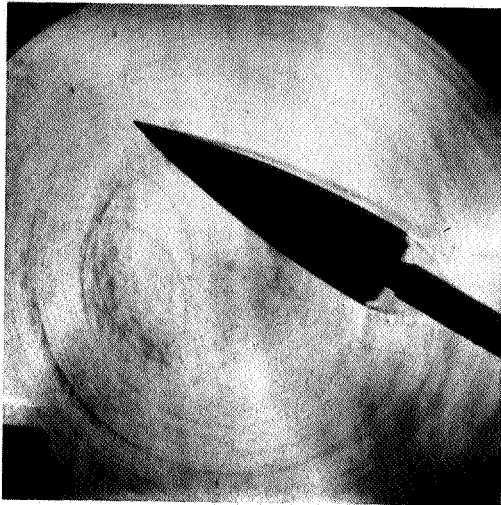
40 1.0

(b) $M = 0.6$, $R_d = 0.8 \times 10^6$

ORIGINAL PAGE IS
OF POOR QUALITY

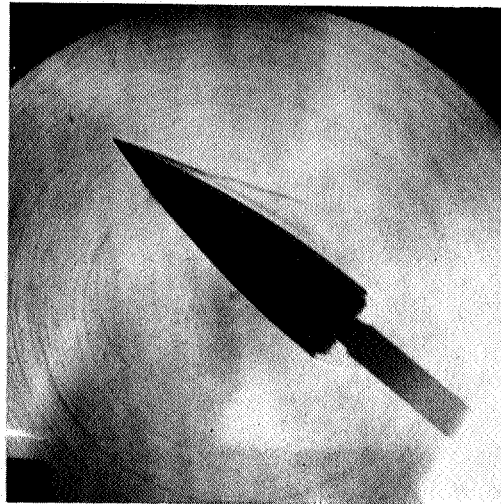
C_Y α , deg

0 30

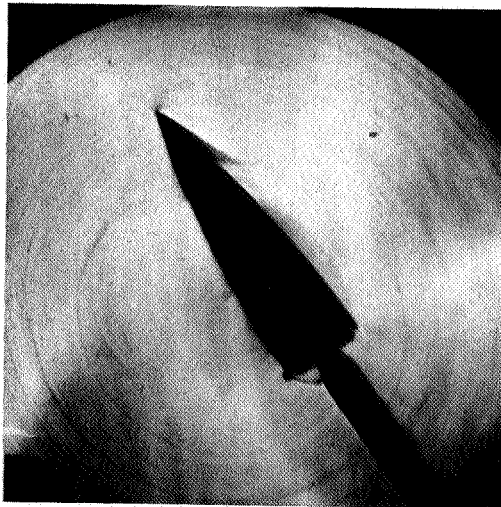


α , deg C_Y

40 0.6



0.4 55



(c) $M = 0.6$, $R_d = 1.8 \times 10^6$

ORIGINAL PAGE IS
OF POOR QUALITY

α , deg

30



VORTEX PAIR

SHOCK WAVE

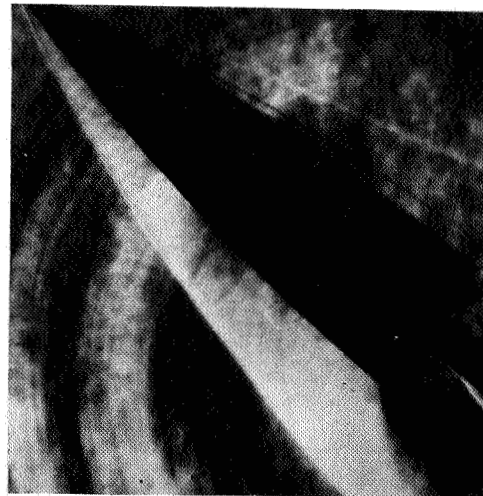
α , deg



40

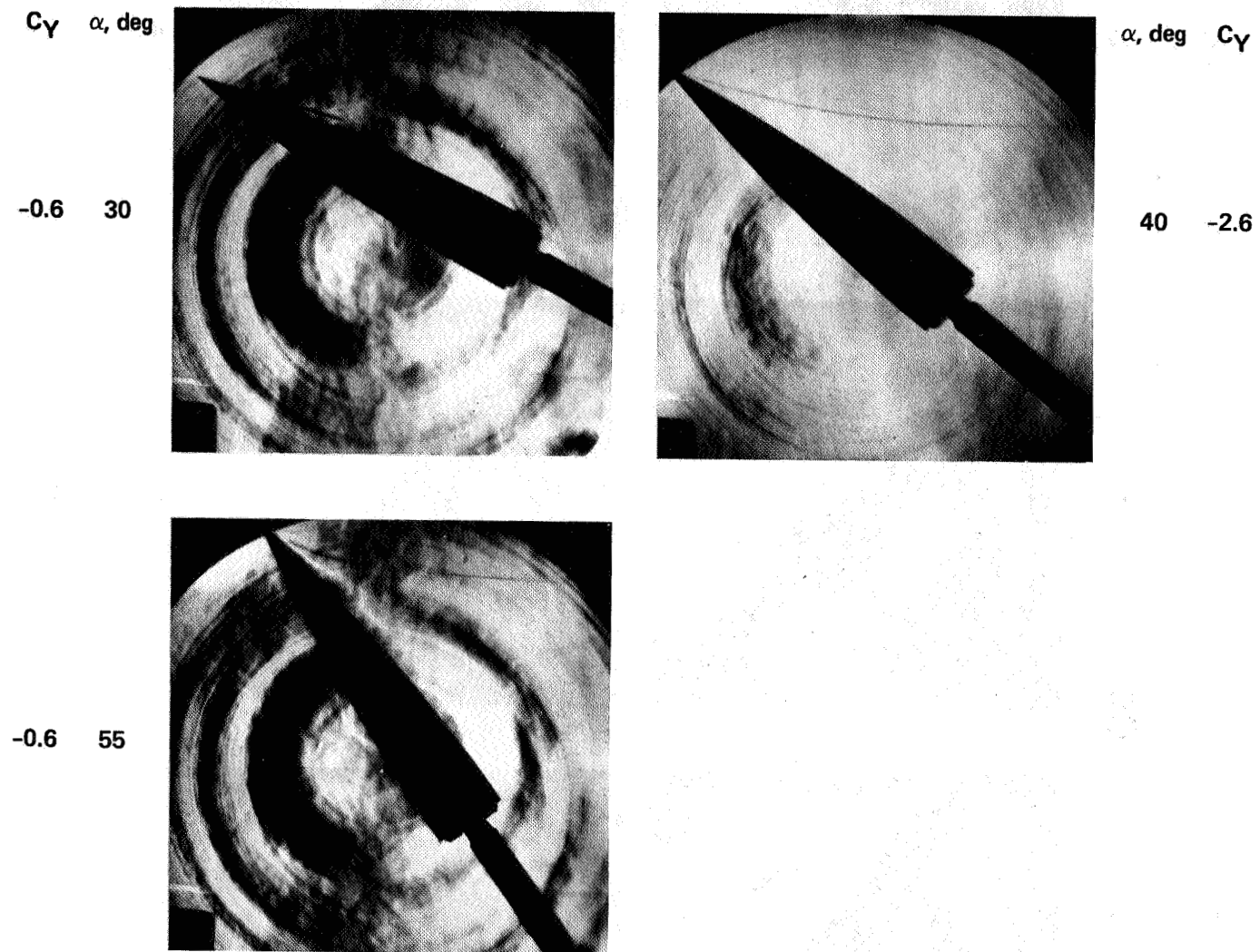


40



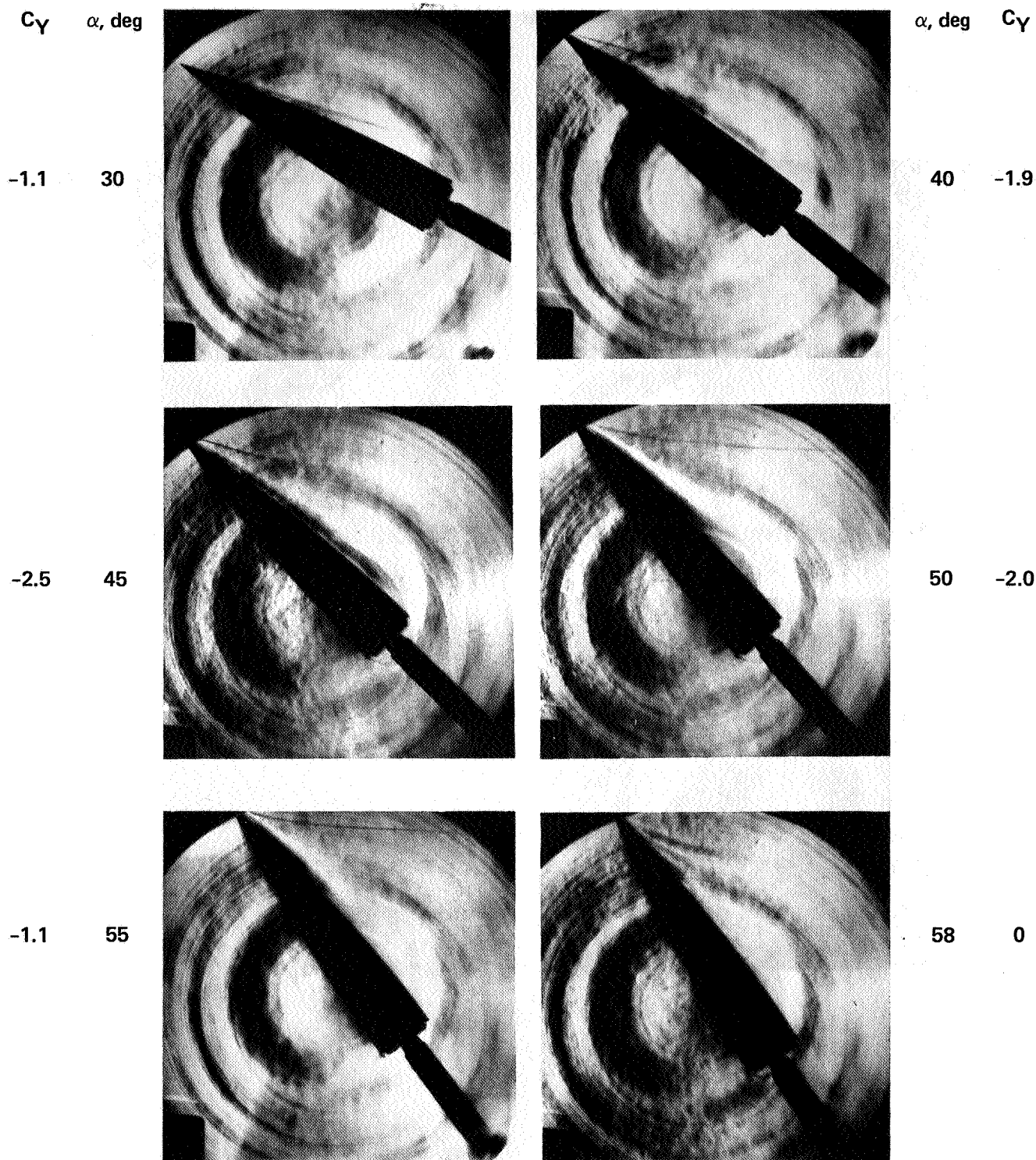
(d) $M = 2.0$, $R_d = 0.8 \times 10^6$, $C_Y = 0$

ORIGINAL PAGE IS
OF POOR QUALITY



(a) $M = 0.25$, $R_d = 0.8 \times 10^6$

Figure 5.— Schlieren photographs of 5-ogive.

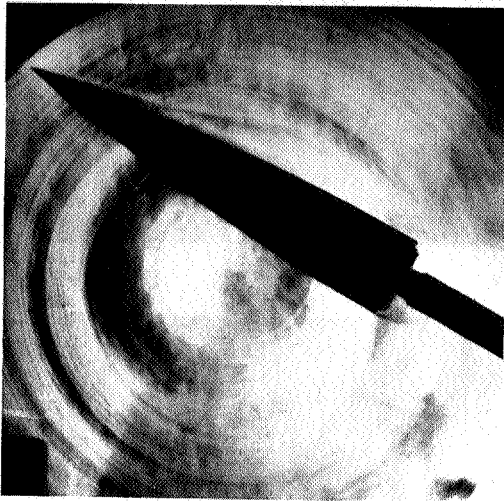


(b) $M = 0.6$, $R_d = 0.8 \times 10^6$

ORIGINAL PAGE IS
OF POOR QUALITY

C_y α , deg

-0.5 30



α , deg C_y

40 0.6



-0.2 55

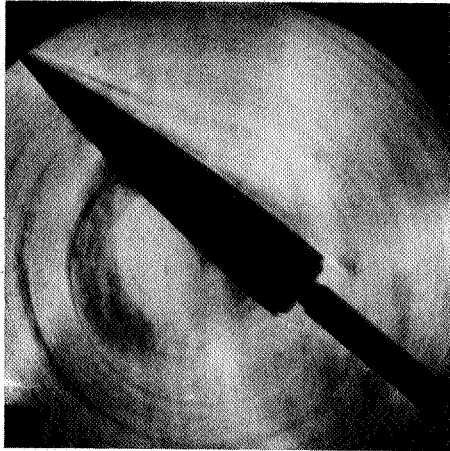


(c) $M = 0.6$, $R_d = 1.8 \times 10^6$

ORIGINAL PAGE IS
OF POOR QUALITY

C_Y α , deg

-2.0 40



α , deg C_Y

45 -1.4



0.2 50



55 -0.3

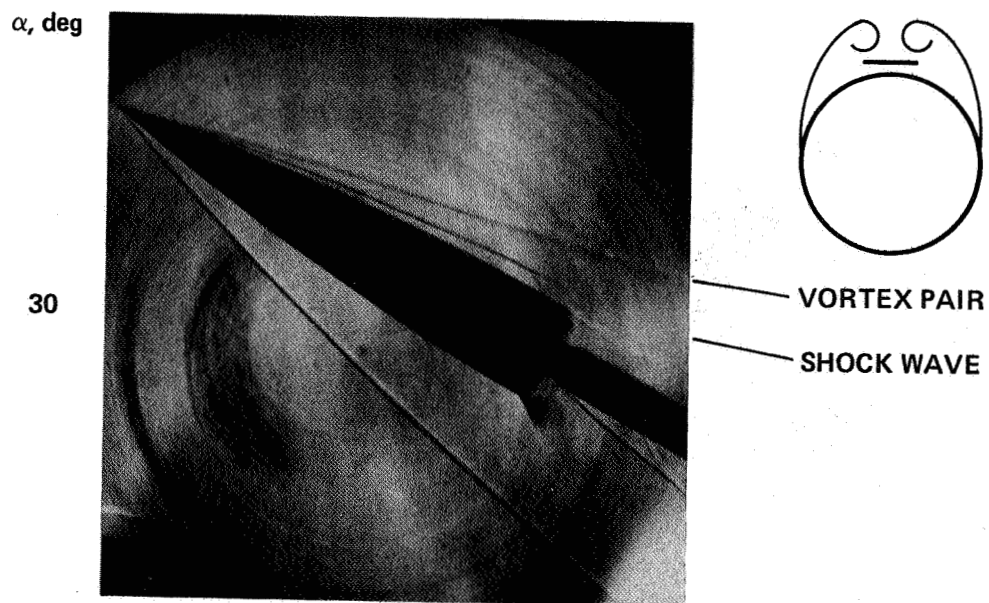


-0.1 58



(d) $M = 0.8$, $R_d = 0.8 \times 10^6$

ORIGINAL PAGE IS
OF POOR QUALITY



(e) $M = 2.0$, $R_d = 0.8 \times 10^6$, $C_Y = 0$

ORIGINAL PAGE IS
OF POOR QUALITY

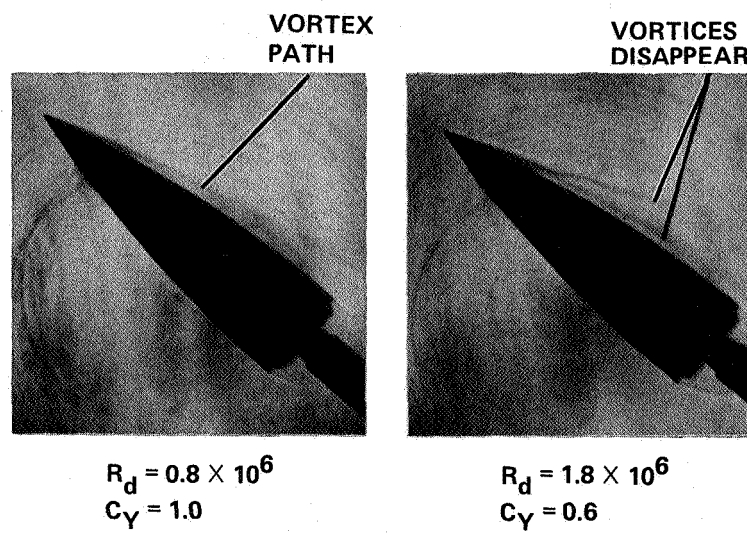


Figure 6.— Effect of Reynolds number on vortex traces from schlieren photographs: 3.5-ogive, $M = 0.6$, $\alpha = 40^\circ$.

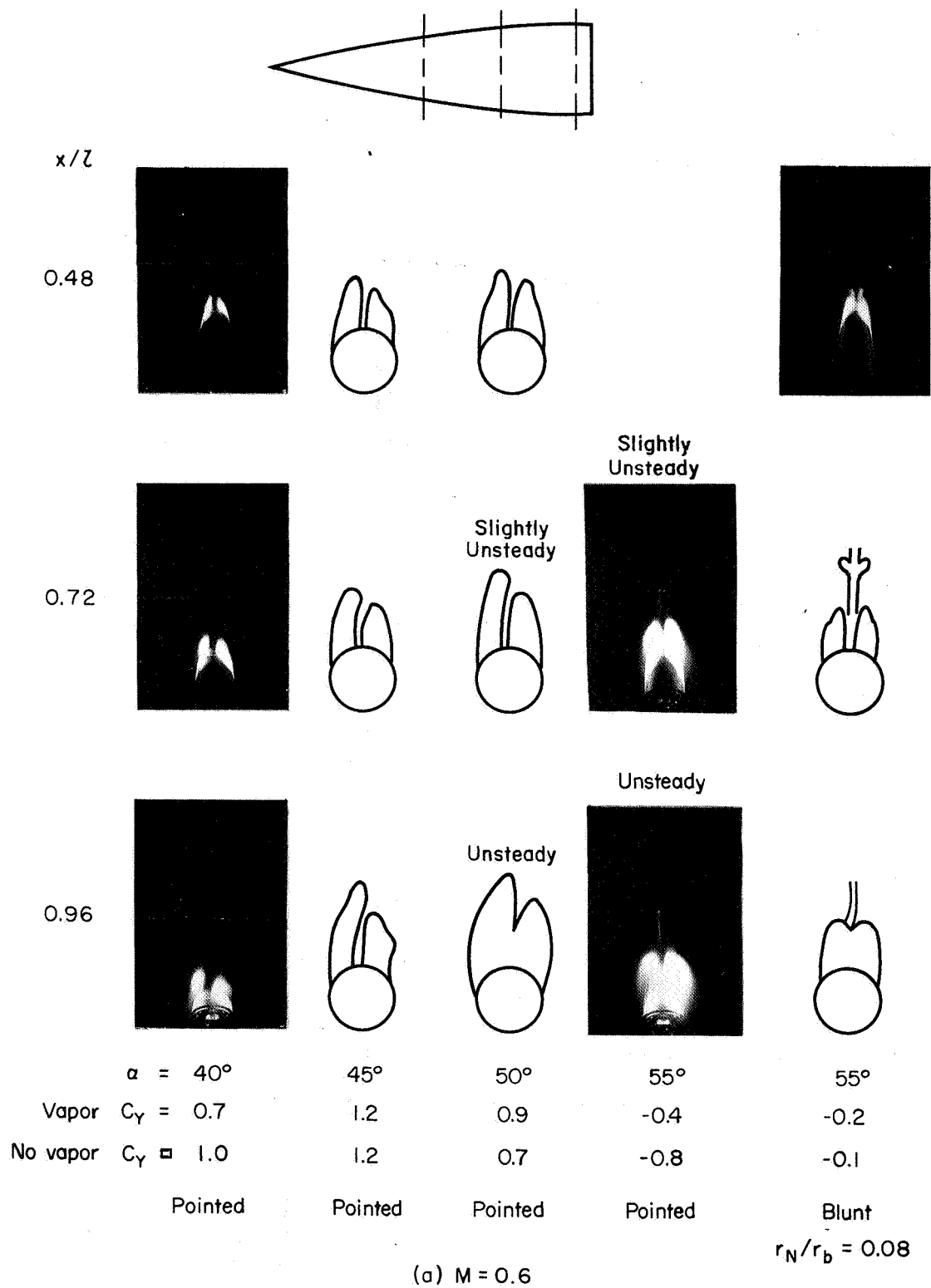
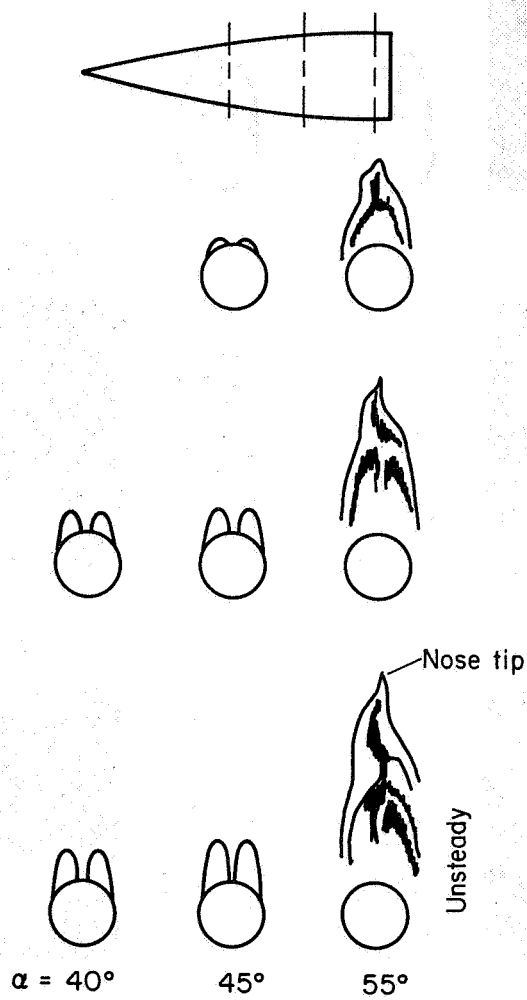
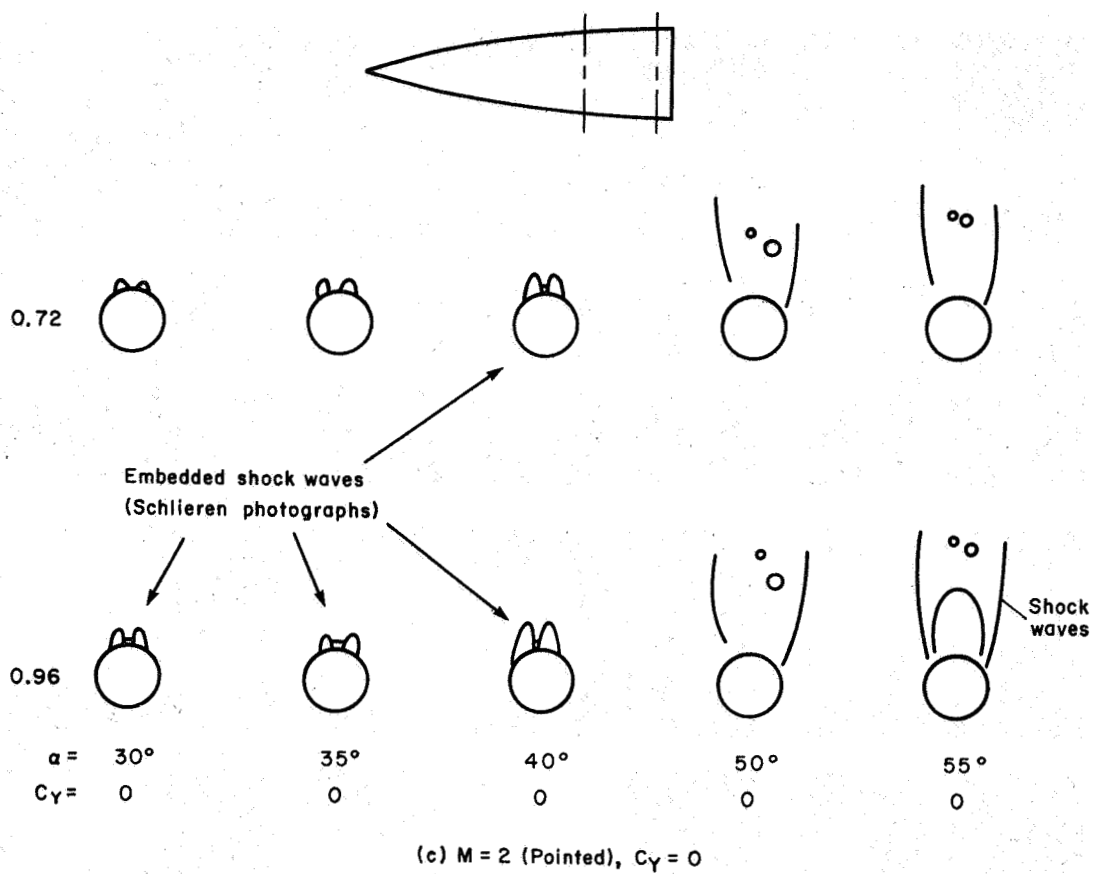


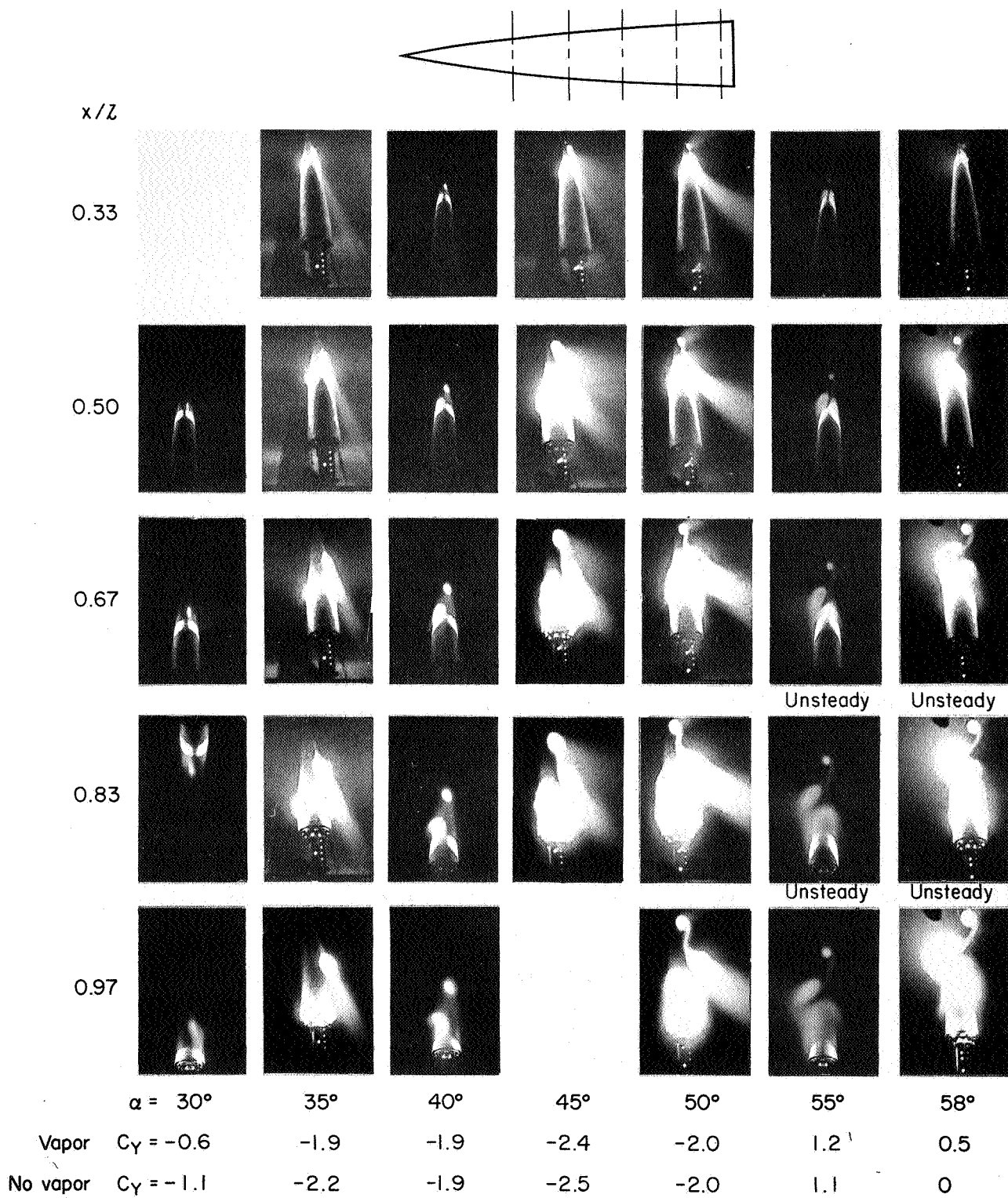
Figure 7.— Vapor-screen photographs and sketches from movies for 3.5-ogive at $R_d = 0.8 \times 10^6$.



(b) $M = 0.8$, $C_\gamma = 0$, pointed

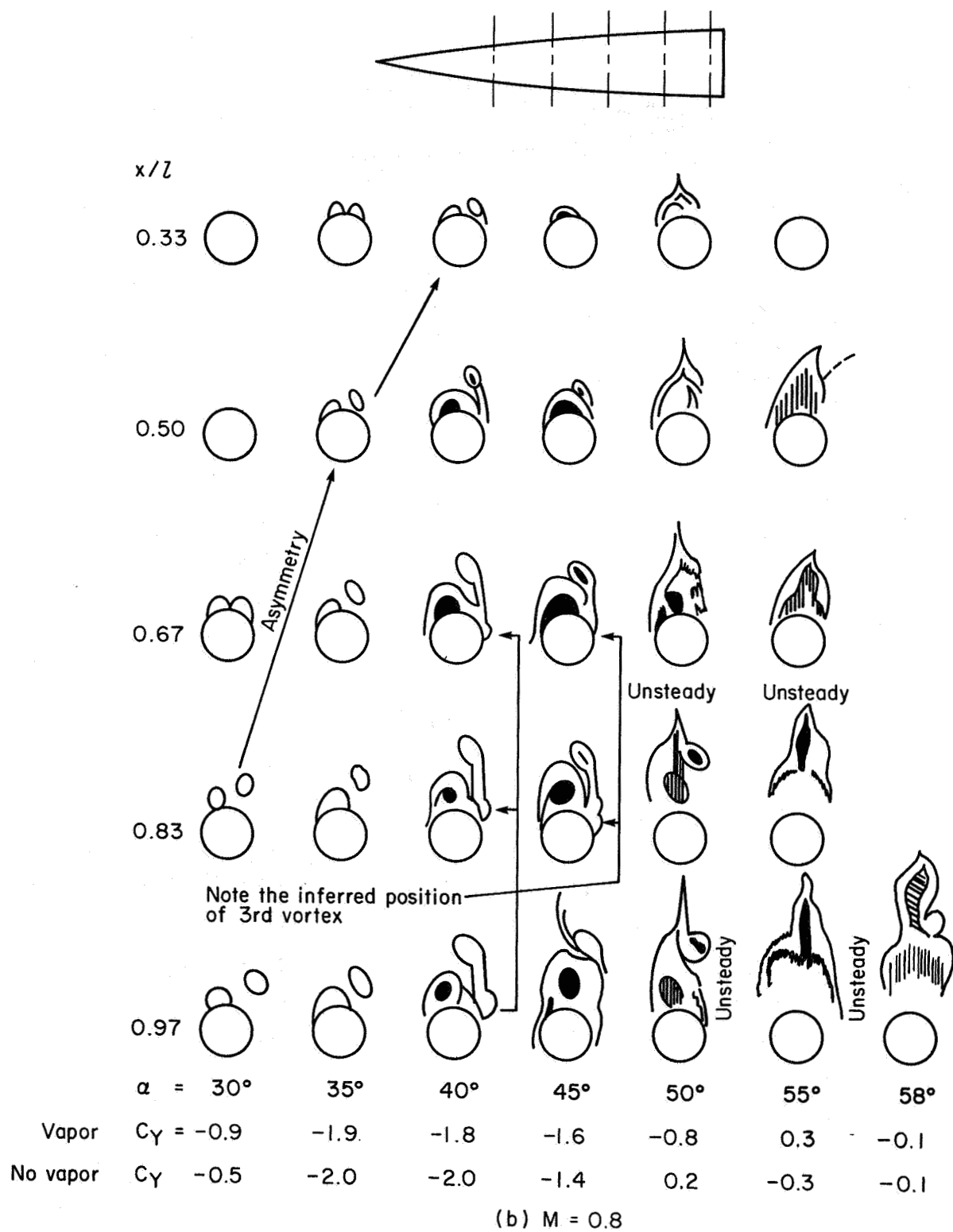


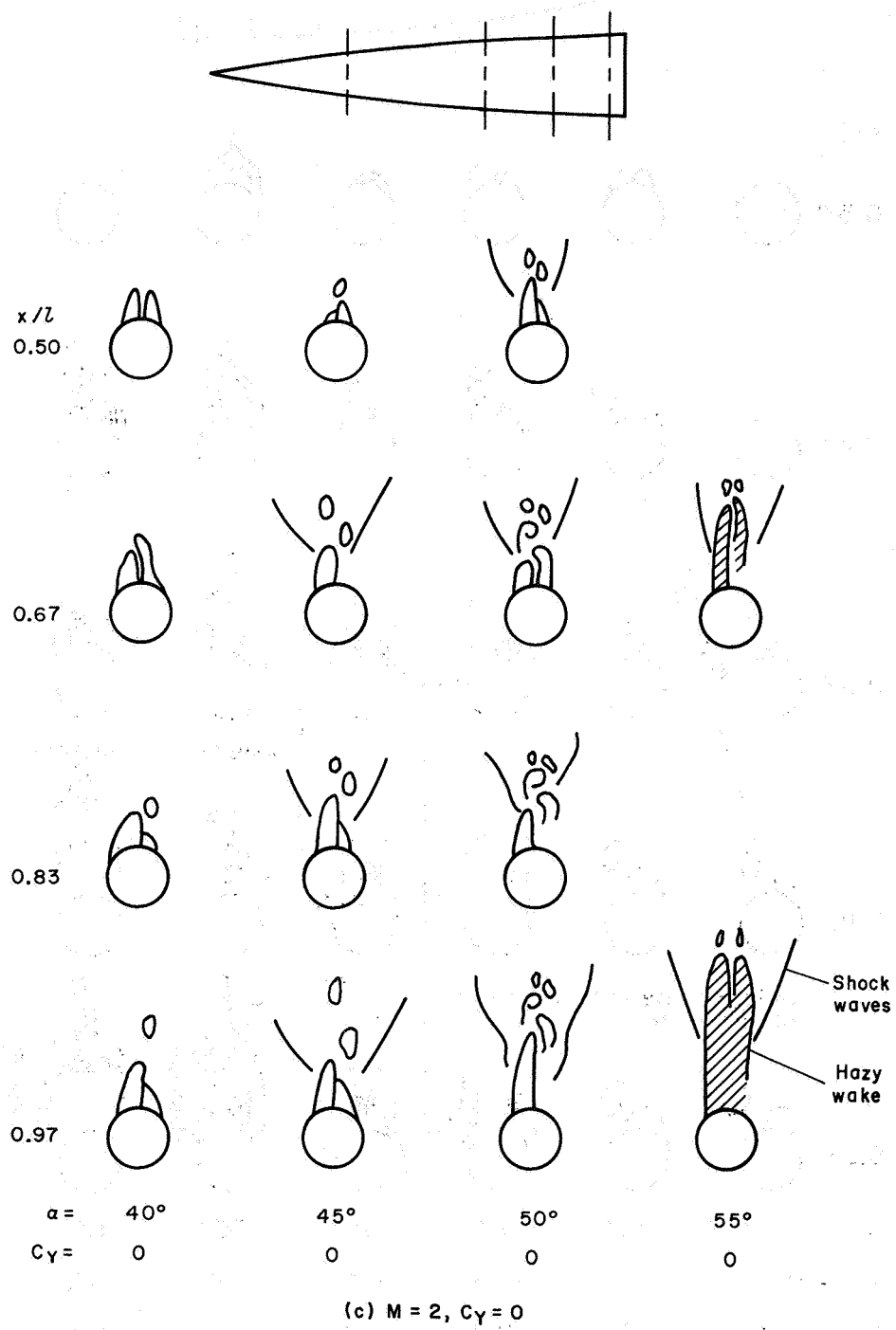
ORIGINAL PAGE IS
OF POOR QUALITY



(a) $M = 0.6$

Figure 8.— Vapor-screen photographs and sketches from movies for 5-ogive at $R_d = 0.8 \times 10^6$.





ORIGINAL PAGE IS
OF POOR QUALITY

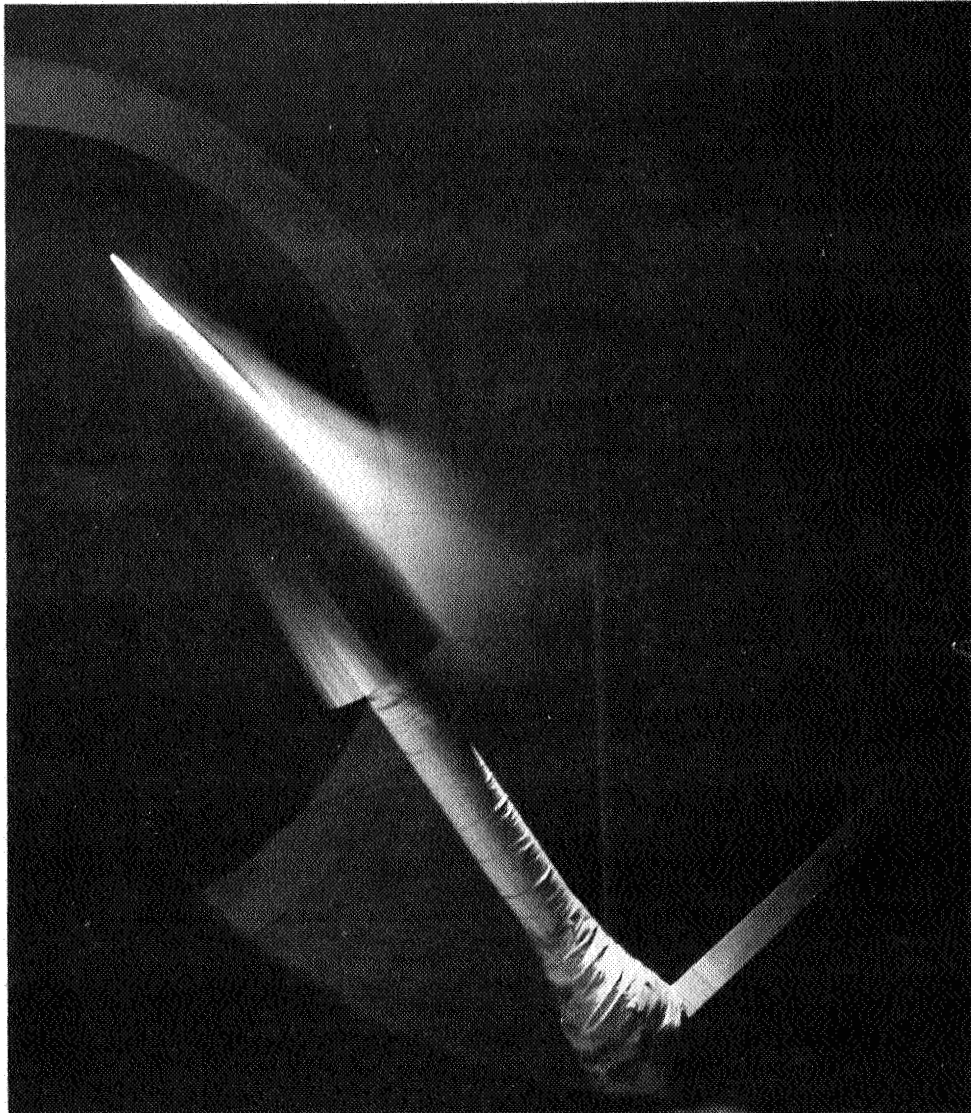


Figure 9.— Vapor-trail photographs of 3.5-ogive: $M = 0.6$, $R_d = 1.8 \times 10^6$, $\alpha = 45^\circ$, $C_Y = 1.4$.

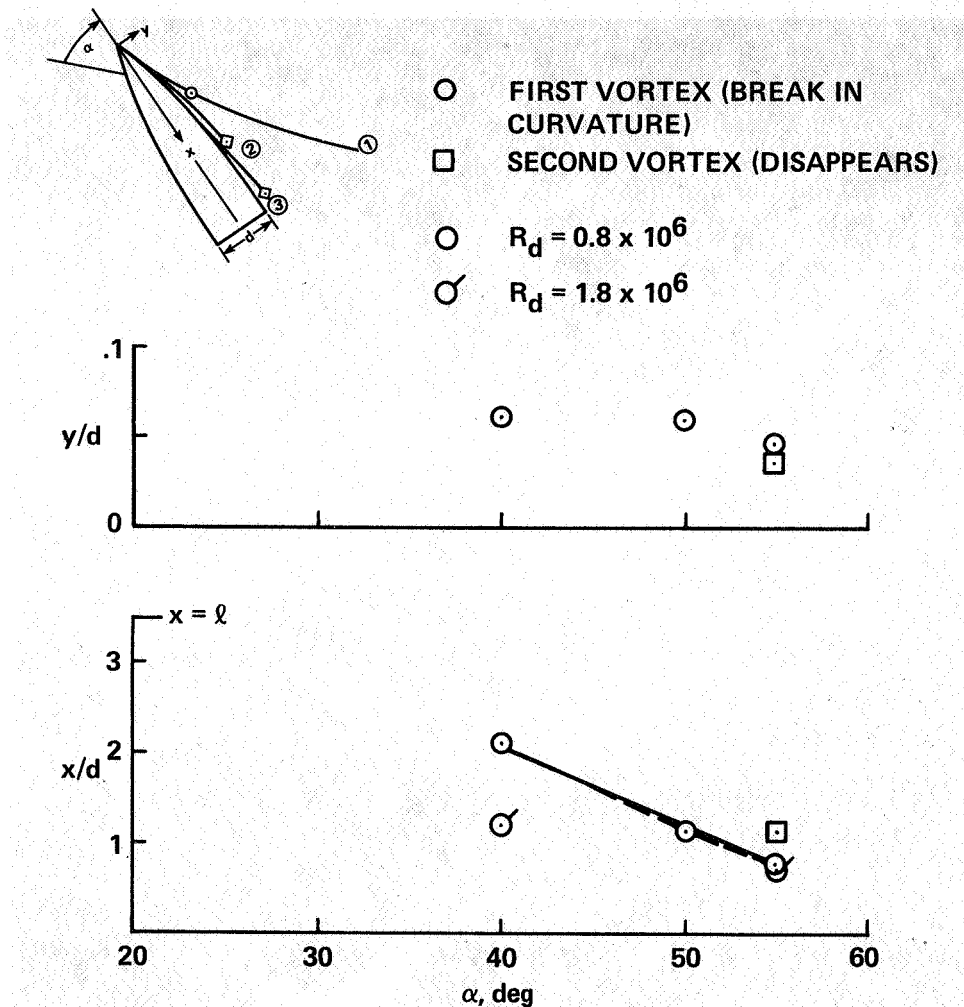


Figure 10.— Measured position of vortex shedding from schlieren photographs for 3.5-ogive at $M = 0.25$.

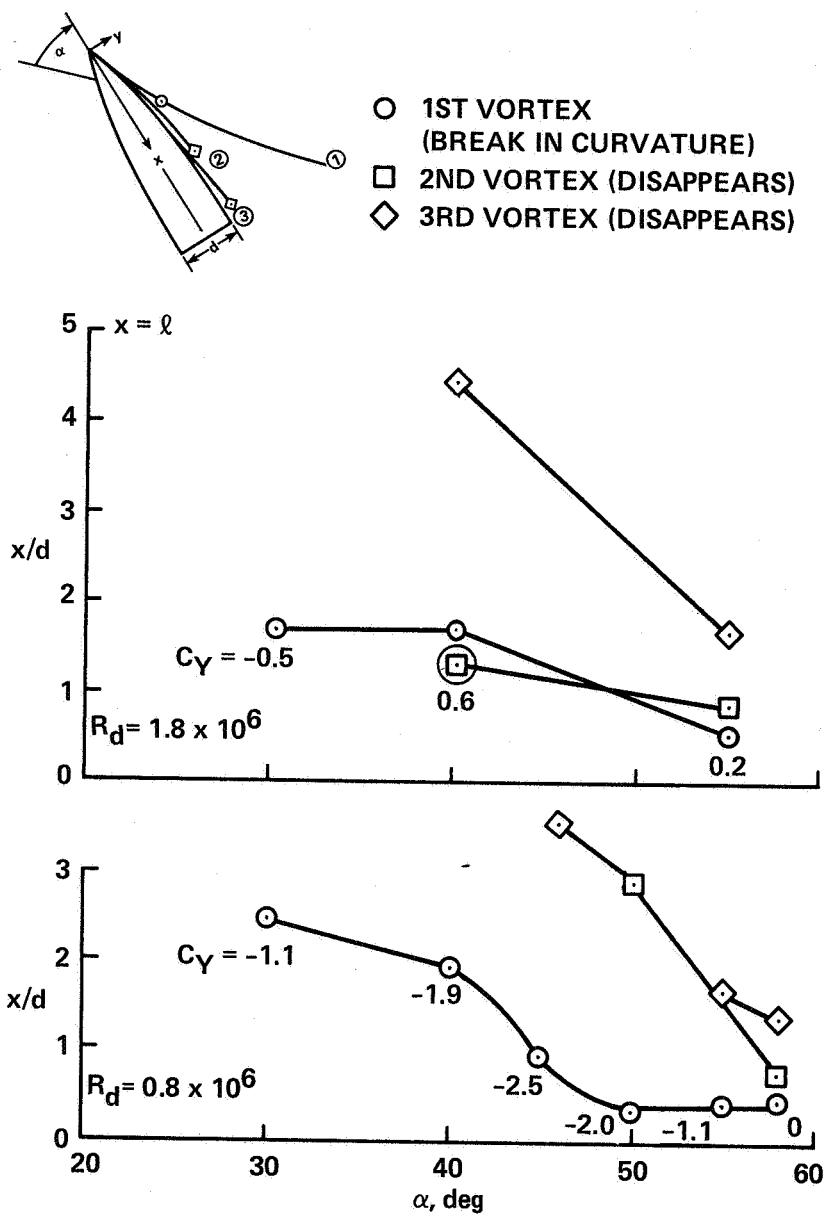


Figure 11.— Measured position of vortex shedding from schlieren photographs for 5-ogive at $M = 0.6$.

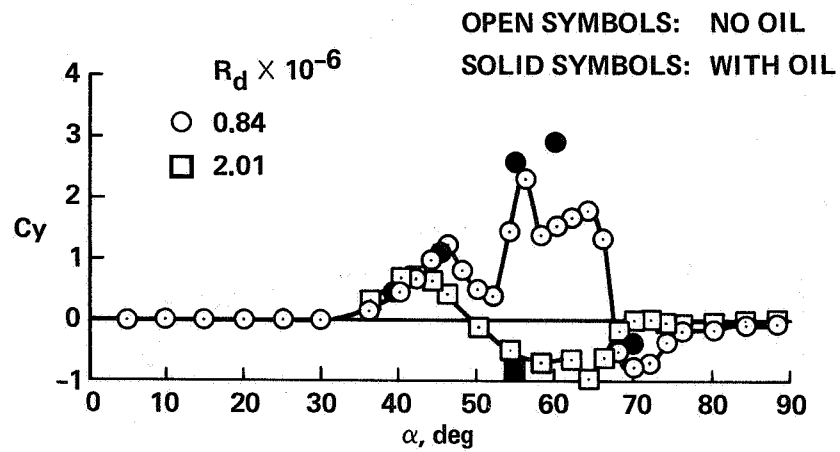
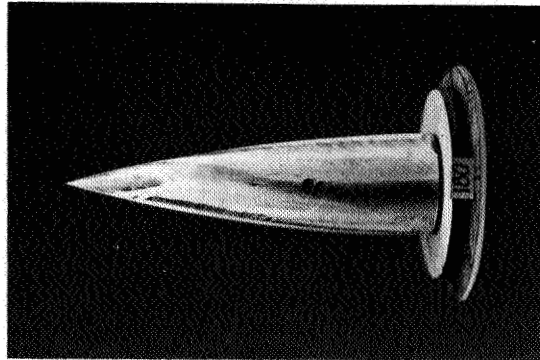
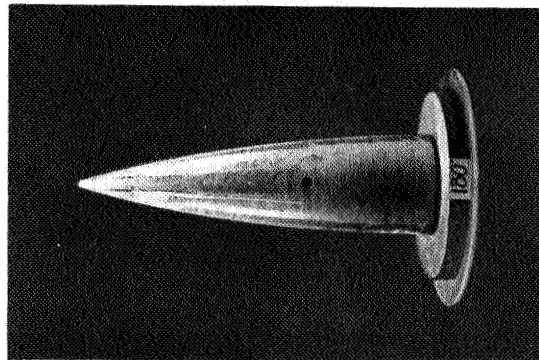


Figure 12.— Effect of oil on side-force measurements for 3.5-ogive at $M = 0.25$.

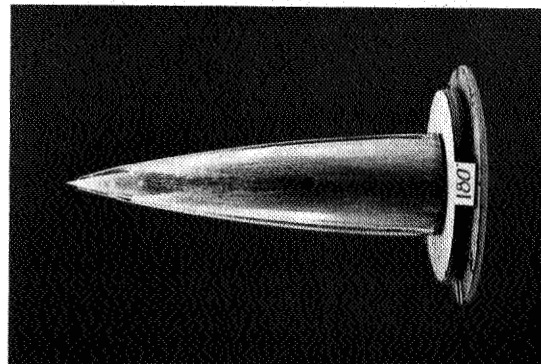
ORIGINAL PAGE IS
OF POOR QUALITY



(a) POINTED NOSE



(b) BLUNT NOSE,
RADIUS = 8.35 % OF BASE RADIUS



(c) NOSE STRAKES,
WIDTH = 4.17 % OF BASE RADIUS

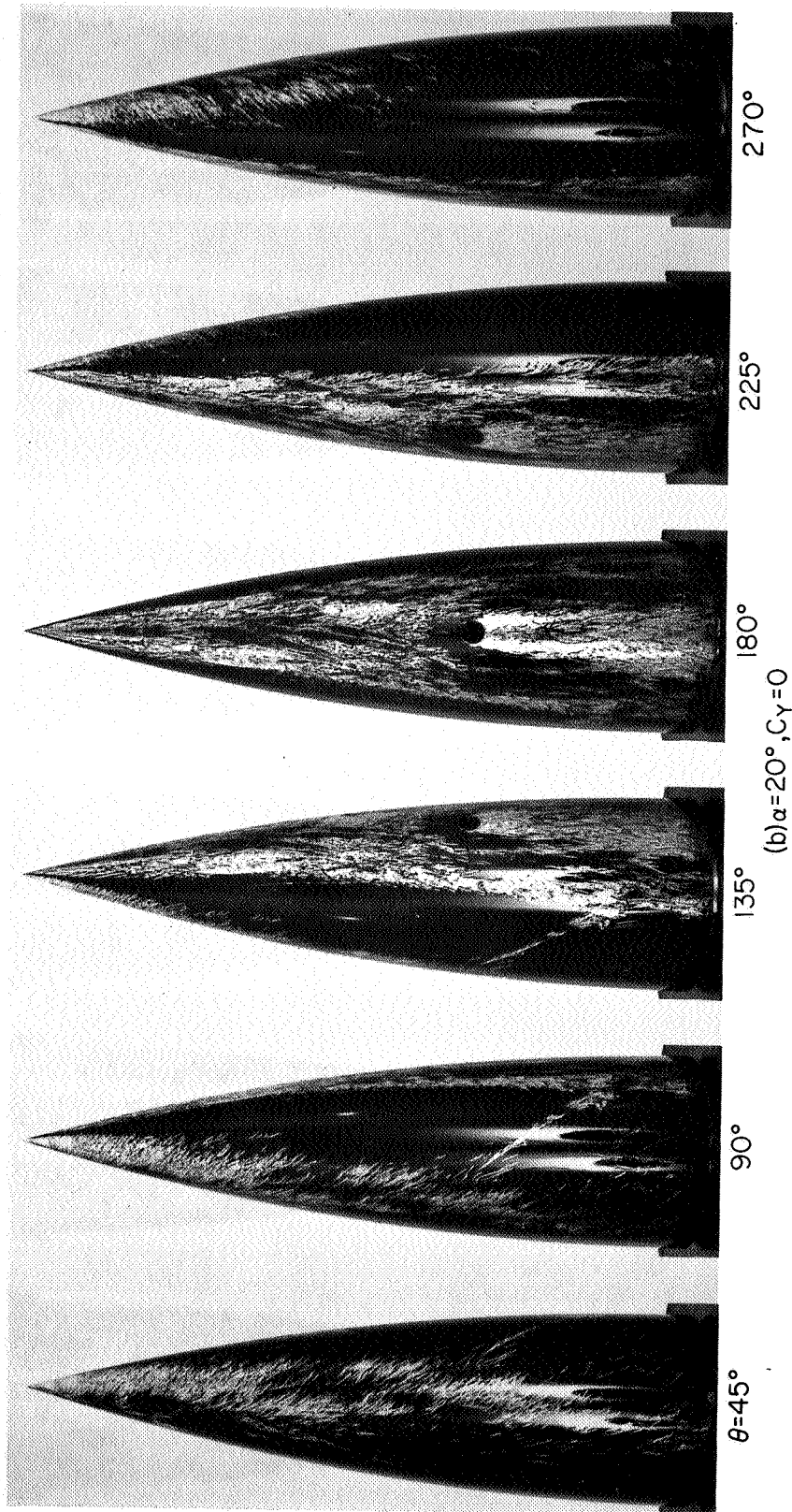
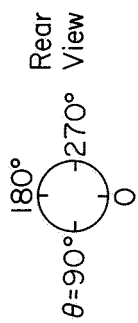
Figure 13.— Effect of blunt nose and nose strakes on oil-flow patterns for 3.5-ogive: $M = 0.25$, $R_d = 0.8 \times 10^6$.



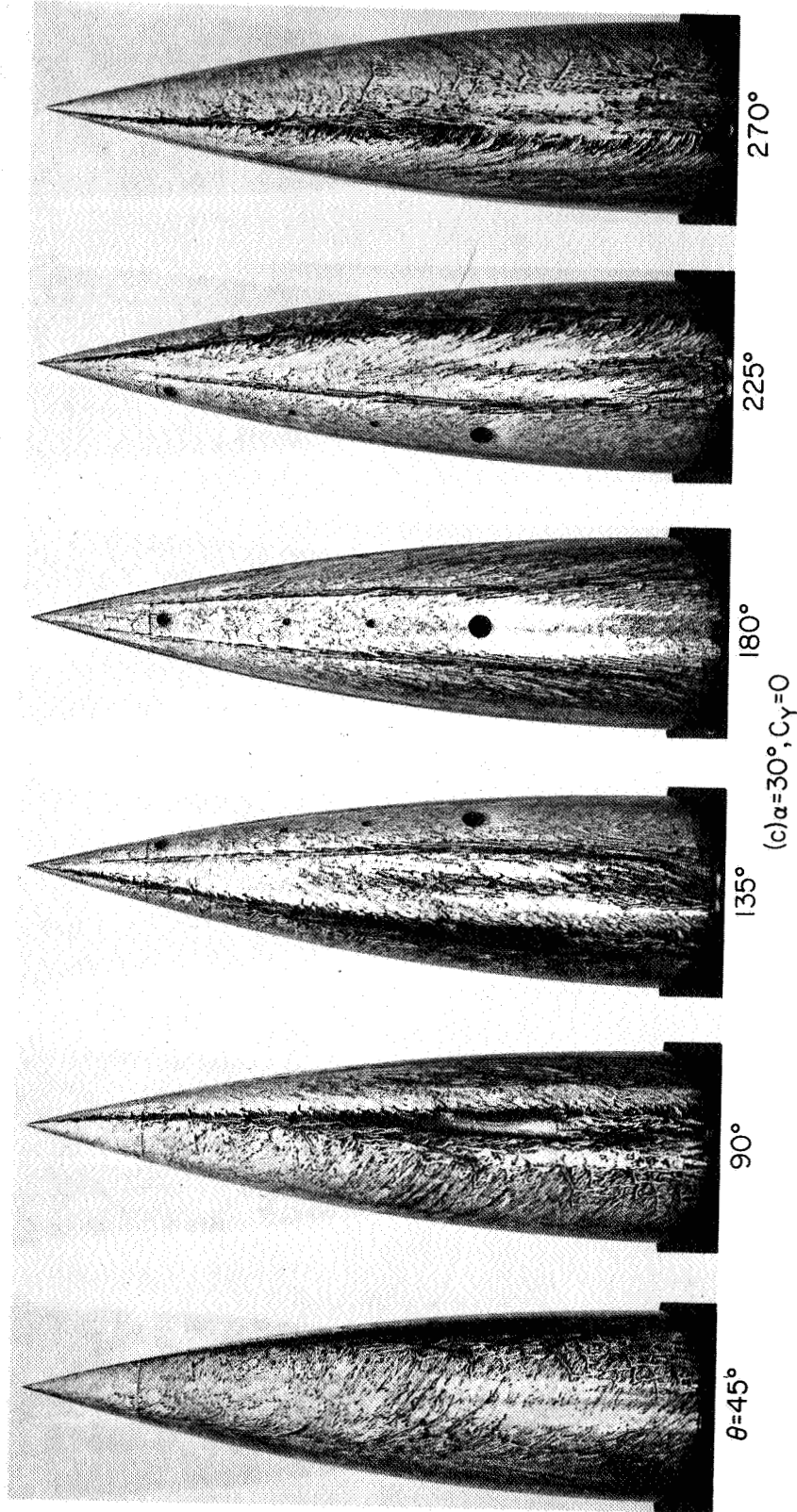
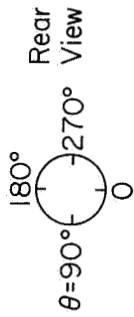
(a) $\alpha = 0$, $C_Y = 0$

Figure 14.— Oil-flow photographs for 3.5-ogive: $M = 0.25$, $R_d = 0.3 \times 10^6$.

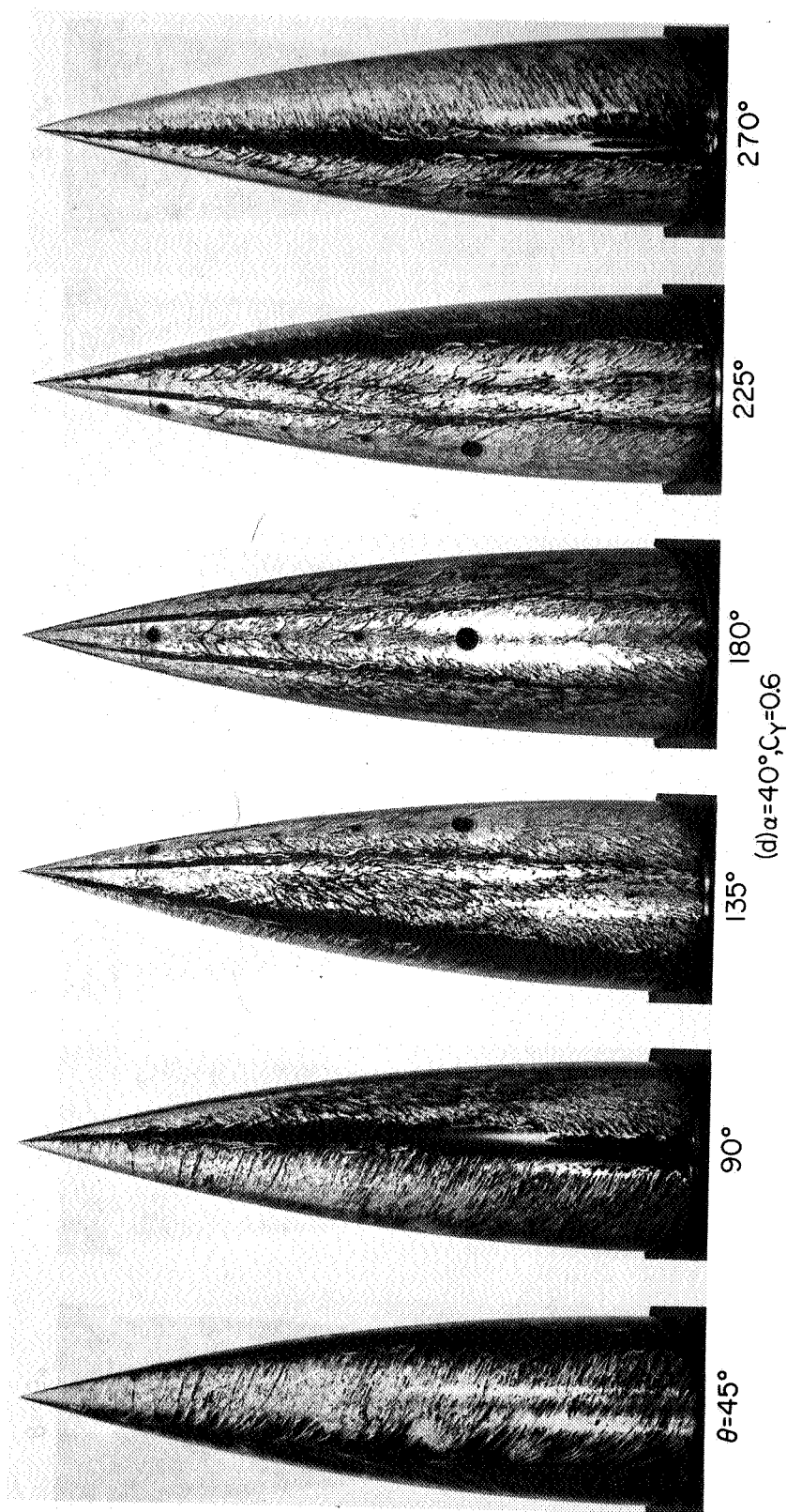
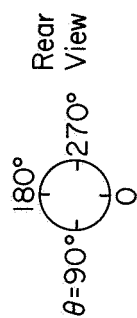
ORIGINAL PAGE IS
OF POOR QUALITY



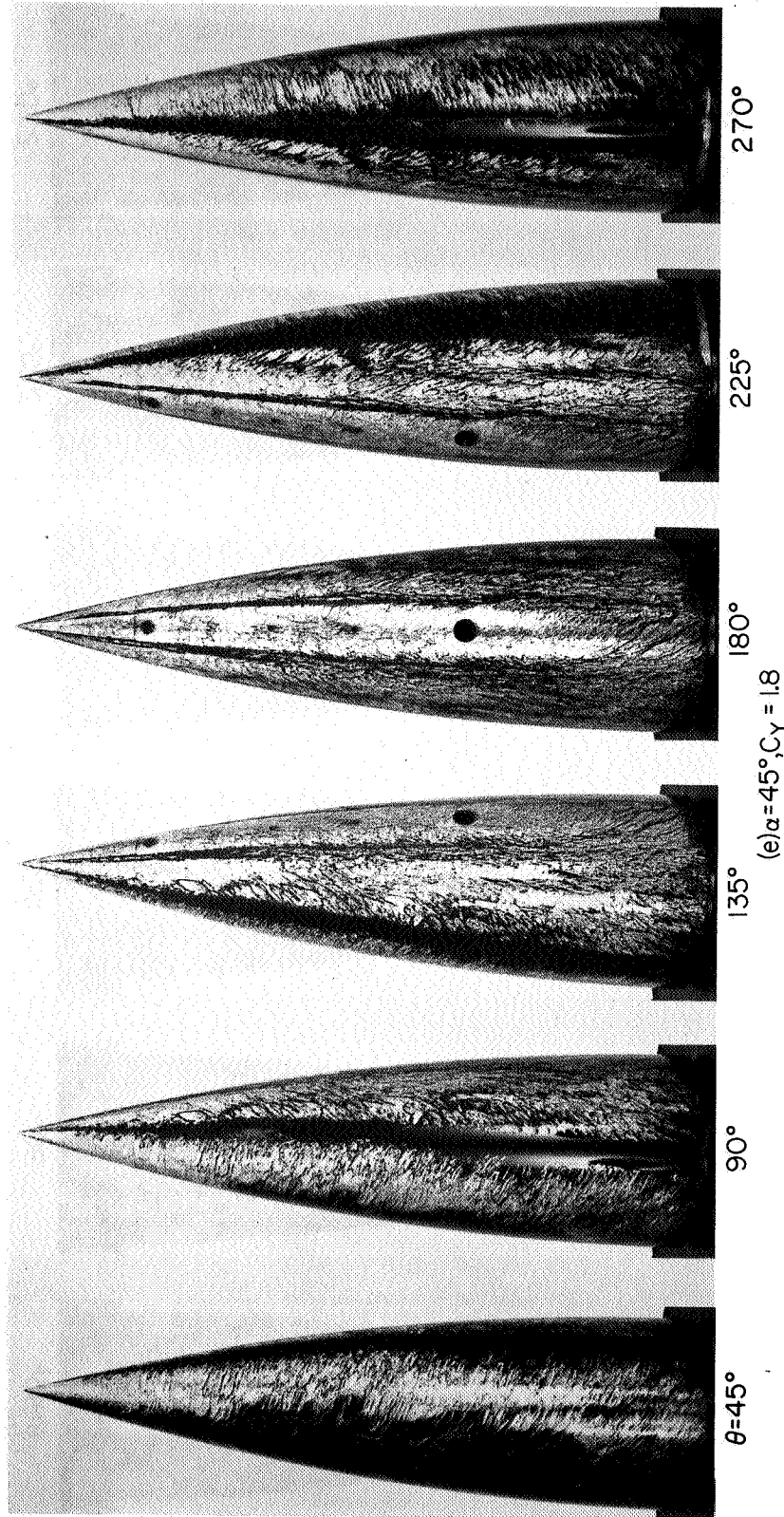
ORIGINAL PAGE IS
OF POOR QUALITY



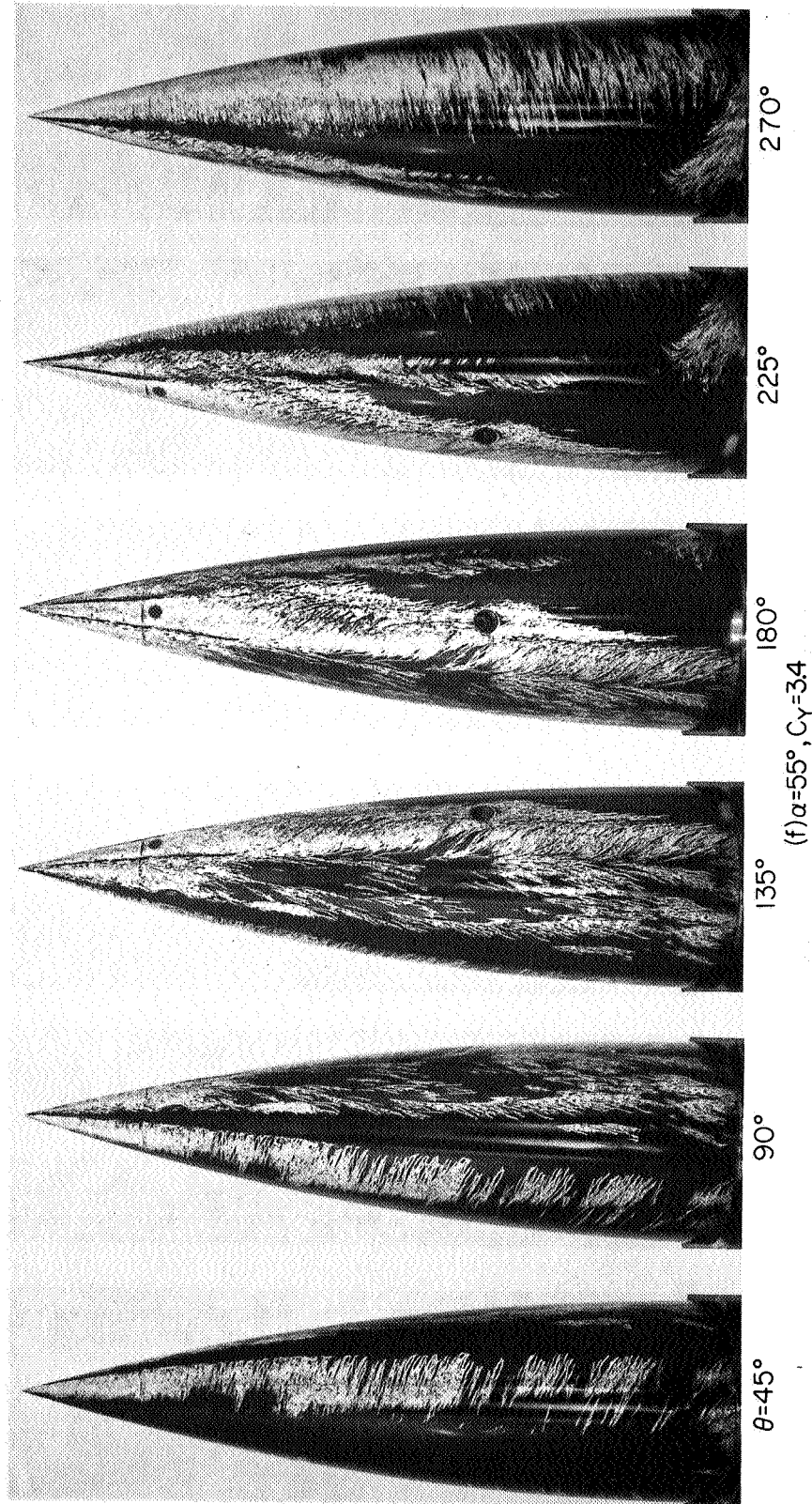
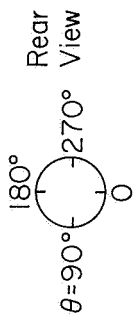
ORIGINAL PAGE IS
OF POOR QUALITY

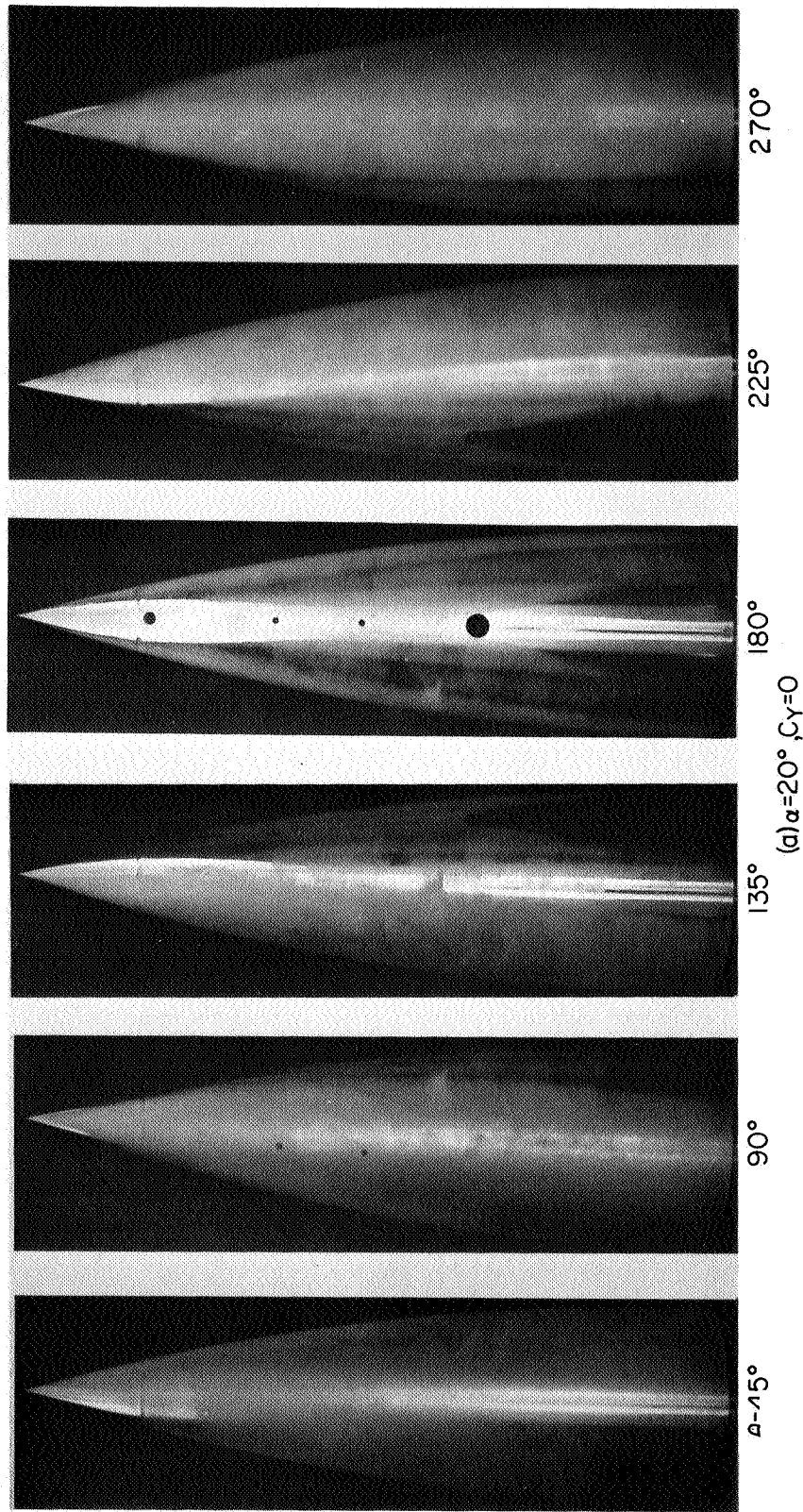
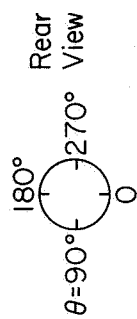


Rear View
180°
θ=90° 270°
0



ORIGINAL PAGE IS
OF POOR QUALITY

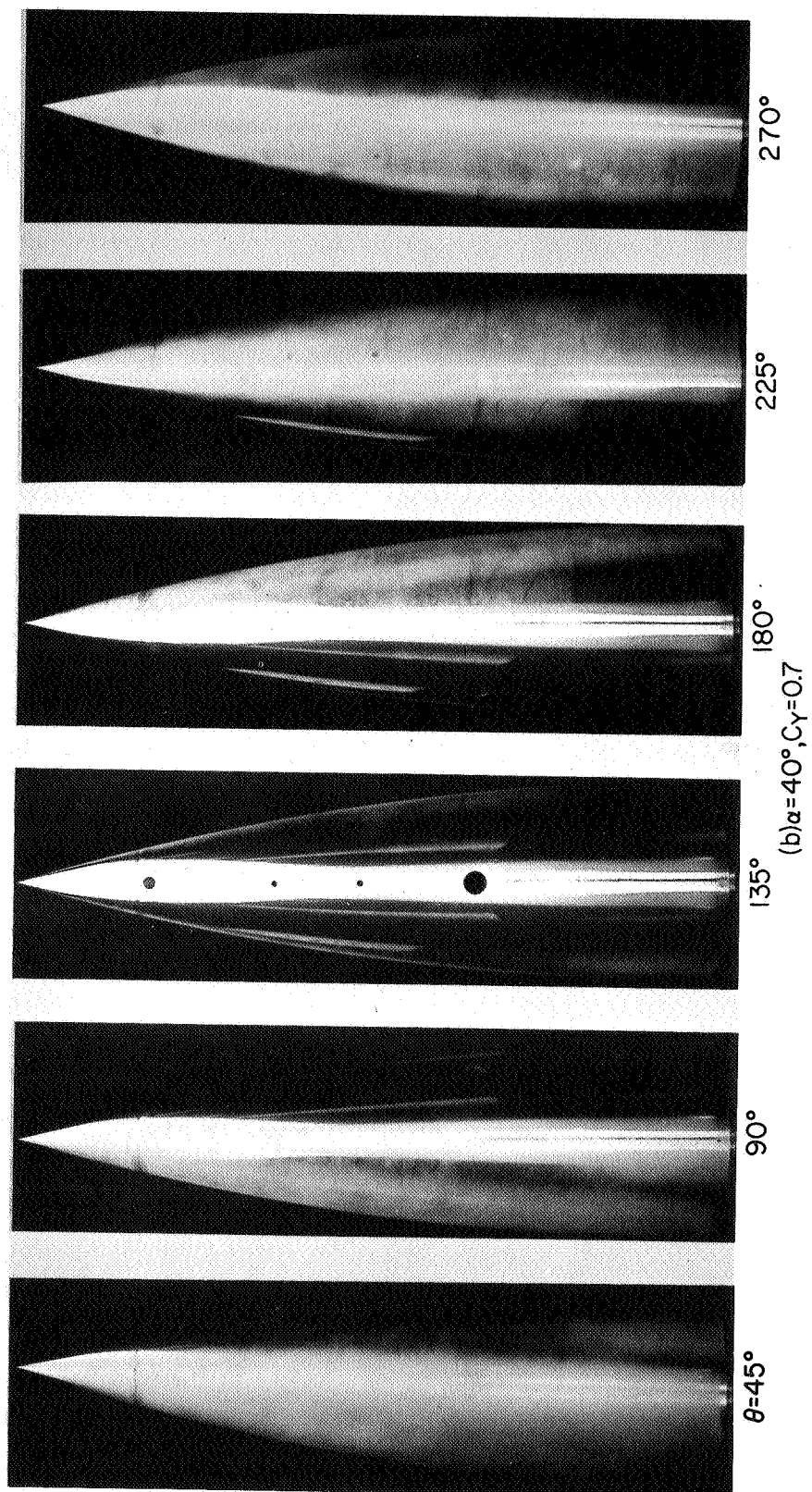
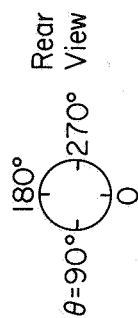


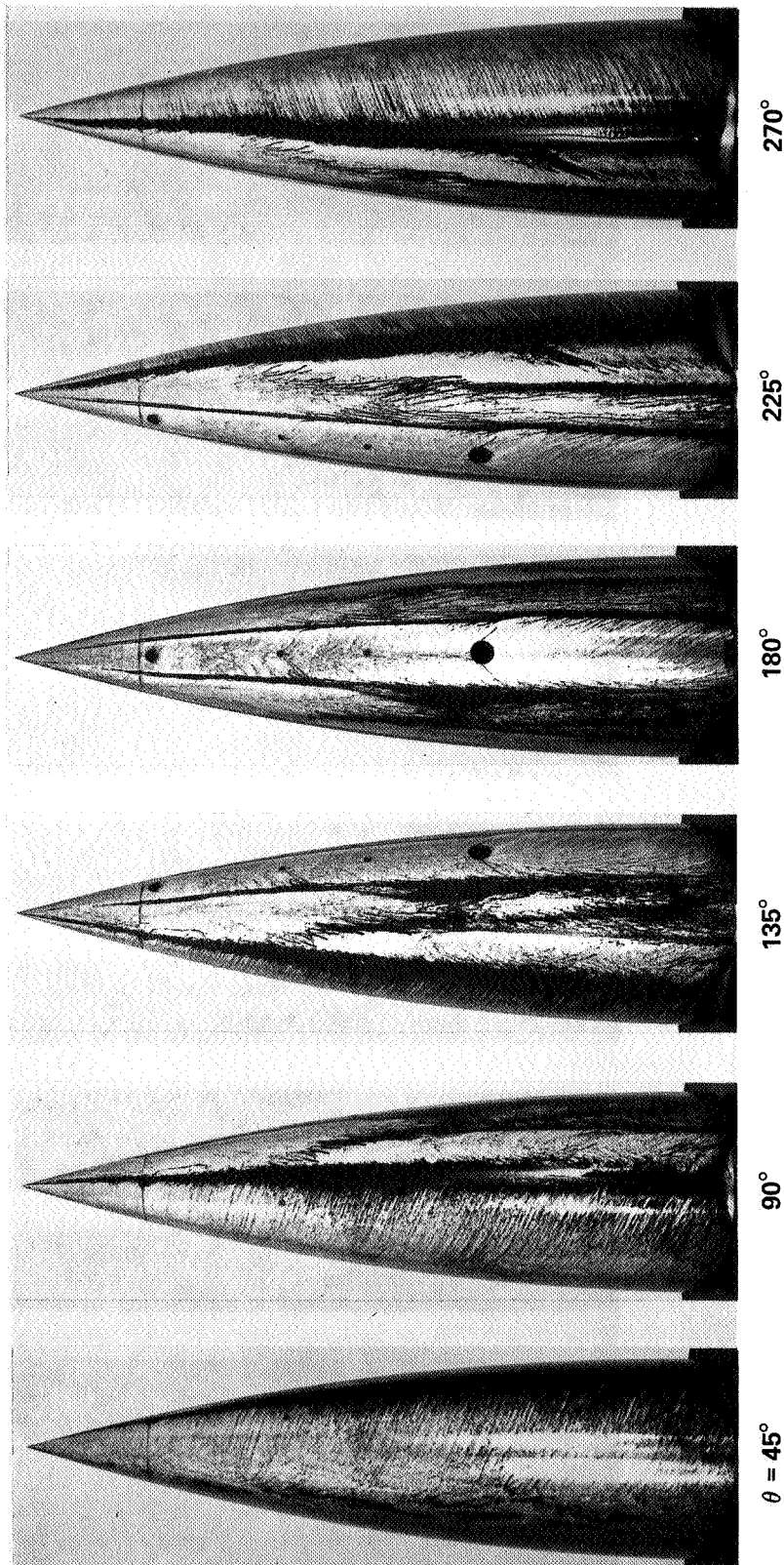
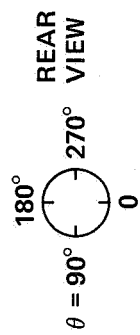


(a) $\alpha = 20^\circ$, $C_Y = 0$

Figure 15.— Sublimation photographs for 3.5-ogive: $M = 0.25$, $R_d = 0.3 \times 10^6$.

ORIGINAL PAGE IS
OF POOR QUALITY

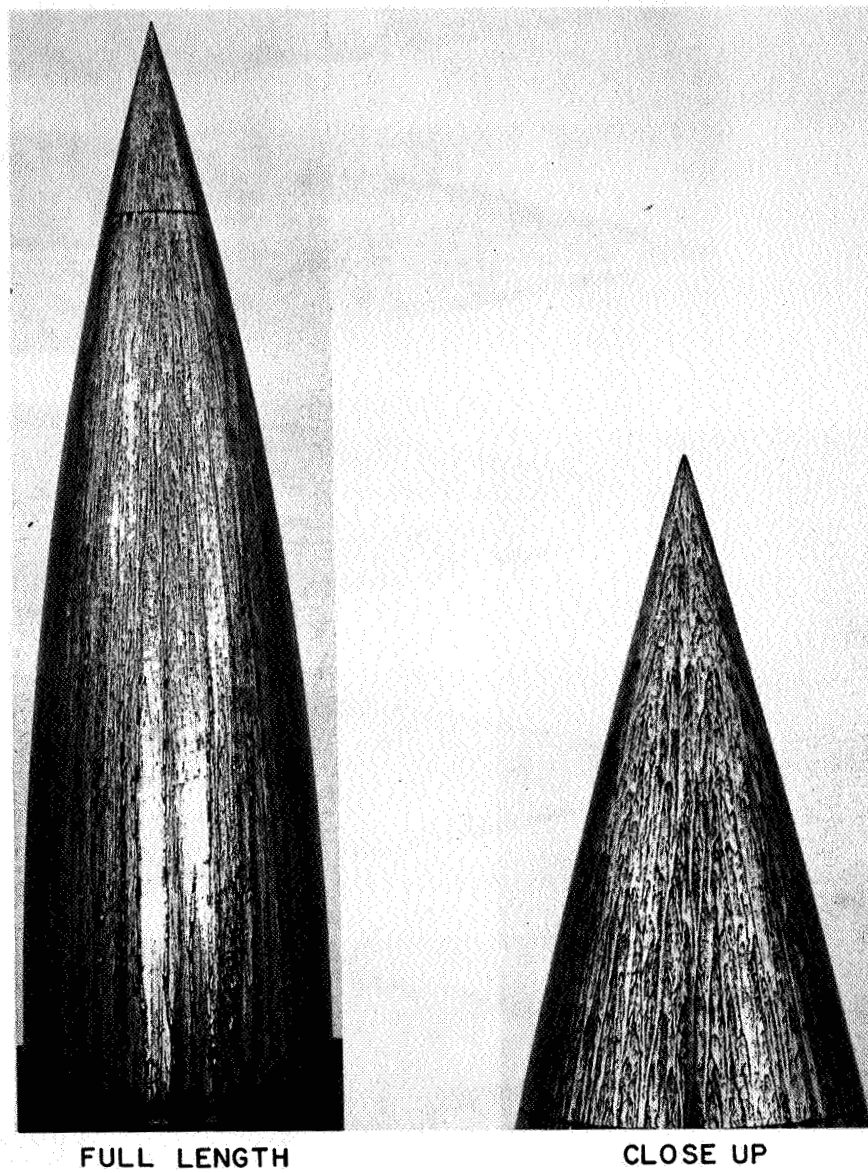




$\alpha = 40^\circ, C_Y = 0.6$

Figure 16.— Oil-flow photographs for 3.5-ogive: $M = 0.25, R_d = 0.5 \times 10^6, \alpha = 40^\circ, C_Y = 0.6$.

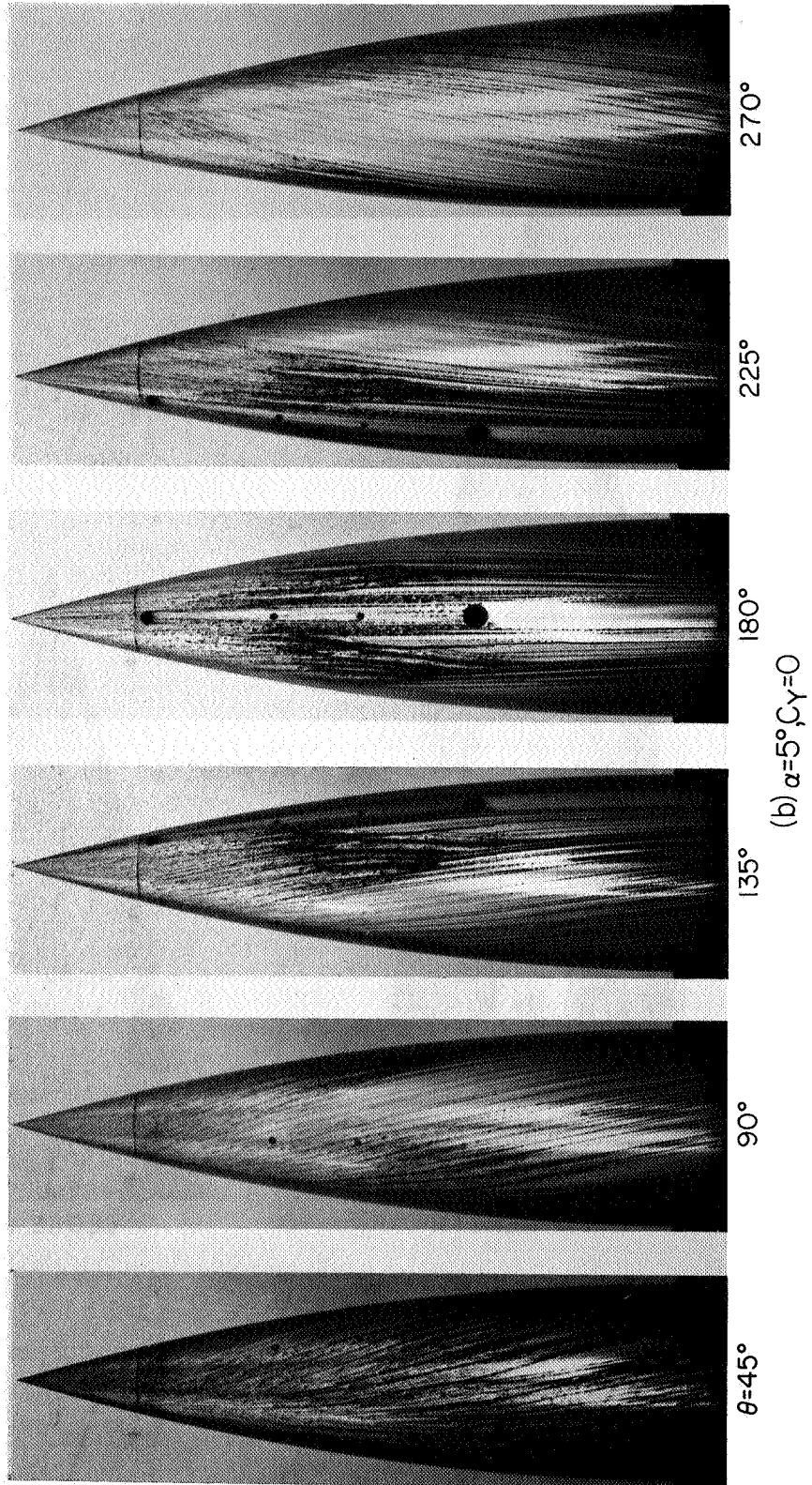
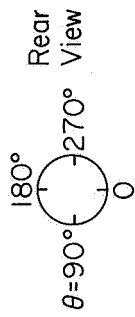
ORIGINAL PAGE IS
OF POOR QUALITY



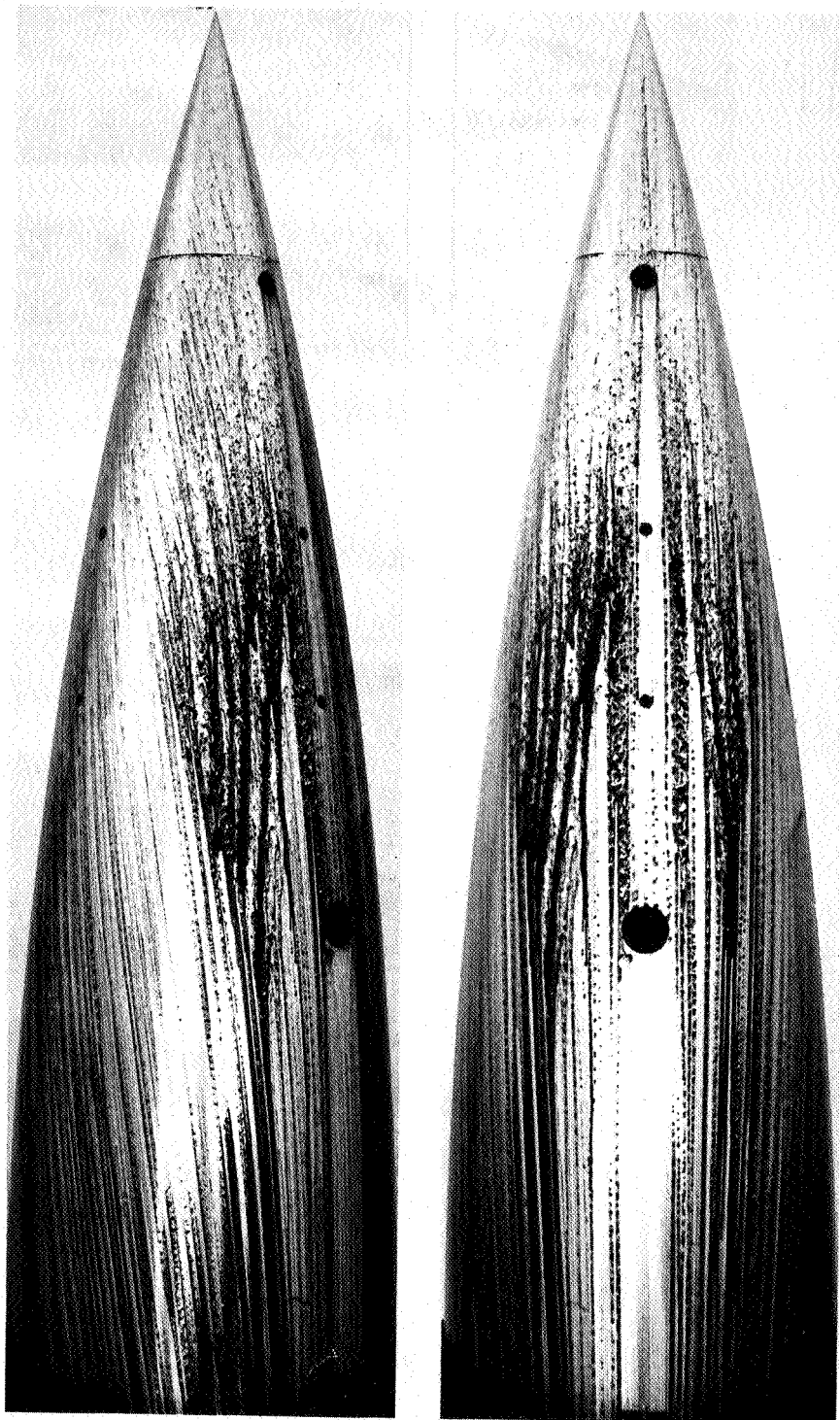
(a) $\alpha = 0, C_Y = 0$

Figure 17.— Oil-flow photographs for 3.5-ogive: $M = 0.25, R_d = 0.8 \times 10^6$.

ORIGINAL PAGE IS
OF POOR QUALITY



ORIGINAL PAGE IS
OF POOR QUALITY

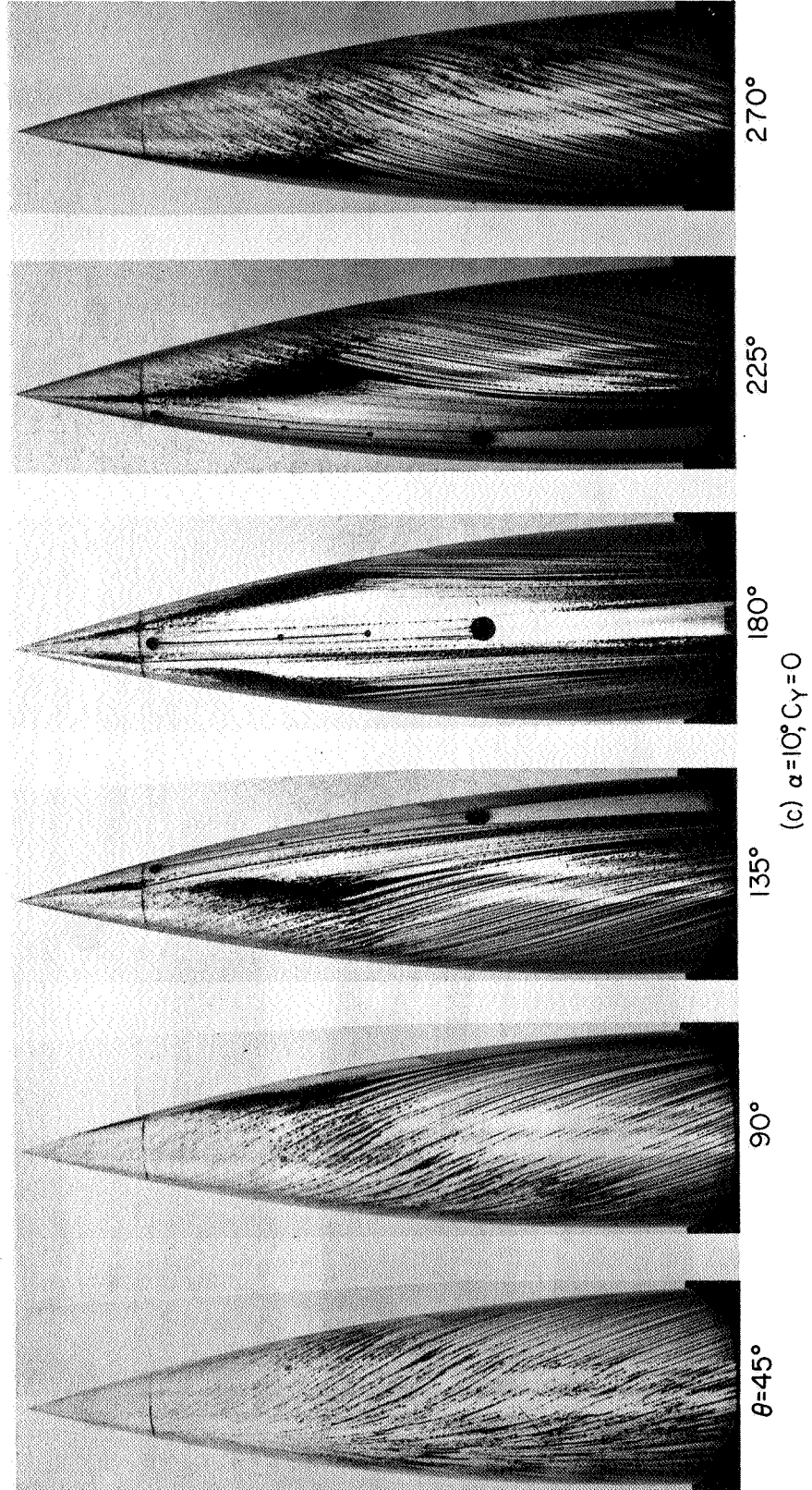
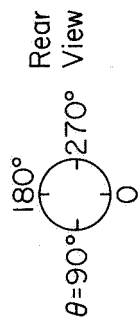


$\theta = 135^\circ$

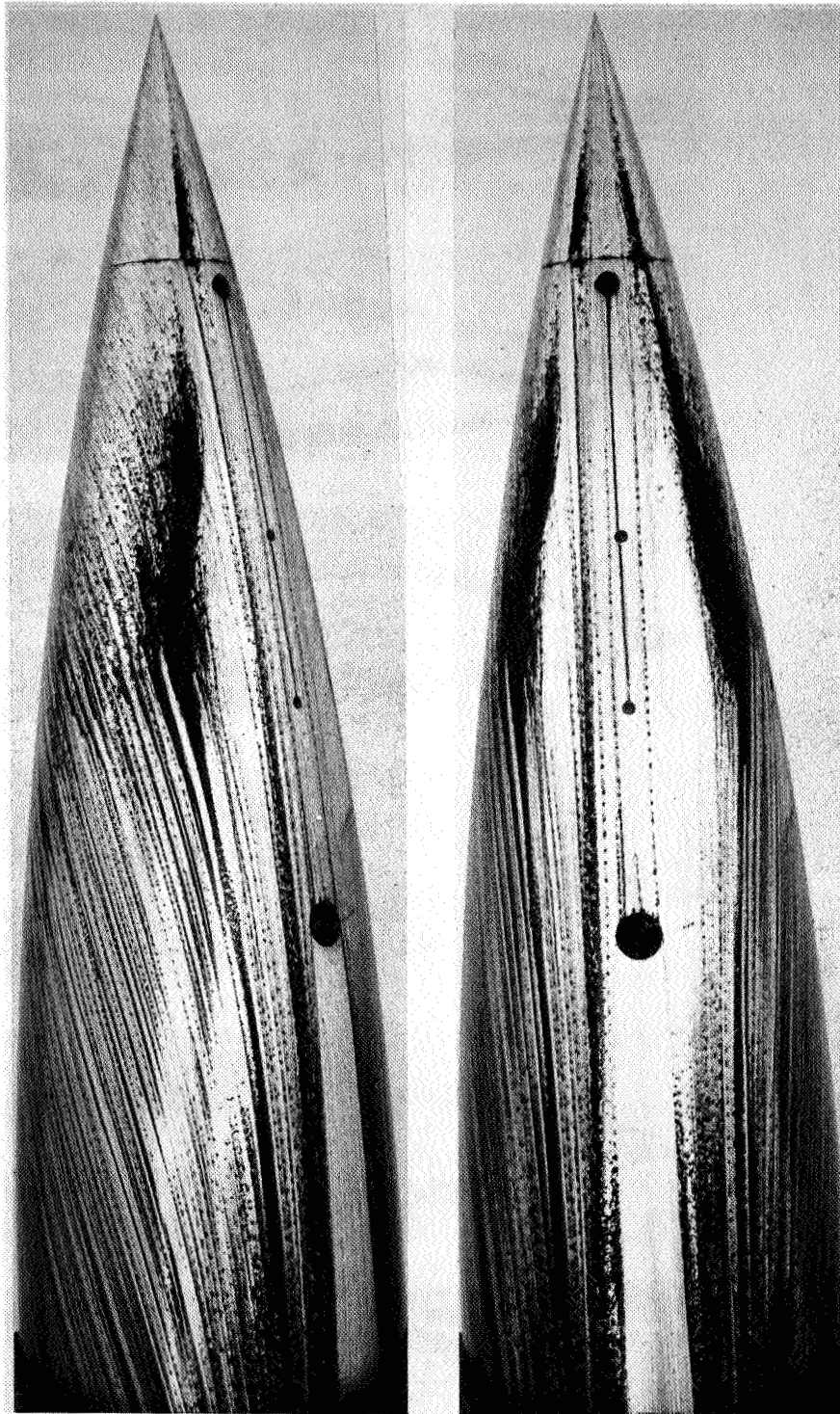
180°

(b) CONCLUDED, $\alpha = 5^\circ$, $C_Y = 0$

ORIGINAL PAGE IS
OF POOR QUALITY



ORIGINAL PAGE IS
OF POOR QUALITY

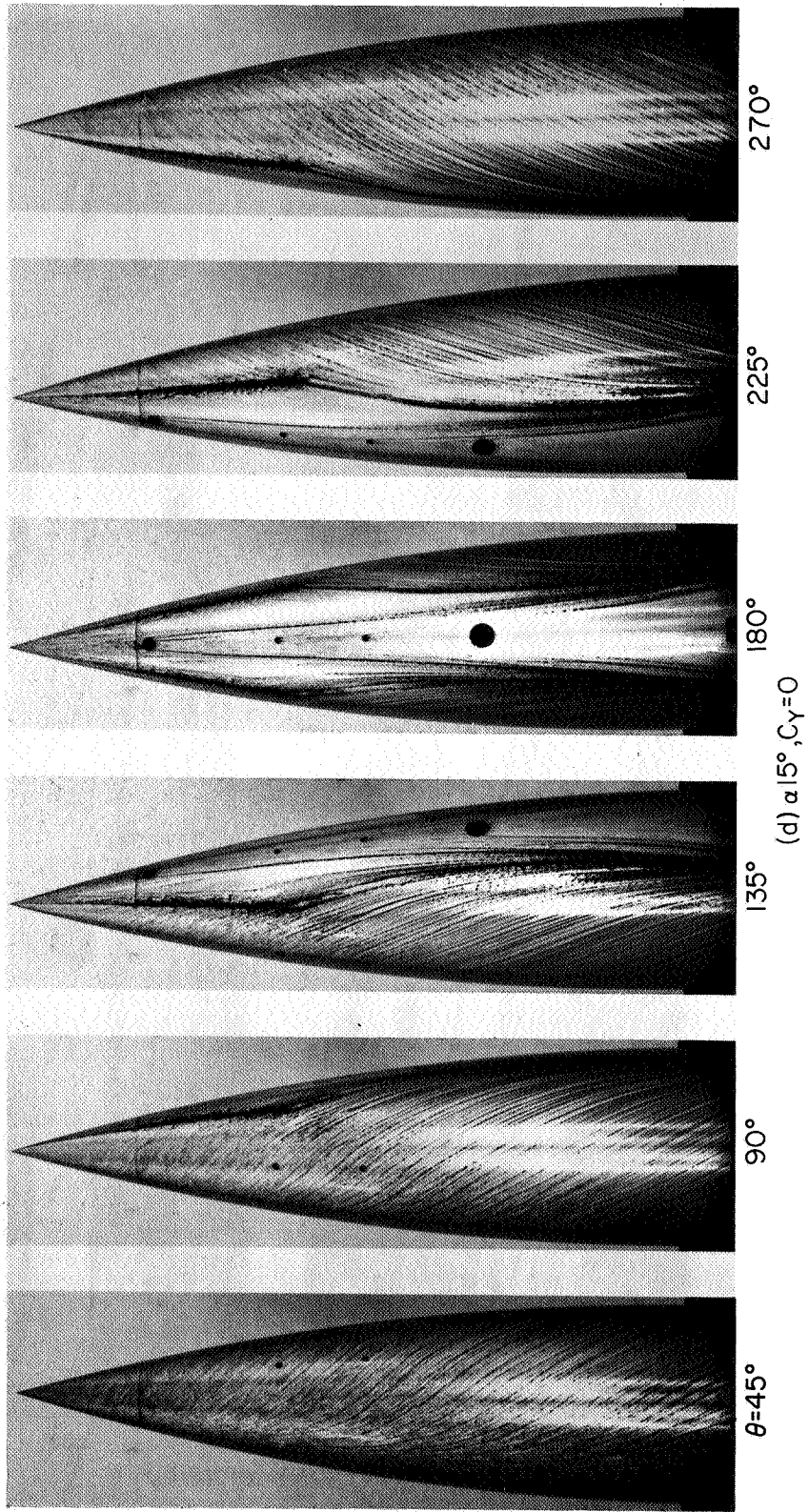
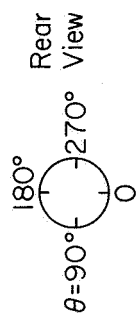


$\theta = 135^\circ$

180°

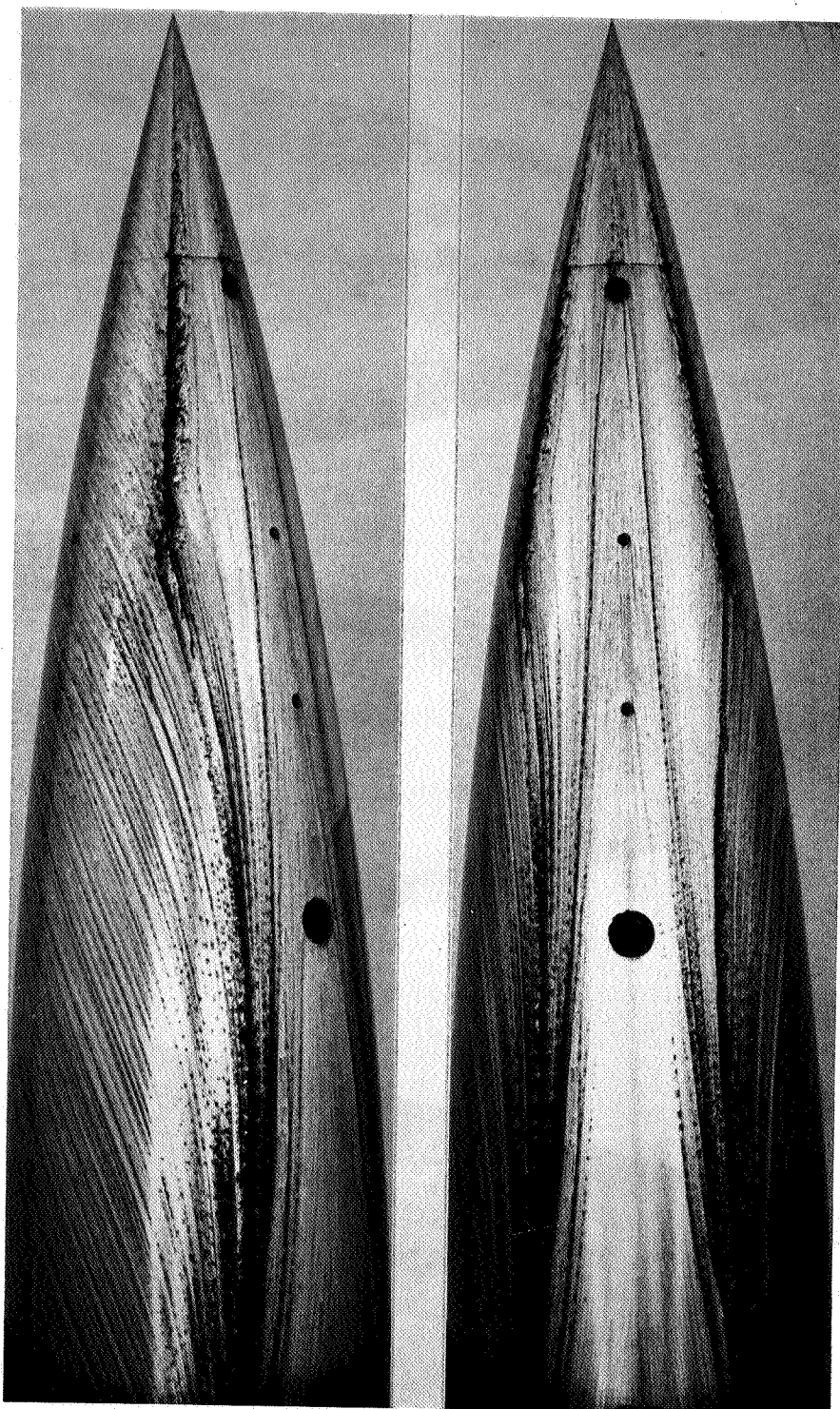
(c) CONCLUDED, $\alpha = 10^\circ$, $C_Y = 0$

ORIGINAL PAGE IS
OF POOR QUALITY



ORIGINAL PAGE IS
OF POOR QUALITY

ORIGINAL PAGE IS
OF POOR QUALITY

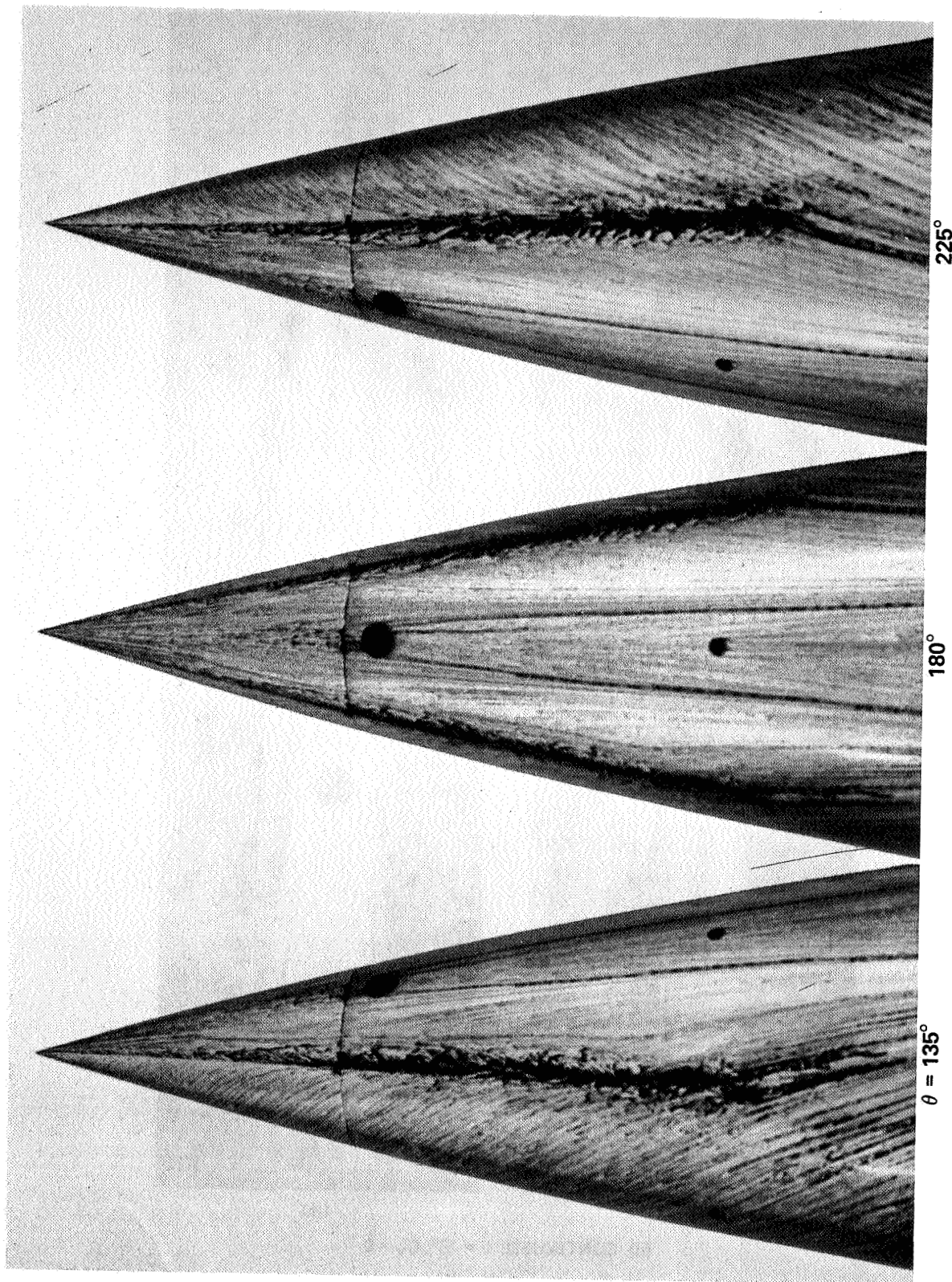


$\theta = 135^\circ$

180°

(d) CONTINUED, $\alpha = 15^\circ$, $C_Y = 0$

ORIGINAL PAGE IS
OF POOR QUALITY



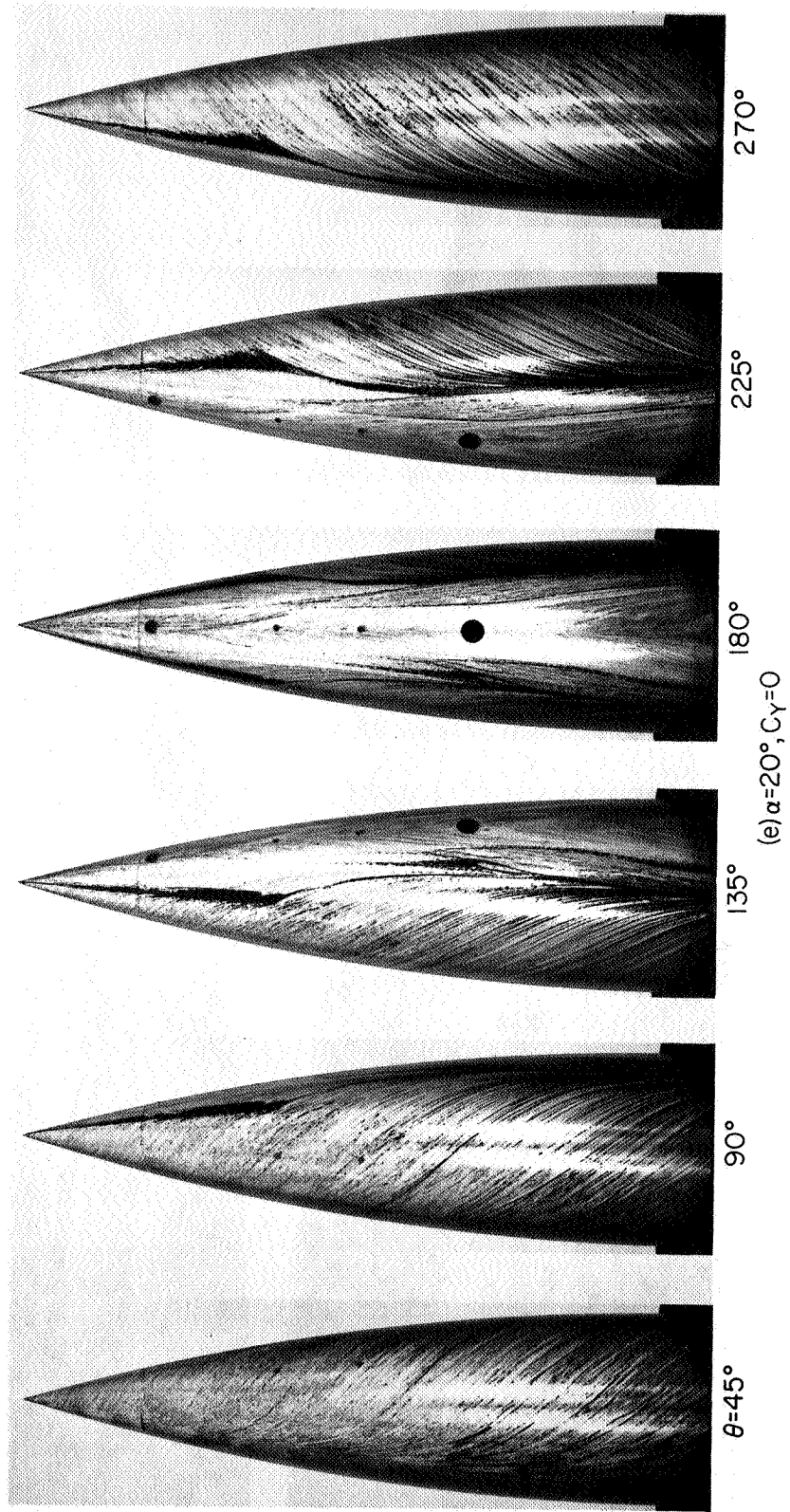
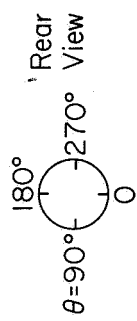
225°

180°

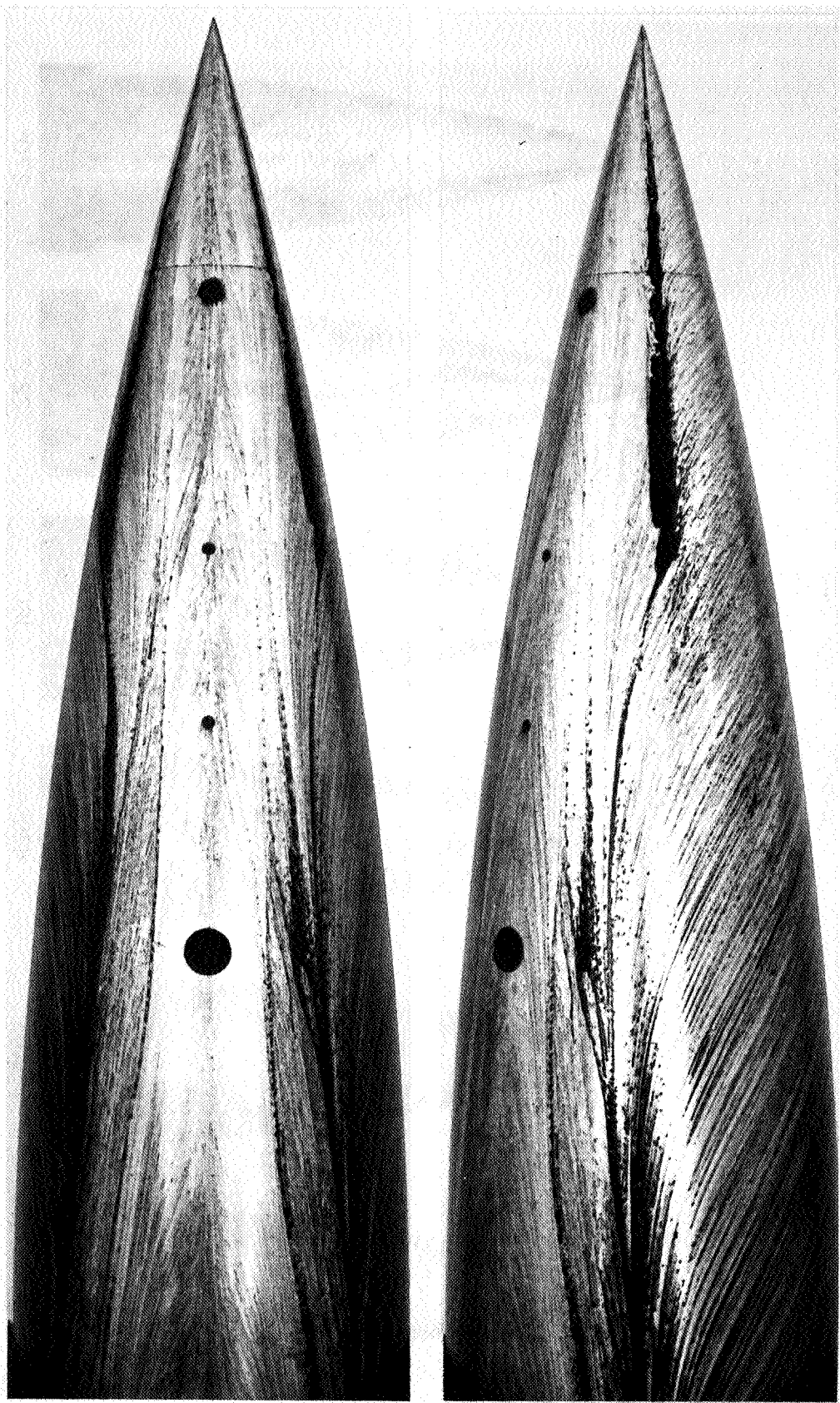
$\theta = 135^\circ$

(d) CONCLUDED, $\alpha = 15^\circ$, $C_Y = 0$

ORIGINAL PAGE IS
OF POOR QUALITY



3 22 73 14342
VTIRUD 8001

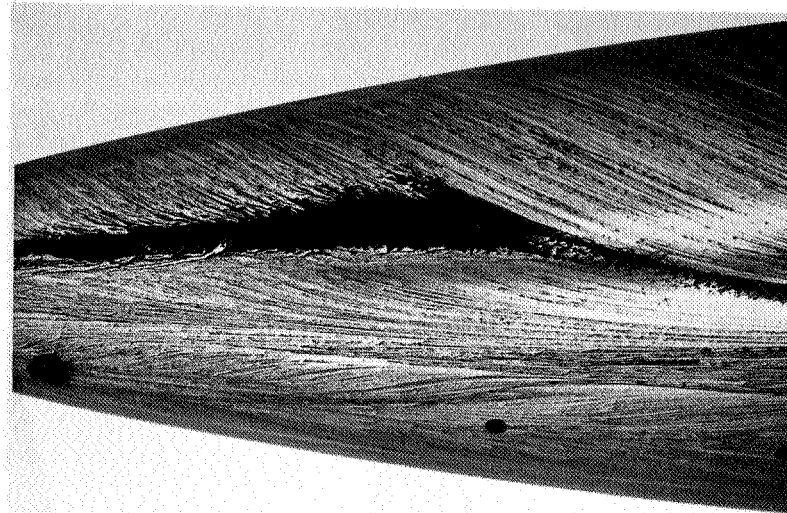


$\theta = 180^\circ$

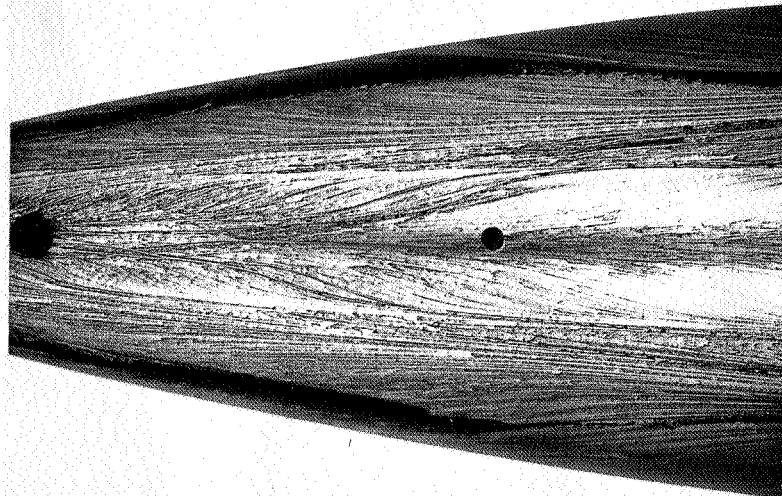
225°

(e) CONTINUED, $\alpha = 20^\circ$, $C_Y = 0$

ORIGINAL PAGE IS
OF POOR QUALITY

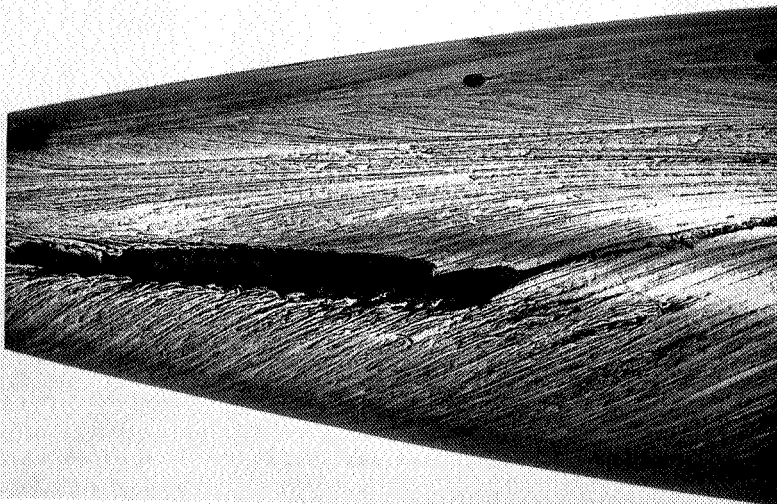


225°

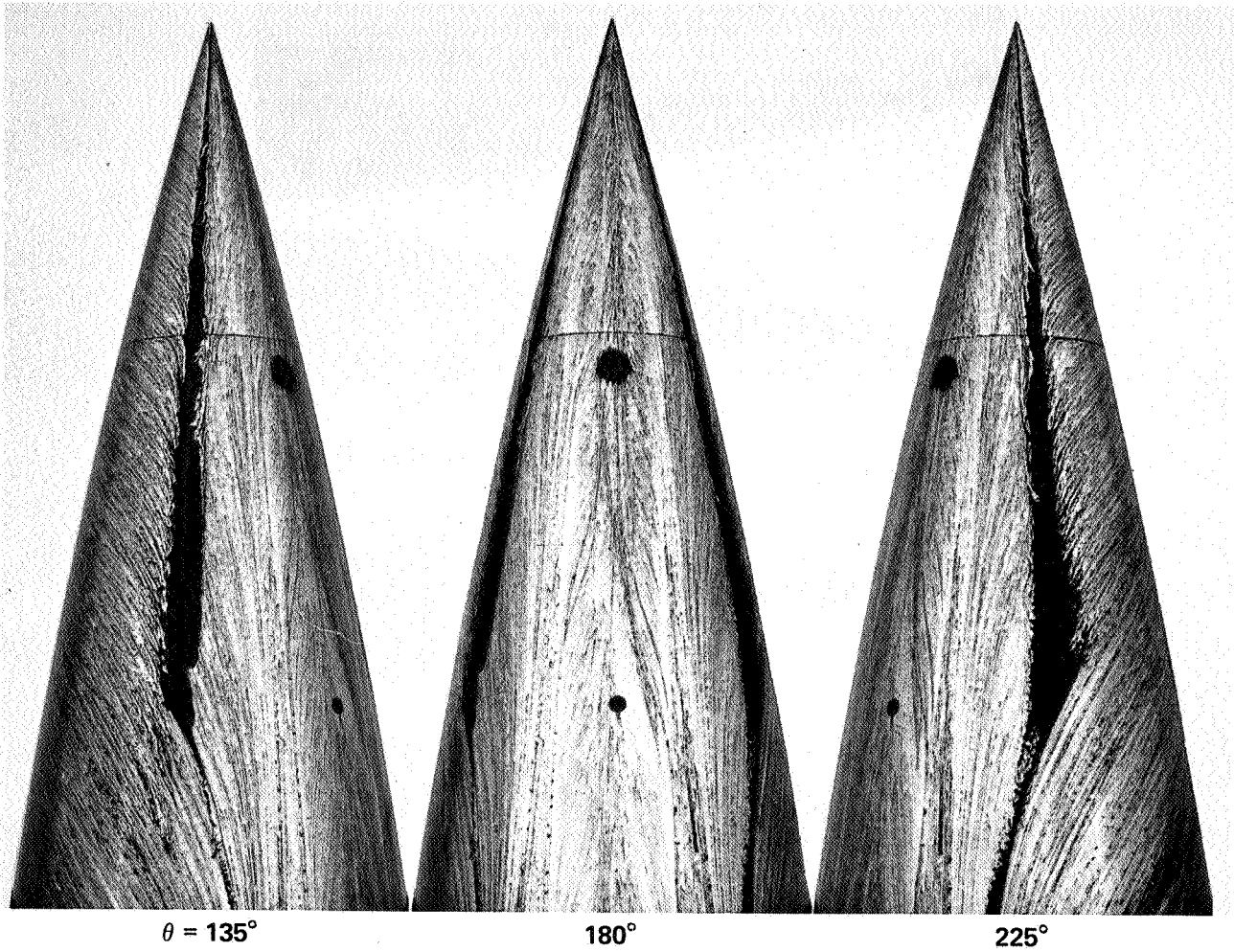


180°

(e) CONTINUED, $\alpha = 20^\circ$

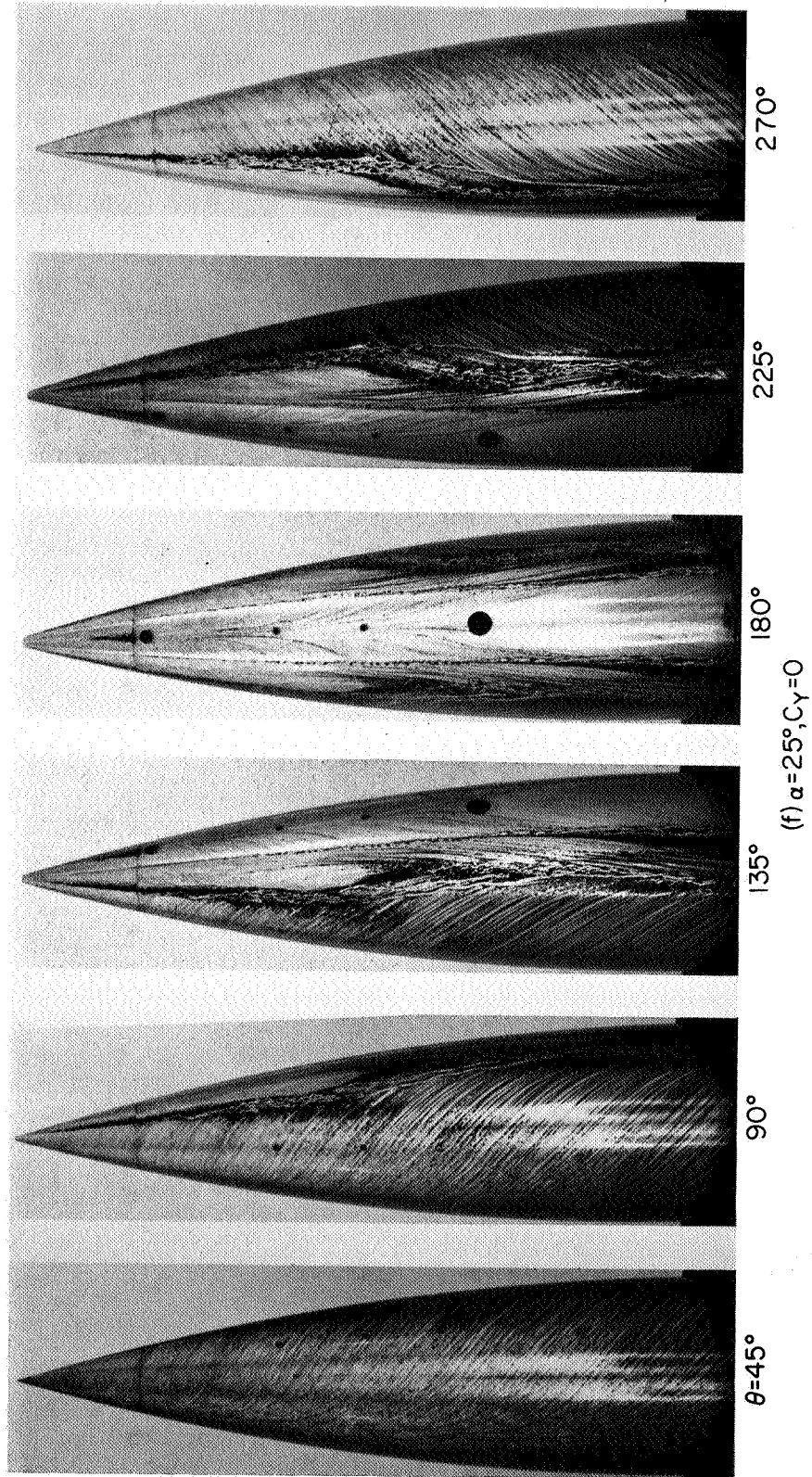
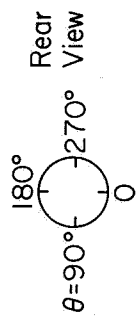


$\theta = 135^\circ$

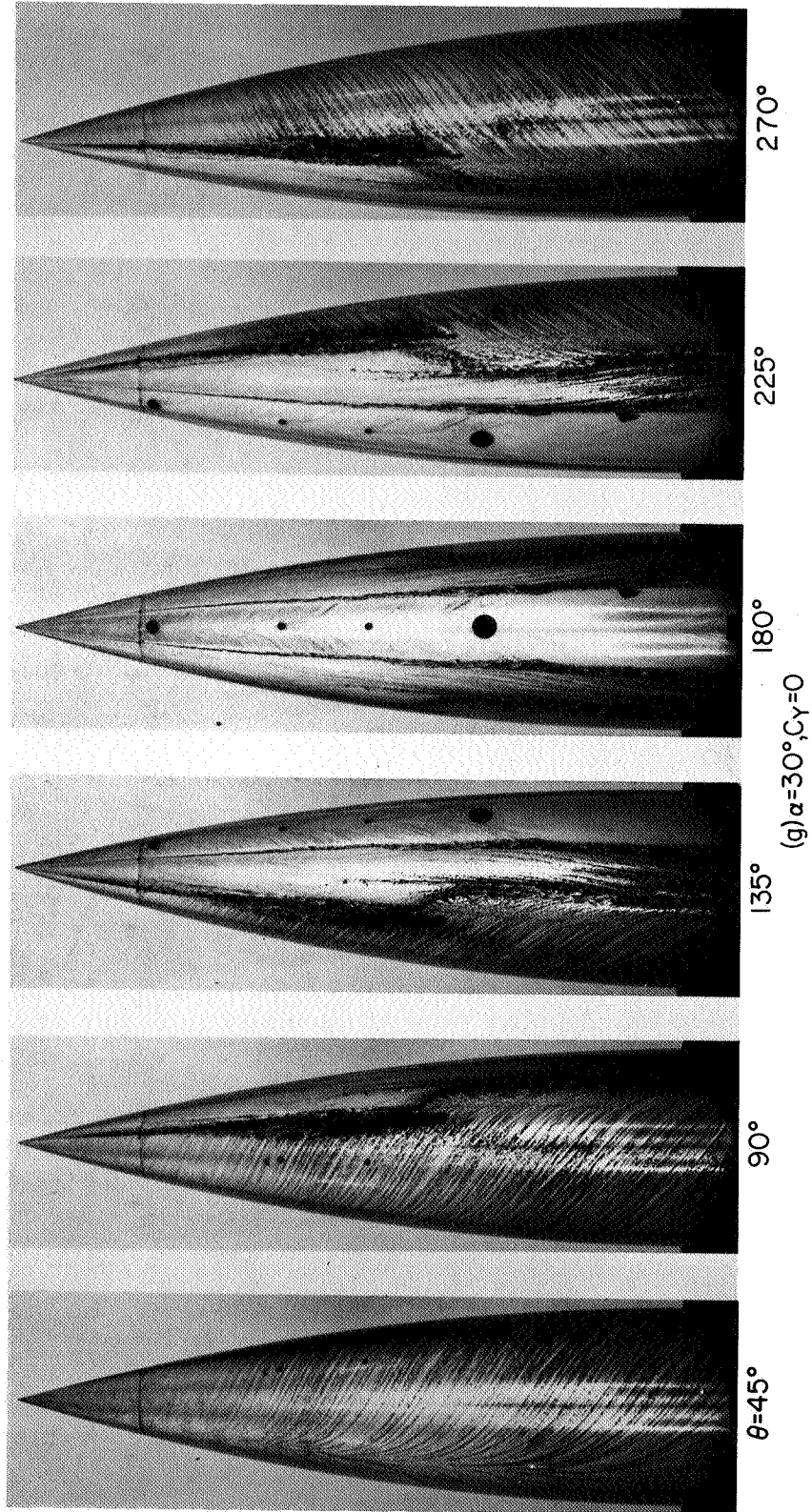
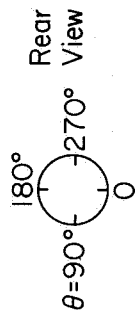


(e) CONCLUDED, $\alpha = 20^\circ$, $C_Y = 0$

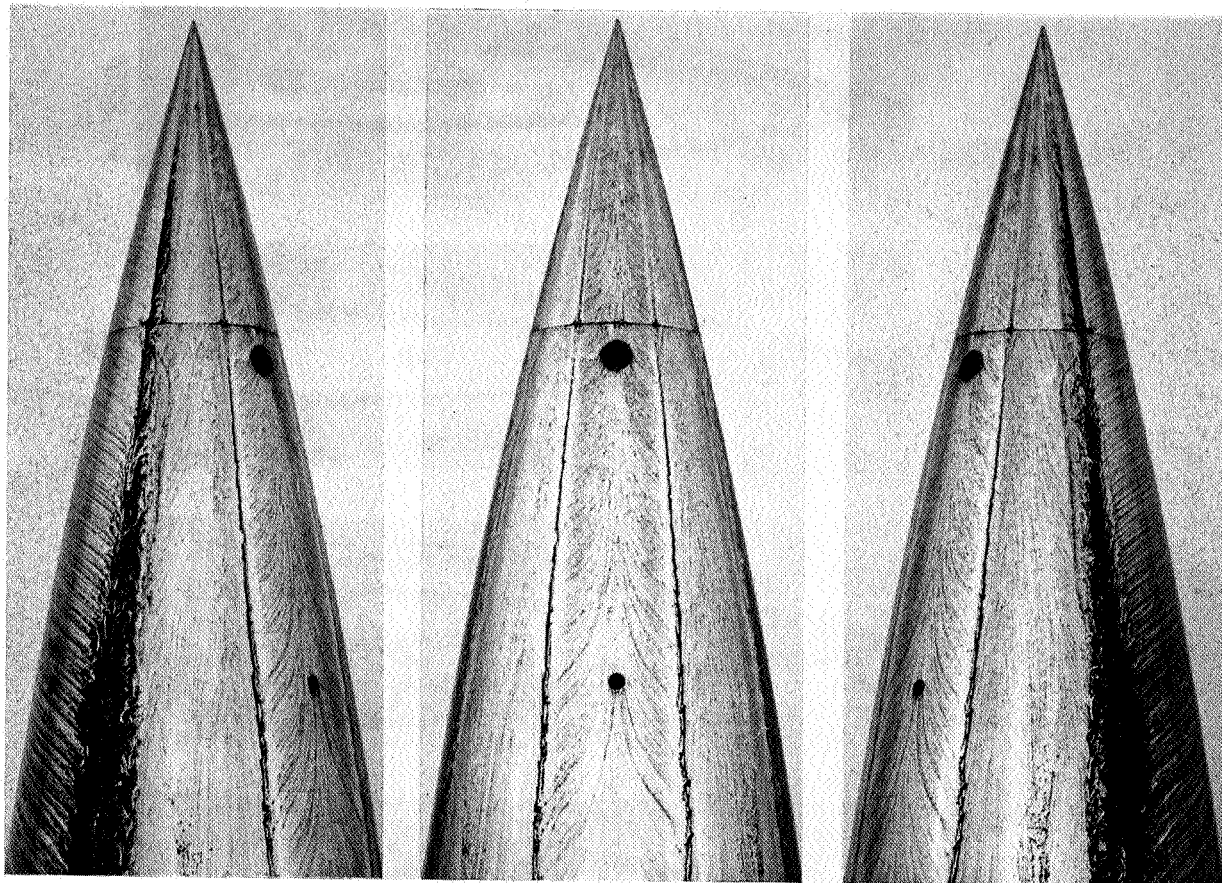
ORIGINAL PAGE IS
OF POOR QUALITY



ORIGINAL PAGE IS
OF POOR QUALITY



ORIGINAL PAGE IS
OF POOR QUALITY

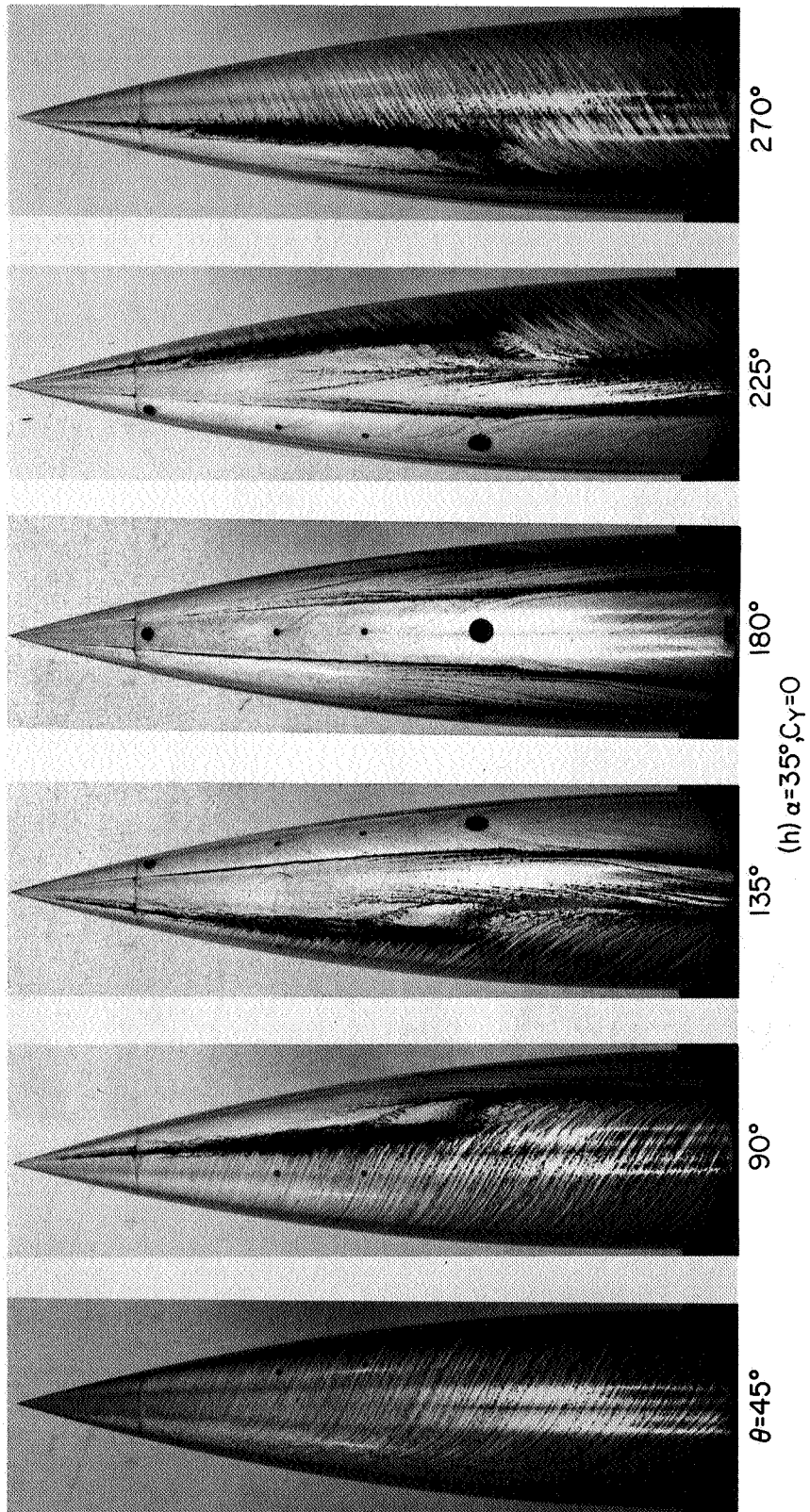
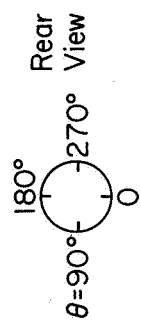


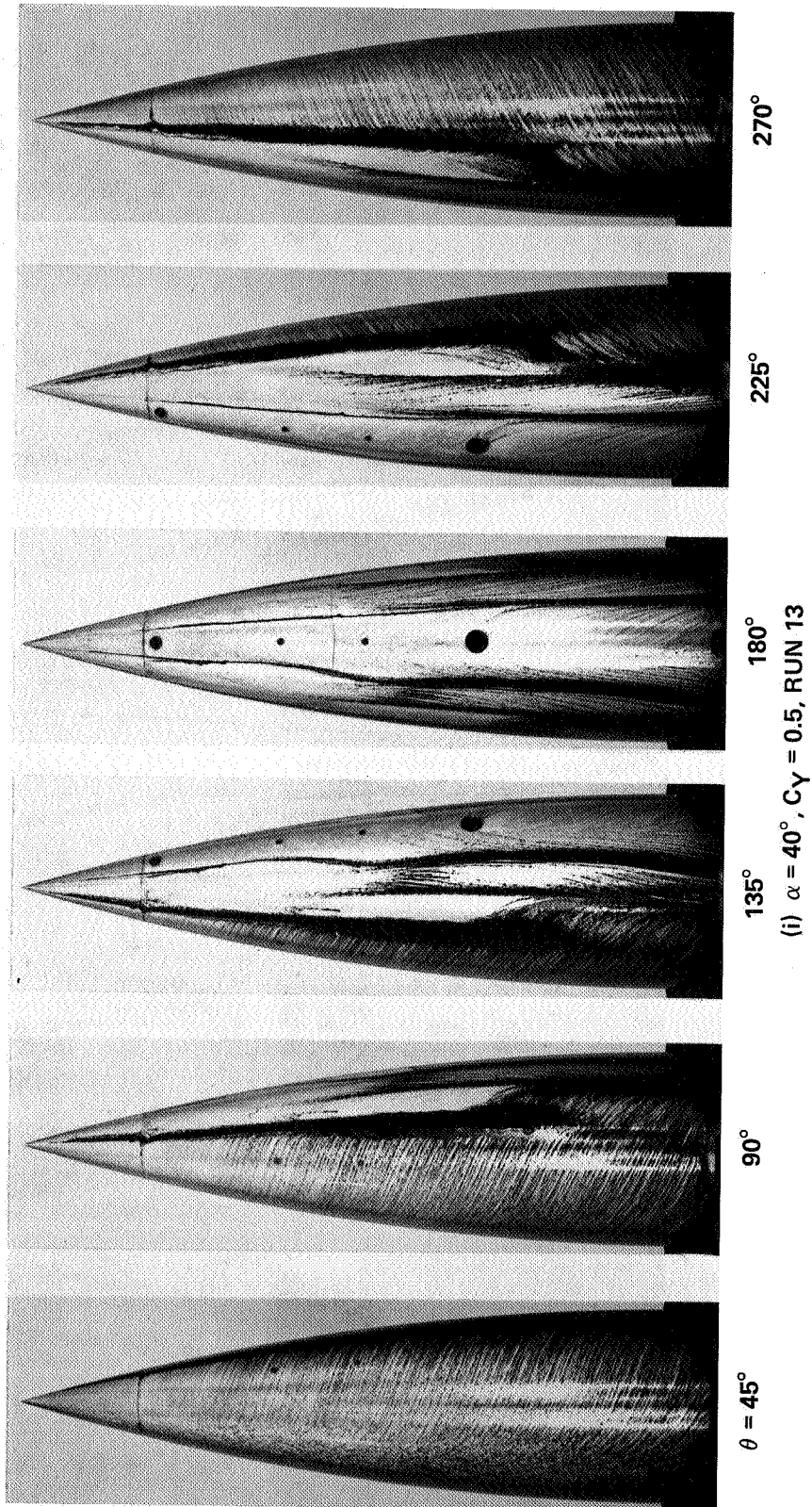
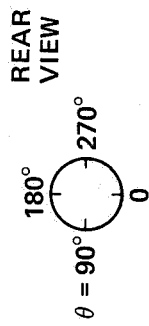
$\theta = 135^\circ$

180°

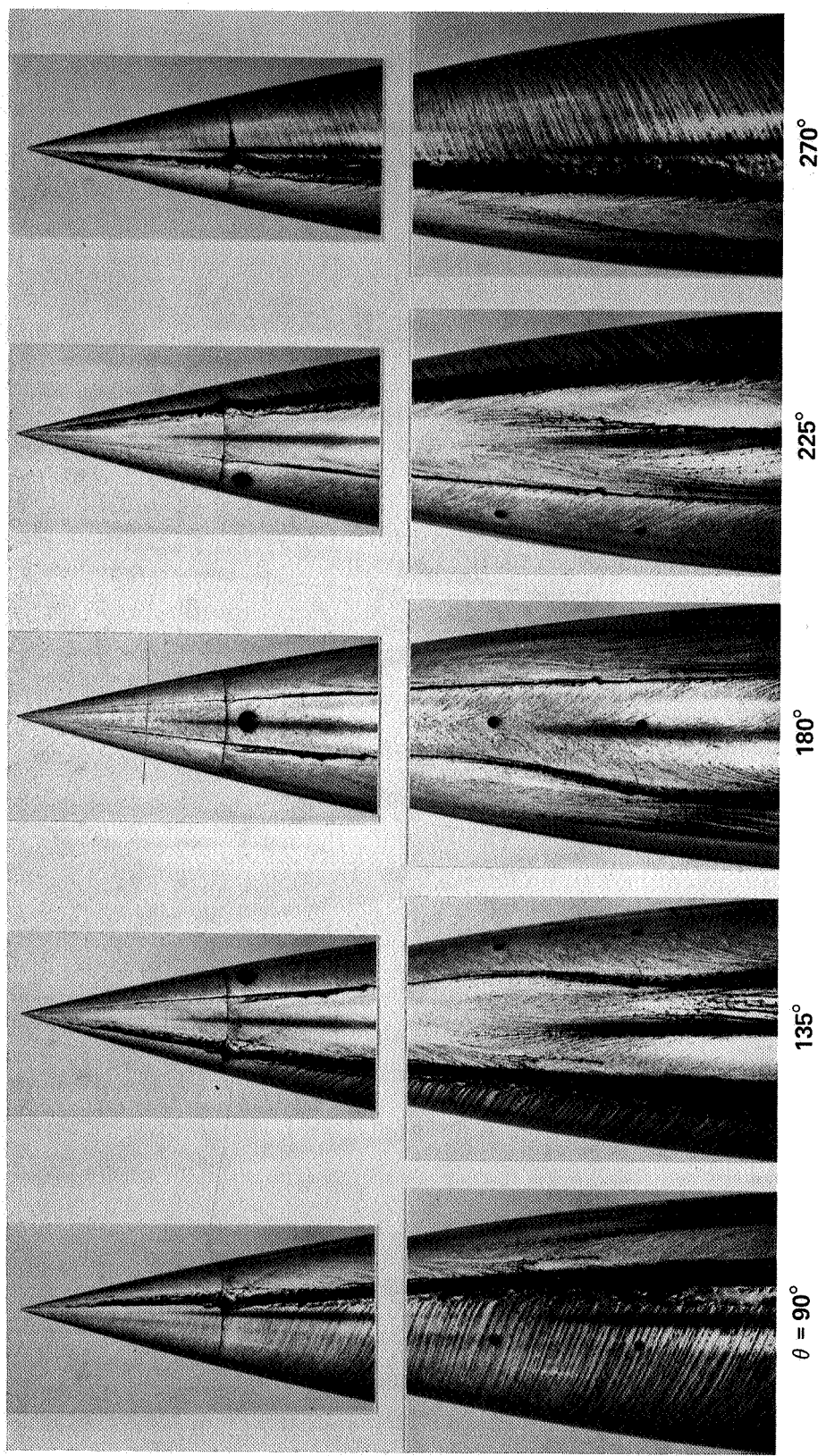
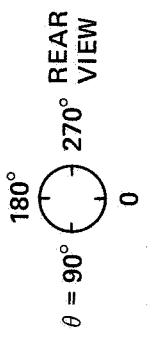
225°

(g) CONCLUDED, $\alpha = 30^\circ$, $C_Y = 0$



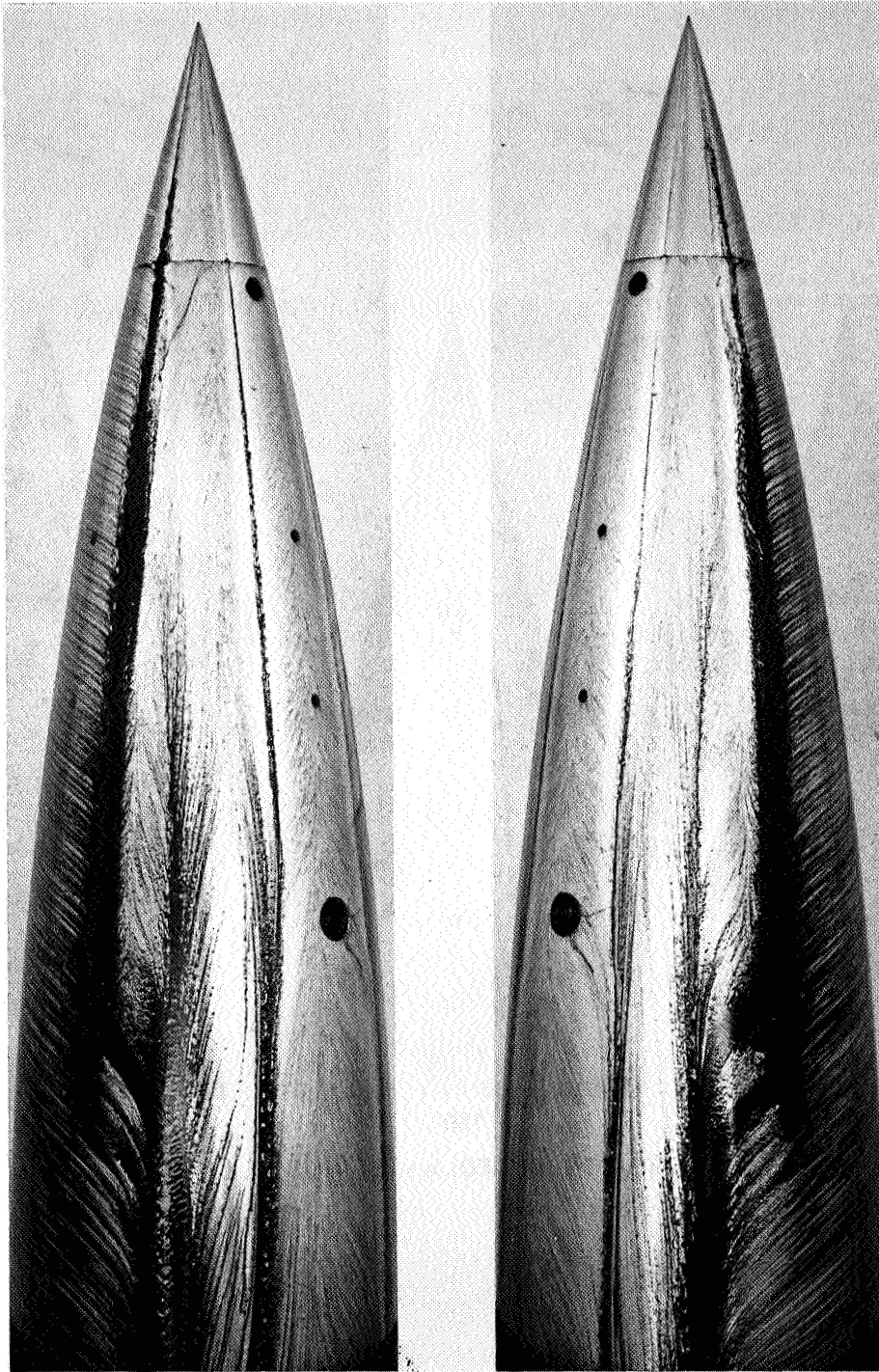


OF 1008 C-11
 11-010 9001 70



(i) CONTINUED, $\alpha = 40^\circ$, RUN 13

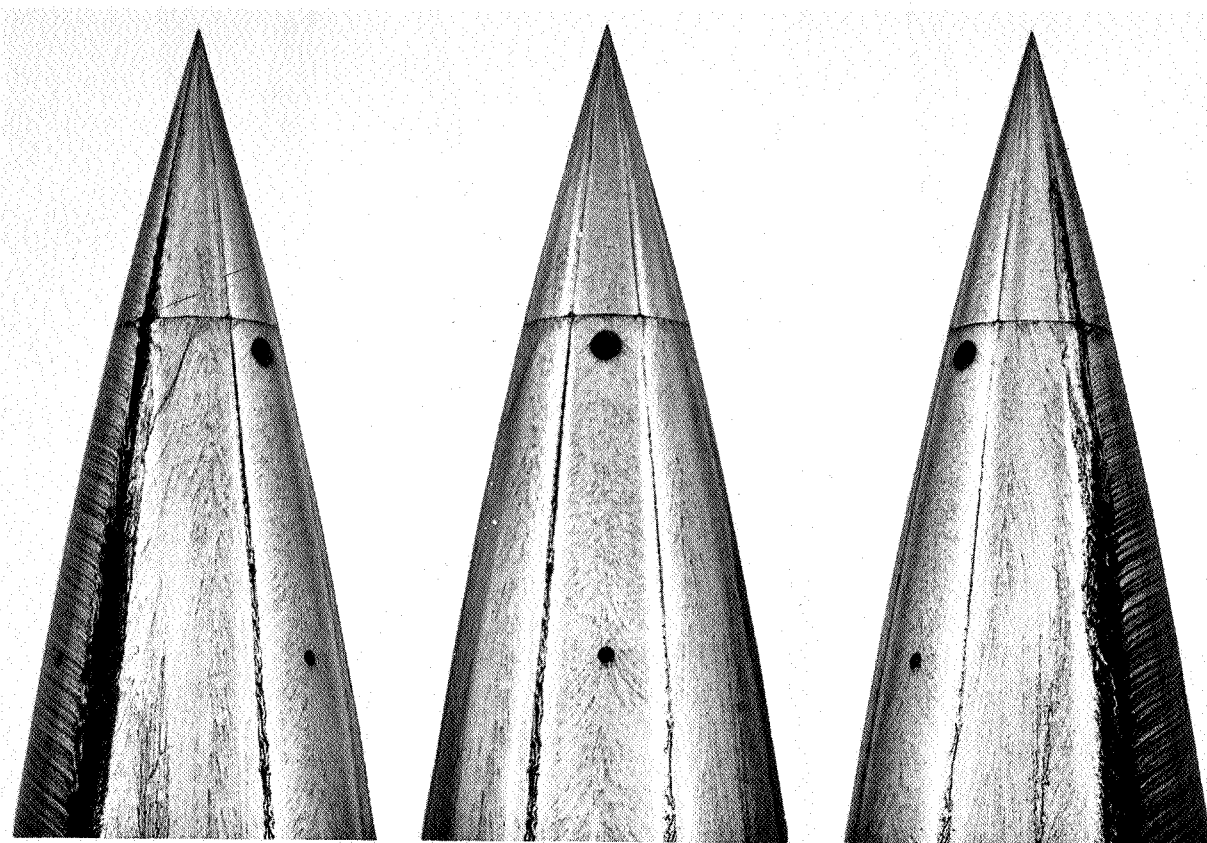
ORIGINAL PAGE IS
OF POOR QUALITY



$\theta = 135^\circ$

225°

(i) CONTINUED, $\alpha = 40^\circ$, RUN 15



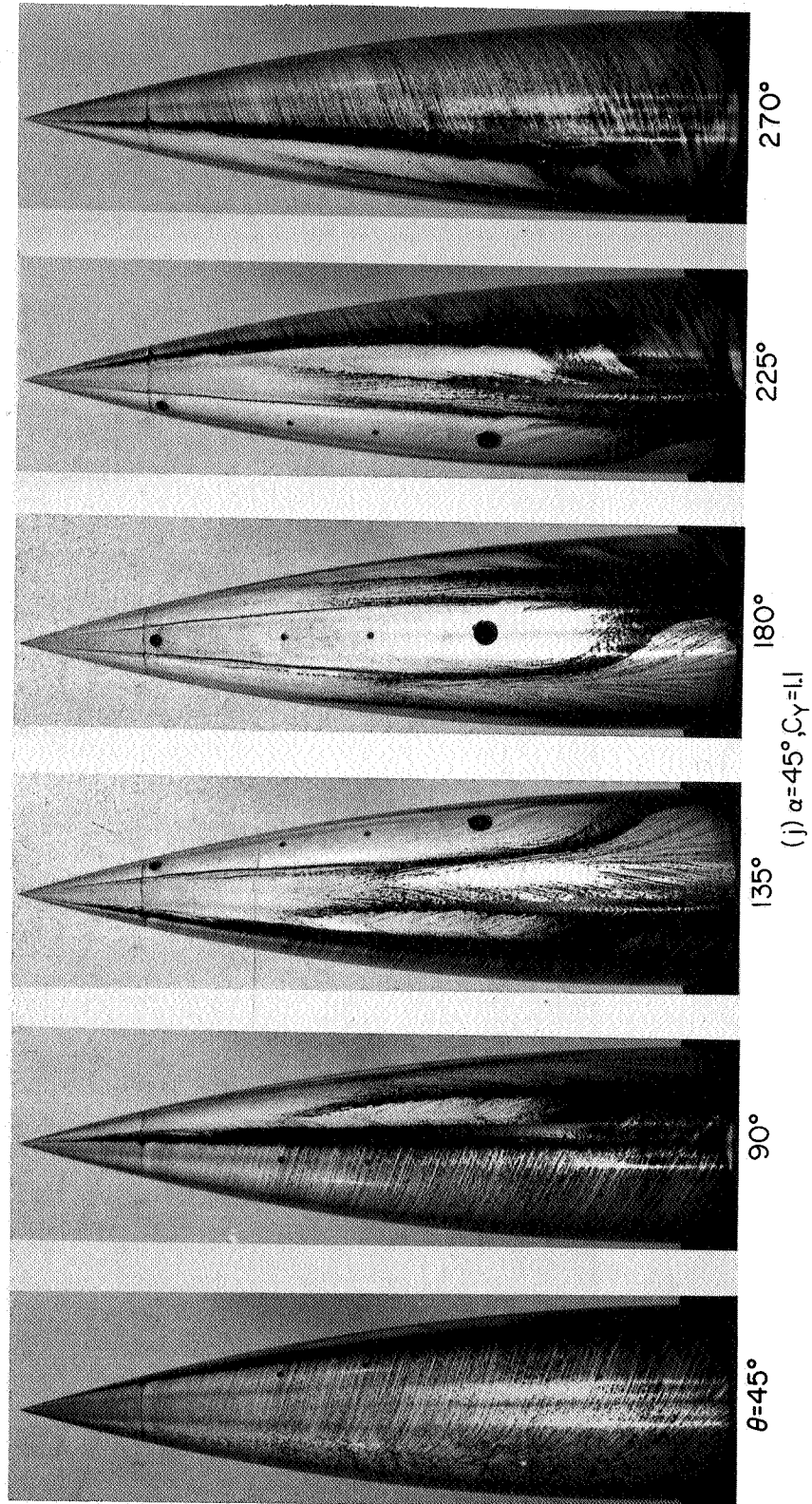
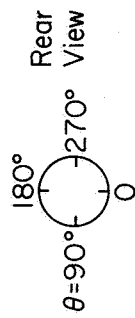
$\theta = 135^\circ$

180°

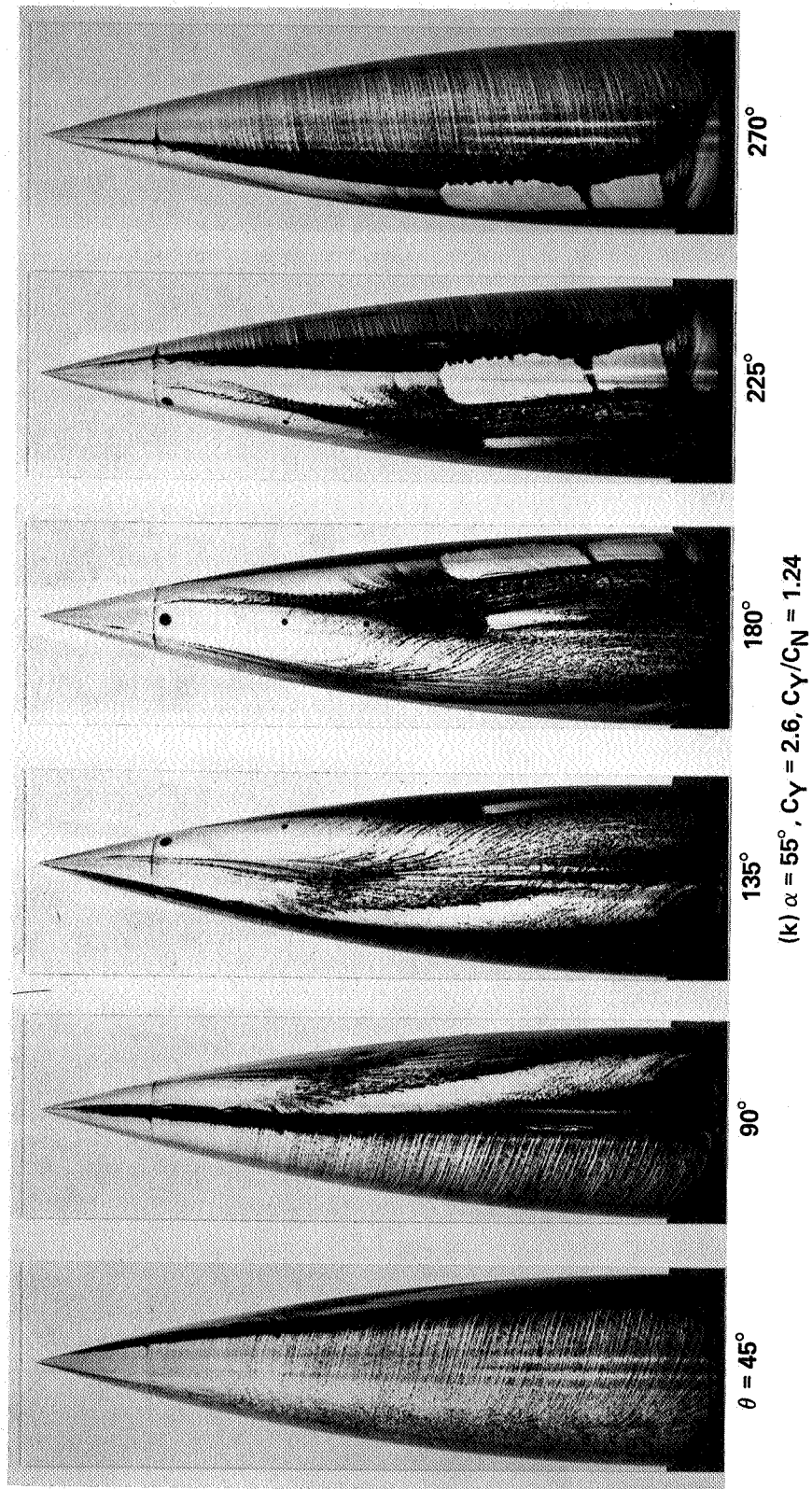
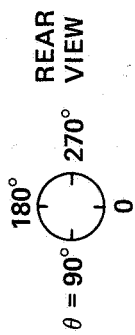
225°

(i) CONCLUDED, $\alpha = 40^\circ$, RUN 15

ORIGINAL PAGE IS
OF POOR QUALITY

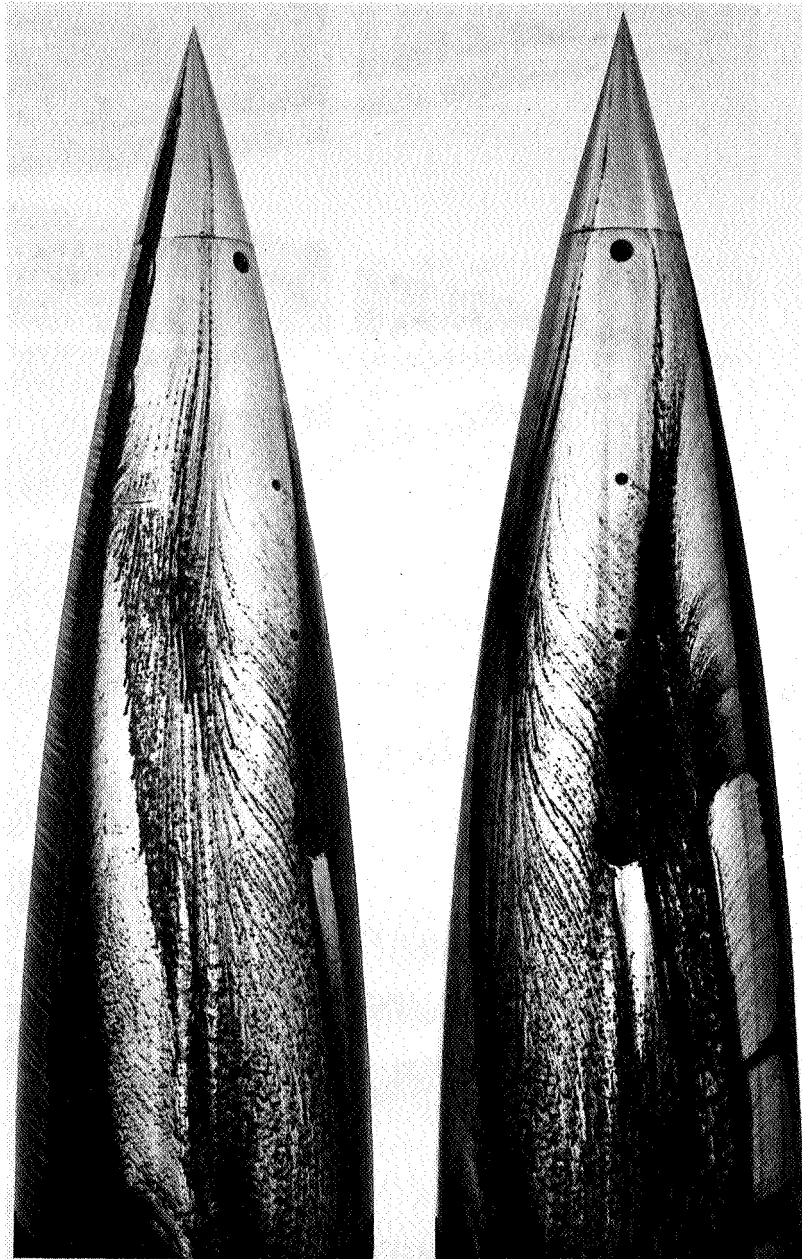


OF 2175 JAN
 YTLAND 5047



3104 11-11-60
STANDARD FORM NO. 64

ORIGINAL PAGE IS
OF POOR QUALITY



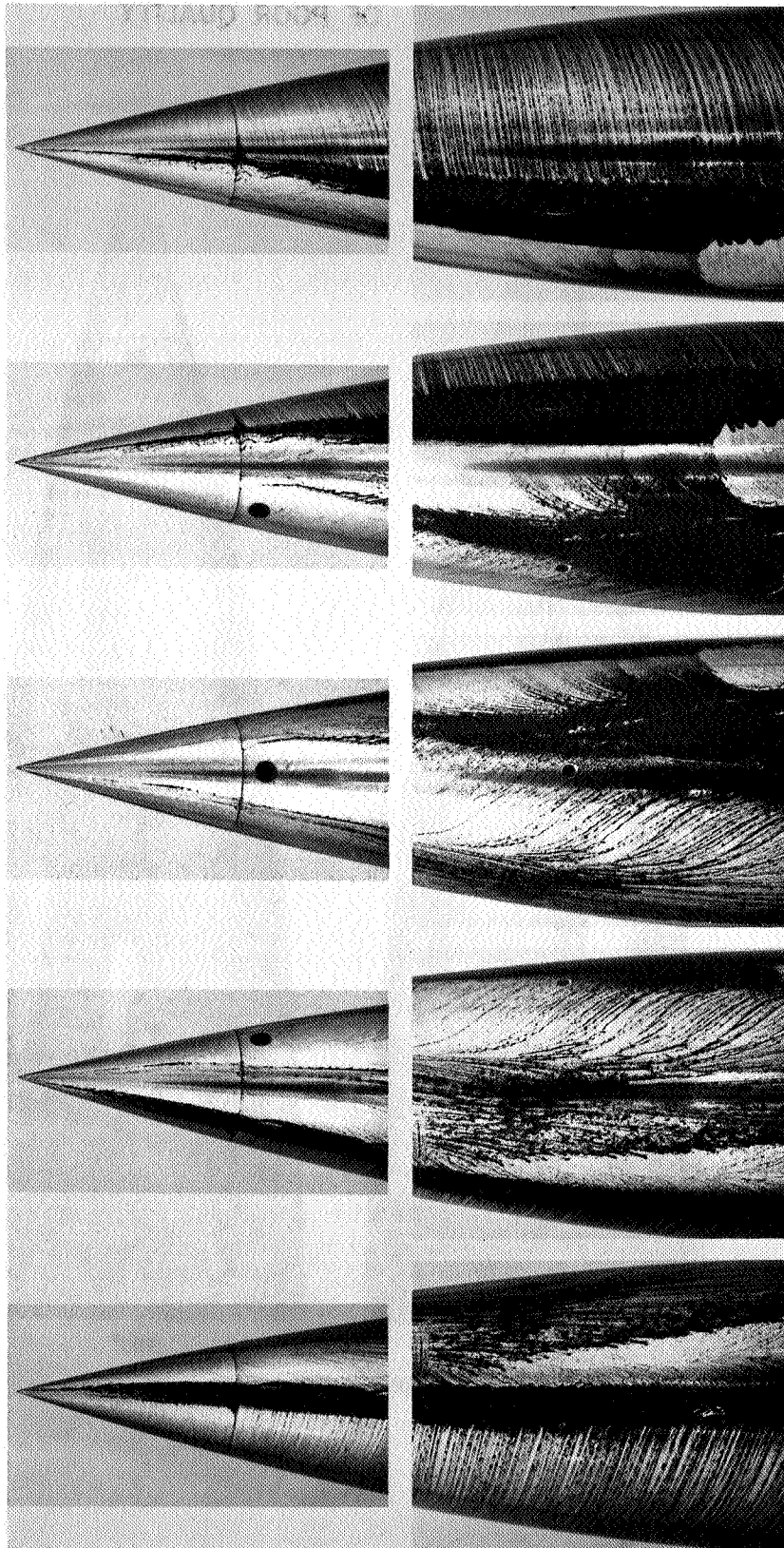
$\theta = 135^\circ$

180°

(k) CONTINUED, $\alpha = 55^\circ$

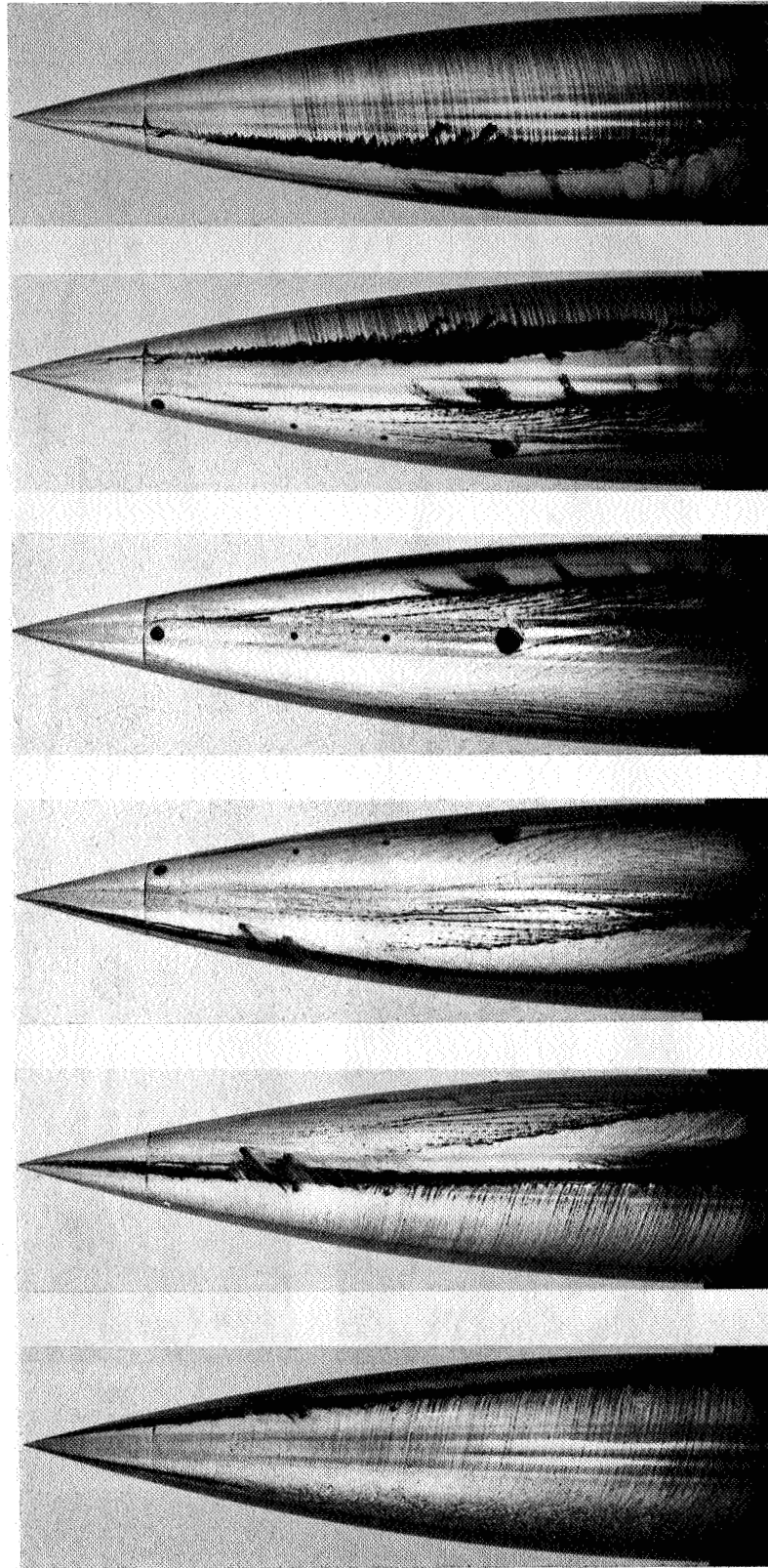
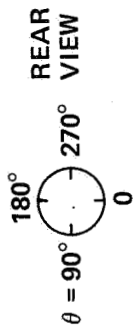
ORIGINAL PAGE IS
OF POOR QUALITY.

180°
θ = 90° REAR VIEW
270°
0

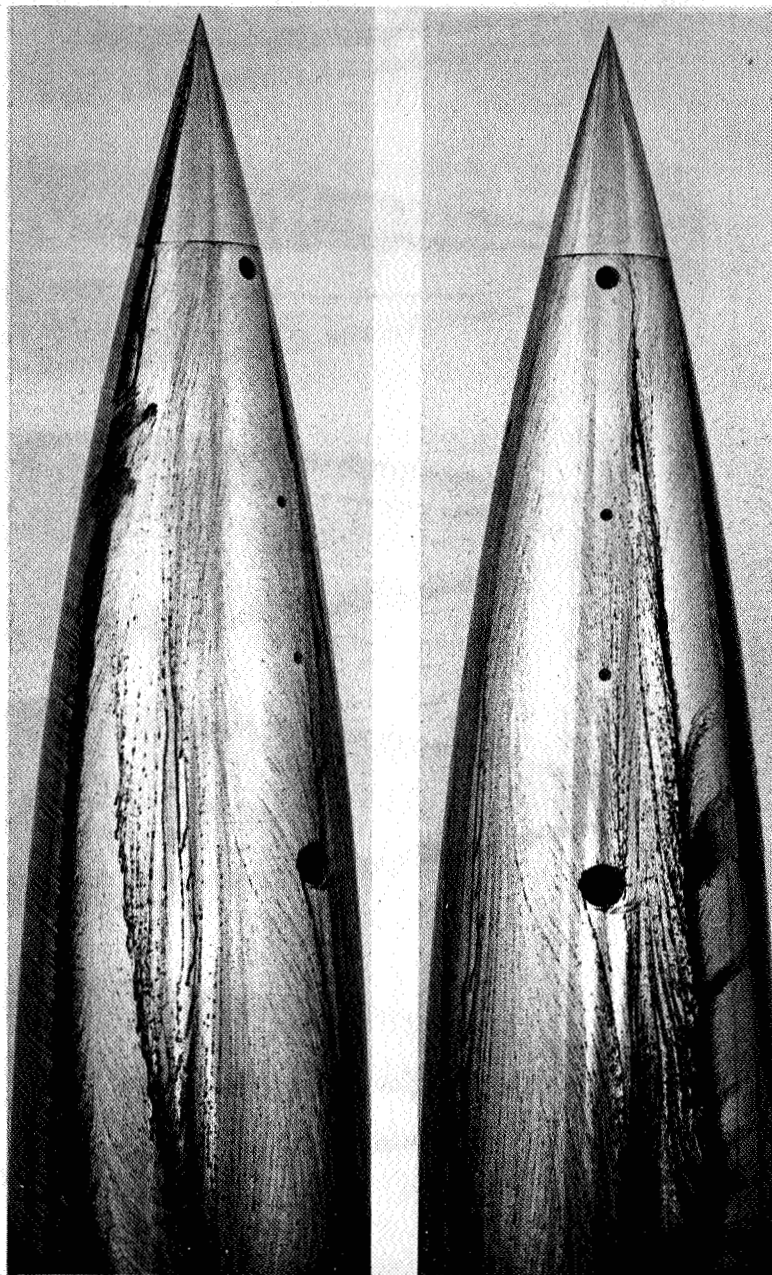


(k) Concluded: α = 55°

ORIGINAL PAGE IS
OF POOR QUALITY



(I) $\alpha = 60^\circ$, $C_Y = 2.9$, $C_Y/C_N = 1.40$

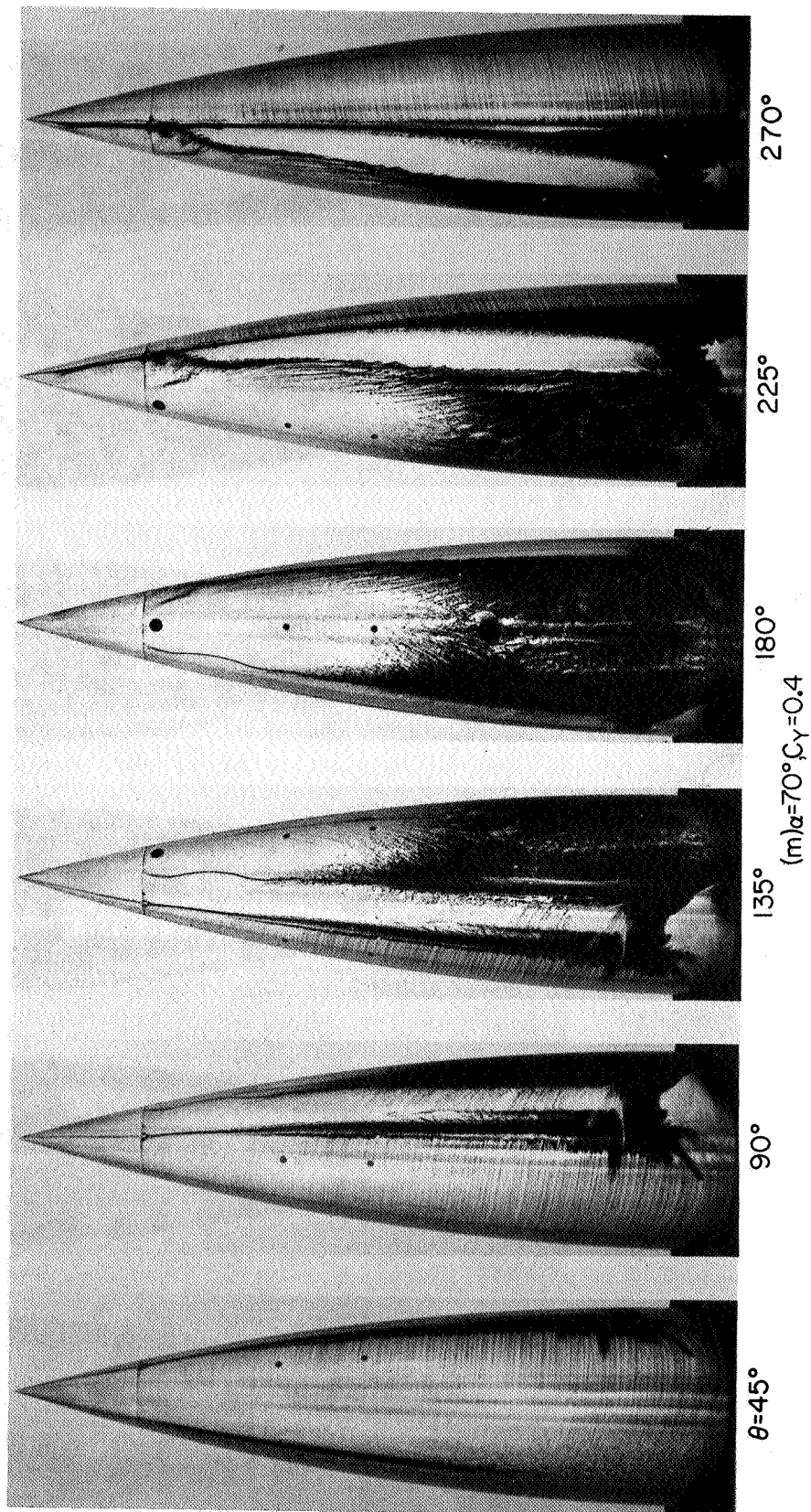
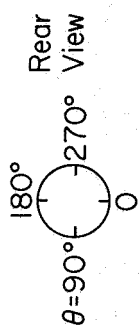


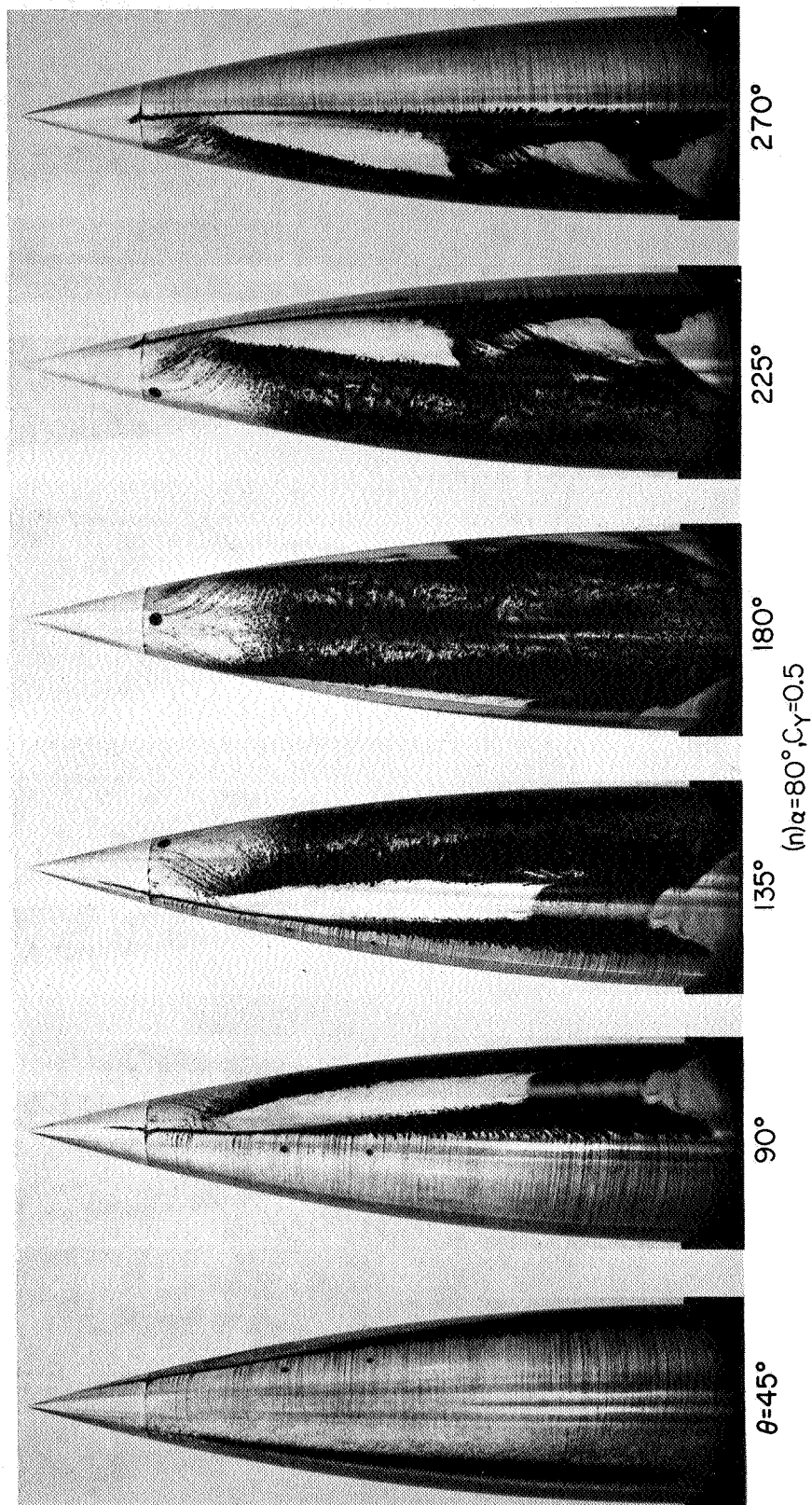
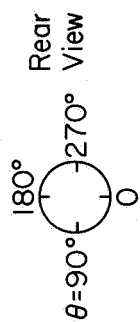
$\theta = 135^\circ$

180°

(I) CONCLUDED, $\alpha = 60^\circ$

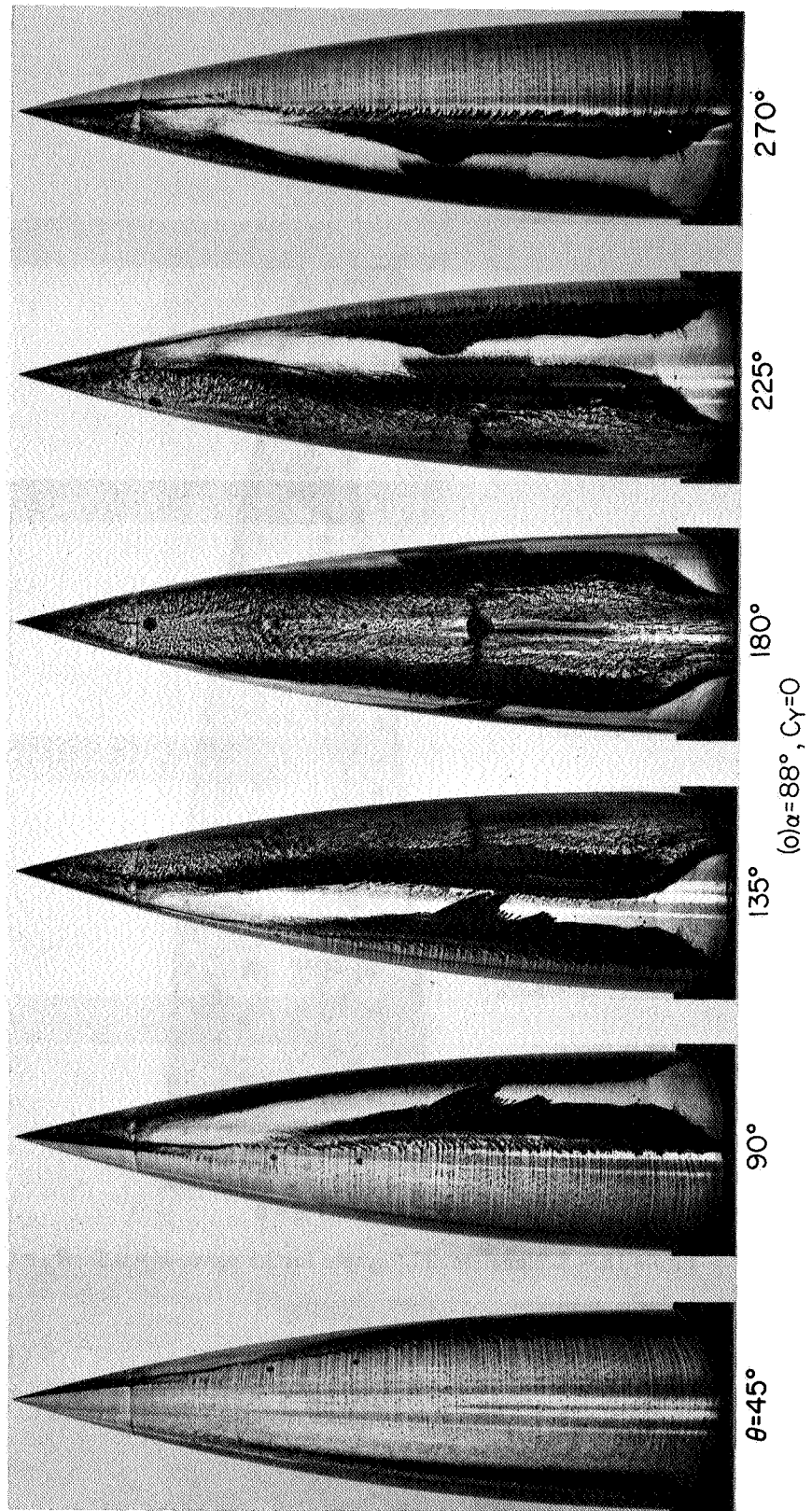
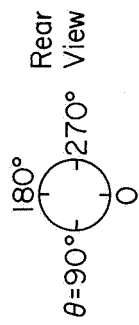
ORIGINAL PAGE IS
OF POOR QUALITY

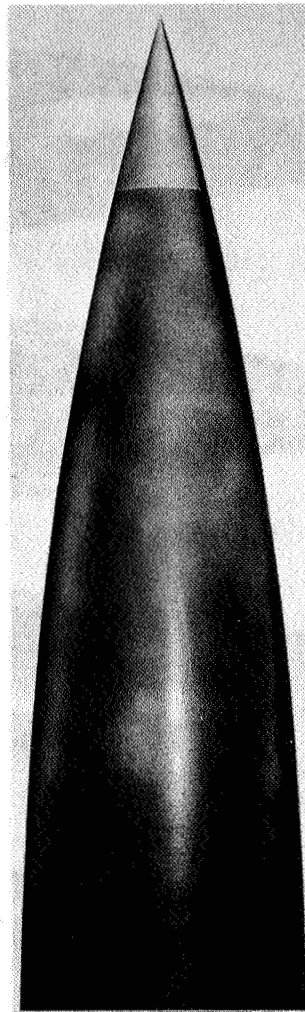




ORIGINAL PAGE IS
 OF POOR QUALITY

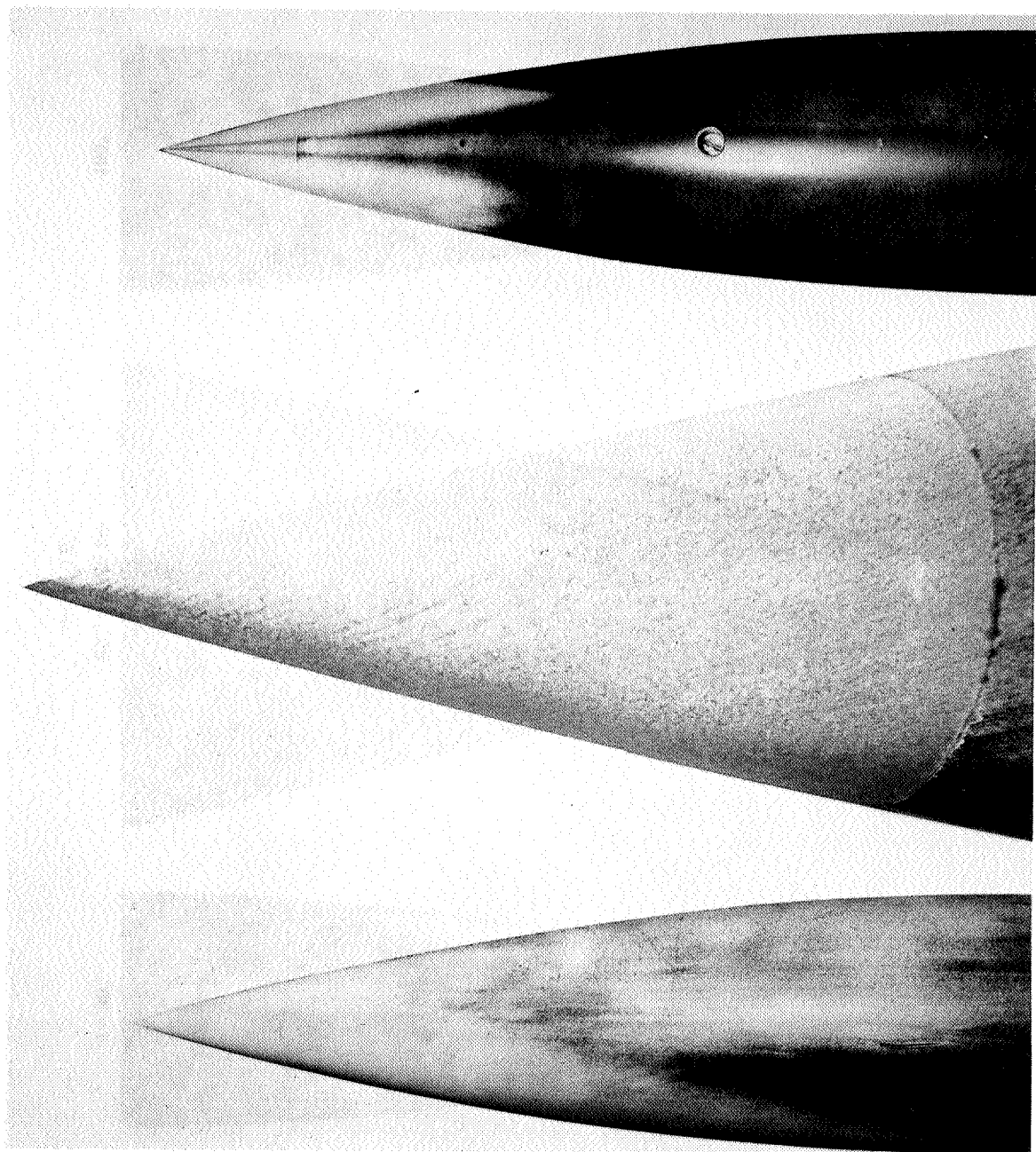
ORIGINAL PAGE IS
OF POOR QUALITY





(a) $\alpha = 0$

Figure 18.— Sublimation photographs for 3.5-ogive: $M = 0.25$, $R_d = 0.8 \times 10^6$.



180°

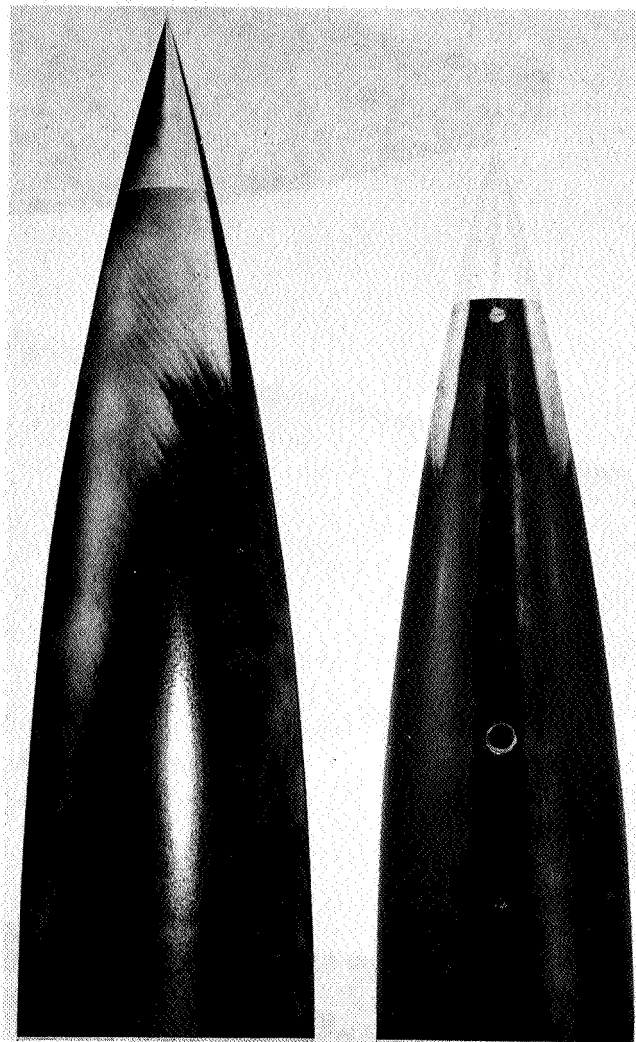
$90^\circ, \text{CLOSE UP}$

(c) $\alpha = 10^\circ$

$\theta = 90^\circ$

ORIGINAL PAGE IS
OF POOR QUALITY

ORIGINAL PAGE IS
OF POOR QUALITY

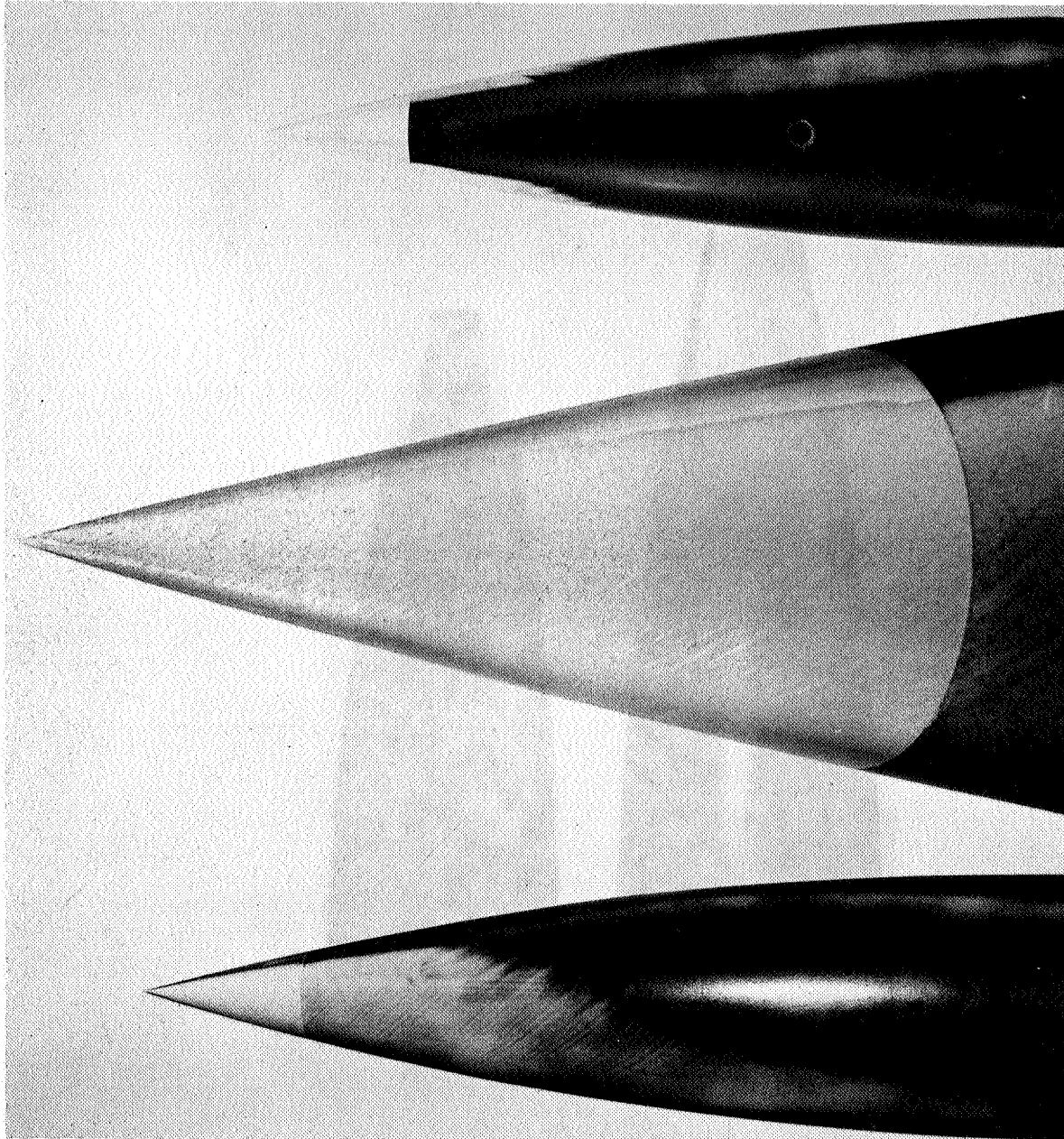


$\theta = 90^\circ$

180°

(d) $\alpha = 15^\circ$

ORIGINAL PAGE IS
OF POOR QUALITY

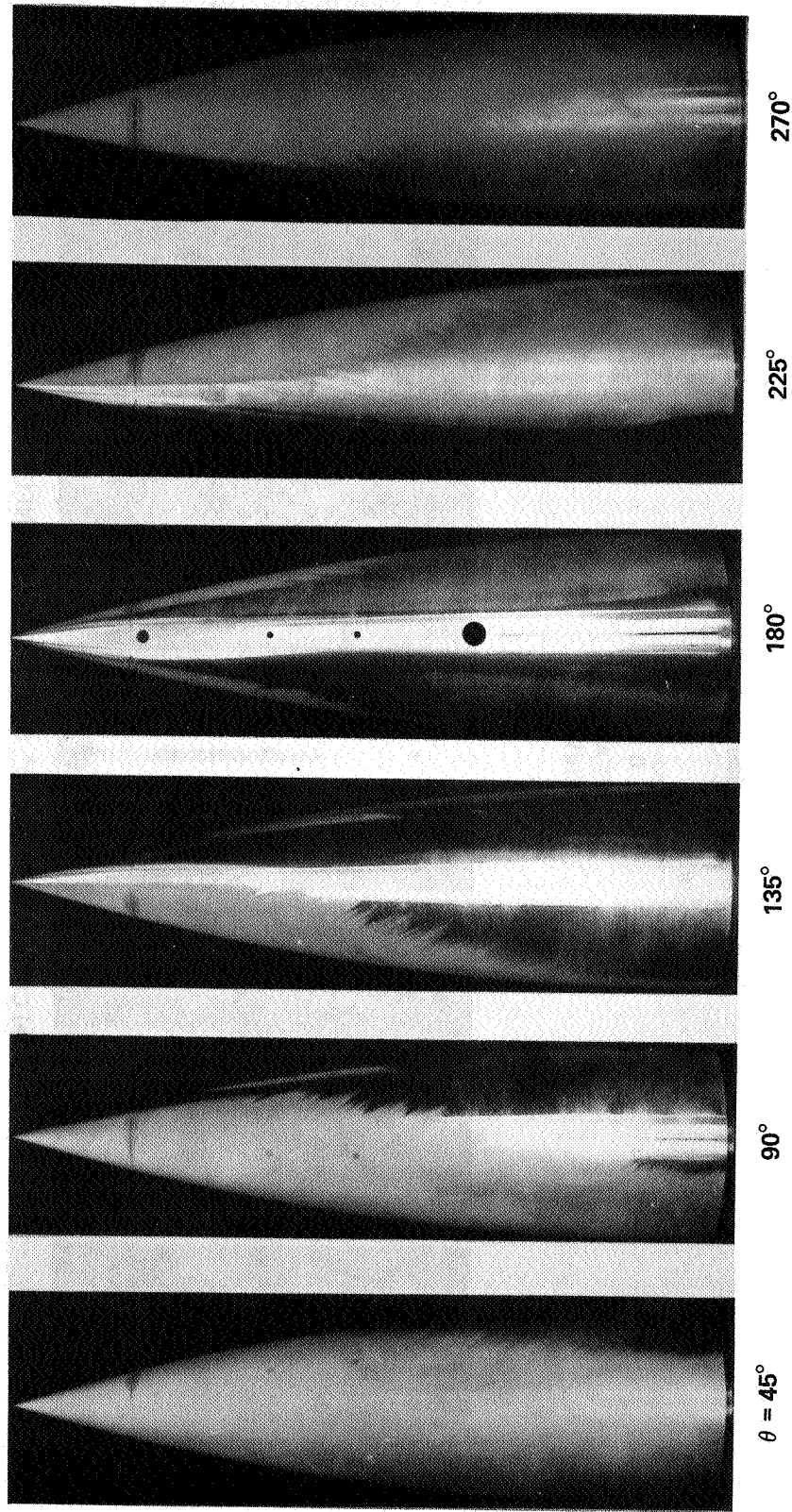
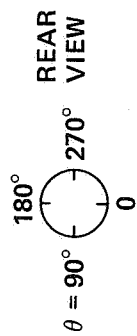


180°

90° , CLOSE UP
(e) $\alpha = 20^\circ$, $C_Y = 0$ (6 FT TUNNEL)

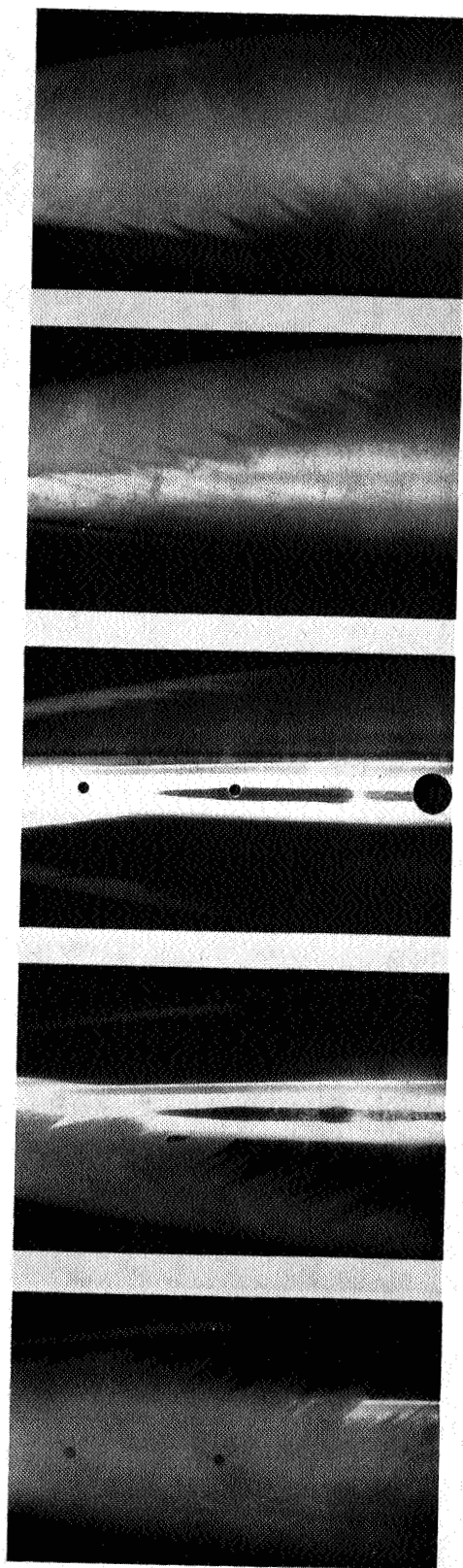
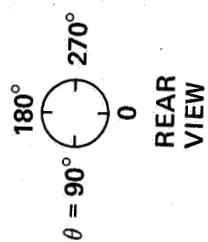
$\theta = 90^\circ$

ORIGINAL PAGE IS
OF POOR QUALITY



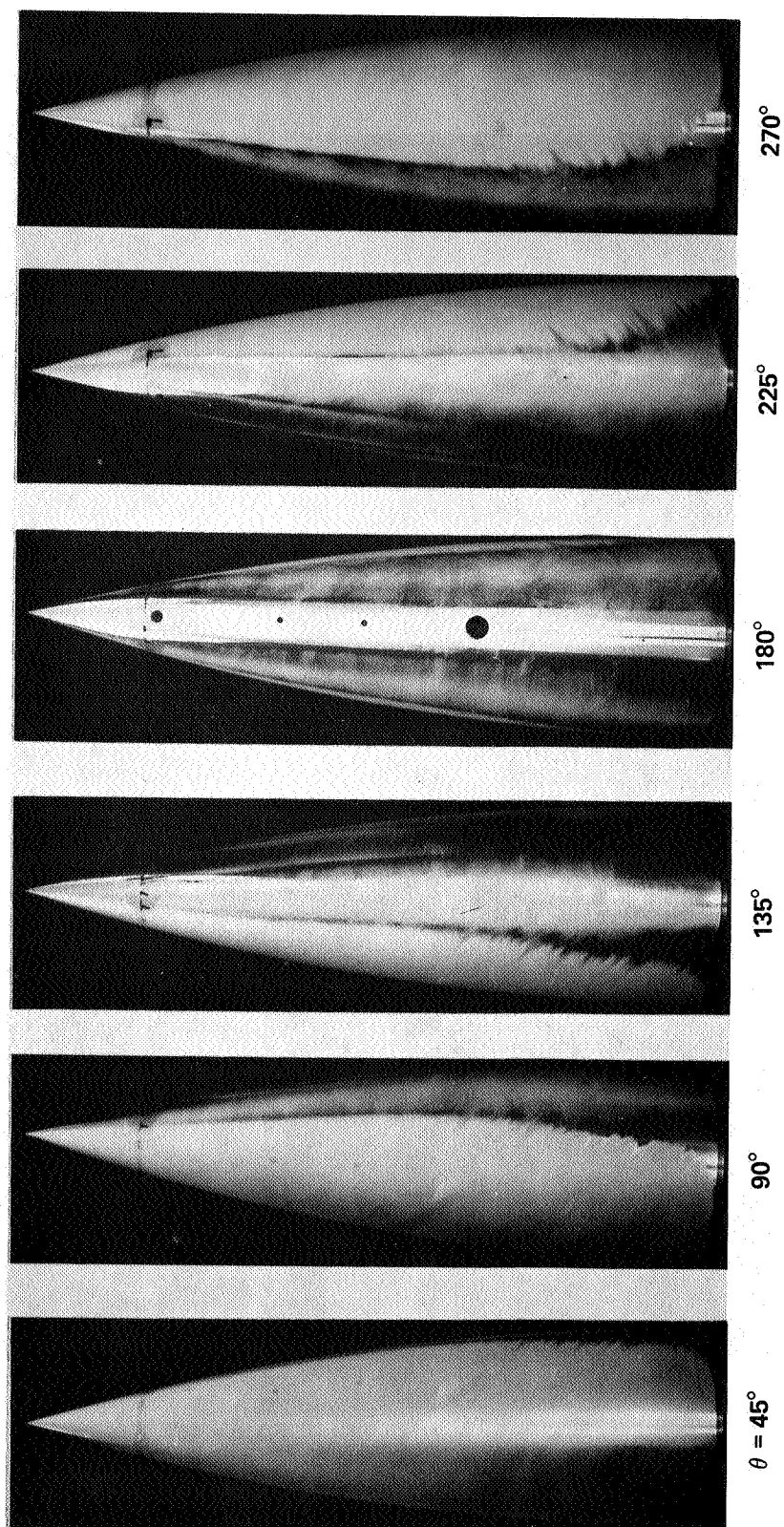
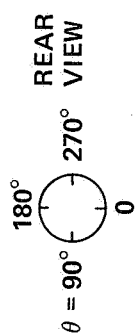
(e) CONTINUED: $\alpha = 20^\circ$, $C_Y = 0$ (12 FT TUNNEL)

C-2



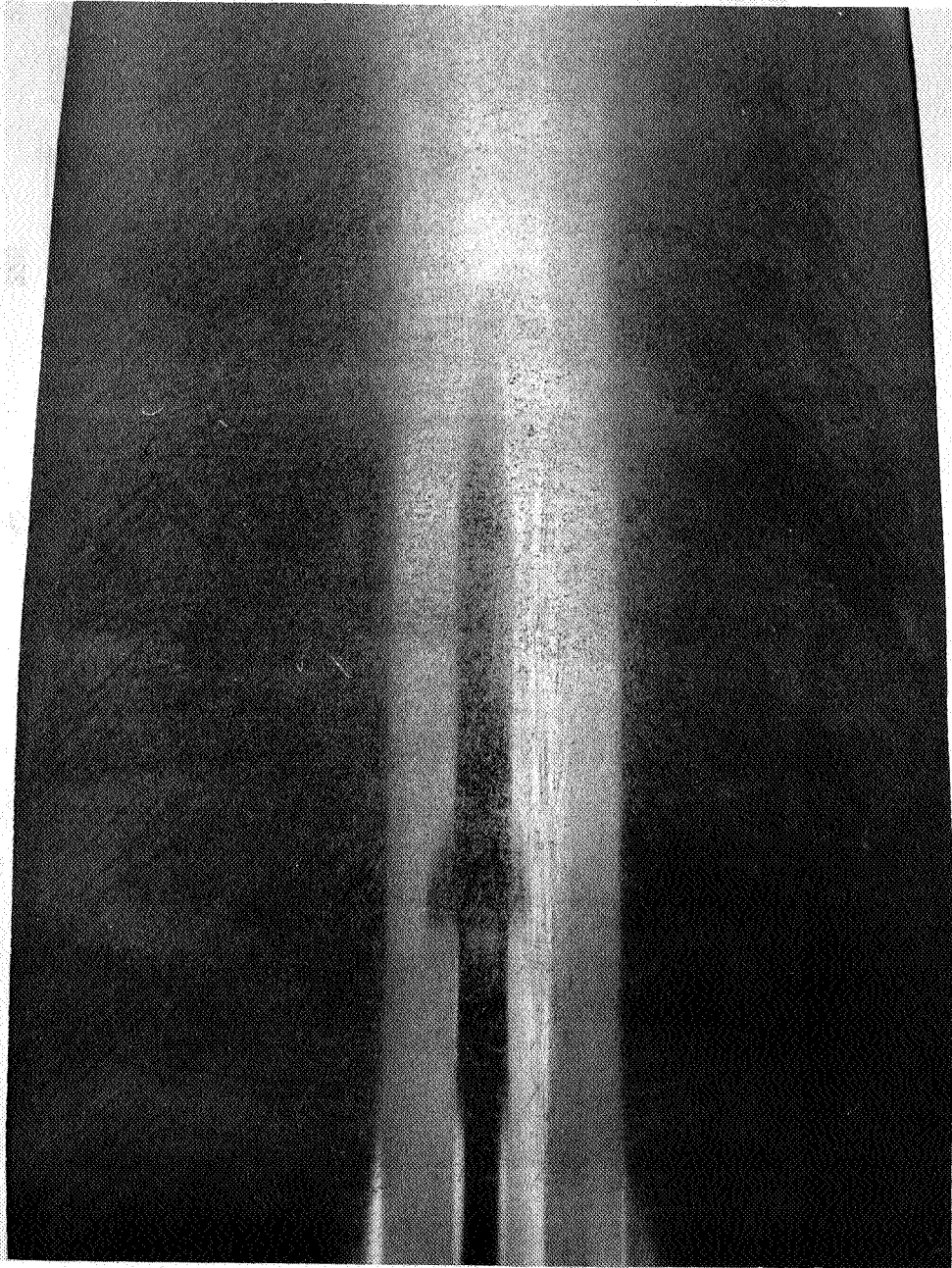
(e) CONCLUDED: $\alpha = 20^\circ$, $C_Y = 0$ (12 FT TUNNEL)

ORIGINAL PAGE IS
OF POOR QUALITY



(f) $\alpha = 40^\circ$, $C_Y = 0.4$

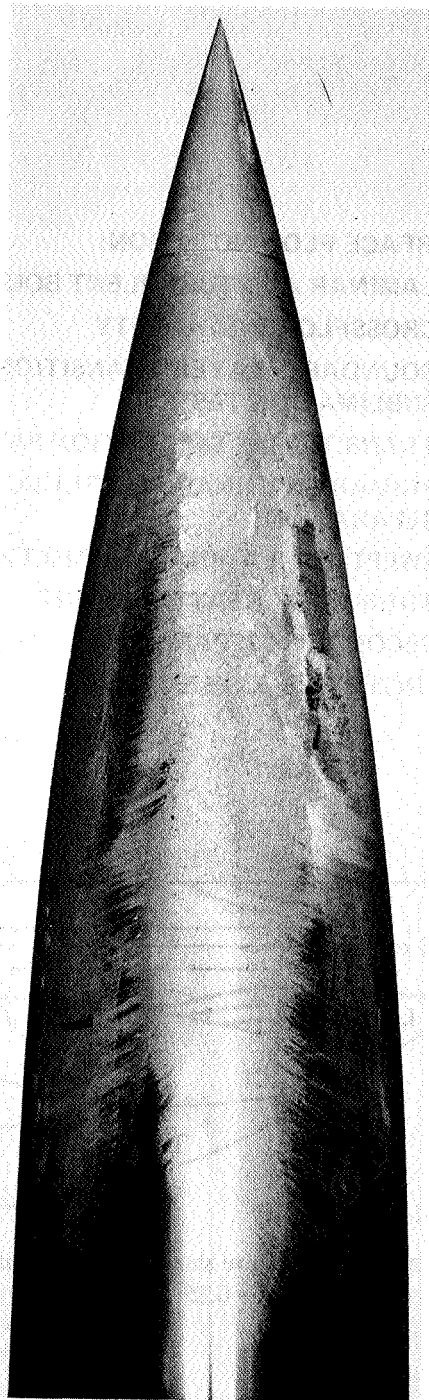
ORIGINAL PAGE IS
OF POOR QUALITY



$\theta = 0$

(f) CONCLUDED, $\alpha = 40^\circ$

ORIGINAL PAGE IS
OF POOR QUALITY



$\theta = 0$

(g) $\alpha = 55^\circ$, $C_Y = 2.6$

KEY TO SURFACE FLOW NOTATION:

L,T	= LAMINAR AND TURBULENT BOUNDARY LAYER
CI	= CROSSFLOW INSTABILITY
TR(∧∧)	= BOUNDARY LAYER TRANSITION FROM SUBLIMATION TESTS
TRS	= TRANSITIONAL SEPARATION PATTERN
LS, TS	= PRIMARY LAMINAR AND TURBULENT SEPARATION
B	= SWEEPED, 3-D, LAMINAR SEPARATION "BUBBLE"
R	= TURBULENT REATTACHMENT
SS	= SECONDARY SEPARATION
?	= UNCERTAIN, CONJECTURE

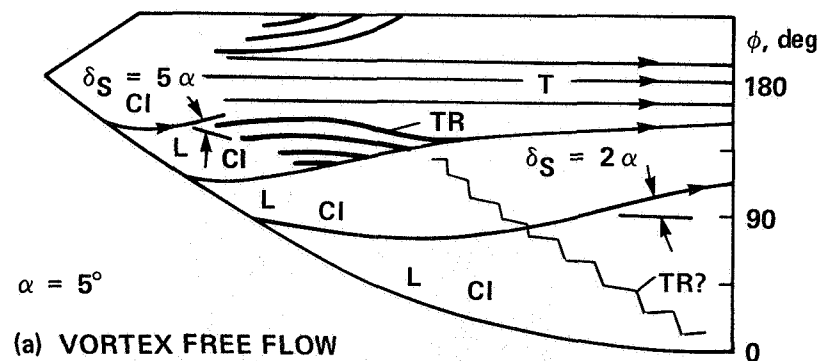
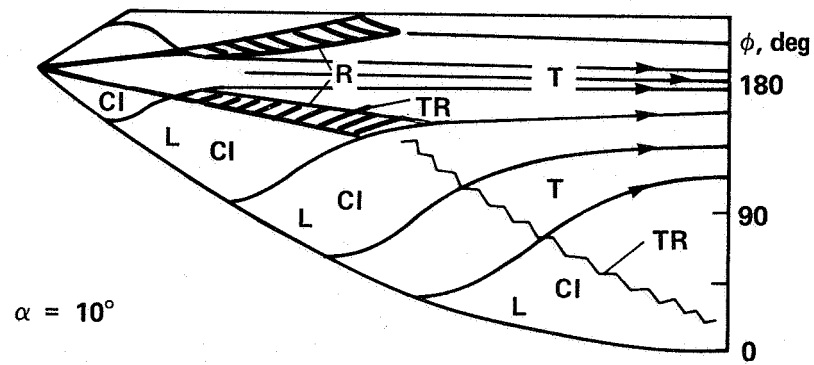
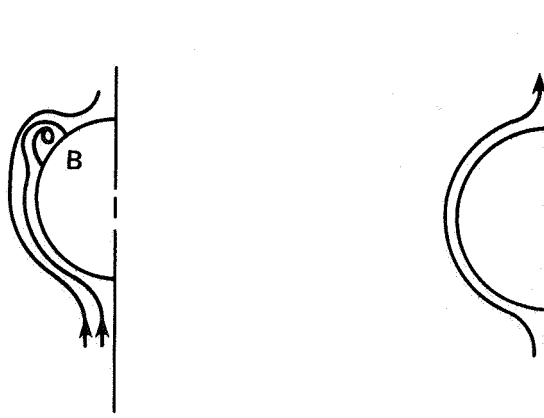
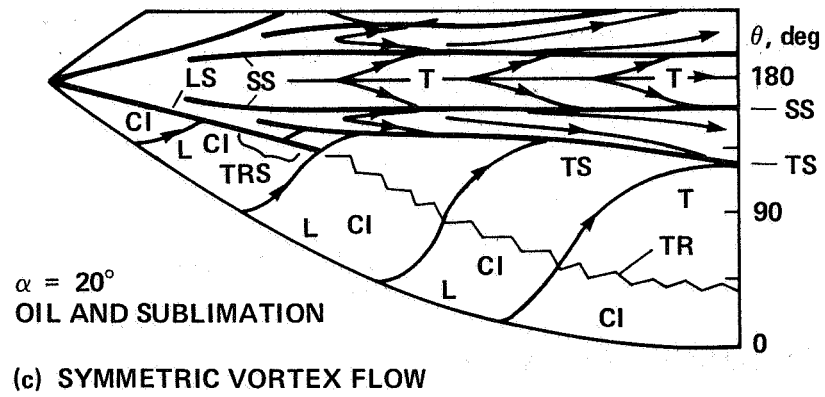
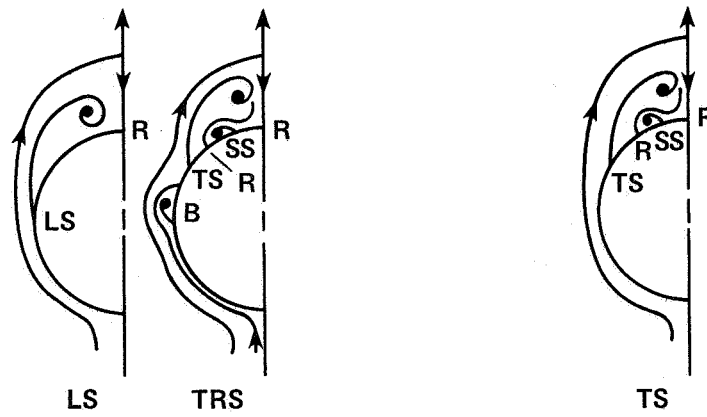
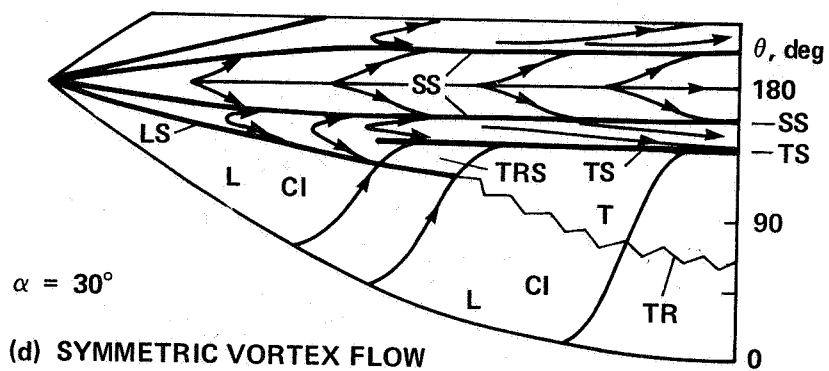
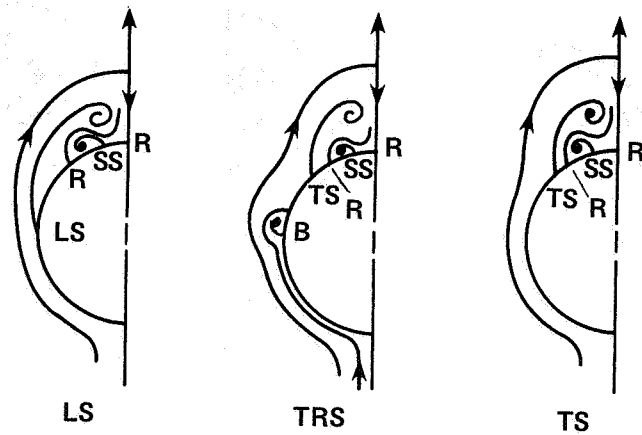


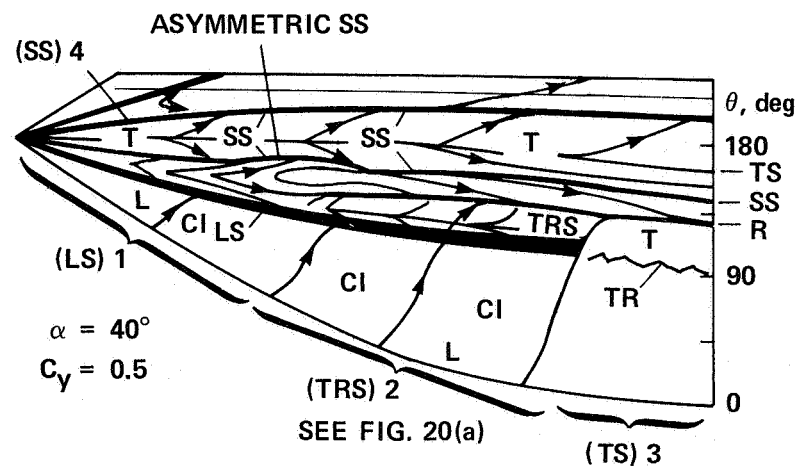
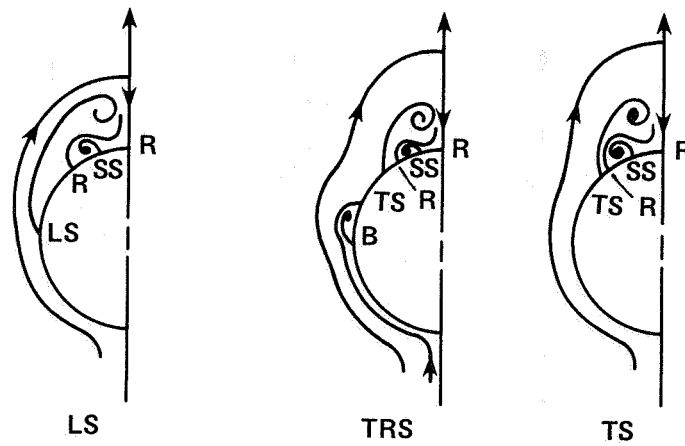
Figure 19.— Sketches of oil-flow patterns for 3.5-ogive showing effect of angle of attack at a transitional Reynolds number: $M = 0.25$, $R_d = 0.8 \times 10^6$.



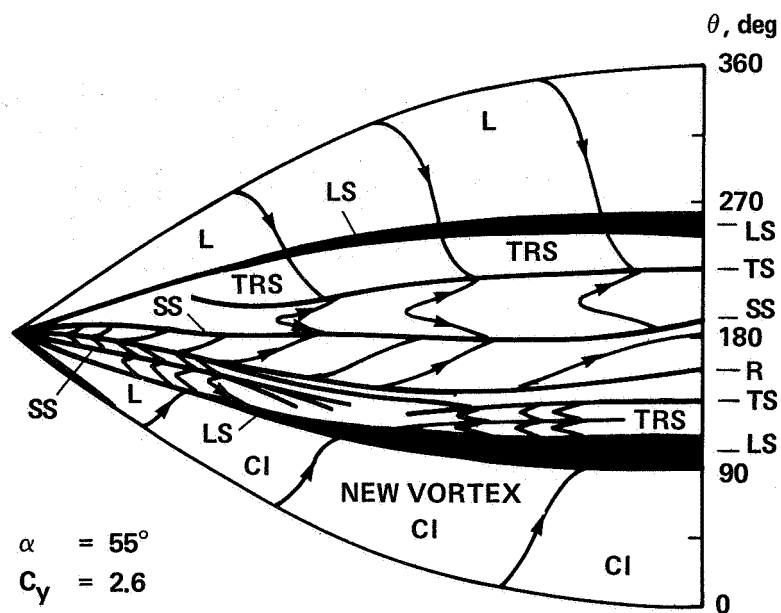
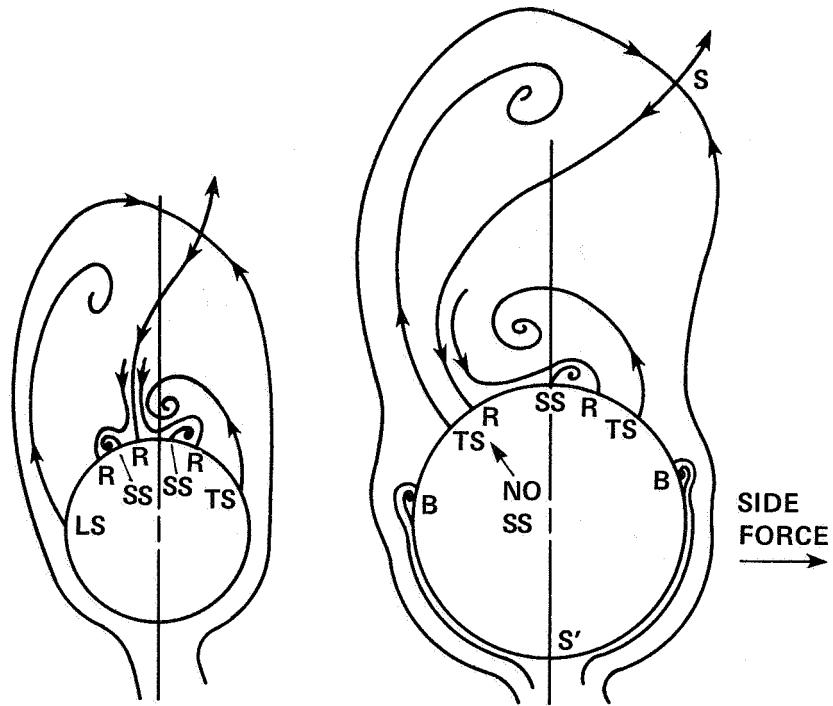
(b) LAMINAR SEPARATION



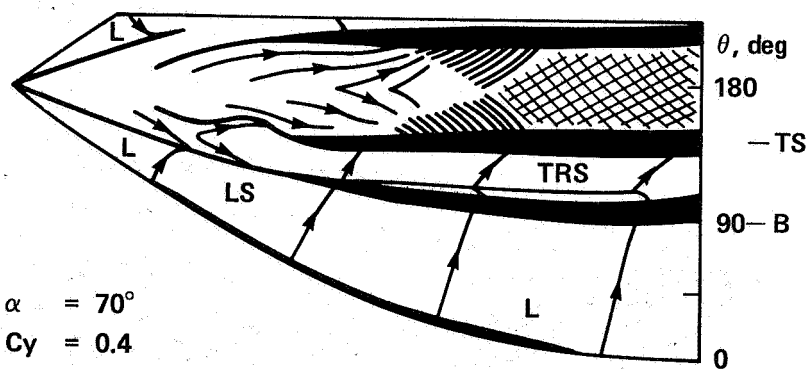
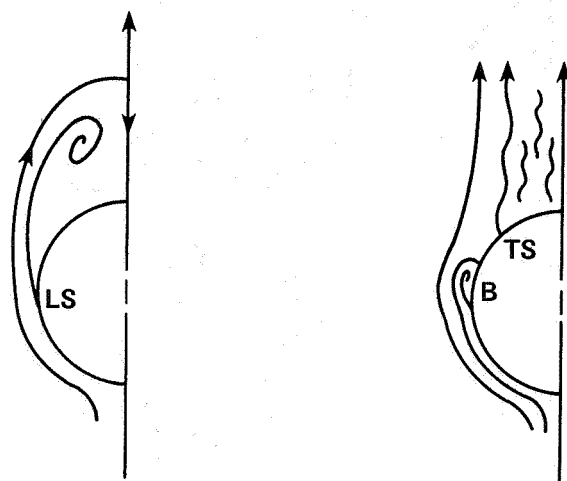




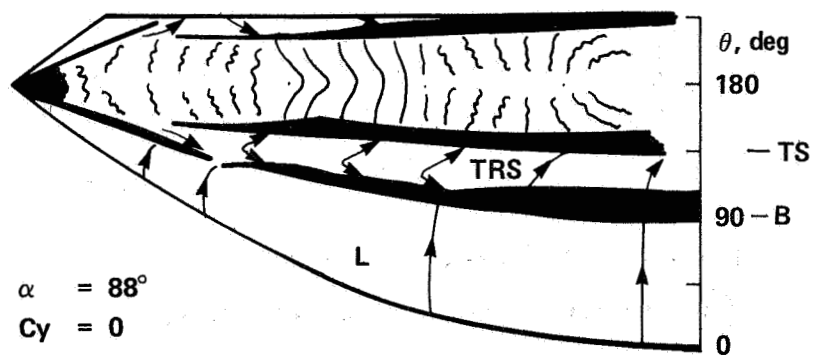
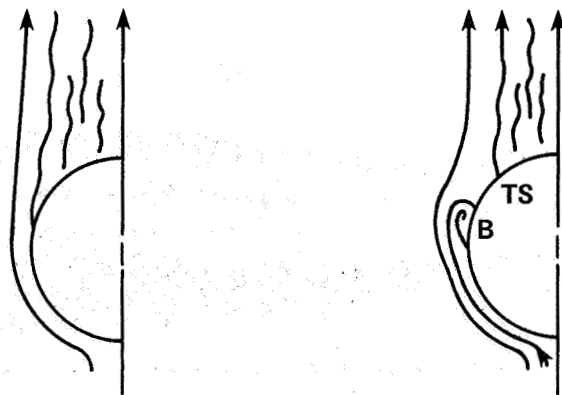
(e) SLIGHTLY ASYMMETRIC VORTEX FLOW



(f) ASYMMETRIC VORTEX FLOW

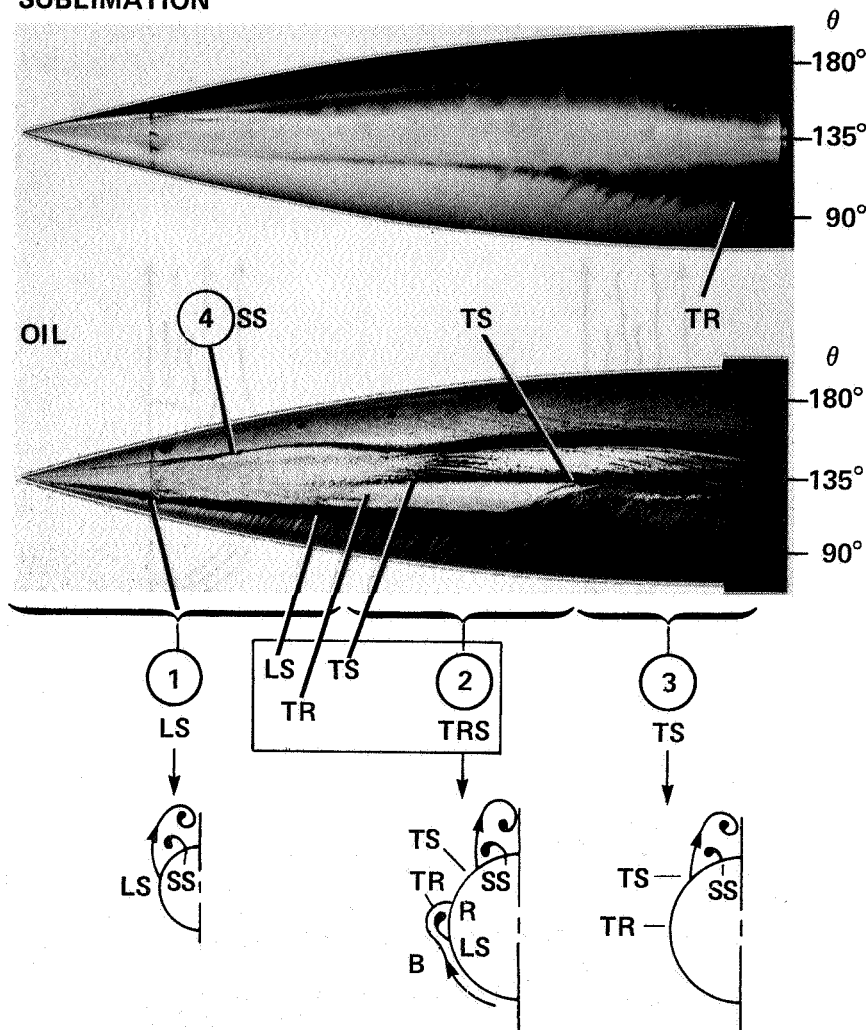


(g) PARTIAL WAKE-LIKE FLOW



(h) UNSTEADY WAKE-LIKE VORTEX FLOW

SUBLIMATION



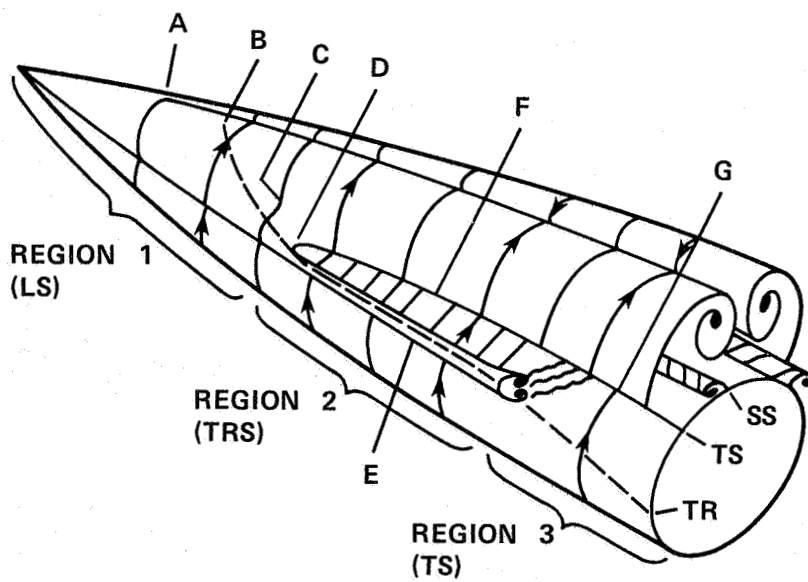
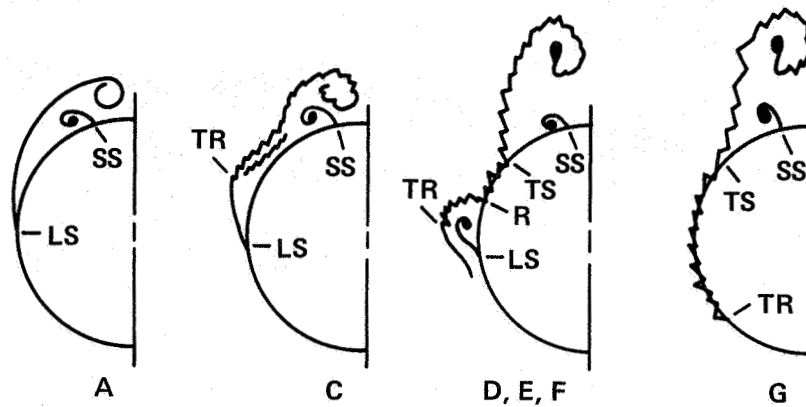
PRINCIPAL FEATURES:

- ① PRIMARY LAMINAR SEPARATION, LS
- ② PRIMARY TRANSITIONAL SEPARATION, TRS = (LS + TR + R + TS)
- ③ PRIMARY TURBULENT SEPARATION, TS
- ④ SECONDARY SEPARATION, SS

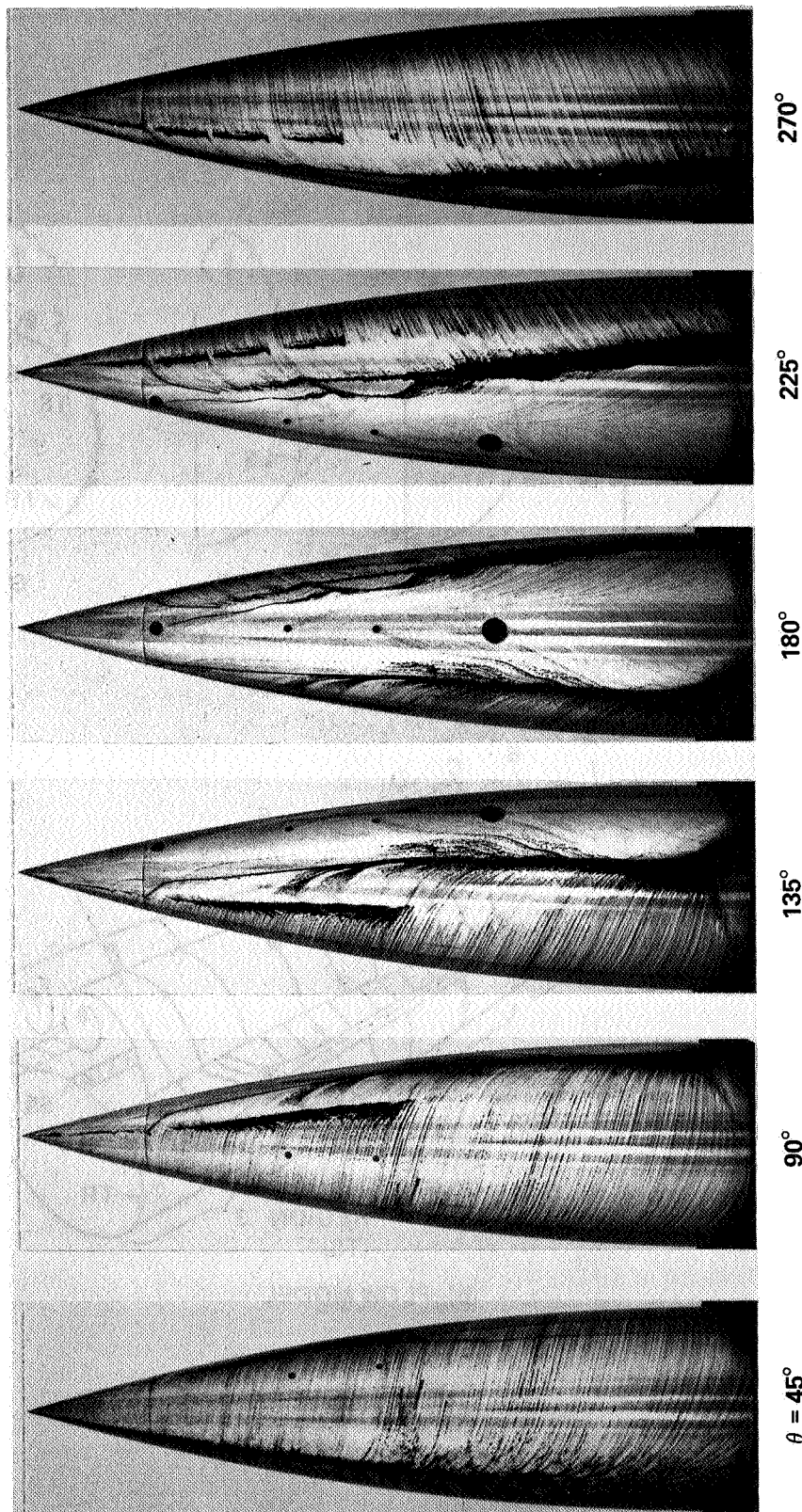
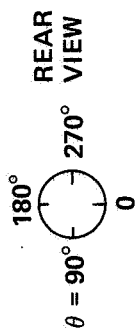
$$\alpha = 40^\circ, C_Y = 0.5$$

(a) SLIGHTLY ASYMMETRIC VORTEX FLOW

Figure 20.— Flow model of principal features of flow pattern for 3.5-ogive at a transitional Reynolds number:
 $M = 0.25, R_d = 0.8 \times 10^6, \alpha = 40^\circ$.



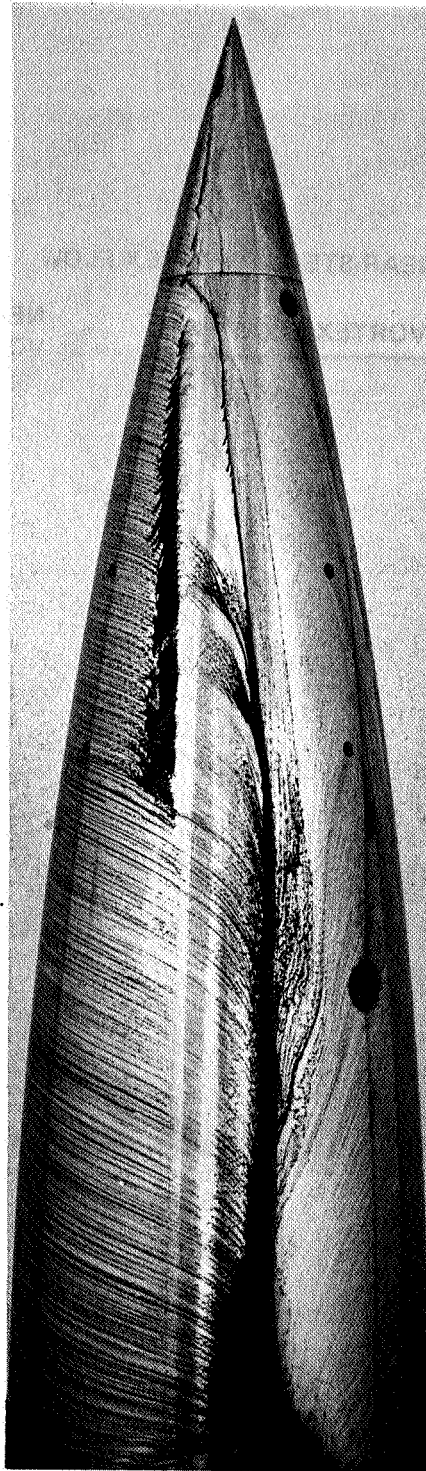
(b) FLOW MODEL



(a) $\alpha = 55^\circ$, $C_Y = 0.8$

Figure 21.— Oil-flow photographs for 3.5-ogive: $M = 0.25$, $R_d = 2 \times 10^6$, $\alpha = 55^\circ$, $C_Y = 0.8$.

ORIGINAL PAGE IS
OF POOR QUALITY



$\theta = 135^\circ$

(b) CONCLUDED, CLOSE UP, $\alpha = 55^\circ$, $C_Y = 0.8$

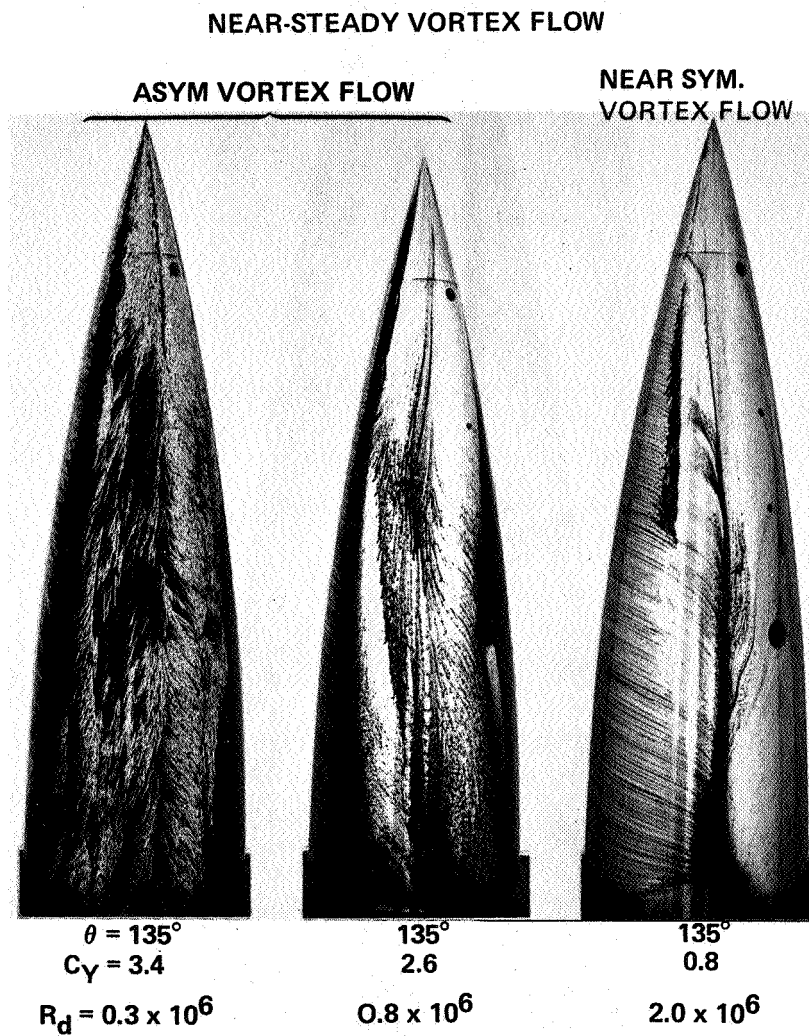
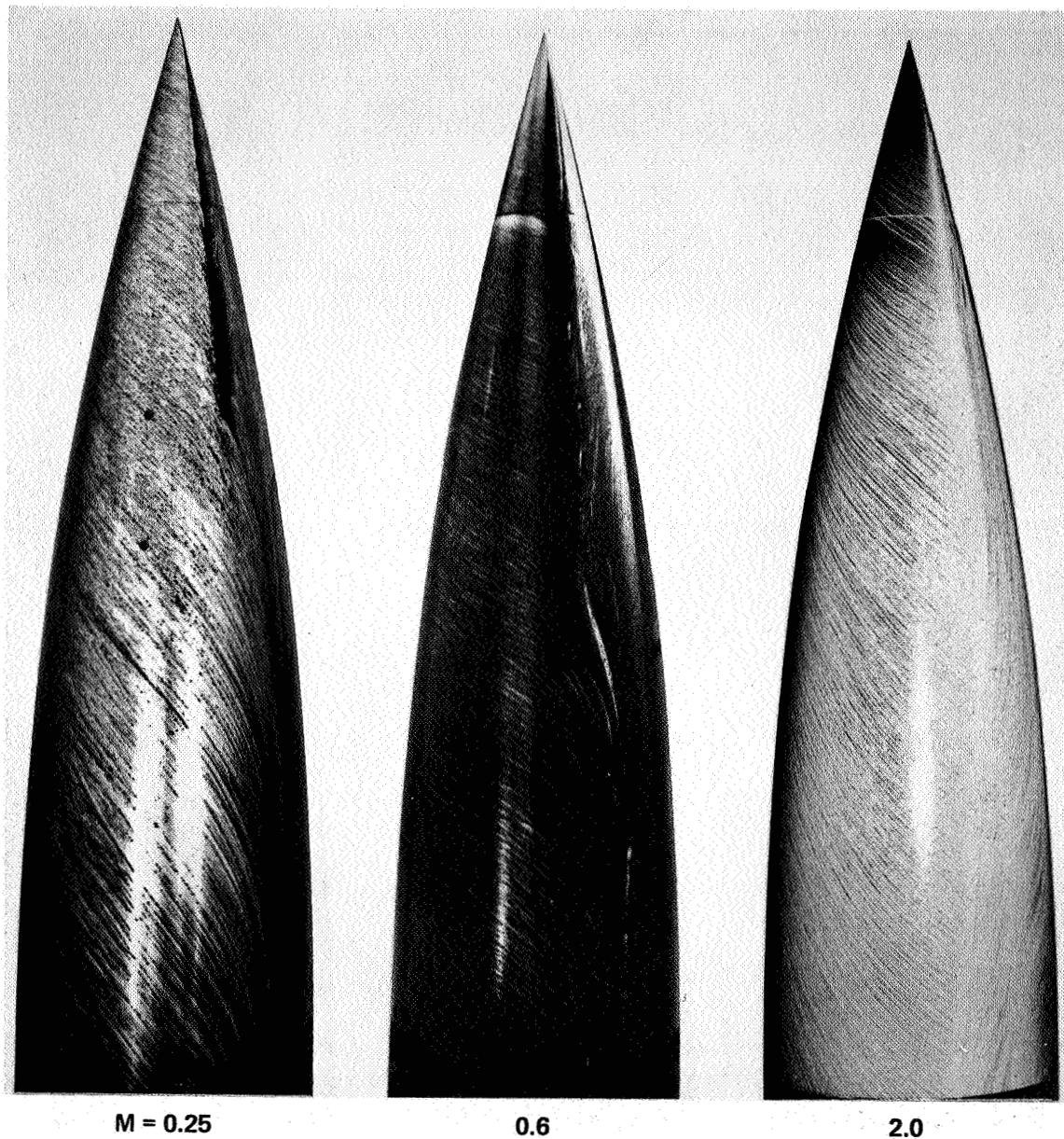


Figure 22.— Effect of Reynolds number on oil-flow patterns for 3.5-ogive: $M = 0.25$, $\alpha = 55^\circ$.

ORIGINAL PAGE IS
OF POOR QUALITY



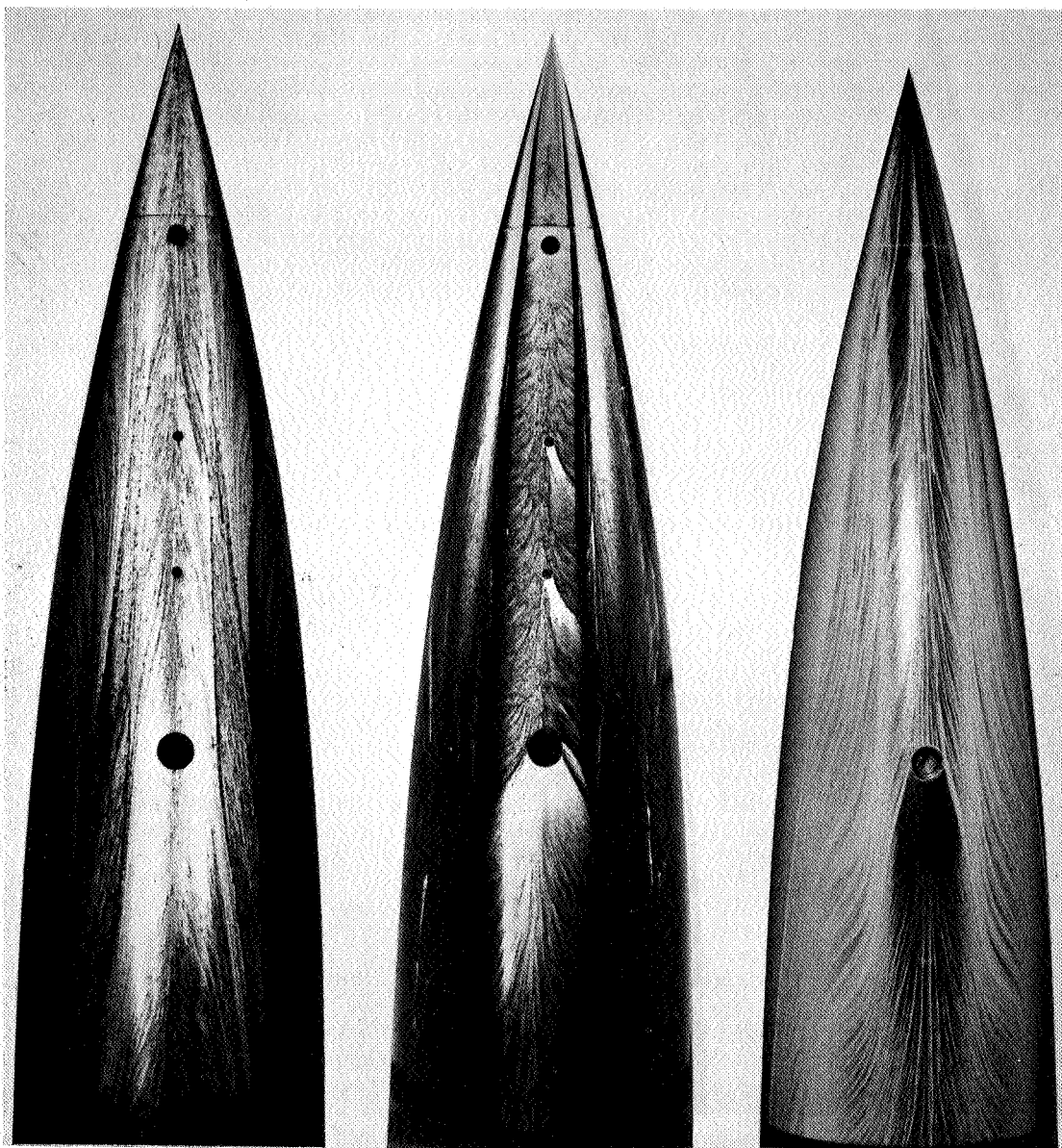
M = 0.25

0.6

2.0

(a) $\alpha = 20^\circ, \theta = 90^\circ$

Figure 23.— Effect of Mach number on oil-flow patterns for 3.5-ogive at $R_d = 0.8 \times 10^6$.



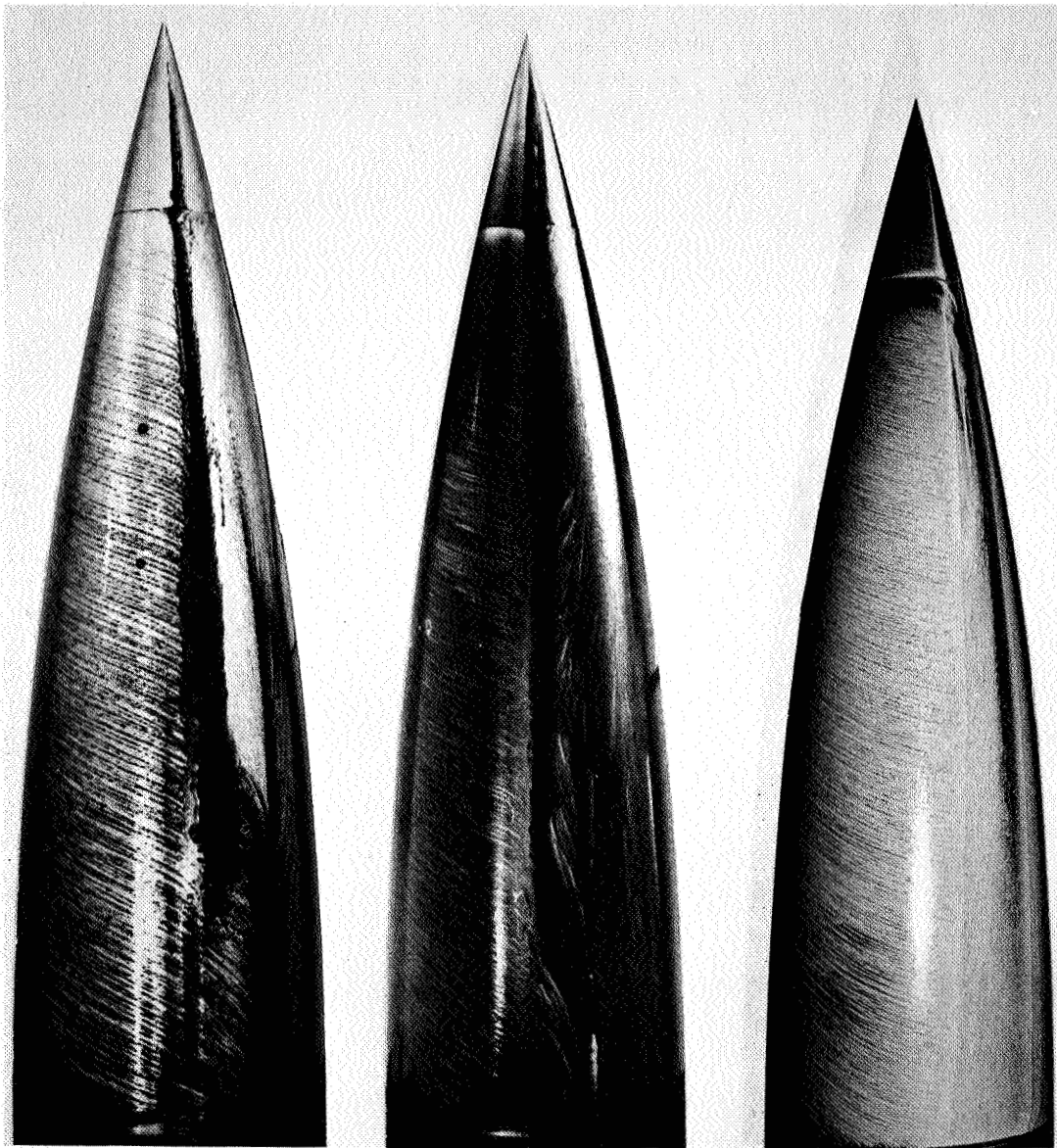
$M = 0.25$

0.6

2.0

(a) CONCLUDED, $\alpha = 20^\circ$, $\theta = 180^\circ$

ORIGINAL PAGE IS
OF POOR QUALITY

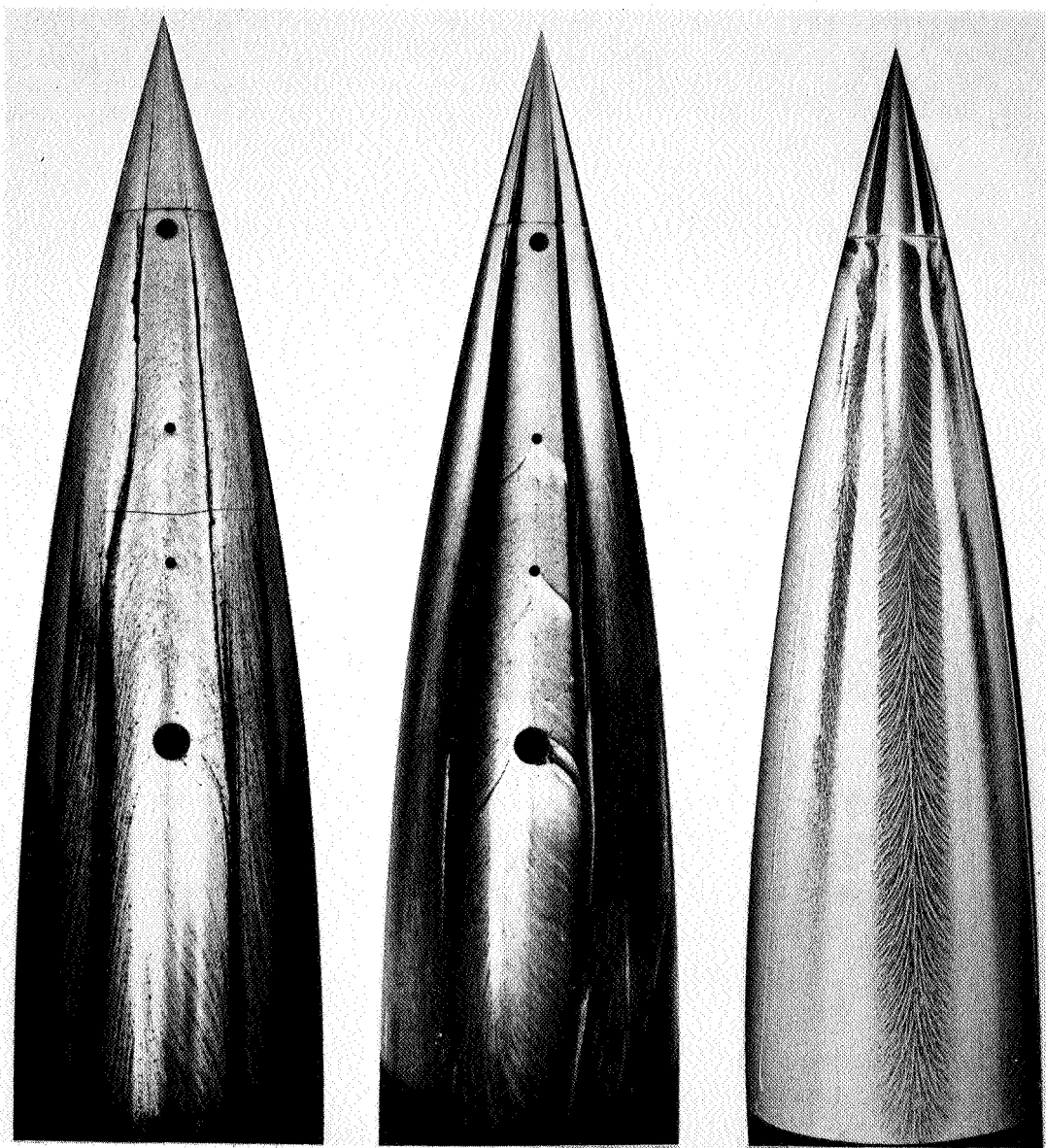


$M = 0.25$

0.6

2.0

(b) $\alpha = 40^\circ, \theta = 90^\circ$

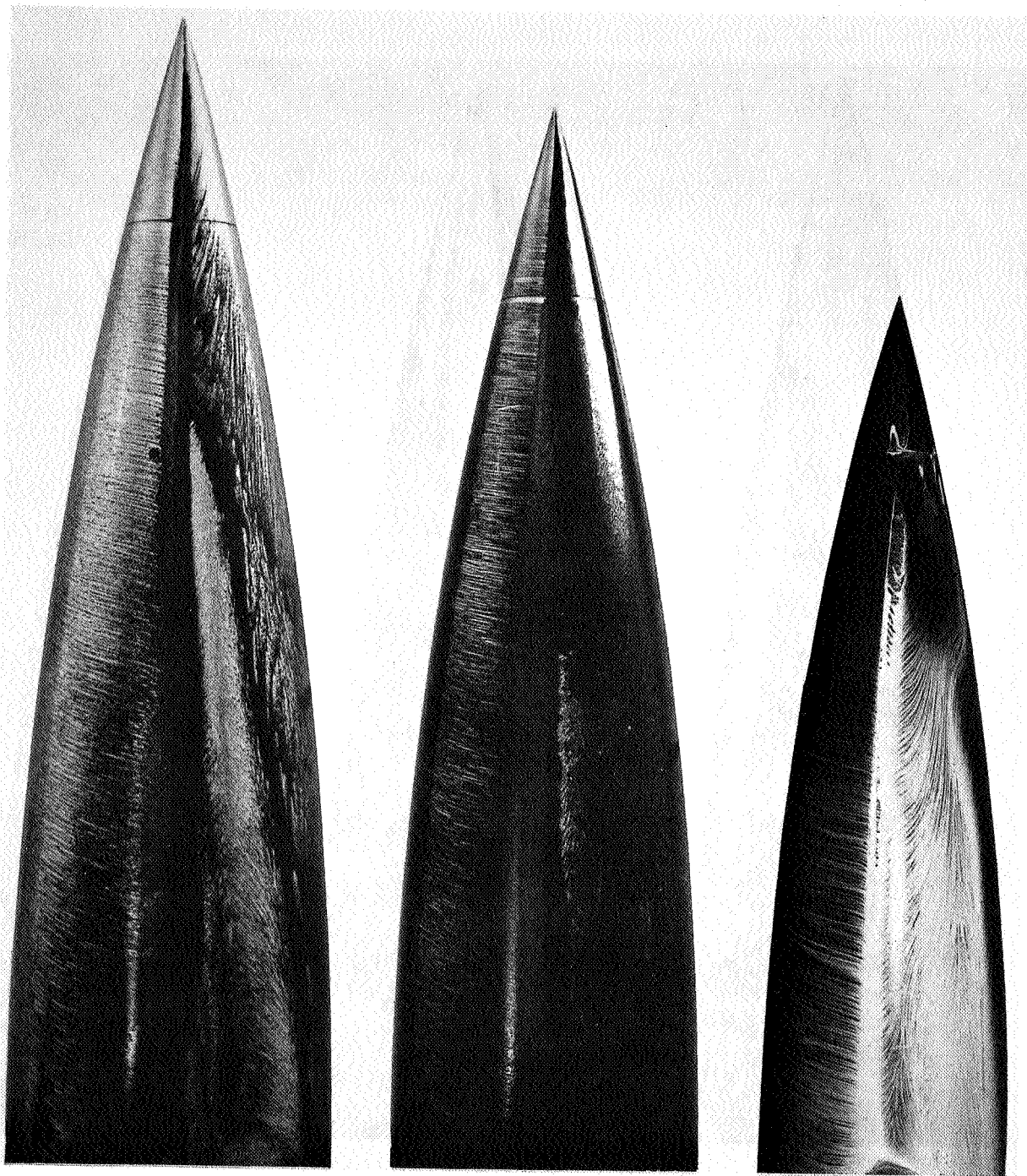


M = 0.25

0.6

2.0

(b) CONCLUDED, $\alpha = 40^\circ$, $\theta = 180^\circ$

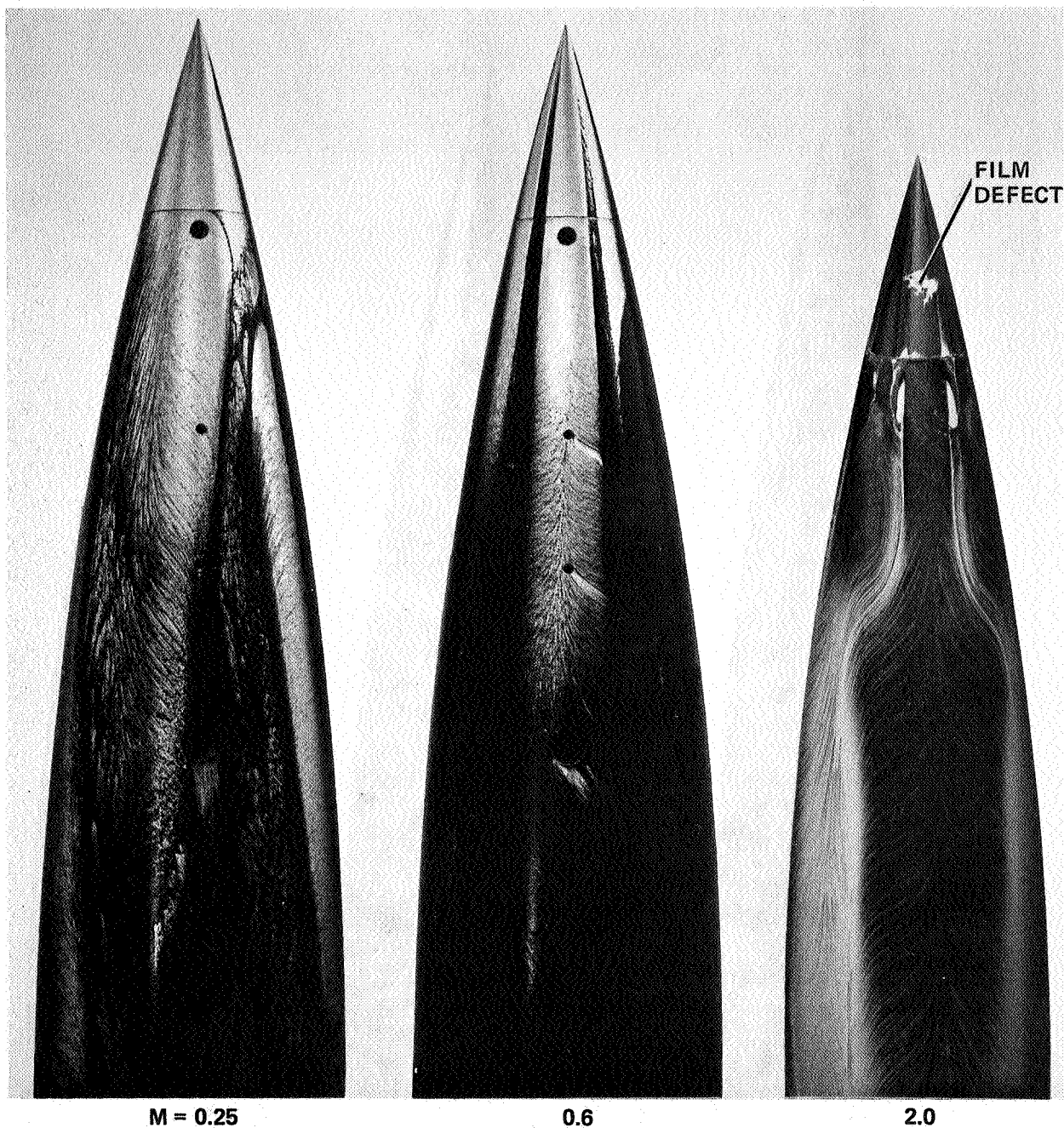


$M = 0.25$

0.6

2.0

(c) $\alpha = 55^\circ, \theta = 90^\circ$



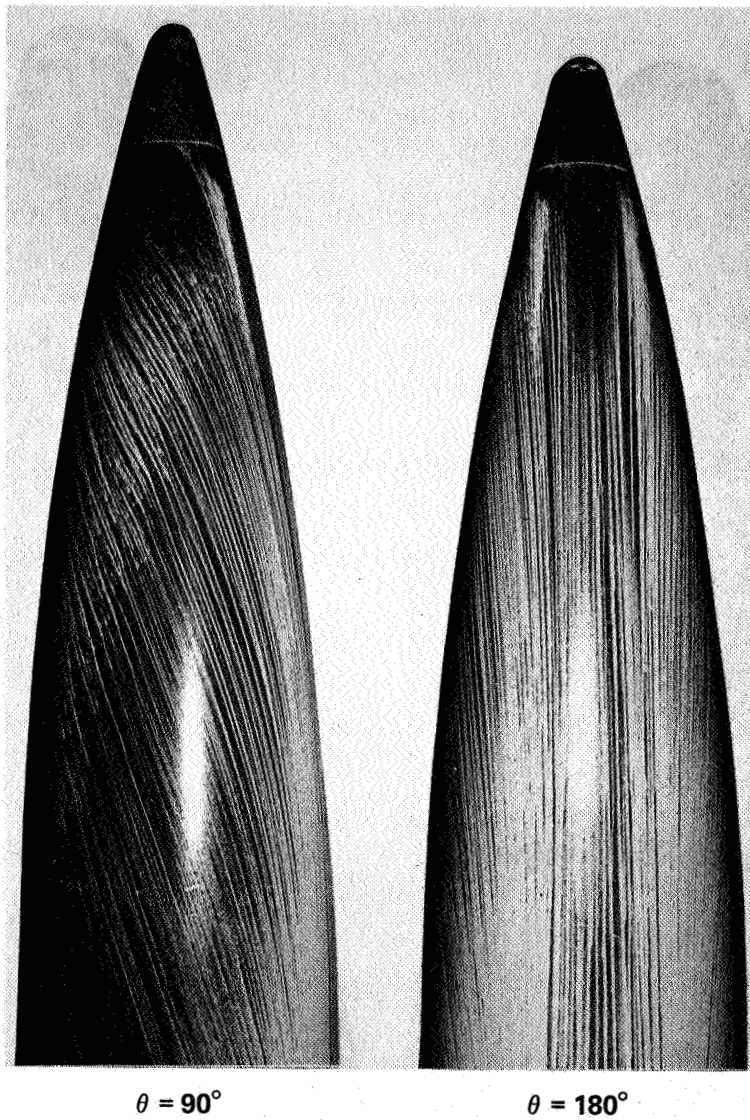
M = 0.25

0.6

2.0

(c) CONCLUDED, $\alpha = 55^\circ$, $\theta = 180^\circ$

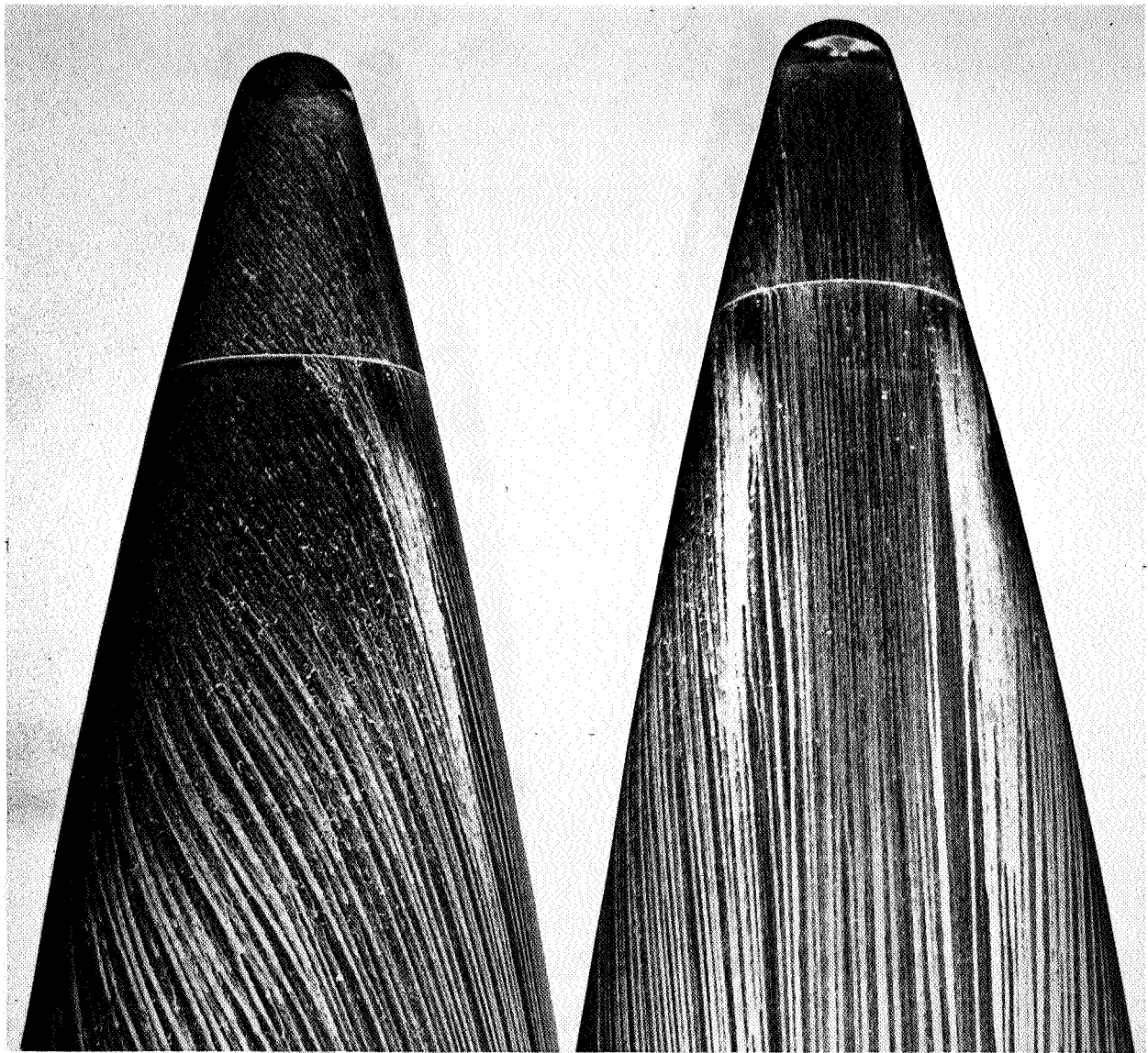
ORIGINAL PAGE IS
OF POOR QUALITY



(a) $\alpha = 10^\circ$

Figure 24.— Effect of bluntness on oil-flow patterns for 3.5 ogive with 16% bluntness ratio: $M = 0.25$, $R_d = 0.8 \times 10^6$.

ORIGINAL PAGE IS
OF POOR QUALITY

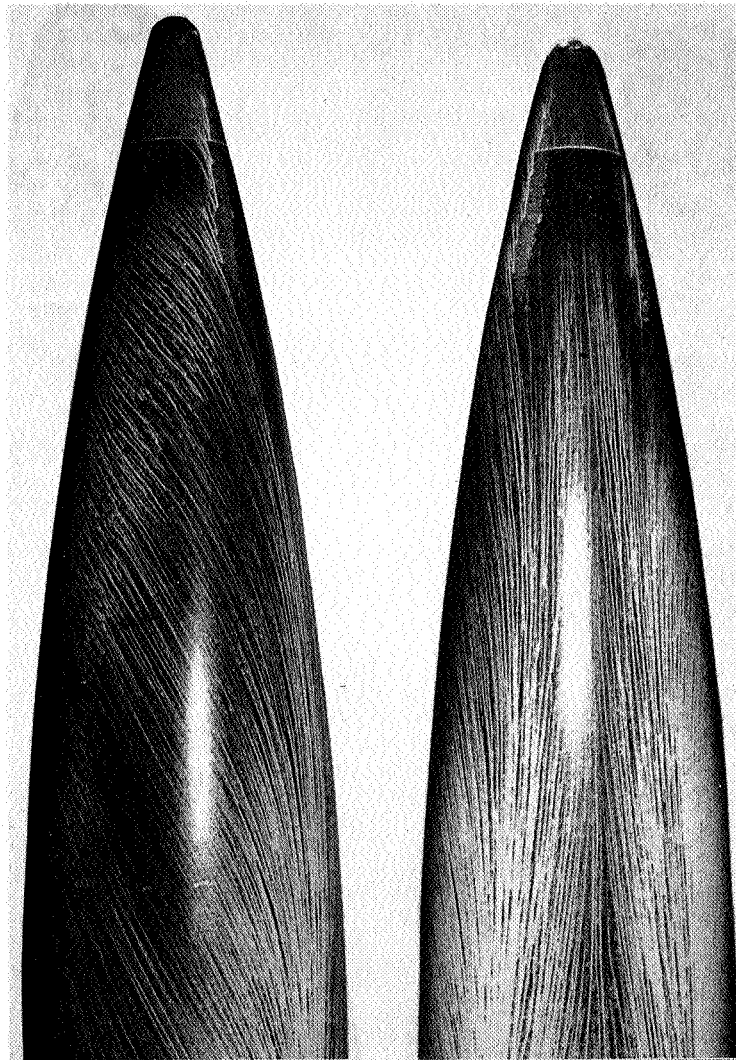


$\theta = 90^\circ$

$\theta = 180^\circ$

(a) $\alpha = 10^\circ$, CONCLUDED, CLOSE UP

ORIGINAL PAGE IS
OF POOR QUALITY

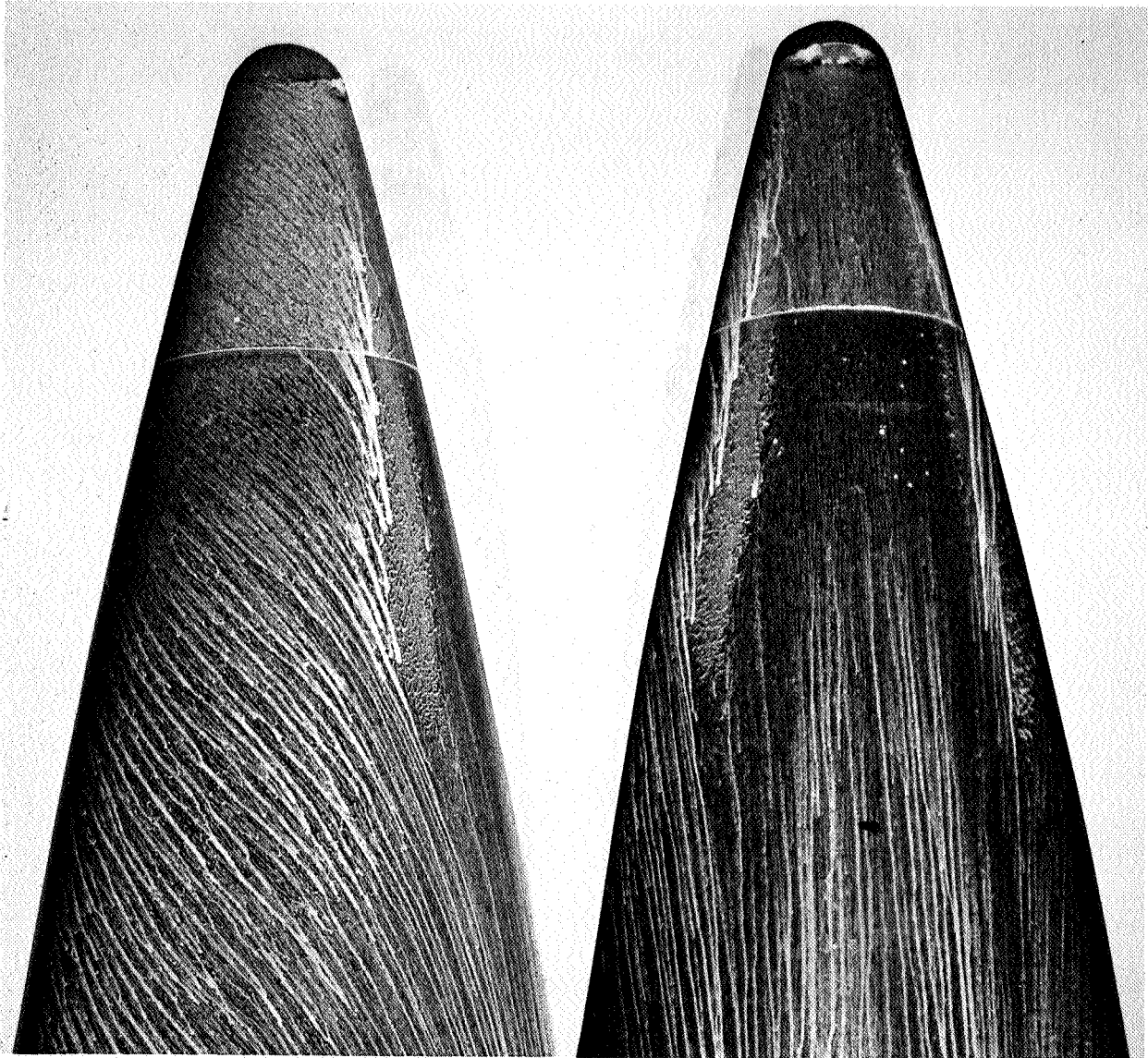


$\theta = 90^\circ$

$\theta = 180^\circ$

(b) $\alpha = 15^\circ$

ORIGINAL PAGE IS
OF POOR QUALITY

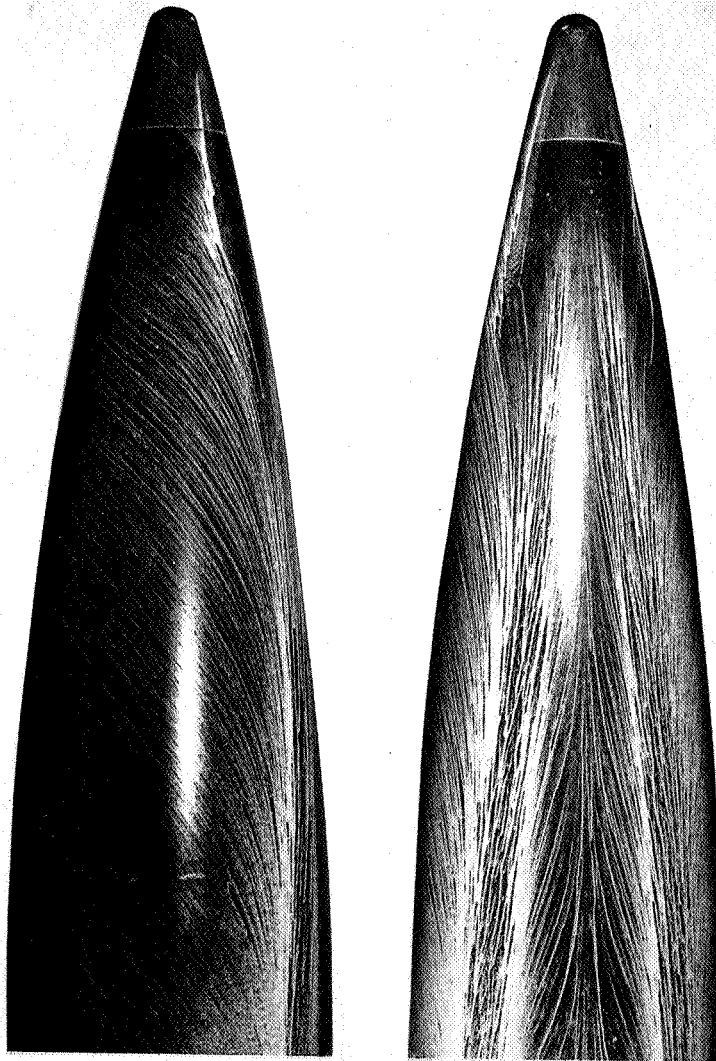


$\theta = 90^\circ$

$\theta = 180^\circ$

(b) $\alpha = 15^\circ$, CONCLUDED, CLOSE UP

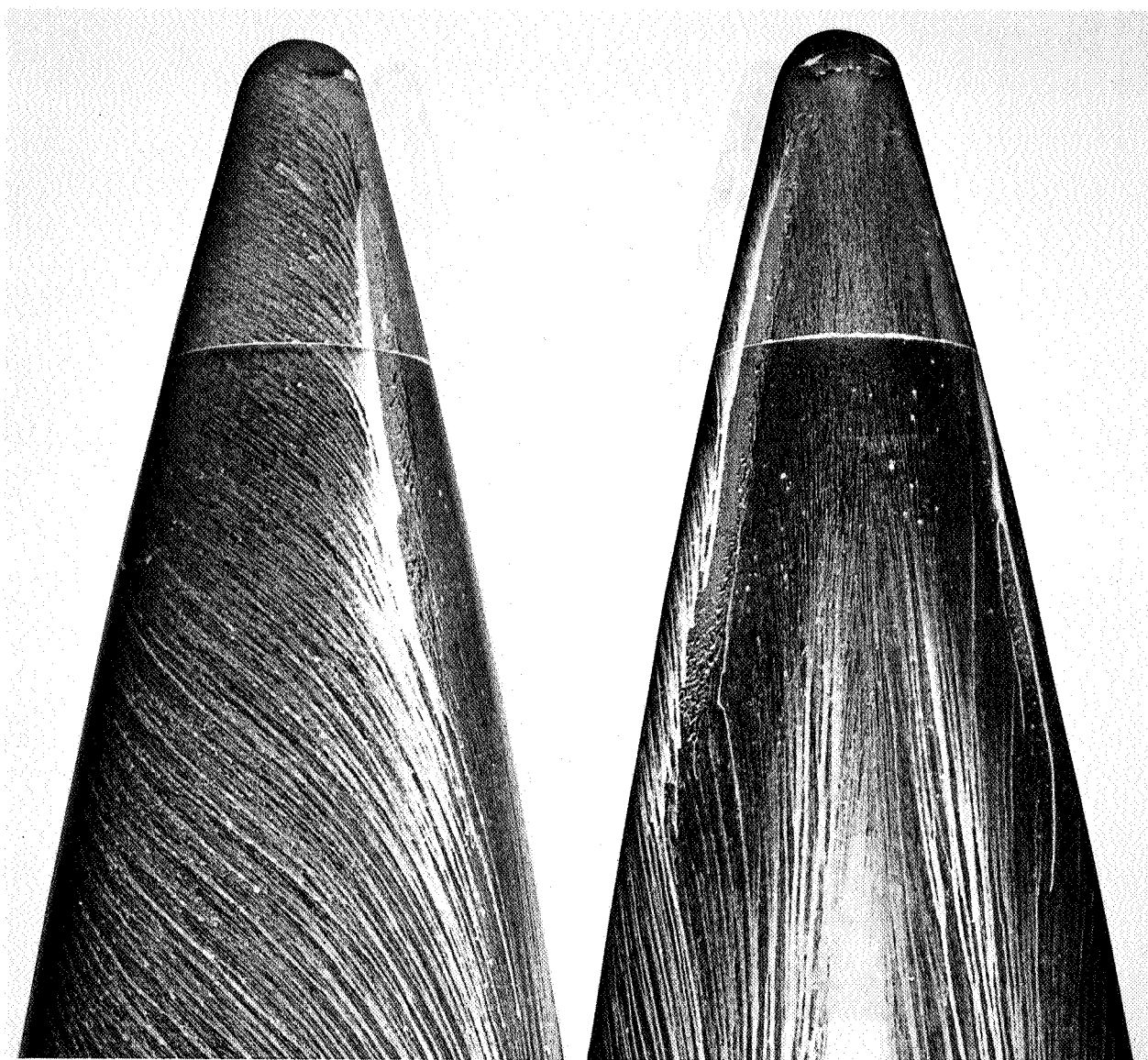
ORIGINAL PAGE IS
OF POOR QUALITY



$\theta = 90^\circ$

$\theta = 180^\circ$

(c) $\alpha = 20^\circ$

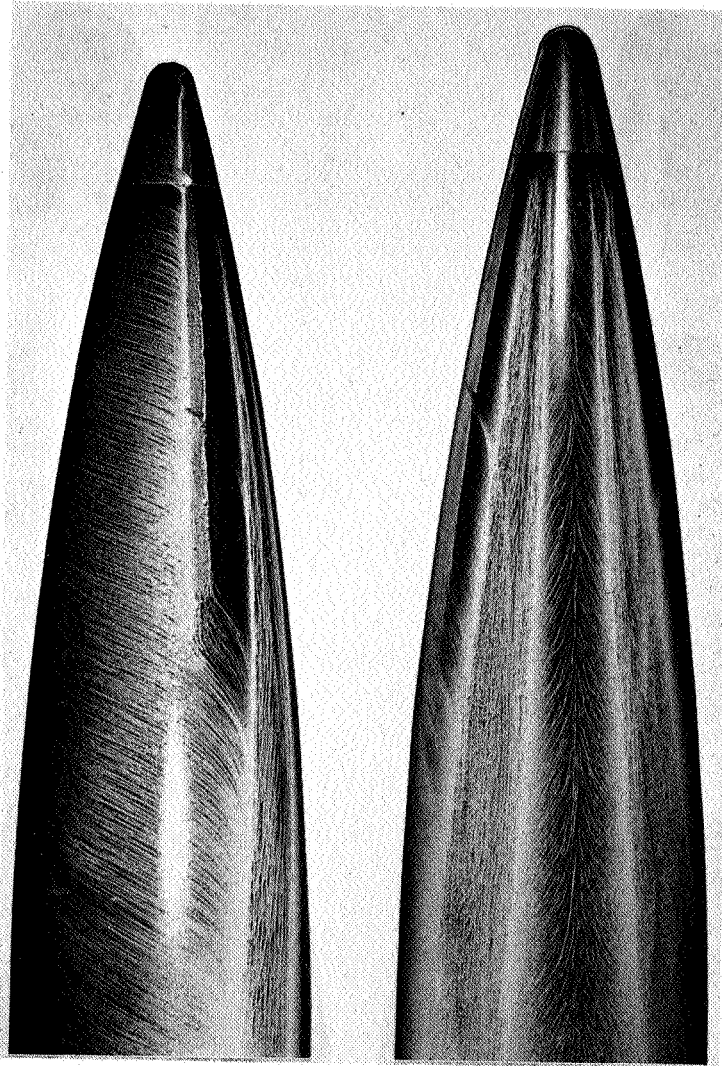


$\theta = 90^\circ$

$\theta = 180^\circ$

(c) $\alpha = 20^\circ$, CONCLUDED, CLOSE UP

ORIGINAL PAGE IS
OF POOR QUALITY

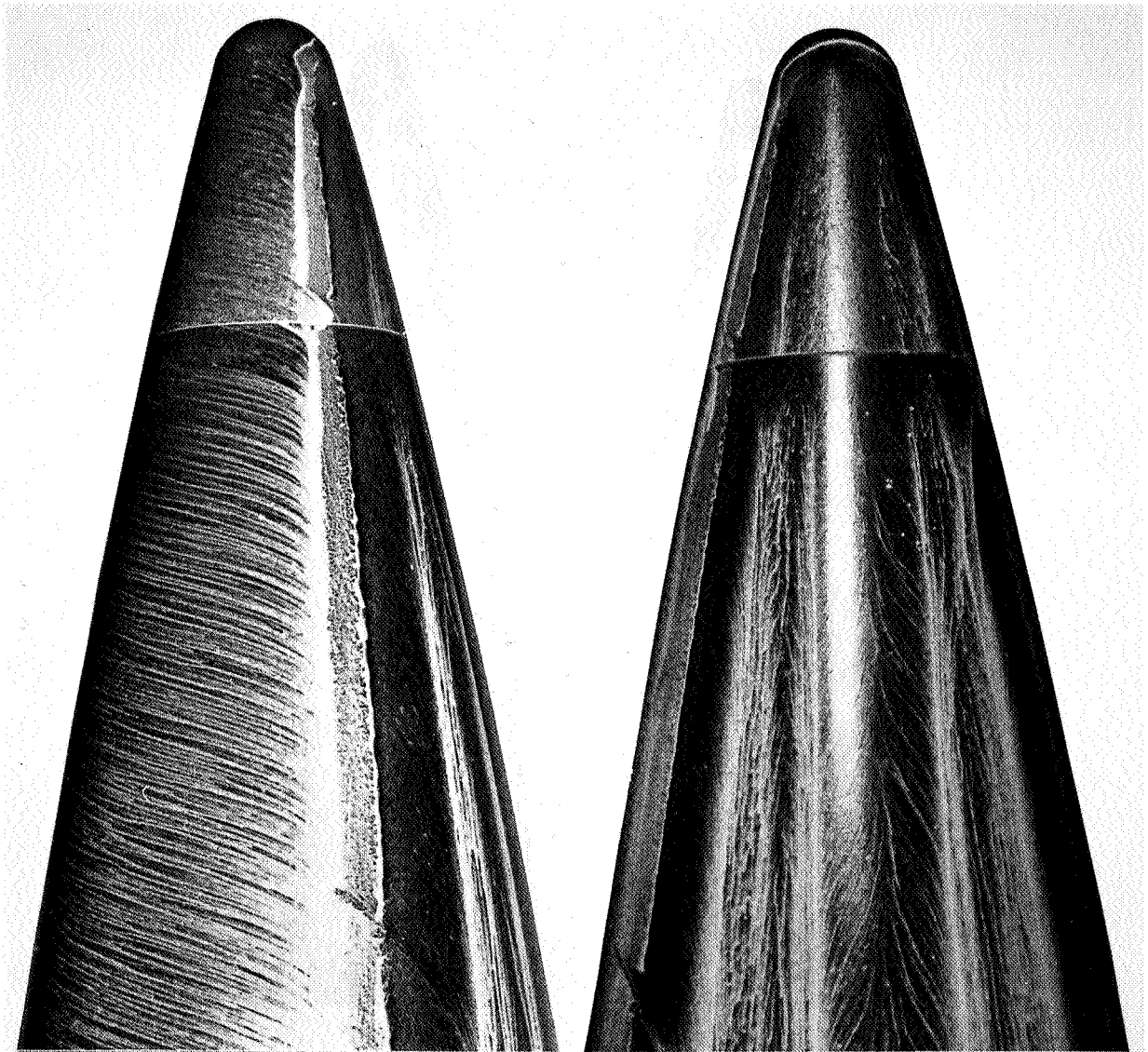


$\theta = 90^\circ$

$\theta = 180^\circ$

(d) $\alpha = 40^\circ$

ORIGINAL PAGE IS
OF POOR QUALITY

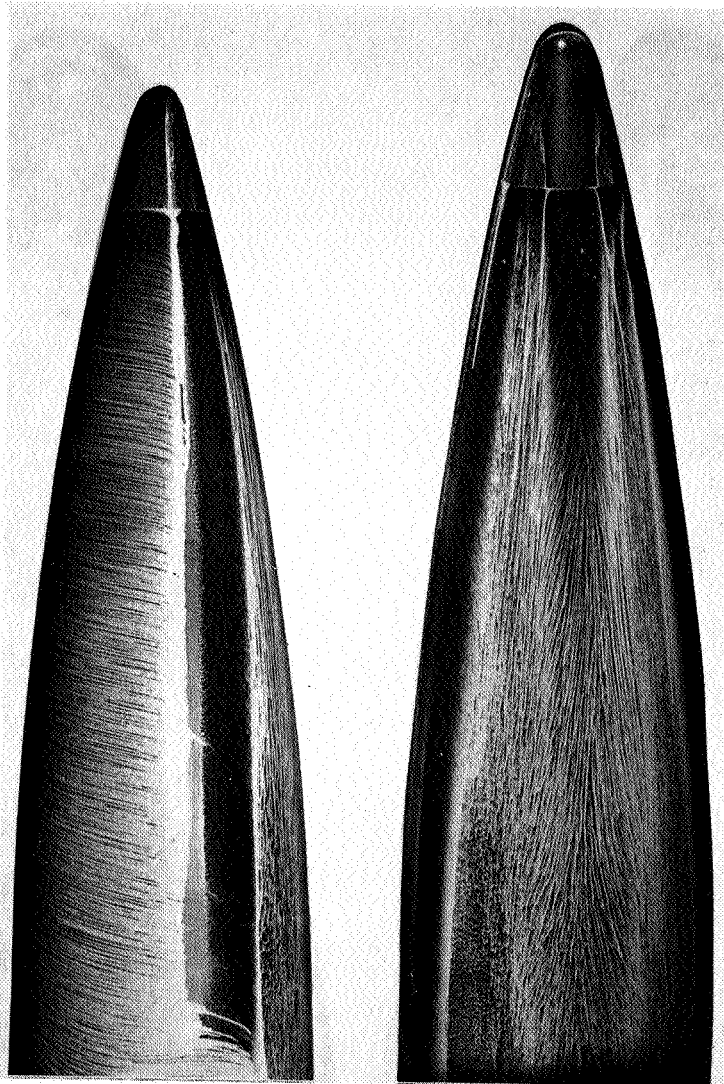


$\Theta = 90^\circ$

$\Theta = 180^\circ$

(d) $\alpha = 40^\circ$, CONCLUDED, CLOSE UP

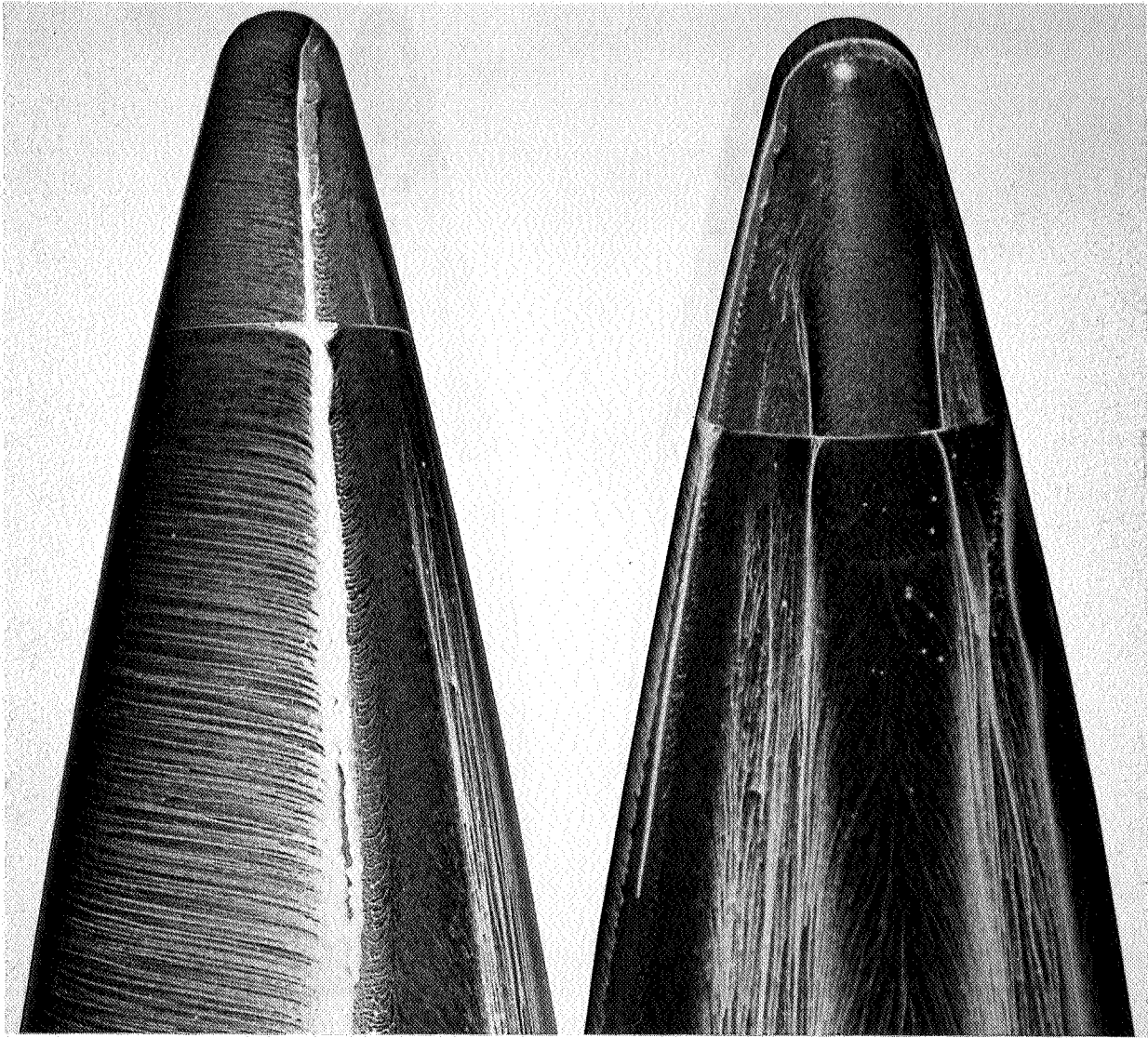
ORIGINAL PAGE IS
OF POOR QUALITY.



$\theta = 90^\circ$

$\theta = 180^\circ$

(e) $\alpha = 55^\circ$

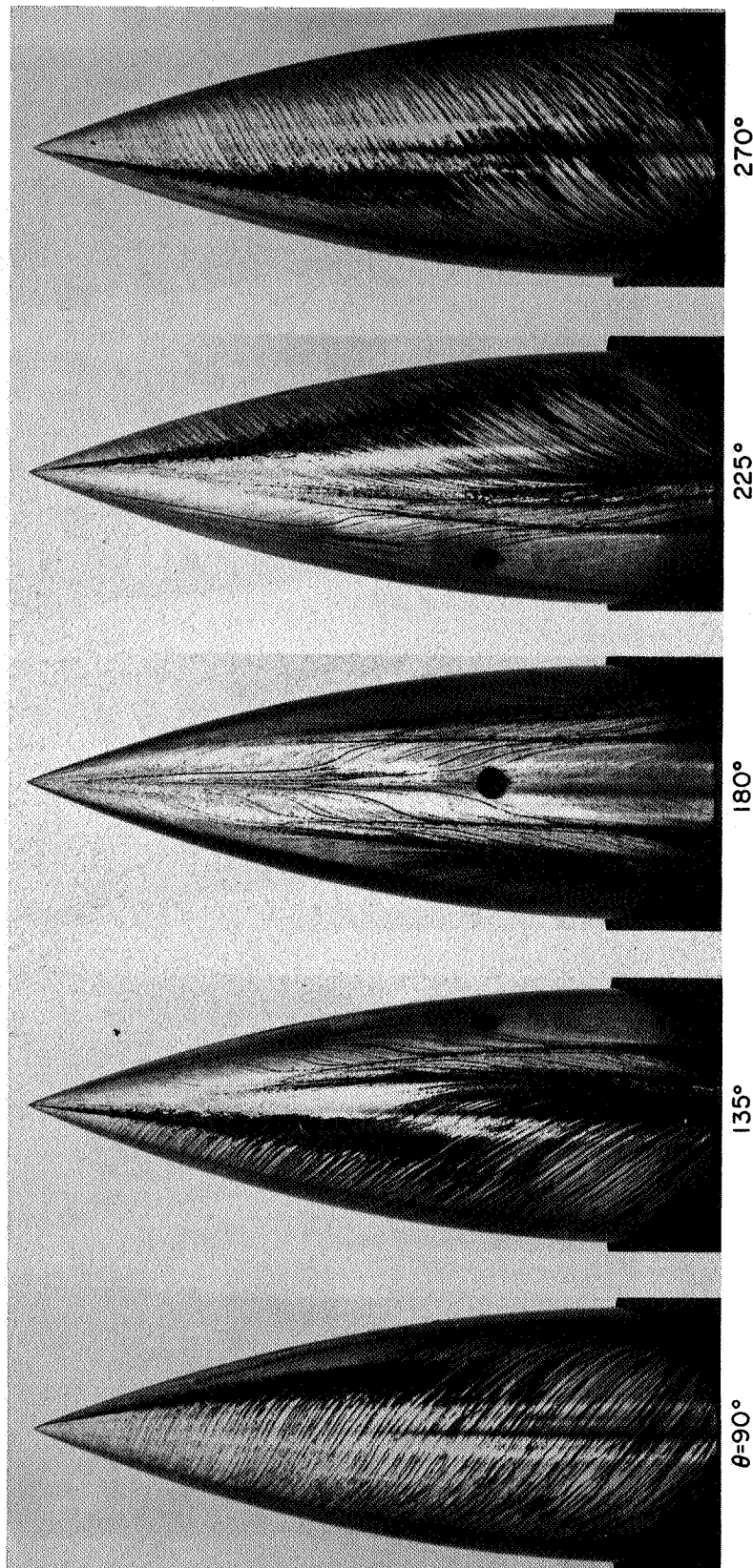
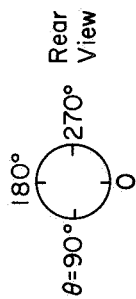


$\Theta = 90^\circ$

(e) $\alpha = 55^\circ$, CONCLUDED, CLOSE UP

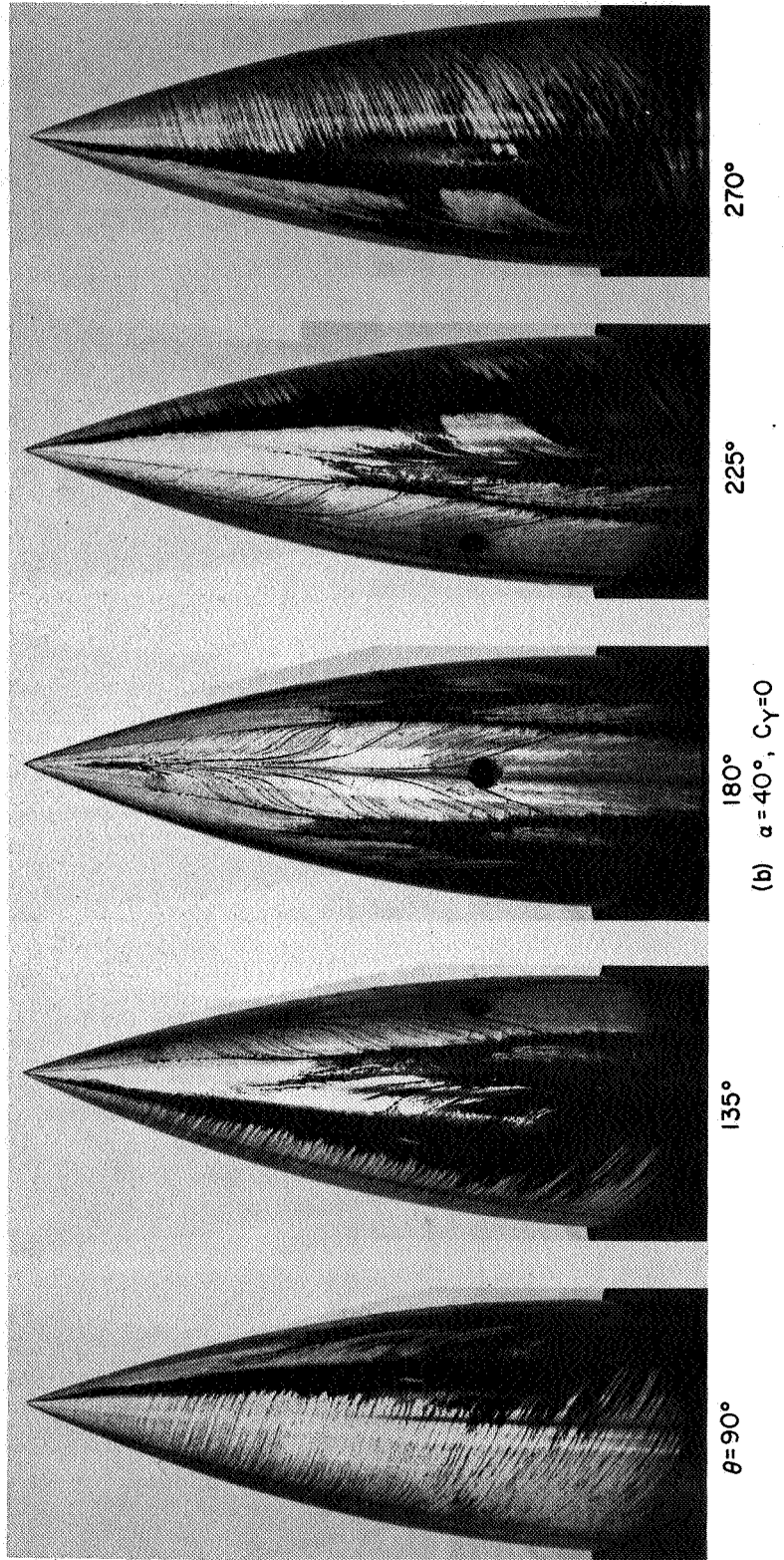
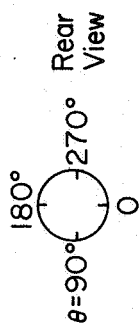
$\Theta = 180^\circ$

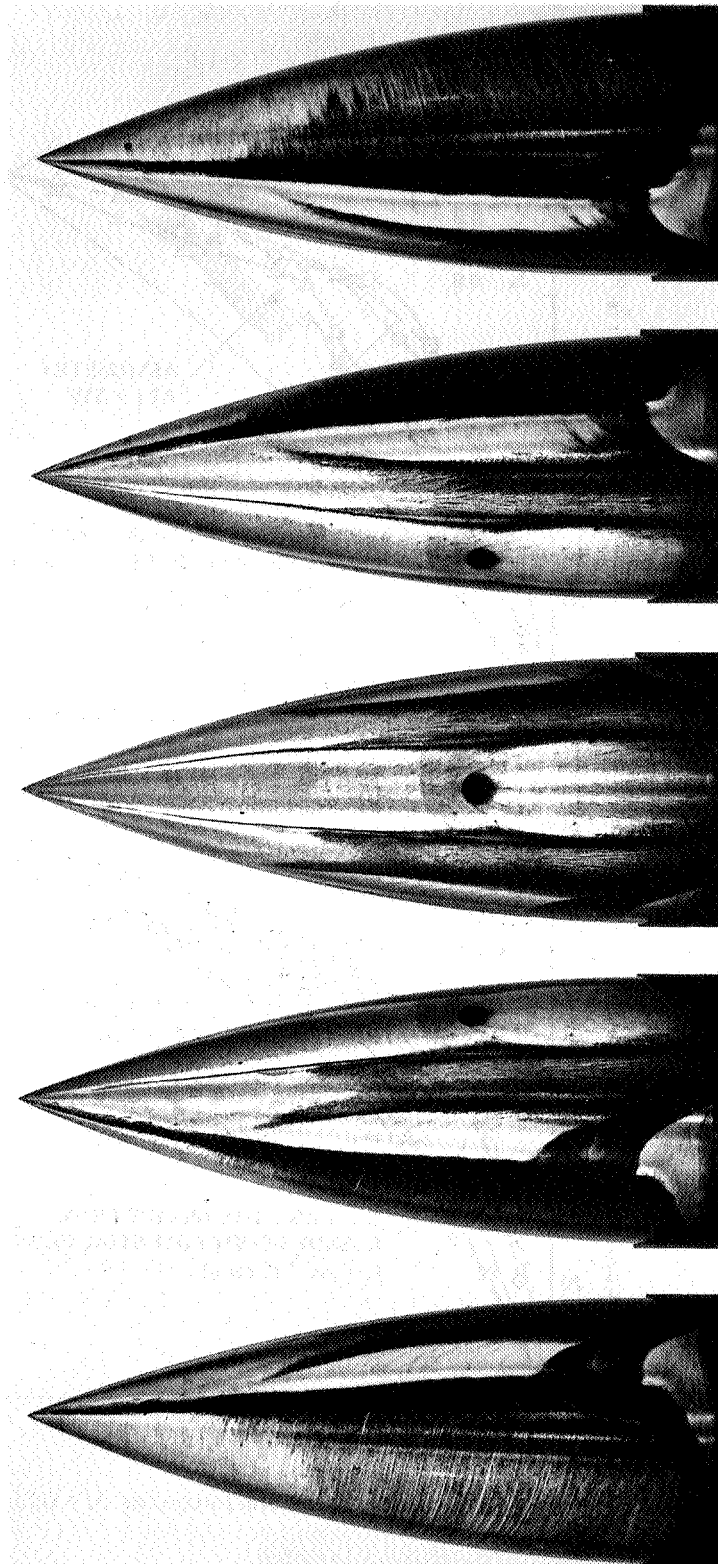
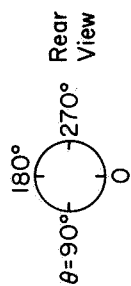
ORIGINAL PAGE IS
OF POOR QUALITY



(a) $\alpha = 30^\circ$, $C_Y = 0$

Figure 25.— Oil flow photographs for 2.5-ogive: $M = 0.25$, $R_d = 0.8 \times 10^6$.





(c) $\alpha = 55^\circ$ $C_Y = 0$

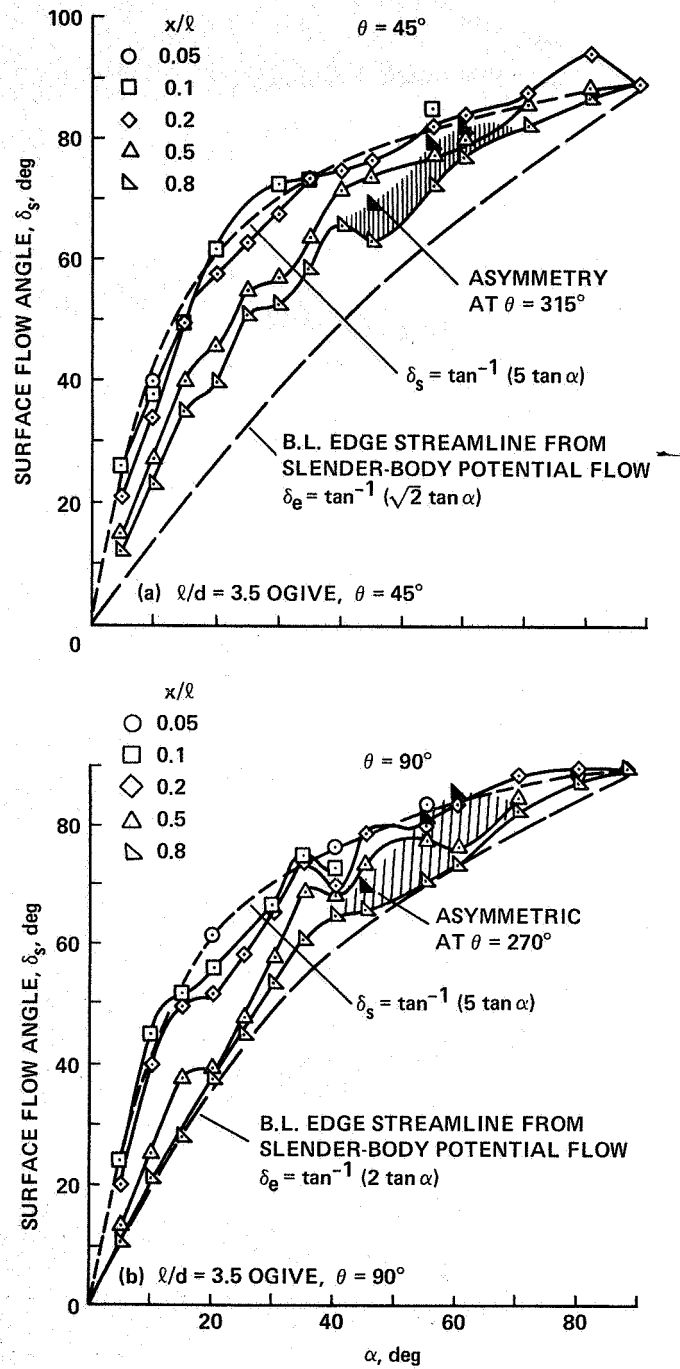
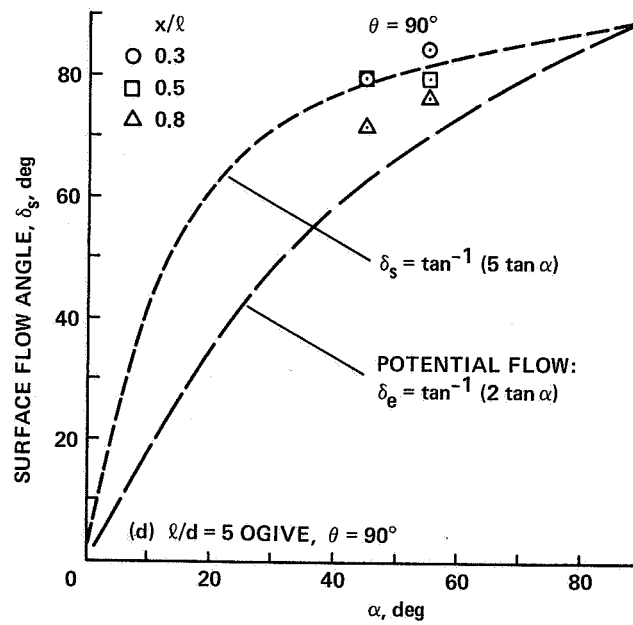
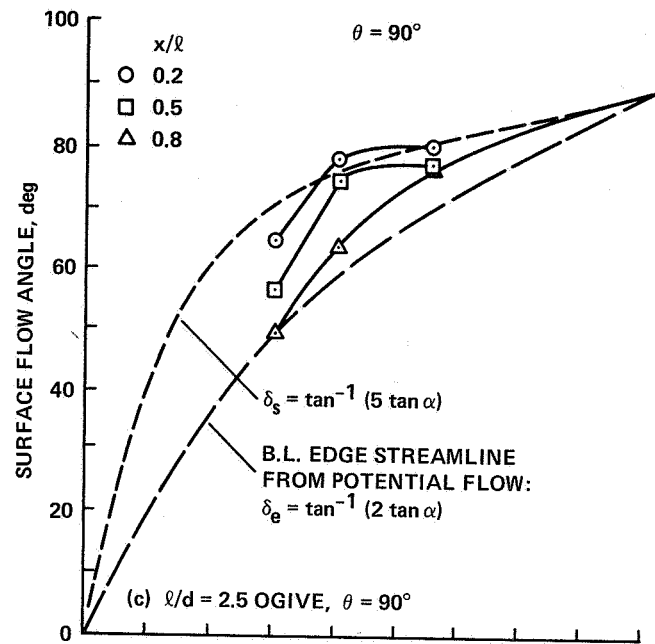
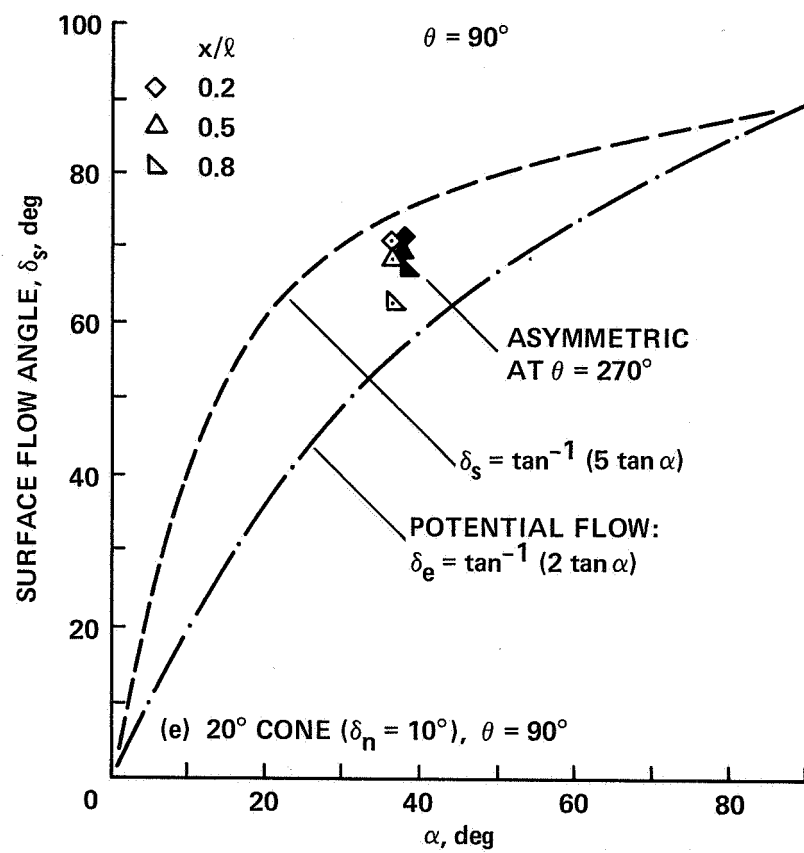


Figure 26.— Measured oil-flow angles for several forebodies: $M = 0.25$, $R_d = 0.8 \times 10^6$.





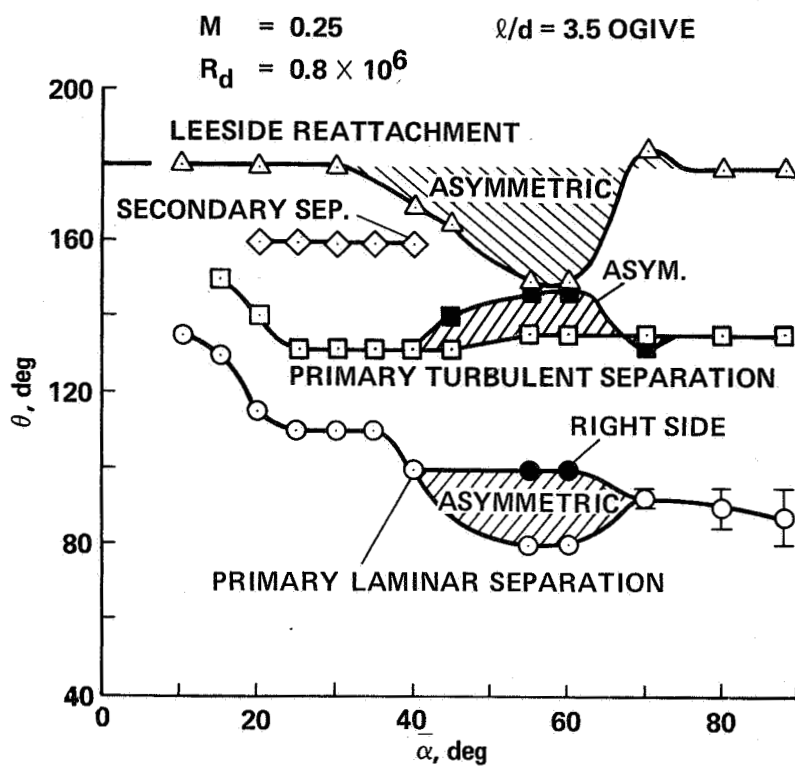


Figure 27.— Location of separation lines for 3.5-ogive: $M = 0.25$, $R_d = 0.8 \times 10^6$.

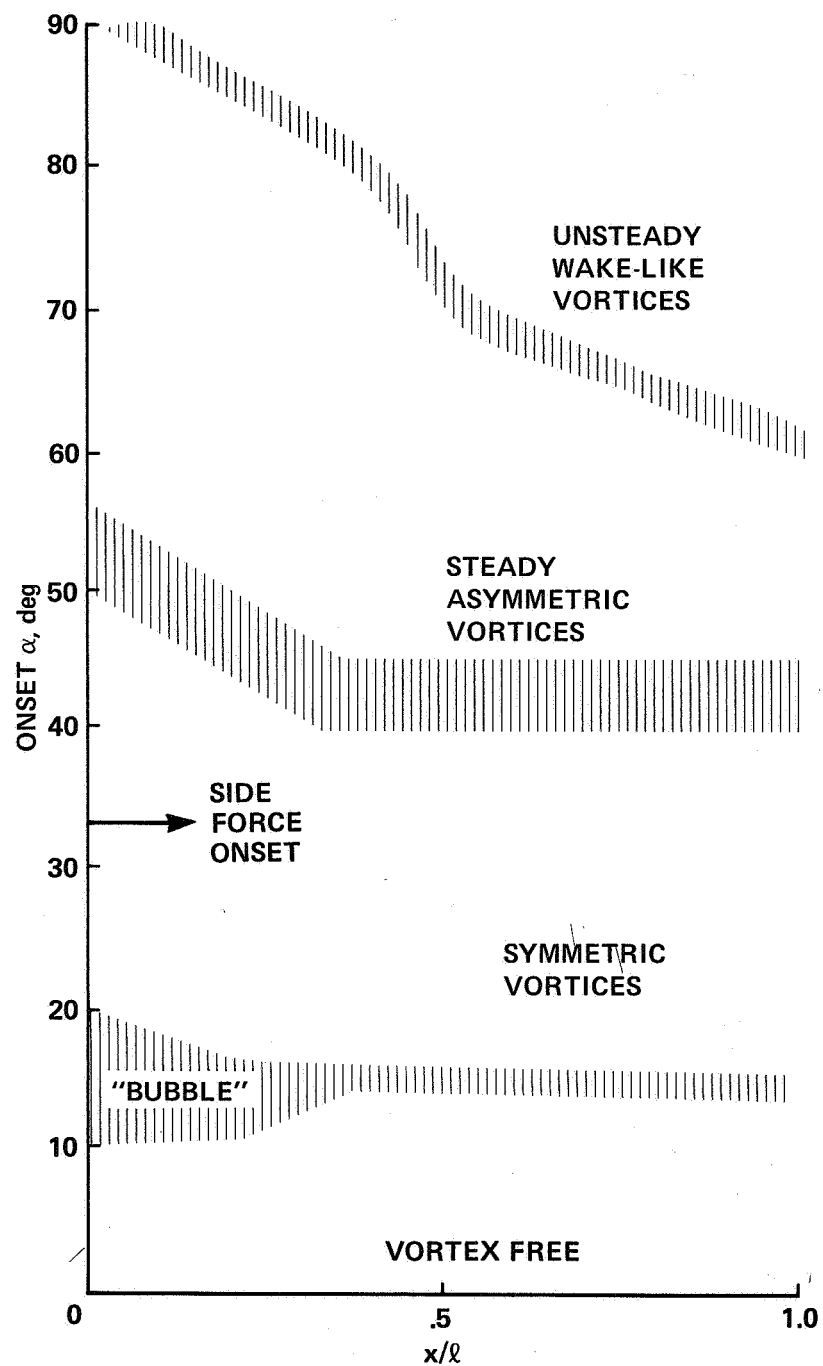


Figure 28.— Angle-of-attack boundaries for onset of various types of vortex-flow regimes for 3.5-ogive:
 $M = 0.25, R_d = 0.8 \times 10^6$.

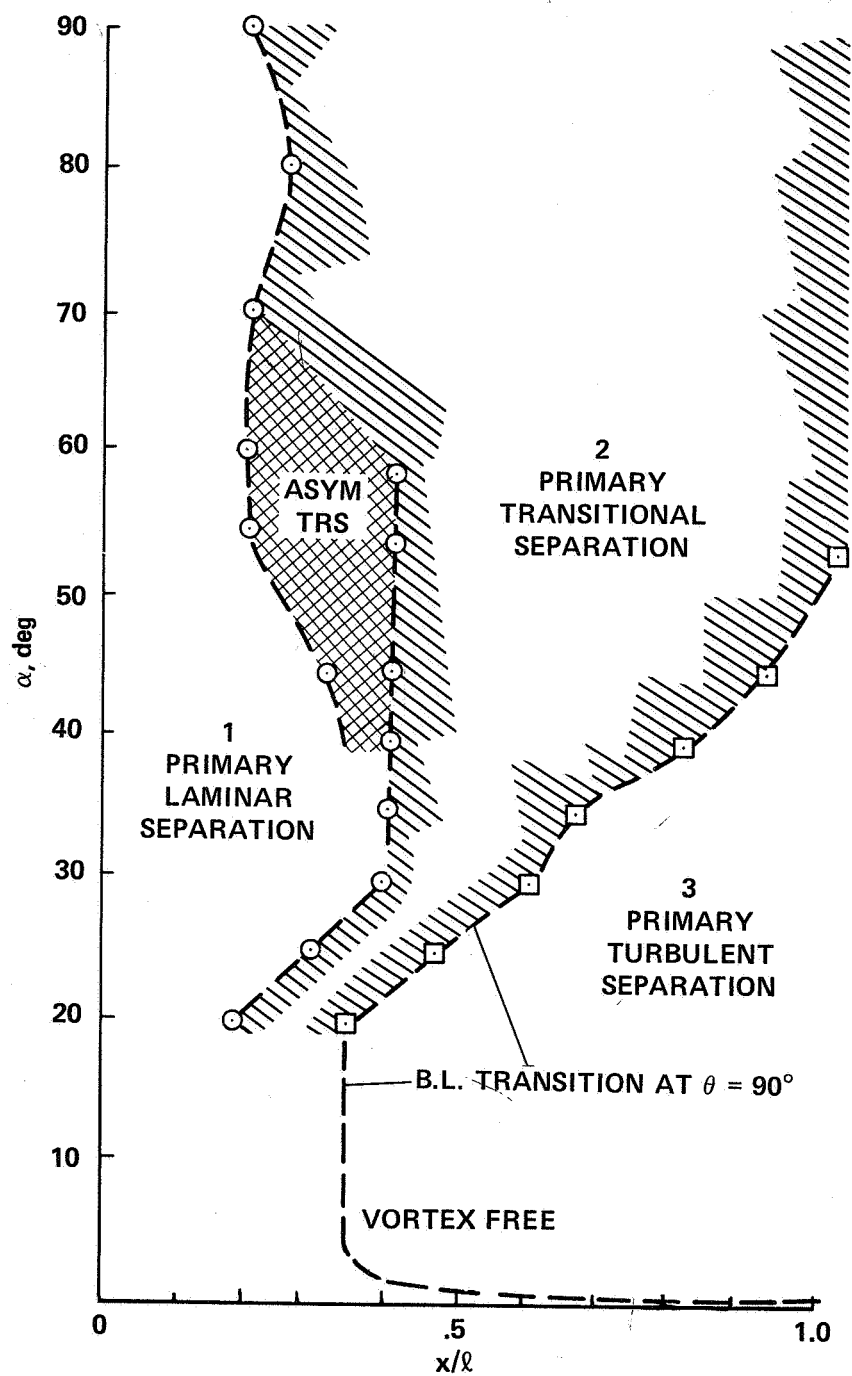


Figure 29.— Longitudinal location for beginning of transitional and turbulent types of primary-separation patterns for 3.5-ogive: $M = 0.25$, $R_d = 0.8 \times 10^6$.

1. Report No. NASA TM-86016		2. Government Accession No.		3. Recipient's Catalog No.	
4. Title and Subtitle FLOW-SEPARATION PATTERNS ON SYMMETRIC FOREBODIES				5. Report Date January 1986	
				6. Performing Organization Code	
7. Author(s) Earl R. Keener				8. Performing Organization Report No. A-9872	
9. Performing Organization Name and Address Ames Research Center Moffett Field, CA 94035				10. Work Unit No.	
				11. Contract or Grant No.	
				13. Type of Report and Period Covered Technical Memorandum	
12. Sponsoring Agency Name and Address National Aeronautics and Space Administration Washington, DC 20546				14. Sponsoring Agency Code 505-31-21	
15. Supplementary Notes Point of Contact: Earl R. Keener, Ames Research Center, MS 277-8, Moffett Field, CA 94035 (415) 694-6260- or FTS 464-6260					
16. Abstract <p>Flow-visualization studies of ogival, parabolic, and conical forebodies were made in a comprehensive investigation of the various types of flow patterns. Schlieren, vapor-screen, oil-flow, and sublimation flow-visualization tests were conducted over an angle-of-attack range from 0° to 88°, over a Reynolds-number range from 0.3×10^6 to 2.0×10^6 (based on base diameter), and over a Mach number range from 0.1 to 2. Several forebody models were tested; however, most of the tests were made with a tangent ogive forebody having a fineness ratio of 3.5, chosen because this forebody experiences large asymmetric forces at high angles of attack at low speed. The principal effects of angle of attack, Reynolds number, and Mach number on the occurrence of vortices, the position of vortex shedding, the principal surface-flow-separation patterns, the magnitude of surface-flow angles, and the extent of laminar and turbulent flow for symmetric, asymmetric, and wake-like flow-separation regimes are presented.</p> <p>It was found that the two-dimensional cylinder analogy was helpful in a qualitative sense in analyzing both the surface-flow patterns and the external flow field. The oil-flow studies showed three types of primary separation patterns at the higher Reynolds numbers owing to the influence of boundary-layer transition: primary-laminar, primary-transitional, and primary-turbulent separation. The effect of angle of attack and Reynolds number is to change the axial location of the onset and extent of the primary transitional and turbulent separation regions. Crossflow inflectional-instability vortices were observed on the windward surface at angles of attack from 5° to 55°. Their effect is to promote early transition. At low angles of attack, near 10°, an unexpected laminar-separation bubble occurs over the forward half of the forebody. At high angles of attack, at which vortex asymmetry occurs, the results support the proposition that the principal cause of vortex asymmetry is the hydrodynamic instability of the inviscid flow field. On the other hand, boundary-layer asymmetries also occur, especially at transitional Reynolds numbers; they contribute significantly to the flow asymmetry. The position of asymmetric vortex shedding moves forward with increasing angle of attack and with increasing Reynolds number, and moves rearward with increasing Mach number.</p>					
17. Key Words (Suggested by Author(s)) Effects of Mach number; Aerodynamics of bodies; High angle of attack; Flow visualization studies; Vortex shedding; Effect of Reynolds number; Boundary-Layer transition			18. Distribution Statement Unclassified - Unlimited Subject Category 02		
19. Security Classif. (of this report) Unclassified		20. Security Classif. (of this page) Unclassified		21. No. of Pages 141	
				22. Price A07	